12-2018

Transparent Conductive Films Based on Polymer-Encapsulated Graphene Oxide Sheets

Mykhailo Savchak
Clemson University, msavcha@g.clemson.edu

TRANSPARENT CONDUCTIVE FILMS BASED ON POLYMER-ENCAPSULATED GRAPHENE OXIDE SHEETS

A Dissertation
Presented to
the Graduate School of
Clemson University

In Partial Fulfillment
of the Requirements for the Degree
Doctor of Philosophy
Materials Science and Engineering

---

by
Mykhailo Savchak
December 2018

Accepted by:
Dr. Igor Luzinov, Committee Chair
Dr. Marek Urban
Dr. Stephen Foulger
Dr. George Chumanov

ABSTRACT

Transparent conductive films (TCFs) play a key role in number of devices, including solar panels, LCD/OLED displays and touchscreens. Graphene has emerged as a promising material in this area due to its unique mechanical and electrical properties. Despite noteworthy progress in the fabrication of large-area graphene sheet-like nanomaterials, the vapor-based processing still requires sophisticated equipment and a multistage handling of the material. An alternative approach to manufacturing functional graphene-based films includes the employment of graphene oxide (GO) micron-scale sheets as precursors. However, search for a scalable manufacturing technique for the production of high-quality GO nanoscale films with high uniformity and high electrical conductivity is still continuing.

The study presented in this dissertation is dedicated to the fabrication and characterization of electrically conductive films made of reduced graphene oxide sheets (rGO) deposited on both rigid and flexible substrates. Here we show that conventional dip-coating technique can offer fabrication of high quality mono- and bilayered films made of GO sheets. The method is based on our recent discovery that encapsulating individual GO sheets in a nanometer-thick copolymer layer poly(Oligo Ethylene Glycol methyl ether Methacrylate [OEGMA]- Glycidyl Methacrylate [GMA]) allows for the nearly perfect formation of the GO layers on hydrophilic substrates. By thermal reduction at 1000 ºC the bilayers (cemented by a carbon-forming polymer linker) are converted into highly conductive and transparent reduced GO films with a high conductivity up to 10^4 S/cm and optical transparency on the level of 90%. The value is the highest electrical conductivity

reported for thermally reduced nanoscale GO films and is close to the conductivity of indium tin oxide (ITO) currently in use for transparent electronic devices, thus making these layers intriguing candidates for replacement of ITO films.

To facilitate the deposition of GO sheets on rigid and flexible hydrophobic substrates, the amphiphilic copolymer poly(Oligo Ethylene Glycol methyl ether Methacrylate [OEGMA]- Glycidyl Methacrylate [GMA]- Lauryl Methacrylate [LMA]) with additional hydrophobic block was used. The results show that the obtained GO layers had well-defined and uniform structure. Thus, it leads to enhanced hydrophobic-hydrophobic (van der Waals) interaction between the hydrophobic substrate and GO. To this end, the morphology, opto-electrical properties and electro-mechanical stability of chemically reduced GO layers are also investigated. Finally, we demonstrate the excellent stability of rGO on polymeric substrates with no delamination or significant loss in conductivity even after 50000 bending cycle.

DEDICATION

I dedicate this dissertation to my loving, supportive and caring wife, Oksana Savchak, whose unconditional love and kind attitude gave me the strength and belief to follow my dreams. I also dedicate this dissertation to my always encouraging and ever faithful parents, Stefan and Mariya Savchak, and to my brother, Vasyl Savchak.

ACKNOWLEDGEMENTS

First, I would like to acknowledge my advisor, Dr. Igor Luzinov, for providing me with this wonderful opportunity to be a part of his research group throughout my graduate study at Clemson University. I am extremely grateful for his wise mentorship, patience, valuable insights, consistent encouragement and support. As a person with an amicable and positive disposition, he always made himself available to answer my questions and give me advice despite his busy schedules. I consider it a great honor to do my doctoral research under his guidance and to grow as a scientist learning from his research experience and expertise. Thank you, Dr. Luzinov, for making a difference in my life and helping me to become a better person.

I must also extend thanks and appreciation to my committee members: Dr. George Chumanov, Dr. Stephen Foulger and Dr. Marek Urban for agreeing to serve on my committee. I'm grateful for their time, support and insightful suggestions for my research.

I'm thankful to Dr. Ruslan Burtovyy for being very encouraging, supportive and teaching me how to use AFM. I thank Dr. Konstantin Kornev for being kind enough to extend his help at various stages of my research, whenever I approached him. A special thanks to Dr. Arthur Salamatin, Dr. Chengqi Zhang and Luke Sande for providing me help with bending tests of thin films.

I would like to acknowledge my friends and group members, Drs. Yuriy Galabura, Jake Townsend, Nikolay Borodinov; Liying Wei, Charles Nikon, Mastooreh Seyedeh, Erik

Sanchez Antonio, Hayley Weir, and Pu Zhu; Drs. Tugba Demir, Fehime Vatansever, Anna Paola Soliani and James Giammarco for their support and inspiring moments.

I also want to express my gratitude to Dr. Olga Kuksenok for her kindness, support and always welcoming me into her group.

A debt of gratitude is owed to my friend Dr. Alex Klep, who always have found time to help fix my car.

I would like to thank Kimberly Ivey, who was always ready to help, teach, and educate me on how to use analytical instruments. Also, I offer special thanks to James Lowe for the academic support in using his experimental tools. I'm especially thankful to Dr. W. Harrell and Daniel Cutshall for providing access to electrical IV measurements; Dr. Tsukruk and Ruilong Ma from Georgia Institute of technology for doing XPS measurements on our samples; Mark Anayee for being a great friend and helping me with the research.

I would also like to thank Dr. Taghi Darroudi, and Mr. Dayton Cash for their help at Electron Microscopy Laboratory.

I thank everyone from the Department of Materials Science and Engineering, Clemson University, for this memorable experience.

TABLE OF CONTENTS

Page

LIST OF FIGURES

LIST OF TABLES

CHAPTER ONE

INTRODUCTION

Transparent conductive films (TCFs), materials possessing high electrical conductivity and optical transparency, have received wide attention due to their applications in solar cells, displays, gas/moisture/biosensors, thin film transistors and many others. ITO (indium tin oxide), for example, is often used when conductivity has to be paired with transparency. However, employment of such metal oxide appears to be increasingly problematic because of limited indium source, its susceptibility to ion diffusion into polymer substrate layers, their instability in acid or base, and the brittle nature of metal oxides [1-7]. Many new materials or structures such as graphene, carbon nanotubes (CNTs)[8], metal nanowires[9], silver nanoparticles [10], conducting polymers [11] have been tested as possible replacement for ITO [12 13]. Graphene (GR), for instance, appears to be a strong contender due to its unique physical and electrical properties: high carrier charge mobility (conductivity on the order of 10^5 S/cm), outstanding mechanical (1 TPa Young's modulus, high flexibility, high aspect ratio) and optical (90 % transmittance for corresponding sheet resistance of 20 Ω/sq) [14]. Whereas this substitution is highly feasible, based on our current knowledge of GR properties the major stumbling block is practical and cost-effective fabrication process including synthesis of GR itself and GR functional pattern formation.

An alternative low-cost and up-scalable method is the reduction of graphene oxide (GO) (an oxidized form of graphene) to its conductive form – reduced graphene oxide (rGO). Moreover, due to the presence of oxygen-containing functional groups physical

properties of GO can be easily tuned with an appropriate chemistry applied, which gives it high processability in various polar solvents (water included) unlike pristine graphene [15]. The literature on graphene-based electronics abounds with the examples of employment of GO sheets in fabrication of large area TCFs [16-18]. To this end, rGO-based films have not yet approached pristine GR in terms of its conductive properties, although its optical properties showed a great promise [19].

When considering the integration of TCFs into flexible electronics the following requirements for TCFs should be met: $R_s \approx 500 - 2{,}000\ \Omega$/sq and T > 90% at 550 nm [14]. Furthermore, flexible electronics have to incorporate all functional attributes of conventional rigid electronics while surviving significant and often repeatable mechanical deformations.[20] Bendable, foldable, rollable, wearable flexible electronic devices assembled on polymeric substrates have been already transforming the ways in which electronics is used.[21-23] The flexible devices are actively considered or already used for a number of applications including packaging, communications, alternative energy, display technology, sensors, biomedical devices, frequency identification tags [20, 23-33]. A key concern for flexible electronic engineering is electro-mechanical behavior of devices or ability of the incorporated materials to withstand the applied mechanical stresses while retaining satisfactory electrical performance [23-24, 34-35]. Thus far, the embedding of GR or GO into bendable electronics has been achieved, but direct and cost-effective deposition of GR/GO on flexible polymeric substrates has proved to be a challenging task [36].

To this end, the ultimate goal of this dissertation was to fabricate and characterize (study its opto-electrical and mechanical properties) electrically conductive reduced

graphene oxide (rGO) films on both rigid and flexible substrates. The work was conducted as follows. First, the methodology for the formation of uniform and well-defined GO mono/bilayers on rigid substrates was developed. Specifically, our approach was based on enveloping GO into especially designed molecular bottlebrush reactive copolymers such as poly(Oligo Ethylene Glycol methyl ether Methacrylate [OEGMA]- Glycidyl Methacrylate [GMA]) (P1) and poly(Oligo Ethylene Glycol methyl ether Methacrylate [OEGMA]- Glycidyl Methacrylate [GMA]- Lauryl Methacrylate [LMA]) (P2), that allows formation of well-defined GO layers via simple dip-coating procedure. Namely, using GO modified with P1 (GO-P1) the uniform films were obtained only on hydrophilic substrates while GO modified with more hydrophobic or amphiphilic copolymer P2 (GO-P2) rendered itself suitable for both hydrophilic and hydrophobic rigid/flexible substrates. Next, chemical or thermal reduction methods were employed to make copolymer-modified GO films electrically conductive. A general schematic of the typical workflow for the fabrication of rGO films on flexible substrate is depicted in **Figure 1.1**.

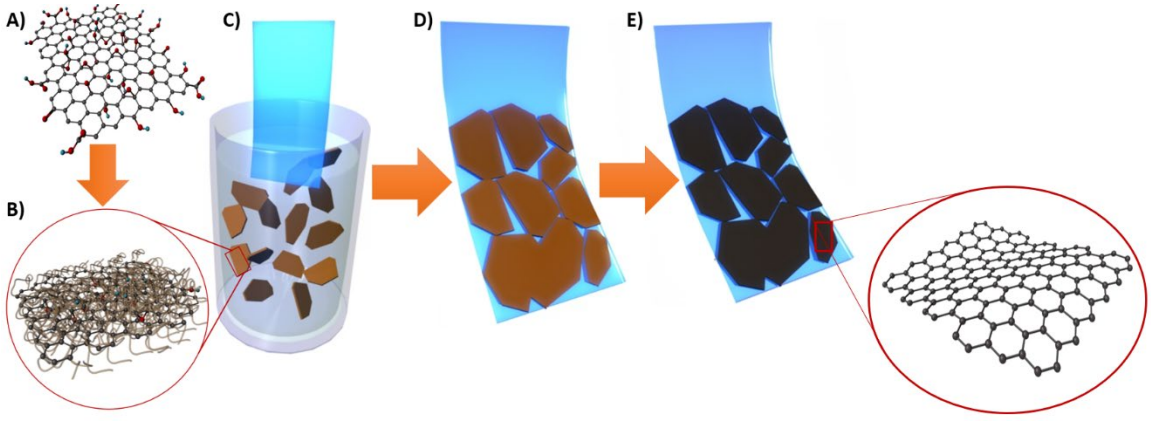

Figure 1.1: (A-E) Diagram representation of the approach employed by this project: A) and B) functionalization of pristine GO sheets with amphiphilic copolymer. C) Deposition of a monolayer of GO enveloped with a polymer layer by dip-coating. D) Final monolayer of polymer-modified GO film on flexible substrate. E) Reduction step.

Specifically, **Figure 1.1A** and **Figure 1.1B** represent the synthesis and modification of GO sheets with copolymer. **Figure 1.1C** represents the dip-coating procedure to achieve monolayer deposition of copolymer-modified GO sheets on the substrate (**Figure 1.1D**). **Figure 1.1E** shows the reduction step at which GO converts to electrically conductive rGO due to removal of GO functionalities and copolymer. The morphology, structure and properties of deposited GO films were characterized using atomic force microscopy (AFM), optical microscopy, Raman spectroscopy, X-ray photon spectroscopy, Fourier transform infrared spectroscopy (FTIR), UV-Vis, thermal gravimetric analysis (TGA), differential scanning calorimetry (DSC) and mechanical testing (tensile and bending tests).

This dissertation is structured as follows:

- **Chapter 2** of this dissertation gives a literature review of methods for the synthesis of graphene/graphene oxide and their structure-property relationship. It also discusses functionalization techniques of GO surface, GO film formation methods and challenges in the fabrication of reduced GO films with high electrical conductivity and optical transparency.
- **Chapter 3** describes the synthesis and characterization of sterically stabilized GO sheets in water, subsequent formation of a monolayer and multilayer (bilayer) films based on polymer modified GO sheets on hydrophilic rigid substrate (SiO_2/Si).
- **Chapter 4** focuses on morphological and opto-electrical properties of thermally reduced GO-P1 monolayers and bi-layers. Furthermore, this chapter discusses the method for electronic band gap determination.

- **Chapter 5** is devoted to the deposition of GO modified with GO-P2 directly on hydrophobic silane-modified SiO_2/Si and polymeric substrates via dip-coating from water solution. Additionally, this chapter includes comparative studies of interaction of GO-P1 and GO-P2 with the hydrophobic interface using quartz crystal microbalance with dissipation monitoring (QCM-D).
- **Chapter 6** discusses morphology, structure, opto-electrical and mechanical properties of chemically reduced GO-P2 films prepared on hydrophobic silane-modified SiO_2/Si as well as polymeric substrates. Specifically, electro-mechanical response and life-cycle durability of rGO-P2 films on plastics of different thicknesses have been investigated.
- **Chapter 7** concludes and summarizes the findings of this dissertation.

References

1. Yin, Z.; Sun, S.; Salim, T.; Wu, S.; Huang, X.; He, Q.; Lam, Y. M.; Zhang, H., Organic Photovoltaic Devices Using Highly Flexible Reduced Graphene Oxide Films as Transparent Electrodes. *Acs Nano* **2010,** *4* (9), 5263-5268.

2. Schlatmann, A. R.; Floet, D. W.; Hilberer, A.; Garten, F.; Smulders, P. J. M.; Klapwijk, T. M.; Hadziioannou, G., Indium contamination from the indium-tin-oxide electrode in polymer light-emitting diodes. *Applied Physics Letters* **1996,** *69* (12), 1764-1766.

3. Scott, J. C.; Kaufman, J. H.; Brock, P. J.; DiPietro, R.; Salem, J.; Goitia, J. A., Degradation and failure of MEH-PPV light-emitting diodes. *Journal of Applied Physics* **1996,** *79* (5), 2745-2751.

4. Andersson, A.; Johansson, N.; Broms, P.; Yu, N.; Lupo, D.; Salaneck, W. R., Fluorine tin oxide as an alternative to indium tin oxide in polymer LEDs. *Advanced Materials* **1998,** *10* (11), 859-+.

5. Boehme, M.; Charton, C., Properties of ITO on PET film in dependence on the coating conditions and thermal processing. *Surface & Coatings Technology* **2005,** *200* (1-4), 932-935.

6. Li, X.; Zhu, Y.; Cai, W.; Borysiak, M.; Han, B.; Chen, D.; Piner, R. D.; Colombo, L.; Ruoff, R. S., Transfer of Large-Area Graphene Films for High-Performance Transparent Conductive Electrodes. *Nano Letters* **2009,** *9* (12), 4359-4363.

7. Han, T.-H.; Kim, H.; Kwon, S.-J.; Lee, T.-W., Graphene-based flexible electronic devices. *Materials Science and Engineering: R: Reports* **2017,** *118* (Supplement C), 1-43.

8. Ou, E. C. W.; Hu, L.; Raymond, G. C. R.; Soo, O. K.; Pan, J.; Zheng, Z.; Park, Y.; Hecht, D.; Irvin, G.; Drzaic, P.; Gruner, G., Surface-Modified Nanotube Anodes for High Performance Organic Light-Emitting Diode. *ACS Nano* **2009,** *3* (8), 2258-2264.

9. Yu, Z.; Zhang, Q.; Li, L.; Chen, Q.; Niu, X.; Liu, J.; Pei, Q., Highly Flexible Silver Nanowire Electrodes for Shape-Memory Polymer Light-Emitting Diodes. *Advanced Materials* **2011,** *23* (5), 664-668.

10. Linnet, J.; Walther, A. R.; Wolff, C.; Albrektsen, O.; Mortensen, N. A.; Kjelstrup-Hansen, J., Transparent and conductive electrodes by large-scale nano-structuring of noble metal thin-films. *Opt. Mater. Express* **2018,** *8* (7), 1733-1746.

11. Cai, M.; Ye, Z.; Xiao, T.; Liu, R.; Chen, Y.; Mayer, R. W.; Biswas, R.; Ho, K.-M.; Shinar, R.; Shinar, J., Extremely Efficient Indium–Tin-Oxide-Free Green Phosphorescent Organic Light-Emitting Diodes. *Advanced Materials* **2012,** *24* (31), 4337-4342.

12. Han, T.-H.; Lee, Y.; Choi, M.-R.; Woo, S.-H.; Bae, S.-H.; Hong, B. H.; Ahn, J.-H.; Lee, T.-W., Extremely efficient flexible organic light-emitting diodes with modified graphene anode. *Nature Photonics* **2012,** *6*, 105.

13. Ning, J.; Hao, L.; Jin, M. H.; Qiu, X. Y.; Shen, Y. D.; Liang, J. X.; Zhang, X. H.; Wang, B.; Li, X. L.; Zhi, L. J., A Facile Reduction Method for Roll-to-Roll Production of High Performance Graphene-Based Transparent Conductive Films. *Advanced Materials* **2017,** *29* (9), 8.

14. Bonaccorso, F.; Sun, Z.; Hasan, T.; Ferrari, A. C., Graphene photonics and optoelectronics. *Nature Photonics* **2010,** *4* (9), 611-622.

15. Kuila, T.; Bose, S.; Mishra, A. K.; Khanra, P.; Kim, N. H.; Lee, J. H., Chemical functionalization of graphene and its applications. *Progress in Materials Science* **2012,** *57* (7), 1061-1105.

16. Cote, L. J.; Kim, F.; Huang, J. X., Langmuir-Blodgett Assembly of Graphite Oxide Single Layers. *Journal of the American Chemical Society* **2009,** *131* (3), 1043-1049.

17. Jia, J. J.; Kan, C.; Lin, X. M.; Shen, X.; Kim, J. K., Effects of processing and material parameters on synthesis of monolayer ultralarge graphene oxide sheets. *Carbon* **2014,** *77*, 244-254.

18. Zhao, J. P.; Pei, S. F.; Ren, W. C.; Gao, L. B.; Cheng, H. M., Efficient Preparation of Large-Area Graphene Oxide Sheets for Transparent Conductive Films. *ACS nano* **2010,** *4* (9), 5245-5252.

19. Eda, G.; Fanchini, G.; Chhowalla, M., Large-area ultrathin films of reduced graphene oxide as a transparent and flexible electronic material. *Nature Nanotechnology* **2008,** *3* (5), 270-274.

20. Harris, K. D.; Elias, A. L.; Chung, H. J., Flexible electronics under strain: a review of mechanical characterization and durability enhancement strategies. *J. Mater. Sci.* **2016,** *51* (6), 2771-2805.

21. Wang, X.; Liu, Z.; Zhang, T., Flexible Sensing Electronics for Wearable/Attachable Health Monitoring. *Small* **2017,** *13* (25), 1602790.

22. Ervin, M. H.; Le, L. T.; Lee, W. Y., Inkjet-Printed Flexible Graphene-Based Supercapacitor. *Electrochimica Acta* **2014,** *147* (Supplement C), 610-616.

23. Siegel, D. S.; Shivakumar, S. J.; National Research Council, *The Flexible Electronics Opportunity*. National Academies Press: Washington, 2014.

24. Katsarelis, C. C. Understanding the impact of mechanical damage on the electrical performance of metallic thin films during strain. MS Thesis, Clemson University, 2017.

25. Jain, K.; Klosner, M.; Zemel, M.; Raghunandan, S., Flexible electronics and displays: High-resolution, roll-to-roll, projection lithography and photoablation processing technologies for high-throughput production. *Proceedings of the IEEE* **2005,** *93* (8), 1500-1510.

26. Kim, S. J.; Choi, K.; Lee, B.; Kim, Y.; Hong, B. H., Materials for Flexible, Stretchable Electronics: Graphene and 2D Materials. In *Annual Review of Materials Research, Vol 45*, Clarke, D. R., Ed. 2015; Vol. 45, pp 63-84.

27. Ma, Y. J.; Jang, K. I.; Wang, L.; Jung, H. N.; Kwak, J. W.; Xue, Y. G.; Chen, H.; Yang, Y. Y.; Shi, D. W.; Feng, X.; Rogers, J. A.; Huang, Y. G., Design of Strain-Limiting Substrate Materials for Stretchable and Flexible Electronics. *Advanced Functional Materials* **2016,** *26* (29), 5345-5351.

28. Trung, T. Q.; Lee, N. E., Materials and devices for transparent stretchable electronics. *Journal of Materials Chemistry C* **2017,** *5* (9), 2202-2222.

29. Wagner, S.; Bauer, S., Materials for stretchable electronics. *Mrs Bulletin* **2012,** *37* (3), 207-217.

30. Wong, W. S.; Salleo, A., *Flexible electronics : materials and applications*. Springer: New York, 2009.

31. Forrest, S. R., The path to ubiquitous and low-cost organic electronic appliances on plastic. *Nature* **2004,** *428* (6986), 911-918.

32. Virkki, J.; Bjorninen, T.; Kellomaki, T.; Merilampi, S.; Shafiq, I.; Ukkonen, L.; Sydanheimo, L.; Chan, Y. C., Reliability of washable wearable screen printed UHF RFID tags. *Microelectronics Reliability* **2014,** *54* (4), 840-846.

33. Park, S.; Vosguerichian, M.; Bao, Z. A., A review of fabrication and applications of carbon nanotube film-based flexible electronics. *Nanoscale* **2013,** *5* (5), 1727-1752.

34. Cairns, D. R.; Crawford, G. P., Electromechanical properties of transparent conducting substrates for flexible electronic displays. *Proceedings of the IEEE* **2005,** *93* (8), 1451-1458.

35. Cordill, M. J.; Glushko, O.; Kreith, J.; Marx, V. M.; Kirchlechner, C., Measuring electro-mechanical properties of thin films on polymer substrates. *Microelectronic Engineering* **2015,** *137*, 96-100.

36. Han, T.-H.; Kim, H.; Kwon, S.-J.; Lee, T.-W., Graphene-based flexible electronic devices. *Materials Science and Engineering: R: Reports* **2017,** *118*, 1-43.

CHAPTER TWO

LITERATURE REVIEW

2.1: Graphene

Graphene is atomically thick, two-dimensional sheet composed of sp^2 carbon atoms arranged in a honeycomb structure, as shown in **Figure 2.1**.

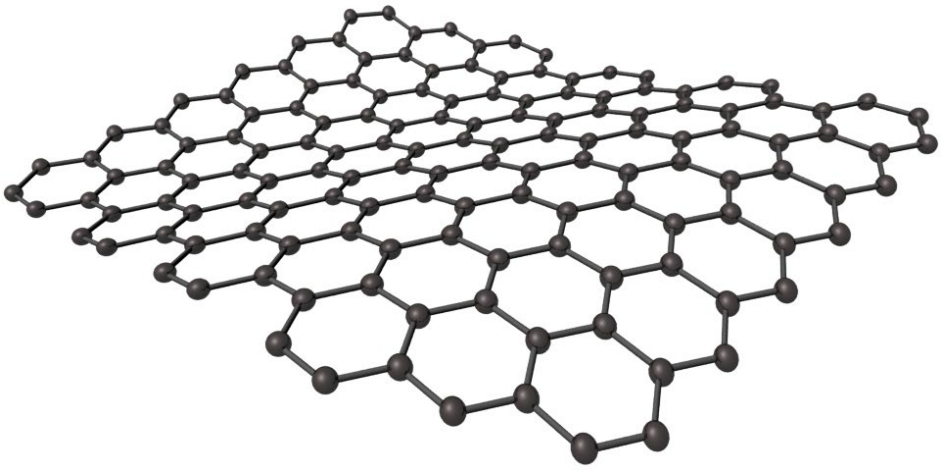

Figure 2.1: Schematics of graphene sheet.

In the last decade GR has emerged as an exciting new material, with potential to impact many scientific and technological fields after Geim and co-workers first isolated GR onto SiO_2 substrate and studied its opto-electrical properties[1-4]. Nowadays, GR has been considered as the most promising candidate for thin flexible electronics due to its high electrical conductivity (up to $1.6*10^5$ S/cm)[12], excellent optical transmittance and chemical stability [13]. In addition, some of GR characteristics demonstrated exceptionally high values, nearing theoretically predicted limits: room temperature charge carrier mobility of $2.5 \cdot 10^5$ cm^2 V^{-1} [14], zero bandgap [15] which can be tuned via lithography [16], a Young modulus of

1TPa and intrinsic strength of 130 GPa [17], thermal conductivity (3,000-5,300 W/(mK)) [18], gas impermeability [19], and large surface area (theoretical limit: 2630 m^2/g) [2-3]. Furthermore, the surge in GR research also paved the way for search and investigation of other 2D materials[20-23]. For instance, the discovery of MXenes imply that combining of such 2D crystals with GR can produce hybrid 2D superstructures (**Figure 2.2)** with wide variety of properties, which can be used for fabrication of flexible field-effect transistors (FETs) [5].

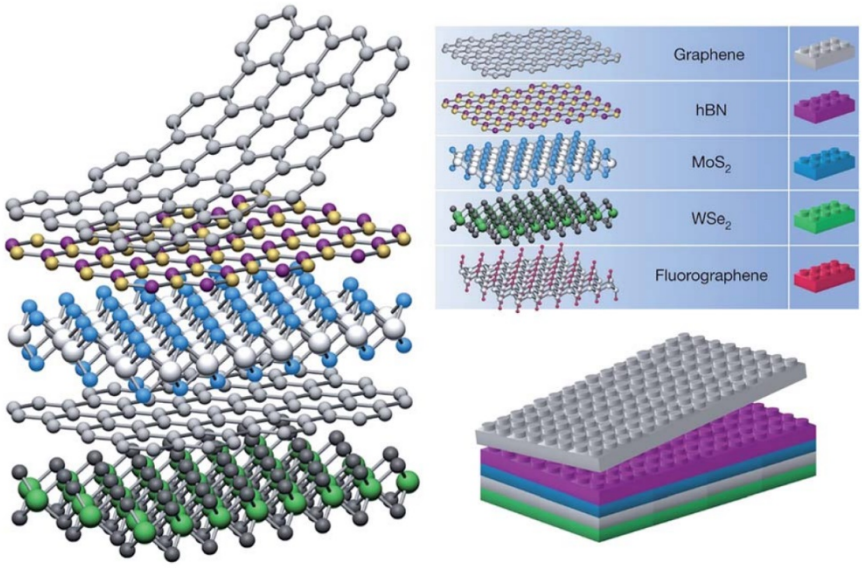

Figure 2.2: Schematic 2D heterostructures based on van der Waals interlayer force [5]. Reprinted by permission of Springer Nature.

2.2: Synthesis of Graphene

The process which allows one to fabricate or extract GR of desired size and purity is referred to as synthesis of graphene. There are a number of operative ways for obtaining mono- and multilayered graphene sheets, which eventually can be categorized into two

distinct strategies: bottom-up and top-down [2, 6, 24]. An overview of graphene synthesis techniques is shown in the flow chart in **Figure 2.3.**

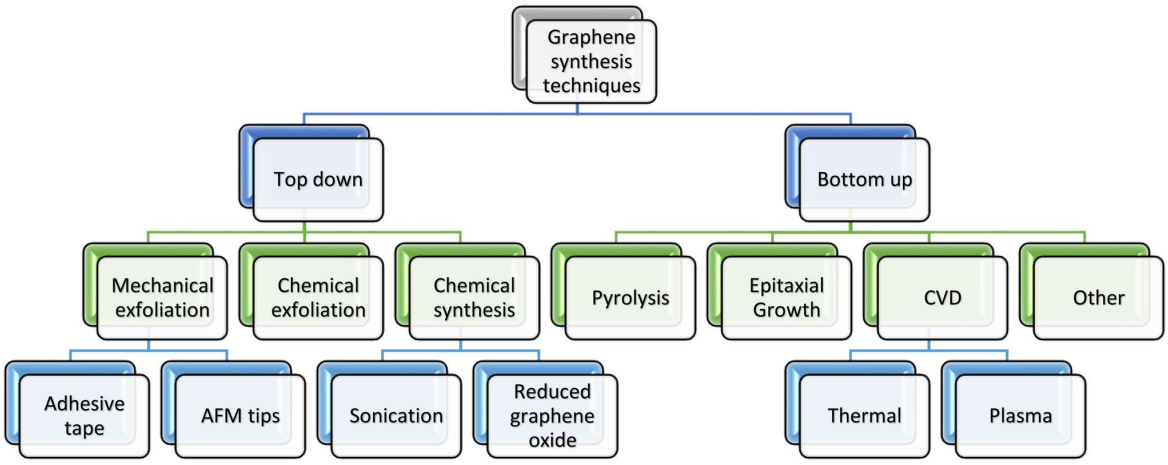

Figure 2.3: A process flow chart of GR synthesis [6]. Reprinted by permission of Springer Nature (open access).

Bottom-up Graphene

Bottom-up GR growth process is based on atom by atom growth. It includes chemical vapor deposition (CVD) on transition metals [25], epitaxial growth on SiC [26], molecular beam epitaxy [27] and others (electron beam irradiation of electrospun PMMA nanofibers [28], arc discharge of graphite [29], thermal carbonization of polycyclic aromatic hydrocarbons [30]). The predominant technique for obtaining larger-scale graphene film is CVD, which allows good control over synthesis, film thickness, and properties. A general mechanism for CVD-based graphene includes the following steps [8]: (1) mass transport of the reactant, (2) reaction of the film precursor, (3) gas molecules diffusion, (4) adsorption of the precursor, (5) precursor diffusion into the substrate, (6) surface reaction, (7) product desorption, and (8) by-product removal (**Figure 2.4**). Typically, a CVD-process requires the presence of transition metal catalyst (Au, Cu, Ni, etc.) to activate chemical reactions of

precursors at the growth substrate surface/interface (or dehydrogenate the precursor species) [25]. High roughness of the catalytic metal surface makes it difficult for GR to grow uniformly and to cover 100% of the substrate.

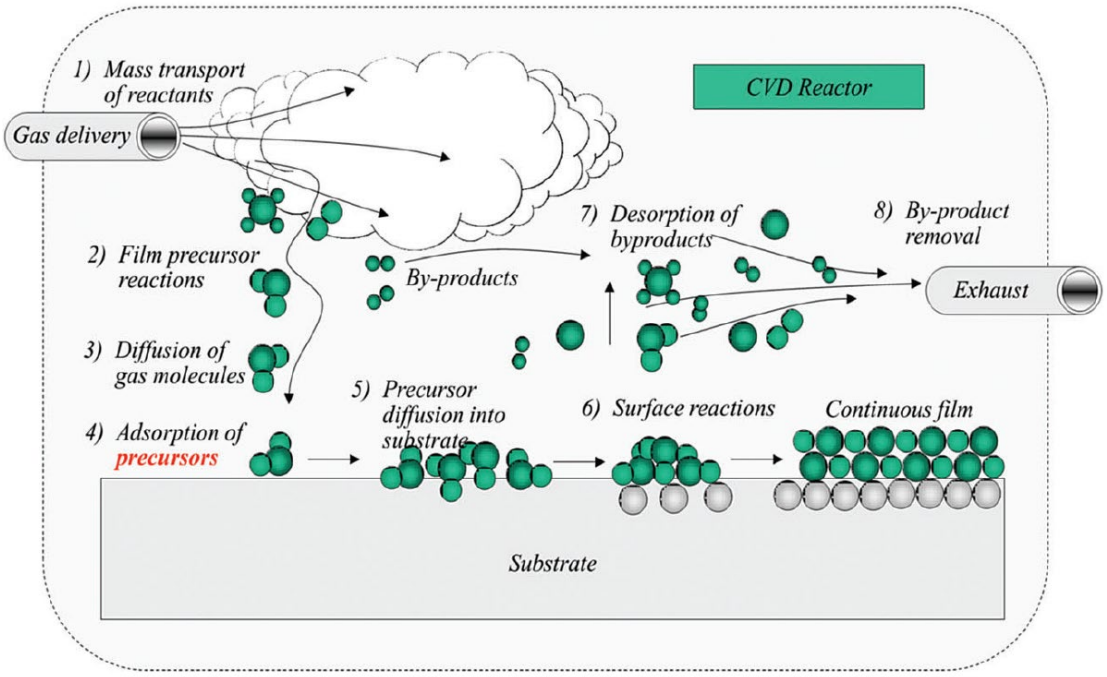

Figure 2.4: Diagram of the general growth mechanism of CVD-based graphene: transport and reaction processes [8]. Reprinted by permission of The Royal Society of Chemistry.

In addition, CVD GR can be contaminated by the residual metallic impurities after etching of the metal substrate. Furthermore, further device integration the film has to be transferred to a targeted substrate via a quite-sophisticated methodology for further device integration. For this reason, there is limited opportunity for scalability, with only two reports describing successful attempts to fabricate larger (10th of centimeter/meter)-scale CVD-obtained graphene films via roll-to-roll transfer with low sheet resistance (150–500 Ω/sq without chemical doping) and high conductivity (10^4 S/cm)[31-32]. We note that the

transferred films had a significant density of defects (e.g., cracks, wrinkles, multilayered islands, non-uniformity, impurities), especially for the monolayer and bi-layered graphene films.

Recently, significant efforts have been made to fabricate GR on semiconductor and dielectric substrates (quartz, SiO_2) using non-catalytic direct-growth of GR, which offers low process cost and shorter experimental processes[33-35]. However, the drawback of this method is the slow growth rate and poor quality of GR compared with the catalytic direct growth, which makes it not suitable for large-area high-quality GR manufacturing[8]. In addition, high temperatures (>1000 ºC) are required for thermal CVD to make up for the absence of metal catalyst[36-37]. In 2017 Zheng et al. reported an innovative method for synthesizing high-quality GR directly on Al_2O_3 and SiO_2 substrates. The method was based on the use of NH_3-assistade microwave plasma-enhanced chemical vapor deposition (MPECVD)[38]. As a result, metal-catalyst-free polycrystalline GR layers were grown at a temperature range of 650 ºC to 750 ºC with sheet resistances in the range of 3.8 – 6.6 kΩ/sq^{-1}.

Direct growth of GR on flexible organic substrates is very attractive for the number of flexible optoelectronics applications [39], health-monitoring sensors [40] and e-skin [41-42]. However, low thermal stability of organic substrates makes it challenging to directly grow GR on the flexibles substrates. Because of that, most of the studied growth methods still rely on the catalytic conversion of organic precursors to graphitic layers.

Kim *et al.* fabricated graphene-graphitic carbon (G-GC) films on a Cu layer deposited on a polyimide substrate using inductively coupled plasma-enhanced CVD. The Cu layer was then etched and G-GC film was then directly transferred onto an underlying flexible substrate. Raman spectroscopy and transmission electron microscopy (TEM) were used to study the structural quality and crystallinity of G-GC films. The electrical and optical properties of the films were measured by four-probe method and UV-Vis respectively. It was shown that opto-electrical properties can be influenced by growth temperature, plasma power and growth time. Sheet resistances in the range of 3.8 – 6.6 $k\Omega/sq^{-1}$ at 80% transparency at 550 nm were achieved [43].

Top-down graphene

In top-down process (**Figure 2.5**), graphene or modified graphene sheets are produced from graphite source by solvothermal synthesis, mechanical/chemical exfoliation, and unzipping carbon nanotubes [44-46]. Exfoliation can be done using such methods as scotch tape, ultrasonication, electric field, transfer printing technique [47].

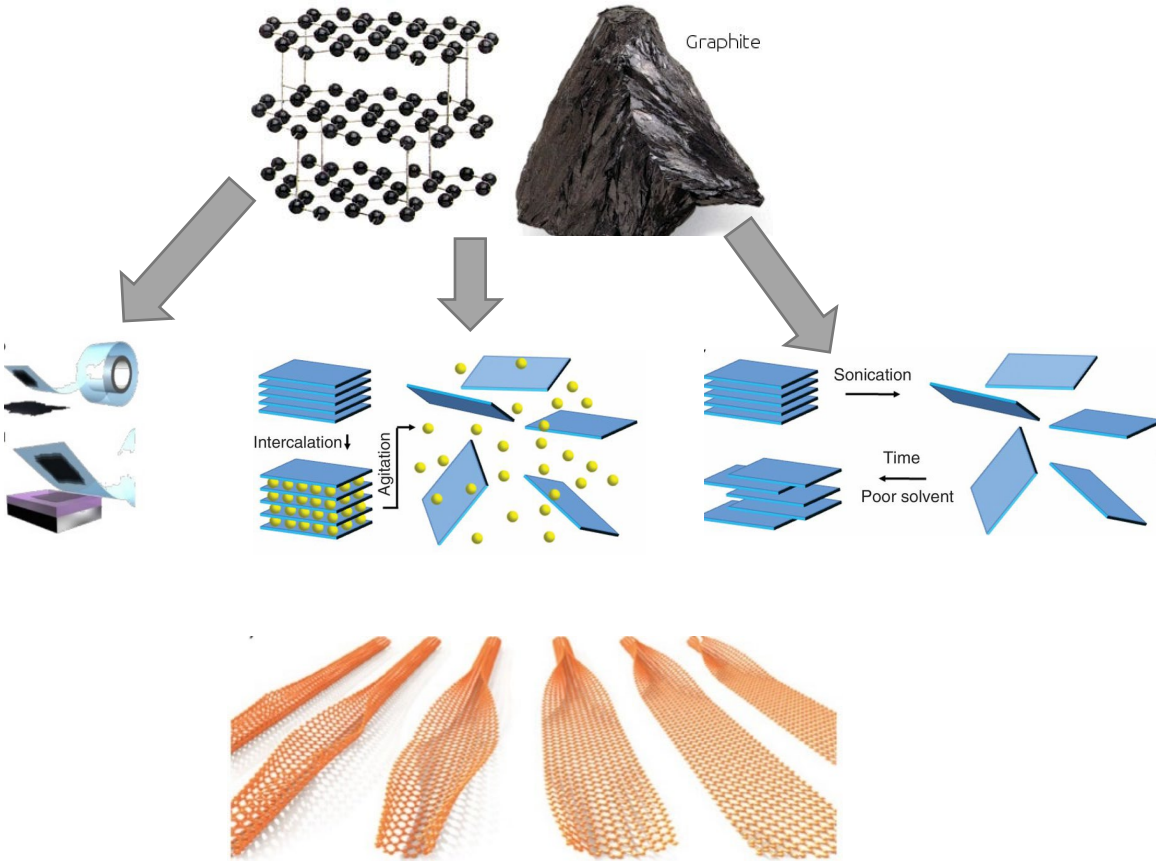

Figure 2.5: Diagram of the top-down approach for GR synthesis. Reproduced with permission.

Chemical exfoliation or synthesis is the most appropriate method for large-scale production of graphene [48]. Graphene obtained by this method is generally referred to as graphene oxide (GO) [49]. Chemical synthesis of GR involves the following steps: (i) oxidation of graphite, which causes an increase in interlayer spacing between stacked GR sheets, and (ii) exfoliation through rapid heating or sonication. Literature reports the following most common synthesis methods of GO: Brodie [50], Staudenmaier [51] and Hummers methods[52].

2.3: Graphene Oxide

GO sheets are monolayers of sp^2-hybridized carbon atoms partially derivatized to sp^3 with hydroxy and epoxy groups on both sides and carboxy/carbonyl groups around the edges [49, 53]. GO has a typical carbon/oxygen ratio of 2/1 [54] (**Figure 2.6**). GO platelets are decorated with carboxylic acid groups at their edges, and epoxy and hydroxyl groups on the basal planes [49].

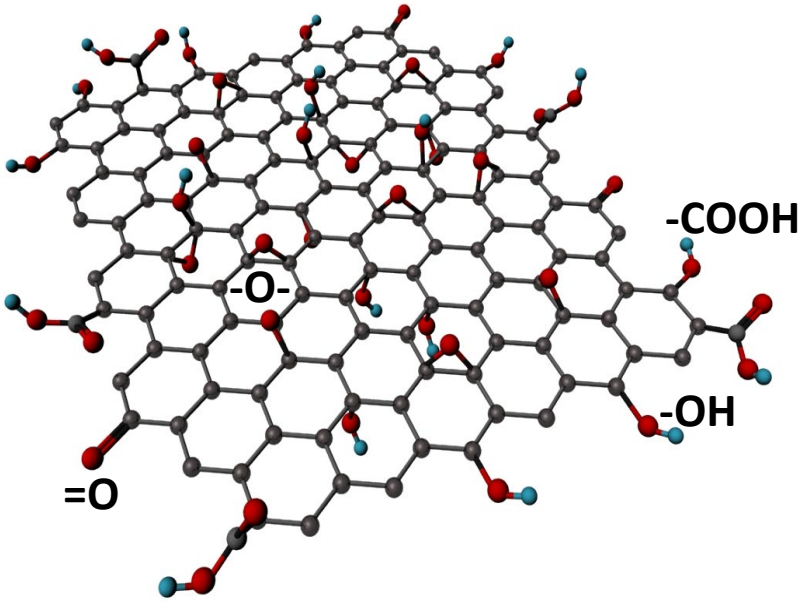

Figure 2.6: Schematic representation of graphene oxide sheet.

GO sheets serve as a "precursor" for its electrically conductive derivative, so-called reduced graphene oxide (rGO)[44]. GO is a poor electrical conductor, because of the defects such as oxygen containing functional groups that are present in the structure. Reduction of GO (which yields rGO) restores to a substantial degree electrical, mechanical and other properties of the graphene [3]. However, certain oxygen amount still remains in RGR structure (about 10% or C/O ~10/1) [55]. The approach based on GO has significant potential

to rapidly grow to industrial scale. The methods of reduction are discussed more in detail in **Section 2.6**. In fact, GO possesses several advantages over pristine graphene materials from a manufacturing point of view: it is inexpensive and can be produced at a large scale from readily available graphite[52]. In addition, GO has excellent dispersibility in polar solvents, including water[56], and its surface can be straightforwardly modified[57]. Therefore, GO has extreme adaptability and compatibility with various liquid media and solid substrates, which are important for the employment of standard methods of layer nanomanufacturing [58-59]. In fact, significant progress has been reached in this area over the past decade, as described in a number of comprehensive review articles on the topic [44-45, 60-63].

2.4: Functionalization of Graphene Oxide

The multiple functional groups and unique 2D morphology make GO ideal template for the construction of different organic/inorganic composites structures. Polymer grafted GO composites drew lots of attention because of their wide applications in high-strength and conductive materials, catalysts and fire retardants[24, 64-66]. Specifically, the GO functional groups can be used to covalently and non-covalently attach functional (macro)molecules to optimize physical and chemical properties of the material[2, 57]. Covalent attachments, which typically involve chemical reactions at the hydroxyl, epoxy and carboxylic acid groups are made using "grafting to" and "grafting from" methods [66-67,68, 69]. The non-covalent physisorption on GO, which involves sp^2 regions, can be realized via π-π stacking, electrostatic or van der Waals interactions [49].

For instance, Lu et al. reported a simple and effective way to enhance the dispersibility of GOs in alkaline cementitious solutions [11]. The method was based on the steric stabilization of GO with polycarboxylate-ether copolymer (PCE) via van der Waals interactions between PMA backbone in PCE and sp^2 – hybridized carbon backbone in GO, as shown in **Figure 2.7**. The improved dispersion of GO in the aqueous solution resulted from the stronger hydrogen bonding and steric repulsion between GO/PCE sheets provided by PEG side chains in PCE copolymer. As a result, GO-PCE-Cement composite showed improvement in flexural and compressive strengths with corresponding values of 14.6 and 27.14 MPa.

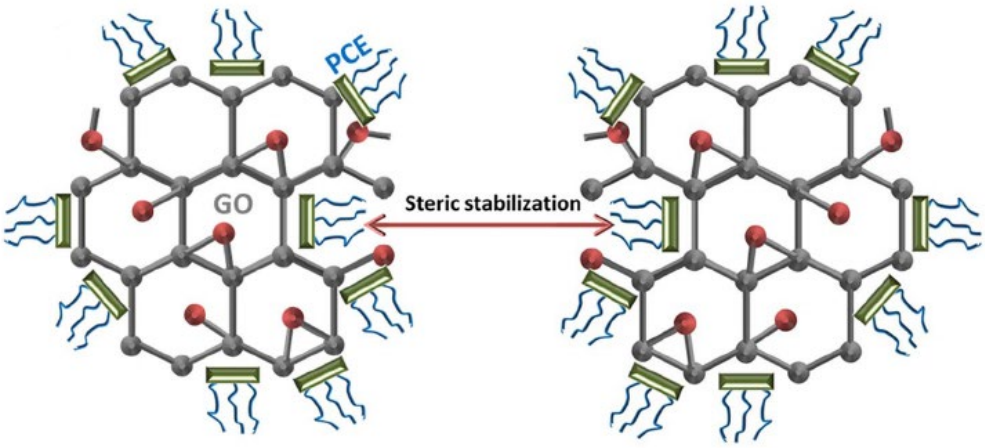

Figure 2.7: Steric stabilization of GO-PCE suspensions via van der Waals interactions[11]. Reprinted by permission of Elsevier.

In the "grafting from" approach, the polymerization is initiated right on the surface of GO [67, 70-72]. For example, Ref.[7] reports "grafting from" technique to fabricate PNIPAM-GO-based thin film, exhibiting temperature- and NIR-controllable wettability via *in situ* free-radical polymerization (**Figure 2.8**). The material obtained in this way demonstrated

a reversible switching of wettability between hydrophobic and hydrophilic states which can be promising for practical applications in smart coatings, sensors, drug delivery and catalysis.

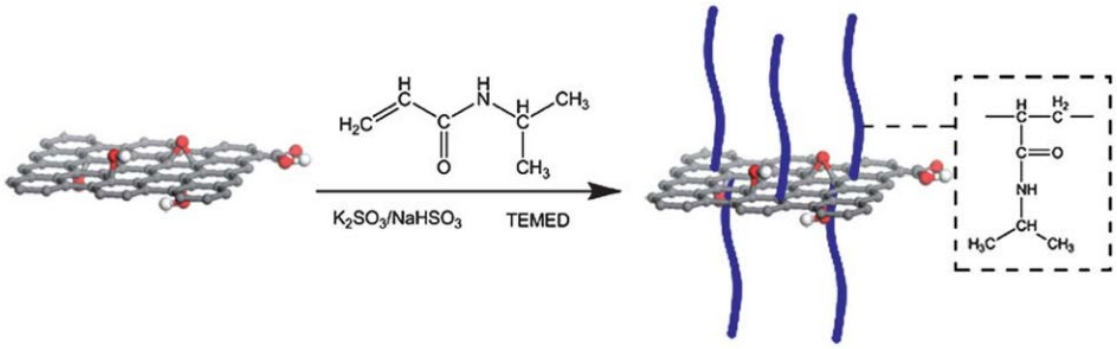

Figure 2.8: Preparation of GO-PNIPAM hybrids via "grafting from" technique using *in situ* free-radical polymerization[7]. Reprinted by permission of The Royal Society of Chemistry.

Cano et al. reported on the modification of GO with poly(vinyl alcohol) (PVA) leading to the mechanical improvement of GO-based composites[9] (**Figure 2.9**). Specifically, Young's modulus and strength of GO-PVA paper material increased by approximately 60% for GO-PVA loadings below 0.3 vol.%.

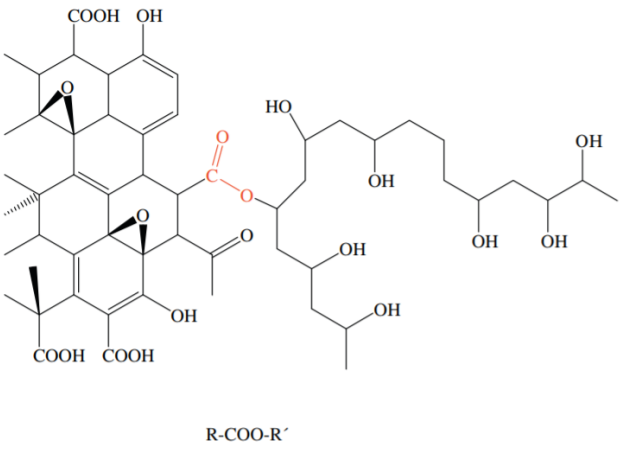

Figure 2.9: Functionalization of GO with PVA by esterification reaction [9]. Reprinted by permission of Elsevier.

2.5: GO Film Formation Methods

To produce highly transparent conductive films, GO sheets should be deposited onto a substrate uniformly without folds or gaps between them. The solution-processing approach is of particular interest since it has great potential to be implemented into roll-to-roll technique for continuous large-scale production of flexible transparent conductors. Therefore, significant effort has been made to produce uniform GO films in a controlled and reproducible manner, including methods such as spin-coating [73], spray-coating [74], ink-jet printing [75], dip-coating [76], Langmuir-Blodgett [L-B] method [77-79], layer-by-layer [L-b-L] deposition [80-83], vacuum filtration [84], rod-coating [85] and drop-casting [86]. However, it is still challenging to control the thickness and property of graphene-based conductive films during the process of fabrication. Among the methods used for the formation of rGO layers dip-coating, spray-coating, and drop-casting have the highest potential to be used for the manufacturing of larger-scale conductive and transparent coatings. However, to the best of our knowledge (beside our recent work[87], described in detail in this dissertation), there are no reports in the scientific literature describing the formation of highly conductive rGO nanoscale layers with a well-defined morphology and properties by these methods. As of today, the most-used method for obtaining several-nm-thick rGO films is spin-coating, which, indeed, allowed the production of highly conductive nanoscale rGO films.[88-92] The best results for the rGO films in terms of perfectness of morphology and electrical/optical properties were also obtained using L-B deposition[93-95] and interfacial self-assembly.[96]

The dip-coating technique is known for its low cost, operating simplicity, coating uniformity and easy scalability. For example, GO material can be deposited on different polymeric substrates via roll-to-roll method (**Figure 2.10**). In addition, the thickness, morphology and opto-electrical properties of the prepared GO-based films can be controlled via withdrawal speed, GO concentration and the number of coating cycles [76].

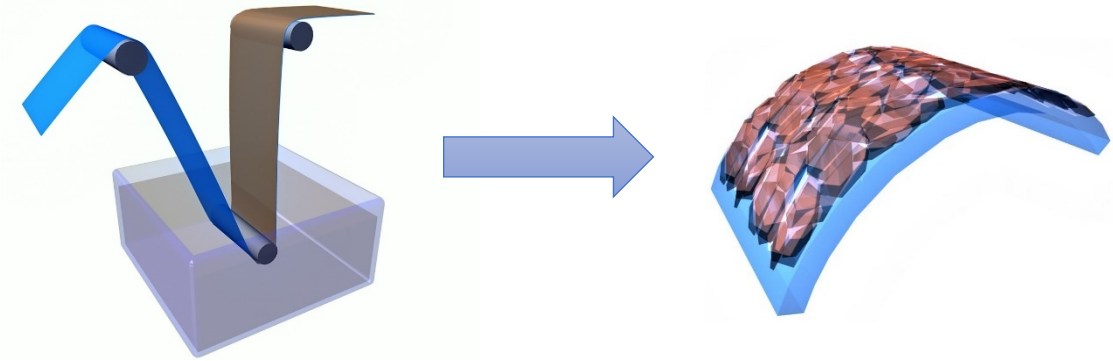

Figure 2.10: Schematic of fabrication of GO film on flexible substrate via dip-coating method.

2.6: Reduction of Graphene Oxide

In general, at the structural/chemical level the aim of the reducing procedures is to remove oxygen containing moieties from the GO structure, restore and expand graphene sp^2 structural regions. Therefore, an effective deoxygenation process or "reduction" must be performed, which aims to convert practically non-conducting GO material ($5*10^{-3}$ S/cm [97], $5*10^{-6}$ S/cm [98]) to its conductive form, reduced graphene oxide [99]. The level of reduction success significantly varies depending on the reduction method applied, but at least several orders of magnitude increase in conductivity is always observed

There are several major techniques allowing the reduction of GO into rGO. Specifically, GO can be reduced to graphene-like structures by chemical, electrochemical, microwave, thermal, hydrothermal, and photothermal reducing techniques [100-103]. The actual conductivity values can be as low as 2 S/cm for hydrazine hydrate[56] and microwave reduction[104] to 10^3 S/cm order of magnitude for high temperature treatment in UHV[105], reduction in the presence of H_2[106] or by HI[100, 104, 107].

High temperature reduction has demonstrated the most promising results. The mechanism of GO transformation upon the heating involves thermal deoxidation (removal of oxygen containing groups from the sheets) [108]. For example, thermally reduced rGO can be produced by heating GO in inert environment and high temperature (600-1000 ºC) [54, 109-110 111]. The additional treatment of the thermally reduced graphene at ~1500 ºC can increase C/O ratio to 660/1 practically eliminating oxygen in the rGO structure. It is necessary to highlight that there are reports published on generation of rGO from GO by *in-situ* (inside polymer matrix) thermal reduction at lower temperatures (2-3h, ~200 ºC) [112-113].

Despite contributing to the increase in conductivity value thermal reduction process often introduces defect into final rGO structure by "pulling out" carbon atoms attached to oxygen from the structure [114-115]. An interesting approach to heal the defects was proposed by Lopez et al[116]. The healing process was performed at high temperature in ethylene vapor (the conditions similar to one used for CVD growing of carbon nanotubes) on previously thermally reduced GO. Two orders of magnitude increase in conductivity value (level of 10^2 S/cm) was observed comparing to standard high temperature annealing

process. Similar effect was demonstrated by Dai et al.[117], but in this case the carbon source (methane) was introduced at high temperature during the reduction process. Thus, the reduction and healing occured at the same time. Yet again, significant increase in conductivity (level of $4*10^2$ S/cm) was achieved. Su et al. [118] also demonstrated the healing effect at high temperatures, but this time produced by large aromatic molecules associated with GO. Reduced GO conductivity as high as 10^3 S/cm was demonstrated.

Although, thermal reduction of GO is a very simple and eco-friendly method it is not suitable for applications in flexible devices. Low temperature chemical reduction [100, 107], on the other hand, is believed to offer the most promising route towards the large scale and low cost production of GR for transparent flexible conductors [10, 119-120]. To date, many reduction reagents have been used such as $NaBH_4$, hydroquinone, sulfur compounds, hydrazine, ascorbic acid, and hydrohalic acids[121]. Among all these processes, the reduction of GO films using hydrohalic acids has been regarded as the fastest way to produce highly conductive graphene in large quantities with preserved integrity [10, 122-123].

Cheng *et al.* have demonstrated the reduction of free-standing GO films at 100 ºC for 1 h using concentrated HI acid [10]. The obtained rGO films demonstrated much higher electrical conductivity (298 S/cm and 85% transparency at 550 nm) and C/O atomic ratio (~12) than those of films reduced by other chemical methods, for example hydrazine. Furthermore, the authors showed that HI-reduced rGO films had preserved original flexibility, strength and integrity. The pathway of HI reduction mechanism is shown in **Figure 2.11**: (a) the ring-opening reaction of an epoxy group and (b) the substitution reaction of a hydroxyl group by halogen atom. Finally, graphene can be produced (final

step (b)) by elimination of iodine atoms [124]. However, one of the drawbacks of using chemical reduction is possible introduction of heteroatomic impurities [49], which may play dual role: (i) iodine can act as a p-type dopant enhancing the conductivity of monolayer Gr [125] or (ii) it can compromise the underlying polymeric substrate by lowering its tensile strength, Young's modulus and making it more brittle (**Appendix** (**Figure A14**)).

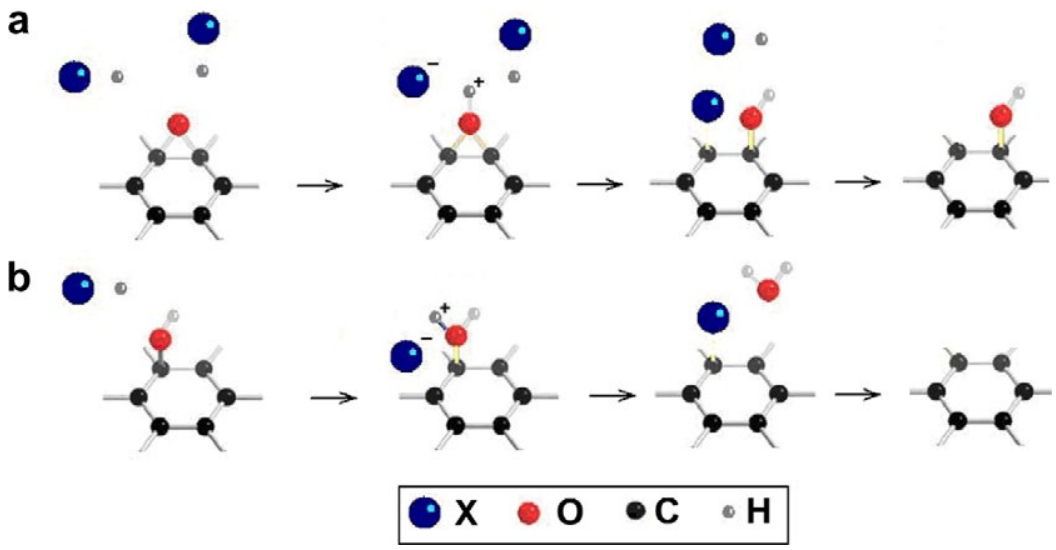

Figure 2.11: Possible reaction mechanism of GO reduction by hydrohalic acids. (a) Ring-opening reaction of an epoxy group. (b) Halogenation substitution reaction of a hydroxyl group. (X = iodine or bromine) [10]. Reprinted by permission of Elsevier.

2.7: Challenges in the Fabrication of rGO Films

During the assembly of GO flakes into larger area films/coatings with a thickness on the order of several nm the electrical characteristics of the films are significantly reduced in comparison to individual graphene sheets. In fact, for these films a conductivity of 10^2-10^3 S/cm and sheet resistance on the level of 10^3 Ω/sq and higher is usually reported[44-45,

[60, 126-129], which is significantly lower than that known for widely-exploited transparent conductive ITO film (~10^4 S/cm[130-131]).

There are at least two major challenges for the layers made of rGO sheets: (i) the properties/morphology of individual rGO sheets and (ii) the properties/morphology of the rGO layers. At the individual rGO sheet level, one has to deal with only a partial reduction of the original GO[108], the presence of numerous defects[132], and a mosaic of conductive and non-conductive parts[133]. All these features reduce the material's ability to conduct electric current. In addition, at the GO layer level, the availability of GO/rGO only in the form of micrometer size sheets causes high inter-sheet contact resistivity [45]. This resistivity originates from untight/imperfect sheet arrangements/contacts in plane (edge-to-edge) and plane-to-plane (stacking) contacts. Therefore, striving for a thinner rGO layer to achieve the largest transparency value dramatically decreases the overall electrical-optical property balance with increase of the contribution of the inter-sheet resistivity. Thus, it is suppressing the facile formation of highly conductive and transparent flexible films for prospective micro/nano-electronic applications. The electrical characteristics of the films are significantly reduced in comparison to individual graphene sheets.

2.8: Transparent Conductive Plastics

Polymeric films are the most common flexible substrates employed in flexible electronic devices. Among key polymer materials are polyimides (such as Kapton), polycarbonate (PC), polyethylene terephthalate (PET), polyethylene naphthalate (PEN), polyarylate (PAR), polydimethylsiloxane (PDMS), polyurethanes (PU), and styrene ethylene butadiene styrene (SEBS).[134-138] When polymeric substrate is selected for a

particular application beside cost the following polymer characteristics have to be taken into account: mechanical properties, mechanical stability, thermal stability, thermal expansion coefficient, solvent resistance, diffusivity, optical clarity, dielectric constant, roughness, surface energy/wettability. However, to the best of our knowledge there are no published reports on the formation of highly conductive rGO nanoscale layers with a well-defined morphology and properties directly from water on flexible polymer hydrophobic substrates/films. One of the major challenges is significant capillary forces affecting "perfectness" of nanoscale structure as water is evaporating. Another challenge is low surface energy of the polymer films. It is shown that even for deposition of less-defined and thicker multilayered coatings it is necessary to overcome low wettability of polymer films by water-based GO suspensions.[139-141] Therefore, GO material cannot be deposited directly on the polymer surface without preliminary (quite harsh) chemical or physical treatment to achieve appropriate water wettability for the polymer film.

There have been done lots of studies on how to make hydrophobic surfaces more hydrophilic including oxygen plasma, ultraviolet exposure, ion-beam etching, acid/base treatments, laser ablation and chemical functionalization to make it more hydrophilic [142, 143, 144, 145]. It is necessary to point that the treatment at the relatively harsh conditions can compromise structural integrity and properties of polymer films. Also, the treatment may generate by-products (e.g. volatile hydrocarbon products as a result UV/ozone treatment) or wastes (such as strong bases/acids) which are not environmentally friendly, which complicate the scale-up of such process.[139]

2.9: Light Absorption in Graphene

The structure of electronic bandgap plays an important role in light-matter interactions in graphene. The band gap is defined as the energy difference between the top of valence band and the bottom of the conduction band [146]. In **Figure 2.12** (left) the schematic of the band structure of pristine graphene is shown [147]. As expected, ideal defect-free graphene reveals typical semi-metallic nature where the bottom of the conduction band overlaps with the top of the valence band. Points of overlap, K and K', are called Dirac points [148]. The electronic states are formed from the additional electron in the p_z orbitals of carbon atoms. Further away from Dirac points there is a saddle point singularity at the M point (van Hove singularity (VHS), ~5 eV gap). At the Γ-point the conduction and valence bands are widely separated ~20 eV gap. The absorption of a photon by graphene may give rise to direct or indirect intraband and interband electron transitions (**Figure 2.12** (right)).

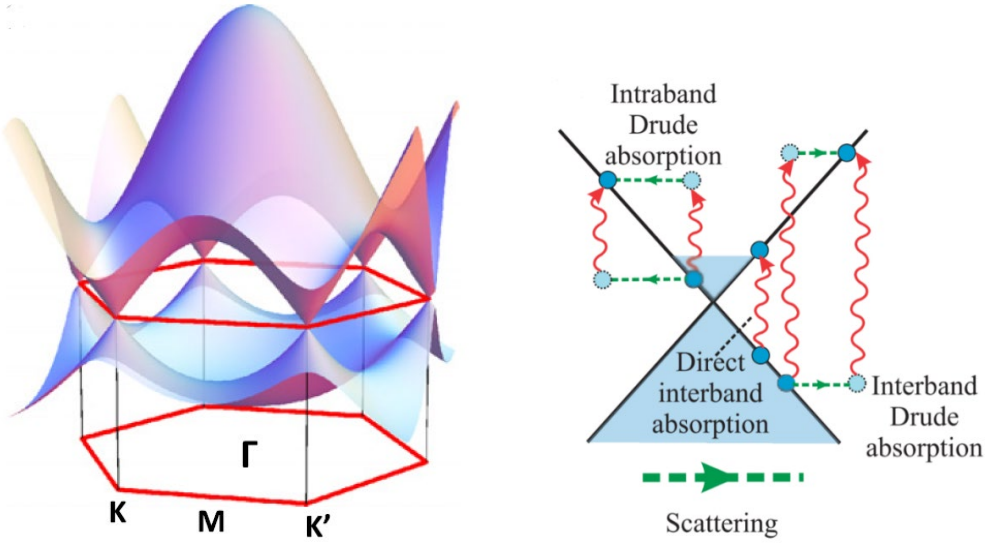

Figure 2.12: Electronic structure of graphene: (a) electronic dispersion of the π-bands in the graphene Brillouin zone showing K- and K'- points and the saddle point (van Hove singularity) at the M-point [147]. Reprinted by permission of Elsevier

An indirect transitions involve number of scattering-assisted effects by disorders (impurity or phonons)[149]. For low photon energies (infrared) the intraband (free-carrier) transitions play dominant role, while for higher photon energies (ultraviolet spectral range) the optical response is primarily due to interband (excitons) transitions[150] at saddle-point singularity (M).

The structure of electronic band gap is strongly influenced by the defects, degree of oxidation and size of graphene sheets [151]. In 2016 Roy and coworkers [152] demonstrated that the distortion of linear dispersion and opening of bandgap at K-point takes place with the addition of different types of oxygen adsorbates and perturbations (**Figure 2.13**). Furthermore, the results presented in Ref. [153] demonstrate that E_g is also sensitive to the measurement environment such as humidity and moisture.

Bhantnagar et. al [151] experimentally and theoretically investigated the optical band gap in graphene-derived nanomaterials (oxidized graphite, graphene oxide and graphene quantum dots) as a function of oxidation as well as size. They showed that the reduction in size of graphene directly influences its optical band gap and conducting behavior. The optical band gap for GO was found in the range 2.7 – 4.2 eV.

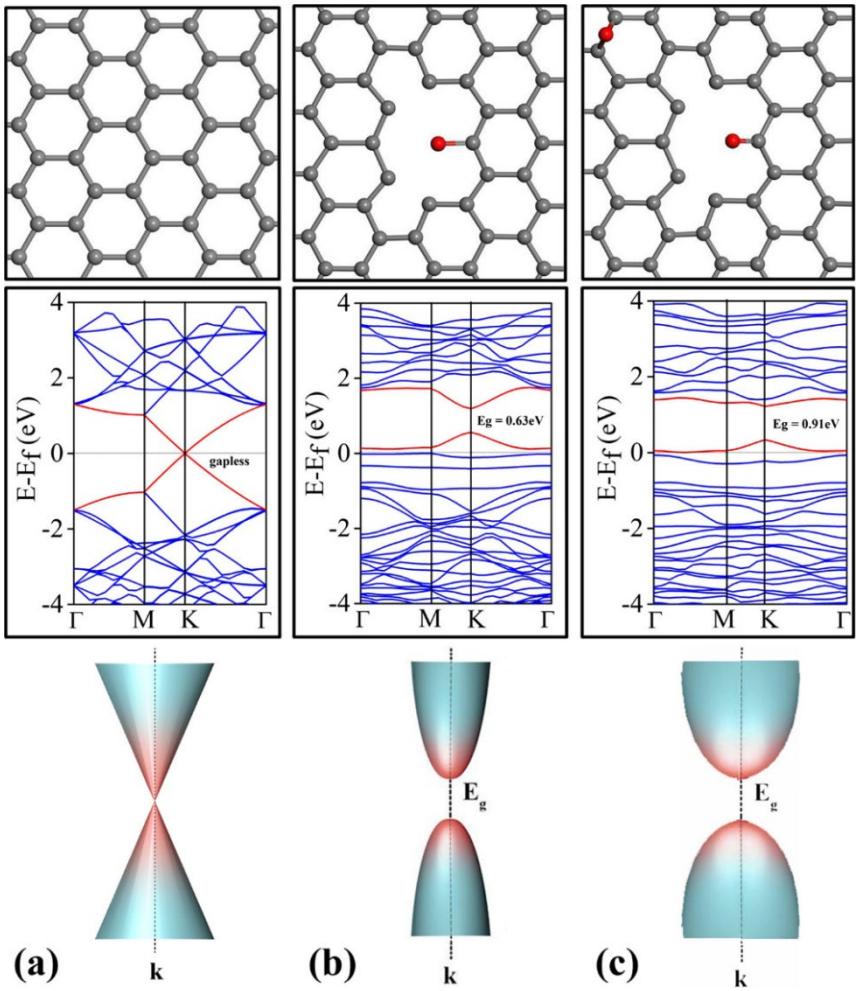

Figure 2.13: Model, calculated band structure and schematic visualization of band dispersions around Dirac K-point of (a) pure graphene (b) graphene with C=O and (c) graphene with C=O and epoxy adsorbed on the surface [152]. Reprinted by permission of Elsevier.

2.10: References

1. Coleman, J. N., Liquid Exfoliation of Defect-Free Graphene. *Accounts of Chemical Research* **2013,** *46* (1), 14-22.

2. Ciesielski, A.; Samorì, P., Graphene via sonication assisted liquid-phase exfoliation. *Chemical Society Reviews* **2014,** *43* (1), 381-398.

3. Kim, H. a. A. A. a. a. M. C. W., Graphene/Polymer Nanocomposites. *Macromolecules* **2010,** *43* (16), 6515--6530.

4. Singh, V.; Joung, D.; Zhai, L.; Das, S.; Khondaker, S. I.; Seal, S., Graphene based materials: Past, present and future. *Progress in Materials Science* **2011,** *56* (8), 1178-1271.

5. Geim, A. K.; Grigorieva, I. V., Van der Waals heterostructures. *Nature* **2013,** *499*, 419.

6. Bhuyan, M. S. A.; Uddin, M. N.; Islam, M. M.; Bipasha, F. A.; Hossain, S. S., Synthesis of graphene. *International Nano Letters* **2016,** *6* (2), 65-83.

7. Qi, J.; Lv, W.; Zhang, G.; Zhang, F.; Fan, X., Poly(N-isopropylacrylamide) on two-dimensional graphene oxide surfaces. *Polymer Chemistry* **2012,** *3* (3), 621-624.

8. Pham, V. P.; Jang, H.-S.; Whang, D.; Choi, J.-Y., Direct growth of graphene on rigid and flexible substrates: progress, applications, and challenges. *Chemical Society Reviews* **2017,** *46* (20), 6276-6300.

9. Cano, M.; Khan, U.; Sainsbury, T.; O'Neill, A.; Wang, Z.; McGovern, I. T.; Maser, W. K.; Benito, A. M.; Coleman, J. N., Improving the mechanical properties of graphene oxide based materials by covalent attachment of polymer chains. *Carbon* **2013,** *52*, 363-371.

10. Pei, S.; Zhao, J.; Du, J.; Ren, W.; Cheng, H.-M., Direct reduction of graphene oxide films into highly conductive and flexible graphene films by hydrohalic acids. *Carbon* **2010,** *48* (15), 4466-4474.

11. Lu, Z.; Hanif, A.; Ning, C.; Shao, H.; Yin, R.; Li, Z., Steric stabilization of graphene oxide in alkaline cementitious solutions: Mechanical enhancement of cement composite. *Materials & Design* **2017,** *127*, 154-161.

12. Bae, S.; Kim, H.; Lee, Y.; Xu, X.; Park, J.-S.; Zheng, Y.; Balakrishnan, J.; Lei, T.; Ri Kim, H.; Song, Y. I.; Kim, Y.-J.; Kim, K. S.; Özyilmaz, B.; Ahn, J.-H.; Hong, B. H.; Iijima, S., Roll-to-roll production of 30-inch graphene films for transparent electrodes. *Nature Nanotechnology* **2010,** *5*, 574.

13. Lifang, T.; Chenxiao, W.; Mengqi, Z.; Lei, F., Graphene: An Outstanding Multifunctional Coating for Conventional Materials. *Small* **2017,** *13* (13), 1603337.

14. Mayorov, A. S.; Gorbachev, R. V.; Morozov, S. V.; Britnell, L.; Jalil, R.; Ponomarenko, L. A.; Blake, P.; Novoselov, K. S.; Watanabe, K.; Taniguchi, T.; Geim, A. K., Micrometer-Scale Ballistic Transport in Encapsulated Graphene at Room Temperature. *Nano Letters* **2011,** *11* (6), 2396-2399.

15. Zhang, Y. B.; Tang, T. T.; Girit, C.; Hao, Z.; Martin, M. C.; Zettl, A.; Crommie, M. F.; Shen, Y. R.; Wang, F., Direct observation of a widely tunable bandgap in bilayer graphene. *Nature* **2009,** *459* (7248), 820-823.

16. Han, M. Y.; Özyilmaz, B.; Zhang, Y.; Kim, P., Energy Band-Gap Engineering of Graphene Nanoribbons. *Physical Review Letters* **2007,** *98* (20), 206805.

17. Lee, C.; Wei, X.; Kysar, J. W.; Hone, J., Measurement of the Elastic Properties and Intrinsic Strength of Monolayer Graphene. *Science* **2008,** *321* (5887), 385.

18. Balandin, A. A., Thermal properties of graphene and nanostructured carbon materials. *Nature Materials* **2011,** *10*, 569.

19. Bunch, J. S.; Verbridge, S. S.; Alden, J. S.; van der Zande, A. M.; Parpia, J. M.; Craighead, H. G.; McEuen, P. L., Impermeable Atomic Membranes from Graphene Sheets. *Nano Letters* **2008,** *8* (8), 2458-2462.

20. Naguib, M.; Mashtalir, O.; Carle, J.; Presser, V.; Lu, J.; Hultman, L.; Gogotsi, Y.; Barsoum, M. W., Two-Dimensional Transition Metal Carbides. *ACS Nano* **2012,** *6* (2), 1322-1331.

21. Mashtalir, O.; Naguib, M.; Mochalin, V. N.; Dall'Agnese, Y.; Heon, M.; Barsoum, M. W.; Gogotsi, Y., Intercalation and delamination of layered carbides and carbonitrides. *Nature Communications* **2013,** *4*, 1716.

22. Vogt, P.; De Padova, P.; Quaresima, C.; Avila, J.; Frantzeskakis, E.; Asensio, M. C.; Resta, A.; Ealet, B.; Le Lay, G., Silicene: Compelling Experimental Evidence for Graphenelike Two-Dimensional Silicon. *Physical Review Letters* **2012,** *108* (15), 155501.

23. Bianco, E.; Butler, S.; Jiang, S.; Restrepo, O. D.; Windl, W.; Goldberger, J. E., Stability and Exfoliation of Germanane: A Germanium Graphane Analogue. *ACS Nano* **2013,** *7* (5), 4414-4421.

24. Kim, H.; Abdala, A. A.; Macosko, C. W., Graphene/Polymer Nanocomposites. *Macromolecules* **2010,** *43* (16), 6515-6530.

25. Seah, C.-M.; Chai, S.-P.; Mohamed, A. R., Mechanisms of graphene growth by chemical vapour deposition on transition metals. *Carbon* **2014,** *70*, 1-21.

26. Huang, H.; Chen, S.; Wee, A. T. S.; Chen, W., 1 - Epitaxial growth of graphene on silicon carbide (SiC). In *Graphene*, Skákalová, V.; Kaiser, A. B., Eds. Woodhead Publishing: 2014; pp 3-26.

27. Moreau, E.; Godey, S.; Ferrer, F. J.; Vignaud, D.; Wallart, X.; Avila, J.; Asensio, M. C.; Bournel, F.; Gallet, J. J., Graphene growth by molecular beam epitaxy on the carbon-face of SiC. *Applied Physics Letters* **2010,** *97* (24), 241907.

28. Duan, H. G.; Xie, E. Q.; Han, L., Turning electrospun poly(methyl methacrylate) nanofibers into graphitic nanostructures by in situ electron beam irradiation. *Journal of Applied Physics* **2008,** *103* (4), 046105.

29. Subrahmanyam, K. S.; Panchakarla, L. S.; Govindaraj, A.; Rao, C. N. R., Simple Method of Preparing Graphene Flakes by an Arc-Discharge Method. *The Journal of Physical Chemistry C* **2009,** *113* (11), 4257-4259.

30. Chanyshev, A. D.; Litasov, K. D.; Furukawa, Y.; Kokh, K. A.; Shatskiy, A. F., Temperature-induced oligomerization of polycyclic aromatic hydrocarbons at ambient and high pressures. *Scientific Reports* **2017,** *7*, 7889.

31. Bae, S.; Kim, H.; Lee, Y.; Xu, X. F.; Park, J. S.; Zheng, Y.; Balakrishnan, J.; Lei, T.; Kim, H. R.; Song, Y. I.; Kim, Y. J.; Kim, K. S.; Ozyilmaz, B.; Ahn, J. H.; Hong, B. H.; Iijima, S., Roll-to-roll production of 30-inch graphene films for transparent electrodes. *Nat. Nanotechnol.* **2010,** *5* (8), 574-578.

32. Kobayashi, T.; Bando, M.; Kimura, N.; Shimizu, K.; Kadono, K.; Umezu, N.; Miyahara, K.; Hayazaki, S.; Nagai, S.; Mizuguchi, Y.; Murakami, Y.; Hobara, D., Production of a 100-m-long high-quality graphene transparent conductive film by roll-to-roll chemical vapor deposition and transfer process. *Appl. Phys. Lett.* **2013,** *102* (2), 4.

33. Lei, D.; Liu, Y.; Zhiting, H.; Jiazhen, Z.; Chunlai, H.; Liaoxin, S.; Lin, W.; Dacheng, W.; Gang, C.; Wei, L., Thickness-controlled direct growth of nanographene and nanographite film on non-catalytic substrates. *Nanotechnology* **2018,** *29* (21), 215711.

34. Hwang, S. W.; Shin, H.; Lee, B.; Choi, S.-H., Non-catalytic direct synthesis of graphene on Si (111) wafers by using inductively-coupled plasma chemical vapor deposition. *Journal of the Korean Physical Society* **2016,** *69* (4), 536-540.

35. Susumu, K.; Jung-Gon, K.; Noriyuki, H.; Kenji, K.; Hiroshi, H., Non-catalytic direct growth of nanographene on MgO substrates. *Japanese Journal of Applied Physics* **2014,** *53* (5S1), 05FD06.

36. Jianyi, C.; Yunlong, G.; Lili, J.; Zhiping, X.; Liping, H.; Yunzhou, X.; Dechao, G.; Bin, W.; Wenping, H.; Gui, Y.; Yunqi, L., Near-Equilibrium Chemical Vapor Deposition of High-Quality Single-Crystal Graphene Directly on Various Dielectric Substrates. *Advanced Materials* **2014,** *26* (9), 1348-1353.

37. Chen, J.; Wen, Y.; Guo, Y.; Wu, B.; Huang, L.; Xue, Y.; Geng, D.; Wang, D.; Yu, G.; Liu, Y., Oxygen-Aided Synthesis of Polycrystalline Graphene on Silicon Dioxide Substrates. *Journal of the American Chemical Society* **2011,** *133* (44), 17548-17551.

38. Zheng, S.; Zhong, G.; Wu, X.; D'Arsiè, L.; Robertson, J., Metal-catalyst-free growth of graphene on insulating substrates by ammonia-assisted microwave plasma-enhanced chemical vapor deposition. *RSC Advances* **2017,** *7* (53), 33185-33193.

39. Wu, H.-Q.; Linghu, C.-Y.; Lu, H.-M.; Qian, H., Graphene applications in electronic and optoelectronic devices and circuits. *Chinese Physics B* **2013,** *22* (9), 098106.

40. Liu, Y.; Wang, H.; Zhao, W.; Zhang, M.; Qin, H.; Xie, Y., Flexible, Stretchable Sensors for Wearable Health Monitoring: Sensing Mechanisms, Materials, Fabrication Strategies and Features. *Sensors* **2018,** *18* (2).

41. Qiao, Y.; Wang, Y.; Tian, H.; Li, M.; Jian, J.; Wei, Y.; Tian, Y.; Wang, D.-Y.; Pang, Y.; Geng, X.; Wang, X.; Zhao, Y.; Wang, H.; Deng, N.; Jian, M.; Zhang, Y.; Liang, R.; Yang, Y.; Ren, T.-L., Multilayer Graphene Epidermal Electronic Skin. *ACS Nano* **2018**.

42. An, J.; Le, T.-S. D.; Huang, Y.; Zhan, Z.; Li, Y.; Zheng, L.; Huang, W.; Sun, G.; Kim, Y.-J., All-Graphene-Based Highly Flexible Noncontact Electronic Skin. *ACS Applied Materials & Interfaces* **2017,** *9* (51), 44593-44601.

43. Yong-Jin, K.; Sang Jin, K.; Myung Hee, J.; Kwang Yeol, C.; Sukang, B.; Seoung-Ki, L.; Youngbin, L.; Dolly, S.; Bora, L.; Huiyoun, S.; Myungshin, C.; Kyuho, P.; Jong-Hyun, A.; Byung Hee, H., Low-temperature growth and direct transfer of graphene–graphitic carbon films on flexible plastic substrates. *Nanotechnology* **2012,** *23* (34), 344016.

44. Ferrari, A. C.; Bonaccorso, F.; Fal'ko, V.; Novoselov, K. S.; Roche, S.; Boggild, P.; Borini, S.; Koppens, F. H. L.; Palermo, V.; Pugno, N.; Garrido, J. A.; Sordan, R.; Bianco, A.; Ballerini, L.; Prato, M.; Lidorikis, E.; Kivioja, J.; Marinelli, C.; Ryhanen, T.; Morpurgo, A.; Coleman, J. N.; Nicolosi, V.; Colombo, L.; Fert, A.; Garcia-Hernandez, M.; Bachtold, A.; Schneider, G. F.; Guinea, F.; Dekker, C.; Barbone, M.; Sun, Z. P.; Galiotis, C.; Grigorenko, A. N.; Konstantatos, G.; Kis, A.; Katsnelson, M.; Vandersypen, L.; Loiseau, A.; Morandi, V.; Neumaier, D.; Treossi, E.; Pellegrini, V.; Polini, M.; Tredicucci, A.; Williams, G. M.; Hong, B. H.; Ahn, J. H.; Kim, J. M.; Zirath, H.; van Wees, B. J.; van der Zant, H.; Occhipinti, L.; Di Matteo, A.; Kinloch, I. A.; Seyller, T.; Quesnel, E.; Feng, X. L.; Teo, K.; Rupesinghe, N.; Hakonen, P.; Neil, S. R. T.; Tannock, Q.; Lofwandera, T.;

Kinaret, J., Science and technology roadmap for graphene, related two-dimensional crystals, and hybrid systems. *Nanoscale* **2015,** *7* (11), 4598-4810.

45. Garg, R.; Elmas, S.; Nann, T.; Andersson, M. R., Deposition methods of graphene as electrode material for organic solar cells. *Adv. Energy Mater.* **2017,** *7* (10).

46. Novoselov, K. S.; Geim, A. K.; Morozov, S. V.; Jiang, D.; Zhang, Y.; Dubonos, S. V.; Grigorieva, I. V.; Firsov, A. A., Electric field effect in atomically thin carbon films. *Science* **2004,** *306* (5696), 666-669.

47. Yi, M.; Shen, Z., A review on mechanical exfoliation for the scalable production of graphene. *Journal of Materials Chemistry A* **2015,** *3* (22), 11700-11715.

48. Zhang, L.; Liang, J.; Huang, Y.; Ma, Y.; Wang, Y.; Chen, Y., Size-controlled synthesis of graphene oxide sheets on a large scale using chemical exfoliation. *Carbon* **2009,** *47* (14), 3365-3368.

49. Dreyer, D. R.; Park, S.; Bielawski, C. W.; Ruoff, R. S., The chemistry of graphene oxide. *Chemical Society Reviews* **2010,** *39* (1), 228-240.

50. Brodie BC. Hydration behavior and dynamics of water molecules in graphite oxide. Ann

Chim Phys 1860; 59: 466-72.

51. Staudenmaier, L., Verfahren zur Darstellung der Graphitsäure. B*erichte der deutschen chemischen Gesellschaft 1***898,** 3*1* (2), 1481-1487.

52. Hummers, W. S.; Offeman, R. E., Preparation of Graphitic Oxide. J*ournal of the American Chemical Society 1***958,** 8*0* (6), 1339-1339.

53. Stankovich, S.; Dikin, D. A.; Dommett, G. H. B.; Kohlhaas, K. M.; Zimney, E. J.; Stach, E. A.; Piner, R. D.; Nguyen, S. T.; Ruoff, R. S., Graphene-based composite materials. N*ature 2***006,** 4*42* (7100), 282-286.

54. McAllister, M. J.; Li, J.-L.; Adamson, D. H.; Schniepp, H. C.; Abdala, A. A.; Liu, J.; Herrera-Alonso, M.; Milius, D. L.; Car, R.; Prud'homme, R. K.; Aksay, I. A., Single sheet functionalized graphene by oxidation and thermal expansion of graphite. C*hemistry of Materials 2***007,** 1*9* (18), 4396-4404.

55. Stankovich, S.; Piner, R. D.; Chen, X. Q.; Wu, N. Q.; Nguyen, S. T.; Ruoff, R. S., Stable aqueous dispersions of graphitic nanoplatelets via the reduction of exfoliated graphite oxide in the presence of poly(sodium 4-styrenesulfonate). J*ournal of Materials Chemistry 2***006,** 1*6* (2), 155-158.

56. Stankovich, S.; Dikin, D. A.; Piner, R. D.; Kohlhaas, K. A.; Kleinhammes, A.; Jia, Y.; Wu, Y.; Nguyen, S. T.; Ruoff, R. S., Synthesis of graphene-based nanosheets via chemical reduction of exfoliated graphite oxide. C*arbon 2*007, 4*5* (7), 1558-1565.

57. Layek, R. K.; Nandi, A. K., A review on synthesis and properties of polymer functionalized graphene. P*olymer 2*013, 5*4* (19), 5087-5103.

58. Shao, J.-J.; Lv, W.; Yang, Q.-H., Self-assembly of graphene oxide at interfaces. A*dv. Mater. 2*014, 2*6* (32), 5586-5612.

59. Wang, X.; Zhi, L.; Müllen, K., Transparent, conductive graphene electrodes for dye-sensitized solar cells. N*ano Lett. 2*007, 8 (1), 323-327.

60. Pang, S. P.; Hernandez, Y.; Feng, X. L.; Mullen, K., Graphene as transparent electrode material for organic electronics. A*dv. Mater. 2*011, 2*3* (25), 2779-2795.

61. Zheng, Q. B.; Li, Z. G.; Yang, J. H.; Kim, J. K., Graphene oxide-based transparent conductive films. P*rog. Mater Sci. 2*014, 6*4,* 200-247.

62. Lopez-Naranjo, E. J.; Gonzalez-Ortiz, L. J.; Apatiga, L. M.; Rivera-Munoz, E. M.; Manzano-Ramirez, A., Transparent electrodes: a review of the use of carbon-based nanomaterials. J. *Nanomater. 2*016, 12.

63. Huang, X.; Yin, Z. Y.; Wu, S. X.; Qi, X. Y.; He, Q. Y.; Zhang, Q. C.; Yan, Q. Y.; Boey, F.; Zhang, H., Graphene-based materials: synthesis, characterization, properties, and applications. S*mall 2*011, 7 (14), 1876-1902.

64. Cai, D.; Song, M., Recent advance in functionalized graphene/polymer nanocomposites. J*ournal of Materials Chemistry 2*010, 2*0* (37), 7906-7915.

65. Wan, Y.-J.; Tang, L.-C.; Gong, L.-X.; Yan, D.; Li, Y.-B.; Wu, L.-B.; Jiang, J.-X.; Lai, G.-Q., Grafting of epoxy chains onto graphene oxide for epoxy composites with improved mechanical and thermal properties. C*arbon 2*014, 6*9,* 467-480.

66. Dehnert, M.; Spitzner, E.-C.; Beckert, F.; Friedrich, C.; Magerle, R., Subsurface Imaging of Functionalized and Polymer-Grafted Graphene Oxide. M*acromolecules 2*016, 4*9* (19), 7415-7425.

67. Ma, L.; Yang, X.; Gao, L.; Lu, M.; Guo, C.; Li, Y.; Tu, Y.; Zhu, X., Synthesis and characterization of polymer grafted graphene oxide sheets using a Ce(IV)/HNO3 redox system in an aqueous solution. C*arbon 2*013, 5*3,* 269-276.

68. Chyasnavichyus, Maryus, "SYNTHESIS AND CHARACTERIZATION OF NANOSCALE FLUORESCENT POLYMER FILMS" (2012). All Dissertations. 1015.

https://tigerprints.clemson.edu/all_dissertations/1015

69. Galabura, Yuriy, "SYNTHESIS AND CHARACTERIZATION OF NANOSCALE POLYMER FILMS GRAFTED TO METAL SURFACES" (2014). All Dissertations. 1300.

https://tigerprints.clemson.edu/all_dissertations/1300

70. Thomas, H. R.; Phillips, D. J.; Wilson, N. R.; Gibson, M. I.; Rourke, J. P., One-step grafting of polymers to graphene oxide. Pol*ymer chemistry 201***5, 6** (*4*8), 8270-8274.

71. Zhang, B.; Zhang, Y.; Peng, C.; Yu, M.; Li, L.; Deng, B.; Hu, P.; Fan, C.; Li, J.; Huang, Q., Pre*paration of polymer decorated graphene oxide by γ-ray induced graft polymerization. 2*012; Vol. 4, p 1742-8.

72. Nagata, K.; Kawahara, T.; Hashimoto, K.; Fujiki, K.; Tamesue, S.; Yamauchi, T.; Tsubokawa, N., Grafting of polymers onto graphene oxide by cationic and anionic polymerization initiated by the surface-initiating groups. Com*posite Interfaces 201***5, 22** *(1*), 25-37.

73. Perrozzi, F.; Prezioso, S.; Ottaviano, L., Graphene oxide: from fundamentals to applications. Jou*rnal of Physics: Condensed Matter 201***5, 27** *(1*), 013002.

74. Pham, V. H.; Cuong, T. V.; Hur, S. H.; Shin, E. W.; Kim, J. S.; Chung, J. S.; Kim, E. J., Fast and simple fabrication of a large transparent chemically-converted graphene film by spray-coating. Car*bon 201***0, 48** *(7*), 1945-1951.

75. Torrisi, F.; Hasan, T.; Wu, W.; Sun, Z.; Lombardo, A.; Kulmala, T. S.; Hsieh, G.-W.; Jung, S.; Bonaccorso, F.; Paul, P. J.; Chu, D.; Ferrari, A. C., Inkjet-Printed Graphene Electronics. ACS *Nano 201***2, 6** (*4*), 2992-3006.

76. Sun, H. B.; Yang, J.; Zhou, Y. Z.; Zhao, N.; Li, D., Preparation of reduced graphene oxide films by dip coating technique and their electrical conductivity. Mat*erials Technology 201***4, 29** *(1*), 14-20.

77. Mangadlao, J. D.; Santos, C. M.; Felipe, M. J. L.; de Leon, A. C. C.; Rodrigues, D. F.; Advincula, R. C., On the antibacterial mechanism of graphene oxide (GO) Langmuir-Blodgett films. Che*m. Commun. 201***5, 51** *(1*4), 2886-2889.

78. Zheng, Q. B.; Zhang, B.; Lin, X. Y.; Shen, X.; Yousefi, N.; Huang, Z. D.; Li, Z. G.; Kim, J. K., Highly transparent and conducting ultralarge graphene oxide/single-walled carbon nanotube hybrid films produced by Langmuir-Blodgett assembly. Jou*rnal of Materials Chemistry 201***2, 22** *(4*8), 25072-25082.

79. Kim, F.; Cote Laura, J.; Huang, J., Graphene Oxide: Surface Activity and Two-Dimensional Assembly. Adv*anced Materials 201***0, 22** *(1*7), 1954-1958.

80. Sheng, K.; Bai, H.; Sun, Y.; Li, C.; Shi, G., Layer-by-layer assembly of graphene/polyaniline multilayer films and their application for electrochromic devices. Pol*ymer 201***1, 52** *(2*4), 5567-5572.

81. Choi, W.; Choi, J.; Bang, J.; Lee, J. H., Layer-by-Layer Assembly of Graphene Oxide Nanosheets on Polyamide Membranes for Durable Reverse-Osmosis Applications. Acs *Applied Materials & Interfaces 201***3, 5** (*2*3), 12510-12519.

82. Hu, M.; Mi, B., Layer-by-layer assembly of graphene oxide membranes via electrostatic interaction. Jou*rnal of Membrane Science 201***4, 46***9, 8*0-87.

83. Alkhazali, A. S.; Hamasha, M. M.; Lu, S.; Westgate, C. R., A Comparative Study on Electrical and Mechanical Behavior of Indium Tin Oxide and Poly (3, 4-Ethylenedioxythiophene) Thin Films Under Tensile Loads. IEE*E Transactions on Device and Materials Reliability 201***5, 15** *(2*), 174-180.

84. Eda, G.; Lin, Y.-Y.; Miller, S.; Chen, C.-W.; Su, W.-F.; Chhowalla, M., Transparent and conducting electrodes for organic electronics from reduced graphene oxide. App*lied Physics Letters 200***8, 92** *(2*3), 233305.

85. Wang, J.; Liang, M.; Fang, Y.; Qiu, T.; Zhang, J.; Zhi, L., Rod-Coating: Towards Large-Area Fabrication of Uniform Reduced Graphene Oxide Films for Flexible Touch Screens. Adv*anced Materials 201***2, 24** *(2*1), 2874-2878.

86. Zhao, C. L.; Xing, L.; Xiang, J. H.; Cui, L. J.; Jiao, J. B.; Sai, H. Z.; Li, Z. Y.; Li, F., Formation of uniform reduced graphene oxide films on modified PET substrates using drop-casting method. Par*ticuology 201***4, 17**, *6*6-73.

87. Savchak, M.; Borodinov, N.; Burtovyy, R.; Anayee, M.; Hu, K.; Ma, R.; Grant, A. M.; Li, H.; Cutshall, D.; Wen, Y.-M.; Koley, G.; Harrell, W. R.; Chumanov, G.; Tsukruk, V. V.; Luzinov, I., Highly conductive and transparent reduced graphene oxide nanoscale films via thermal conversion of polymer-encapsulated graphene oxide sheets. ACS *Applied Materials & Interfaces 201***8, A**ccepted: DOI 10.1021/acsami.7b16500.

88. Garg, R.; Elmas, S.; Nann, T.; Andersson, M. R., Deposition Methods of Graphene as Electrode Material for Organic Solar Cells. Adv. *Energy Mater. 201***7, 7,** *1601393.*

*8*9. Ferrari, A. C.; Bonaccorso, F.; Fal'ko, V.; Novoselov, K. S.; Roche, S.; Boggild, P.; Borini, S.; Koppens, F. H. L.; Palermo, V.; Pugno, N.; Garrido, J. A.; Sordan, R.; Bianco, A.; Ballerini, L.; Prato, M.; Lidorikis, E.; Kivioja, J.; Marinelli, C.; Ryhanen, T.; Morpurgo, A.; Coleman, J. N.; Nicolosi, V.; Colombo, L.; Fert, A.; Garcia-Hernandez, M.; Bachtold, A.; Schneider, G. F.; Guinea, F.; Dekker, C.; Barbone, M.; Sun, Z. P.; Galiotis, C.; Grigorenko, A. N.; Konstantatos, G.; Kis, A.; Katsnelson, M.; Vandersypen, L.; Loiseau, A.; Morandi, V.; Neumaier, D.; Treossi, E.; Pellegrini, V.; Polini, M.; Tredicucci, A.; Williams, G. M.; Hong, B. H.; Ahn, J. H.; Kim, J. M.; Zirath, H.; van Wees, B. J.; van

der Zant, H.; Occhipinti, L.; Di Matteo, A.; Kinloch, I. A.; Seyller, T.; Quesnel, E.; Feng, X. L.; Teo, K.; Rupesinghe, N.; Hakonen, P.; Neil, S. R. T.; Tannock, Q.; Lofwandera, T.; Kinaret, J., Science and Technology Roadmap for Graphene, Related Two-Dimensional Crystals, and Hybrid Systems. Nan*oscale 201***5, 7,** *4*598-4810.

90. Wu, J. B.; Agrawal, M.; Becerril, H. A.; Bao, Z. N.; Liu, Z. F.; Chen, Y. S.; Peumans, P., Organic Light-Emitting Diodes on Solution-Processed Graphene Transparent Electrodes. ACS *Nano 201***0, 4,** *4*3-48.

91. Becerril, H. A.; Mao, J.; Liu, Z.; Stoltenberg, R. M.; Bao, Z.; Chen, Y., Evaluation of Solution-Processed Reduced Graphene Oxide Films as Transparent Conductors. ACS *Nano 200***8, 2,** *4*63-470.

92. Lim, J.; Choi, K.; Rani, J. R.; Kim, J. S.; Lee, C.; Kim, J. H.; Jun, S. C., Terahertz, Optical, and Raman Signatures of Monolayer Graphene Behavior in Thermally Reduced Graphene Oxide Films. Jou*rnal of Applied Physics 201***3, 11**3*, 1*83502

93. Lin, X. Y.; Jia, J. J.; Yousefi, N.; Shen, X.; Kim, J. K., Excellent Optoelectrical Properties of Graphene Oxide Thin Films Deposited on A Flexible Substrate by Langmuir-Blodgett Assembly. Jou*rnal of Materials Chemistry C 201***3, 1,** *6*869-6877.

94. Zheng, Q.-B.; Shi, L.-F.; Yang, J.-H., Langmuir-Blodgett Assembly of Ultra-Large Graphene Oxide Films for Transparent Electrodes. T. *Nonferr. Metal Soc. 201***2, 22**, *2*504-2511.

95. Zheng, Q. B.; Ip, W. H.; Lin, X. Y.; Yousefi, N.; Yeung, K. K.; Li, Z. G.; Kim, J. K., Transparent Conductive Films Consisting of Ultra Large Graphene Sheets Produced by Langmuir-Blodgett Assembly. ACS *Nano 201***1, 5,** *6*039-6051.

96. Zhao, J. P.; Pei, S. F.; Ren, W. C.; Gao, L. B.; Cheng, H. M., Efficient Preparation of Large-Area Graphene Oxide Sheets for Transparent Conductive Films. ACS *Nano 201***0, 4,** *5*245-5252.

97. Gao, W.; Alemany, L. B.; Ci, L.; Ajayan, P. M., New insights into the structure and reduction of graphite oxide. Nat *Chem 200***9, 1** (*5*), 403-408.

98. Park, S.; An, J.; Piner, R. D.; Jung, I.; Yang, D.; Velamakanni, A.; Nguyen, S. T.; Ruoff, R. S., Aqueous Suspension and Characterization of Chemically Modified Graphene Sheets. Che*mistry of Materials 200***8, 20** *(2*1), 6592-6594.

99. Mkhoyan, K. A.; Contryman, A. W.; Silcox, J.; Stewart, D. A.; Eda, G.; Mattevi, C.; Miller, S.; Chhowalla, M., Atomic and Electronic Structure of Graphene-Oxide. Nan*o Letters 200***9, 9** (*3*), 1058-1063.

100. Pei, S. F.; Cheng, H. M., The reduction of graphene oxide. Car*bon 201***2, 50** *(9)*, 3210-3228.

101. Mao, S.; Pu, H. H.; Chen, J. H., Graphene oxide and its reduction: modeling and experimental progress. Rsc *Advances 201***2, 2** (*7*), 2643-2662.

102. Lee, K. H.; Lee, B.; Hwang, S.-J.; Lee, J.-U.; Cheong, H.; Kwon, O.-S.; Shin, K.; Hur, N. H., Large scale production of highly conductive reduced graphene oxide sheets by a solvent-free low temperature reduction. Car*bon 201***4, 69**, *3*27-335.

103. Lee, S.; Eom, S. H.; Chung, J. S.; Hur, S. H., Large-scale production of high-quality reduced graphene oxide. Che*m. Eng. J. 201***3, 23**3*, 2*97-304.

104. Zhao, J.; Pei, S.; Ren, W.; Gao, L.; Cheng, H.-M., Efficient Preparation of Large-Area Graphene Oxide Sheets for Transparent Conductive Films. Acs *Nano 201***0, 4** (*9*), 5245-5252.

105. Becerril, H. A.; Mao, J.; Liu, Z.; Stoltenberg, R. M.; Bao, Z.; Chen, Y., Evaluation of Solution-Processed Reduced Graphene Oxide Films as Transparent Conductors. Acs *Nano 200***8, 2** (*3*), 463-470.

106. Wu, Z.-S.; Ren, W.; Gao, L.; Liu, B.; Jiang, C.; Cheng, H.-M., Synthesis of high-quality graphene with a pre-determined number of layers. Car*bon 200***9, 47** *(2)*, 493-499.

107. Chua, C. K.; Pumera, M., Chemical reduction of graphene oxide: a synthetic chemistry viewpoint. Che*m. Soc. Rev. 201***4, 43** *(1)*, 291-312.

108. Gao, X.; Jang, J.; Nagase, S., Hydrazine and thermal reduction of graphene oxide: reaction mechanisms, product structures, and reaction design. The *Journal of Physical Chemistry C 200***9, 11**4 *(2)*, 832-842.

109. Schniepp, H. C.; Li, J. L.; McAllister, M. J.; Sai, H.; Herrera-Alonso, M.; Adamson, D. H.; Prud'homme, R. K.; Car, R.; Saville, D. A.; Aksay, I. A., Functionalized single graphene sheets derived from splitting graphite oxide. Jou*rnal of Physical Chemistry B 200***6, 11**0 *(1*7), 8535-8539.

110. Steurer, P.; Wissert, R.; Thomann, R.; Mulhaupt, R., Functionalized Graphenes and Thermoplastic Nanocomposites Based upon Expanded Graphite Oxide. Mac*romolecular Rapid Communications 200***9, 30** *(4*-5), 316-327.

111. Zhou, Y.; Bao, Q. L.; Tang, L. A. L.; Zhong, Y. L.; Loh, K. P., Hydrothermal Dehydration for the "Green" Reduction of Exfoliated Graphene Oxide to Graphene and Demonstration of Tunable Optical Limiting Properties. Che*mistry of Materials 200***9, 21** *(1*3), 2950-2956.

112. Tang, H. X.; Ehlert, G. J.; Lin, Y. R.; Sodano, H. A., Highly Efficient Synthesis of Graphene Nanocomposites. Nano *Letters 201***2, 12** *(1*), 84-90.

113. Xiang, C.; Young, C. C.; Wang, X.; Yan, Z.; Hwang, C.-C.; Cerioti, G.; Lin, J.; Kono, J.; Pasquali, M.; Tour, J. M., Large Flake Graphene Oxide Fibers with Unconventional 100% Knot Efficiency and Highly Aligned Small Flake Graphene Oxide Fibers. Adv*anced Materials 201***3, 25** *(3*3), 4592-4597.

114. Schniepp, H. C.; Li, J.-L.; McAllister, M. J.; Sai, H.; Herrera-Alonso, M.; Adamson, D. H.; Prud'homme, R. K.; Car, R.; Saville, D. A.; Aksay, I. A., Functionalized Single Graphene Sheets Derived from Splitting Graphite Oxide. The *Journal of Physical Chemistry B 200***6, 11**0 *(1*7), 8535-8539.

115. Kudin, K. N.; Ozbas, B.; Schniepp, H. C.; Prud'homme, R. K.; Aksay, I. A.; Car, R., Raman Spectra of Graphite Oxide and Functionalized Graphene Sheets. Nano *Letters 200***7, 8** (*1*), 36-41.

116. López, V.; Sundaram, R. S.; Gómez-Navarro, C.; Olea, D.; Burghard, M.; Gómez-Herrero, J.; Zamora, F.; Kern, K., Chemical Vapor Deposition Repair of Graphene Oxide: A Route to Highly-Conductive Graphene Monolayers. Adv*anced Materials 200***9, 21** *(4*6), 4683-4686.

117. Dai, B.; Fu, L.; Liao, L.; Liu, N.; Yan, K.; Chen, Y.; Liu, Z., High-quality single-layer graphene via reparative reduction of graphene oxide. Nano *Res. 201***1, 4** (*5*), 434-439.

118. Su, Q.; Pang, S.; Alijani, V.; Li, C.; Feng, X.; Müllen, K., Composites of Graphene with Large Aromatic Molecules. Adv*anced Materials 200***9, 21** *(3*1), 3191-3195.

119. De Silva, K. K. H.; Huang, H. H.; Joshi, R. K.; Yoshimura, M., Chemical reduction of graphene oxide using green reductants. Car*bon 201***7, 11**9*, 1*90-199.

120. Feng, H.; Cheng, R.; Zhao, X.; Duan, X.; Li, J., A low-temperature method to produce highly reduced graphene oxide. Nat*ure Communications 201***3, 4,** *1*539.

121. Ferrari, A. C.; Bonaccorso, F.; Fal'ko, V.; Novoselov, K. S.; Roche, S.; Bøggild, P.; Borini, S.; Koppens, F. H. L.; Palermo, V.; Pugno, N.; Garrido, J. A.; Sordan, R.; Bianco, A.; Ballerini, L.; Prato, M.; Lidorikis, E.; Kivioja, J.; Marinelli, C.; Ryhänen, T.; Morpurgo, A.; Coleman, J. N.; Nicolosi, V.; Colombo, L.; Fert, A.; Garcia-Hernandez, M.; Bachtold, A.; Schneider, G. F.; Guinea, F.; Dekker, C.; Barbone, M.; Sun, Z.; Galiotis, C.; Grigorenko, A. N.; Konstantatos, G.; Kis, A.; Katsnelson, M.; Vandersypen, L.; Loiseau, A.; Morandi, V.; Neumaier, D.; Treossi, E.; Pellegrini, V.; Polini, M.; Tredicucci, A.; Williams, G. M.; Hee Hong, B.; Ahn, J.-H.; Min Kim, J.; Zirath, H.; van Wees, B. J.; van der Zant, H.; Occhipinti, L.; Di Matteo, A.; Kinloch, I. A.; Seyller, T.; Quesnel, E.; Feng, X.; Teo, K.; Rupesinghe, N.; Hakonen, P.; Neil, S. R. T.; Tannock, Q.; Löfwander, T.;

Kinaret, J., Science and technology roadmap for graphene, related two-dimensional crystals, and hybrid systems. Nan*oscale 201***5, 7** (*1*1), 4598-4810.

122. Das, A. K.; Srivastav, M.; Layek, R. K.; Uddin, M. E.; Jung, D.; Kim, N. H.; Lee, J. H., Iodide-mediated room temperature reduction of graphene oxide: a rapid chemical route for the synthesis of a bifunctional electrocatalyst. Jou*rnal of Materials Chemistry A 201***4, 2** (*5*), 1332-1340.

123. Huang, Z.-D.; Zhang, B.; Oh, S.-W.; Zheng, Q.-B.; Lin, X.-Y.; Yousefi, N.; Kim, J.-K., Self-assembled reduced graphene oxide/carbon nanotube thin films as electrodes for supercapacitors. Jou*rnal of Materials Chemistry 201***2, 22** *(8*), 3591-3599.

124. Kim, H.; Renault, O.; Tyurnina, A.; Simonato, J.-P.; Rouchon, D.; Mariolle, D.; Chevalier, N.; Dijon, J., Doping efficiency of single and randomly stacked bilayer graphene by iodine adsorption. App*lied Physics Letters 201***4, 10**5 *(1*), 011605.

125. Chu, S. W.; Baek, S. J.; Kim, D. C.; Seo, S.; Kim, J. S.; Park, Y. W., Charge transport in graphene doped with diatomic halogen molecules (I2, Br2) near Dirac point. Syn*thetic Metals 201***2, 16**2 *(1*7), 1689-1693.

126. Li, X. L.; Zhang, G. Y.; Bai, X. D.; Sun, X. M.; Wang, X. R.; Wang, E.; Dai, H. J., Highly conducting graphene sheets and Langmuir-Blodgett films. Nat*. Nanotechnol. 200***8, 3** (*9*), 538-542.

127. Wu, J. B.; Becerril, H. A.; Bao, Z. N.; Liu, Z. F.; Chen, Y. S.; Peumans, P., Organic solar cells with solution-processed graphene transparent electrodes. App*l. Phys. Lett. 200***8, 92** *(2*6), 3.

128. Kymakis, E.; Stratakis, E.; Stylianakis, M. M.; Koudoumas, E.; Fotakis, C., Spin coated graphene films as the transparent electrode in organic photovoltaic devices. Thi*n Solid Films 201***1, 52**0 *(4*), 1238-1241.

129. Biswas, S.; Drzal, L. T., A novel approach to create a highly ordered monolayer film of graphene nanosheets at the liquid-liquid interface. Nan*o Lett. 200***9, 9** (*1*), 167-172.

130. Granqvist, C. G.; Hultåker, A., Transparent and conducting ITO films: new developments and applications. Thi*n Solid Films 200***2, 41**1 *(1*), 1-5.

131. Hosono, H.; Ohta, H.; Orita, M.; Ueda, K.; Hirano, M., Frontier of transparent conductive oxide thin films. Vac*uum 200***2, 66** *(3*), 419-425.

132. Gómez-Navarro, C.; Meyer, J. C.; Sundaram, R. S.; Chuvilin, A.; Kurasch, S.; Burghard, M.; Kern, K.; Kaiser, U., Atomic structure of reduced graphene oxide. Nan*o Lett. 201***0, 10** *(4*), 1144-1148.

133. Mattevi, C.; Eda, G.; Agnoli, S.; Miller, S.; Mkhoyan, K. A.; Celik, O.; Mastrogiovanni, D.; Granozzi, G.; Garfunkel, E.; Chhowalla, M., Evolution of electrical, chemical, and structural properties of transparent and conducting chemically derived graphene thin films. Adv. *Funct. Mater. 200*9**, 19** *(1*6), 2577-2583.

134. Harris, K. D.; Elias, A. L.; Chung, H. J., Flexible electronics under strain: a review of mechanical characterization and durability enhancement strategies. J. *Mater. Sci. 201*6**, 51** *(6*), 2771-2805.

135. MacDonald, W. A.; Looney, M. K.; MacKerron, D.; Eveson, R.; Adam, R.; Hashimoto, K.; Rakos, K., Latest advances in substrates for flexible electronics. Jou*rnal of the Society for Information Display 200*7**, 15** *(1*2), 1075-1083.

136. MacDonald, W. A.; Looney, M. K.; MacKerron, D.; Eveson, R.; Rakos, K., Designing and manufacturing substrates for flexible electronics. Pla*stics Rubber and Composites 200*8**, 37** *(2*-4), 41-45.

137. Zardetto, V.; Brown, T. M.; Reale, A.; Di Carlo, A., Substrates for Flexible Electronics: A Practical Investigation on the Electrical, Film Flexibility, Optical, Temperature, and Solvent Resistance Properties. Jou*rnal of Polymer Science Part B-Polymer Physics 201*1**, 49** *(9*), 638-648.

138. Xu, Y., Post-CMOS and Post-MEMS Compatible Flexible Skin Technologies: A Review. IEE*E Sens. J. 201*3**, 13** *(1*0), 3962-3975.

139. Fang, Y. N.; Hester, J. G. D.; deGlee, B.; Tuan, C. C.; Brooke, P. D.; Le, T. R.; Wong, C. P.; Tentzeris, M. M.; Sandhage, K. H., A novel, facile, layer-by-layer substrate surface modification for the fabrication of all-inkjet-printed flexible electronic devices on Kapton. Jou*rnal of Materials Chemistry C 201*6**, 4** (*29*), 7052-7060.

140. Zhao, C.; Xing, L.; Xiang, J.; Cui, L.; Jiao, J.; Sai, H.; Li, Z.; Li, F., Formation of uniform reduced graphene oxide films on modified PET substrates using drop-casting method. Par*ticuology 201*4**, 17**, *6*6-73.

141. Huang, L.; Huang, Y.; Liang, J.; Wan, X.; Chen, Y., Graphene-based conducting inks for direct inkjet printing of flexible conductive patterns and their applications in electric circuits and chemical sensors. Nan*o Research 201*1**, 4** (*7*), 675-684.

142. Wang, X. W.; Liu, Z.; Zhang, T., Flexible Sensing Electronics for Wearable/Attachable Health Monitoring. Sma*ll 201*7**, 13** *(25*), 19.

143. Lipomi, D. J.; Vosgueritchian, M.; Tee, B. C. K.; Hellstrom, S. L.; Lee, J. A.; Fox, C. H.; Bao, Z., Skin-like pressure and strain sensors based on transparent elastic films of carbon nanotubes. Nat*ure Nanotechnology 201*1**, 6,** *7*88.

144. Hu, S.; Ren, X.; Bachman, M.; Sims, C. E.; Li, G. P.; Allbritton, N., Surface Modification of Poly(dimethylsiloxane) Microfluidic Devices by Ultraviolet Polymer Grafting. Ana*lytical Chemistry 200***2, 74** *(1*6), 4117-4123.

145. Barbier, V.; Tatoulian, M.; Li, H.; Arefi-Khonsari, F.; Ajdari, A.; Tabeling, P., Stable Modification of PDMS Surface Properties by Plasma Polymerization: Application to the Formation of Double Emulsions in Microfluidic Systems. Lang*muir 200***6, 22** *(1*2), 5230-5232.

146. Bredas, J.-L., Mind the gap! Mat*erials Horizons 201***4, 1** (*1*), 17-19.

147. Mak, K. F.; Ju, L.; Wang, F.; Heinz, T. F., Optical spectroscopy of graphene: From the far infrared to the ultraviolet. Sol*id State Commun. 201***2, 15**2 *(1*5), 1341-1349.

148. Castro Neto, A. H.; Guinea, F.; Peres, N. M. R.; Novoselov, K. S.; Geim, A. K., The electronic properties of graphene. Rev*iews of Modern Physics 200***9, 81** *(1*), 109-162.

149. Dmitry, S.; Victor, R.; Taiichi, O., Negative dynamic Drude conductivity in pumped graphene. App*lied Physics Express 201***4, 7** (*1*1), 115101.

150. Leandro, M. M.; Kin Fai, M.; Neto, A. H. C.; Peres, N. M. R.; Tony, F. H., Observation of intra- and inter-band transitions in the transient optical response of graphene. New *Journal of Physics 201***3, 15** *(1*), 015009.

151. Deepika, B.; Sukhbir, S.; Sriniwas, Y.; Ashok, K.; Inderpreet, K., Experimental and theoretical investigation of relative optical band gaps in graphene generations. Mat*erials Research Express 201***7, 4** (*1*), 015101.

152. Roy, R.; Thapa, R.; Chakrabarty, S.; Jha, A.; Midya, P. R.; Kumar, E. M.; Chattopadhyay, K. K., Role of oxygen functionality on the band structure evolution and conductance of reduced graphene oxide. Che*mical Physics Letters 201***7, 67**7*, 8*0-86.

153. Yavari, F.; Kritzinger, C.; Gaire, C.; Song, L.; Gulapalli, H.; Borca-Tasciuc, T.; Ajayan, P. M.; Koratkar, N., Tunable Bandgap in Graphene by the Controlled Adsorption of Water Molecules. Sma*ll 201***0, 6** (*2*2), 2535-2538.

CHAPTER THREE

SYNTHESIS AND CHARACTERIZATION OF POLYMER-MODIFIED GO MULTILAYERS

3.1: Introduction

This chapter is devoted to (i) the synthesis and characterization of sterically stabilized GO sheets in water, (ii) subsequent formation of GO monolayer and (iii) then bilayer GO films based on polymer-enveloped GO sheets. A general schematic of the method is depicted in **Figure 3.1A-D**. We employ water-soluble, surface-active and reactive copolymer poly(GMA-stat-OEGMA) [GMA: glycidyl methacrylate; OEGMA: oligo ethylene glycol methyl ether methacrylate] (P1) to generate a nanoscale coating evenly enveloping the GO sheets. This coating allows the dip-coating of the GO monolayer from water-based dispersion onto the surface of non-conductive substrates. To form the bi-layered GO structure, a polymer interlayer/linker made of PAA is deposited on the GO monolayer by adsorption. Specifically, the adsorption deposition process is based on the formation of a complex between the copolymer, covering the GO sheets and the polymer linker. The linker is employed to promote the formation of the second GO monolayer (by dip-coating) and provides carbon atoms for the rGO sheets' "healing" and "welding" during the GO reduction, which will be discussed later in **Chapter 4**.

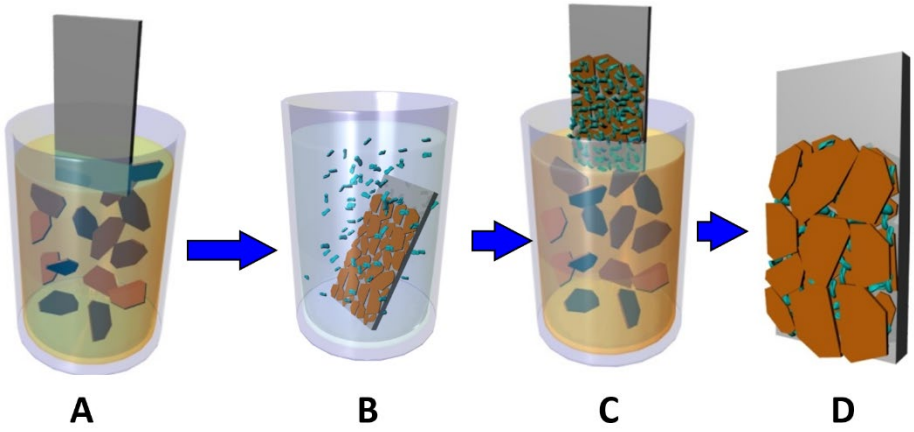

Figure 3.1: (A-D) Schematic representation of the method for nanomanufacturing of rGO-based films. (A): deposition of a monolayer of GO-P1 sheets enveloped with a polymer layer by dip-coating, (B): deposition of a polymer interlayer ("linker") by adsorption, (C): deposition of the second GO layer by dip-coating, (D): final double layer system composed of GO.

3.2: Experimental

3.2.1: Preparation of Graphene Oxide Sheets

The graphene oxide (GO) aqueous suspension was prepared using the Hummers method [1] in Dr. Tsukruk's laboratory. Natural 300-mesh graphite powder (Alfa Aesar) was added with 2.5 g of sodium nitrate ($NaNO_3$) in 107 mL of 98% sulfuric acid (H_2SO_4), which was cooled to 0℃ before mixing. Then 15 g of potassium permanganate ($KMnO_4$) was slowly added with vigorous stirring to avoid the temperature raising above 20℃. The mixture was heated to 35 ± 3 °C and maintained for 30 min before adding 214 mL of water; we then waited for the temperature to raise to 98℃ and maintained at this temperature for 15 min. Finally, 850 mL of warm ultrapure water and 1–2 mL of 30% hydrogen peroxide (H_2O_2) was added sequentially to dissolve the side products of the oxidation (black particulates), during which the color of the solution turned from dark brown to bright

yellow. The as-synthesized graphene oxide suspension was purified via water rinsing and ultracentrifugation (10000 rpm for 1 h) five times to remove the electrolytes.

3.2.2: Synthesis of P1 Copolymer

The procedure of copolymer synthesis was carried out in Dr. Luzinov's laboratory by Dr. Nikolay Borodinov. Poly(glycidyl methacrylate-co-oligoethylene glycol methyl ether methacrylate) copolymer was synthesized by free-radical polymerization initiated by azoisobutyronitrile using glycidyl methacrylate (GMA) and oligoethylene glycol methacrylate (OEGMA, average molecular weight 950 mol/g) monomers using the general method published elsewhere [2]. GMA (97%), azoisobutyronitrile (AIBN), OEGMA, and inhibitor removers (beads for removing hydroquinone and monomethyl ether hydroquinone [MEHQ] and tert-butylcatechol [BHT]) were purchased from Sigma-Alrdich. All solvents used in this study were purchased from VWR International and used as received. P1 was synthesized by the solution polymerization. MEHQ inhibitor remover beads were added to the GMA prior to synthesis. MEHQ and BHT inhibitor remover beads were added to the OEGMA dissolved in methyl ethyl ketone (MEK) prior to synthesis, and the suspensions were shaken for 45 min. The monomers were then filtered using 0.2 μm syringe filters and loaded into the reaction flask with AIBN (0.01M in monomer + MEK solution). The charged OEGMA/GMA molar ratio was 80:20, and the overall monomer concentration was 0.5 M. The solution was kept under nitrogen purge for 45 min and then immersed into a water bath preheated to 50 ˚C. The polymerization reaction was terminated after 1.5 h by opening the flask to the ambient atmosphere and cooling. The product of the

reaction was precipitated in diethyl ether, centrifuged, and dissolved in MEK. This procedure was repeated three times to remove the unreacted monomers and initiator.

Analysis of the copolymer composition by NMR

Nuclear magnetic resonance (NMR) analysis with a Bruker AVANCE-300 spectrometer, TopSpin 1.3 PL4, and Delta 5.0.4 software was used to characterize the copolymer (spectra are shown in **Appendix A1**). The OEGMA:GMA molar ratio was estimated as 68.5:31.5 and corresponds to a 94.0:6.0 mass ratio. The copolymer composition was also investigated with Attenuated Total Reflectance Fourier Transform Infrared Spectroscopy (spectra are not shown). A Thermo Nicolet Magna 550 Fourier transform infrared (FTIR) spectrometer with the Thermo-Spectra Tech Endurance Foundation Series Diamond ATR accessory was used, and 16 scans were averaged. An ATR correction and baseline correction were performed using Thermo Scientific OMNIC software version 8.0. Data processing and plotting were completed using Origin MicroCal 6.1. The ratio of the intensities of the peaks located at 1100 cm^{-1} and 1727 cm^{-1} corresponding to ether and ester bonds, respectively, was used to estimate the composition of the P1: OEGMA:GMA= 63.8:36.2. Therefore, the OEGMA:GMA molar ratio in the copolymer is approximately 66:34, as evidenced by the comparison of the NMR and FTIR measurements. The dynamic light scattering study was used to estimate the molecular weight of the P1 to be $M_W \approx 2858$ kg/mol. Specifically, the Malvern Zetasizer ZS Dynamic Light Scattering and Zeta Potential (DLS-Zeta) instrument was used to measure the size of the polymer coil in methyl ethyl ketone to estimate the molecular weight. A set of

monodisperse polystyrene standards with molecular weights ranging from 200 up to 3000 kDa dissolved in methyl ethyl ketone was used for calibration.

3.2.3: Modification of GO Sheets with P1 Copolymer

For the modification (**Figure 3.2**), an aqueous suspension of GO (~ 0.75-1.5 mg/ml) was mixed with an aqueous solution of P1 (~ 3-4 mg/ml) in a mass ratio of 1:6. During the procedure, the dispersion of P1 was added dropwise to the dispersion of sonicated GOs in 40 ml centrifugation tubes. Such order of mixing ensured that the particles would modify the GOs and prevent nanoparticle bridging between the individual GO sheets. The mixture was vigorously shaken for 15 min and then kept at room temperature on an orbital shaker for at least 4 h up to 24 hours. Next, the suspension of GO-P1 was redistributed into small 2 ml vials and subjected to centrifugation at 15000 rpm (Mini Spin Plus, Eppendorf) for 5-10 minutes. After all solids (GO-P1 sheets) were separated from the rest of the solution, the latter was pipetted out and the remaining GO-P1 particulates were again redispersed into new portion of DI water by rigorous shaking for 10 minutes. Such rinsing procedure was repeated at least 3 times to ensure complete removal of unattached/unreacted P1 chains from aqueous solution of GO-P1.

Then, the content from each 2 ml test-tube was combined into 40 ml centrifugation tubes and centrifuged at 1000 and 500 rpm (Prexision 100 Durafuge) for 15 min to remove any flocculated sheets. Afterwards, the top portion of the suspension was pipetted off until 10 ml of suspension was left. The top portion of the suspension was pipetted off until 2-5 ml of suspension was left. This procedure was repeated two more times.

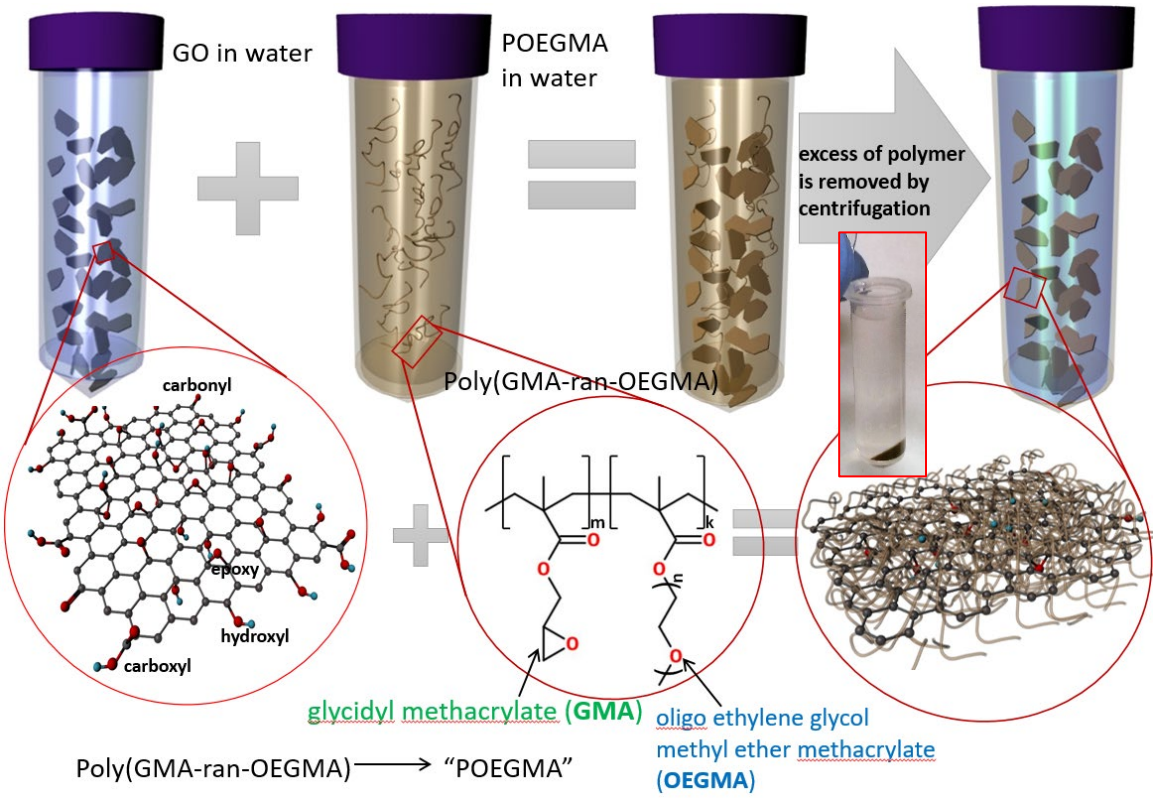

Figure 3.2: Modification of GO sheets with P1 polymer. Insert: GO-P1 (on the bottom) in water after centrifugation at 15000 rpm.

3.2.4: Chemical analysis of GO and GO-P1

Fourier-transform Infrared Spectroscopy (FTIR)

The composition of GO, P1 and GO-P1 materials were also investigated by FTIR. A Thermo Nicolet 6700 FTIR spectrometer equipped with a transmission base plate and a "Continuum" microscope was used for the FTIR studies of the GO and GO-P1 materials. Si wafer (500 µm in thickness). Highly polished silicon wafers, cut to ~2 × 4 cm size, (University Wafer: P/Boron, <100>, 1–10 Ohm·cm, 500 um) were used as substrates for background and sample collection. All films for FTIR measurements were prepared via

drop-casting method followed by at least 24-hour drying in ambient conditions. To achieve high signal-to-noise ratio we used 256 scans during background and sample collection steps. To reduce the influence of moisture and CO_2 (located around 2350 cm^{-1}) all samples were kept in nitrogen-purged chamber for 10-15 minutes prior to the beginning of scan. An FTIR correction and baseline correction were performed using Thermo Scientific OMNIC software version 8.0. Data processing and plotting were completed using Origin 2016 (version 9.3.2, Academic version).

X-ray Photon Spectroscopy

Further analysis of the chemical composition and the chemical states of the GO, GO-P1, and rGO-P1 films were conducted with a Thermal Scientific K-alpha X-ray Photon Spectroscope (XPS) using an aluminum K-alpha radiation X-ray source (1486.7 eV). The survey scans were done by integrating the two scans between the binding energy of -10 and 1350 eV at a 1.0 eV step size and a 50 ms dwell time for each step. The high-resolution elemental spectra were collected by integrating four scans of the corresponding binding energy ranges at a 0.1 eV step size and a 50 ms dwell time. All XPS data were fit using XPSPeak 4.1 software. The background was considered to be Tougaard type, and each component peak shape was considered to be a mixture of Lorentzian and Gaussian (L/G ~ 0.3). All XPS measurements were taken by Drs. Ruilong Ma and Kesong Hu under the supervision of Prof. V. Tsukruk at Georgia Institute of Technology. Highly polished, single-crystal, undoped non-conductive silicon wafers, cut to ~1.5 × 3 cm size, (University Wafer: <100>, 10000–20000 Ohm·cm, 500 um) were used as substrates

3.2.5: Analysis of Thermal Properties of GO and GO-P1

Thermal stability of GO-P1

To study the thermal decomposition of P1, PAA and the GO before and after the modification with P1, thermogravimetric analysis (TGA) was performed using a Q-5000 TA Instruments and AutoTGA 2950HR V5.4A under nitrogen gas from room temperature to 700 °C using a ramp rate of 15 °C min^{-1}.

Differential scanning calorimetry (DSC) (Model 2920; TA Instruments) was carried out at a heating/cooling rate of 20 °C/min. The temperature range of the experiment was set from -100 °C to 100 °C. At least 1 mg of substance was used in each DSC and TGA experiment.

Kinetics of copolymer adsorption

To study the adsorption kinetics we mixed a 3 mg ml^{-1} concentrated water solution of adsorbent (GO) with a 5 mg ml^{-1} P1 in water in ratio 1:6. Such system was held at constant room temperature. Then we gently evacuated small amount of the suspension after 20 minutes, 1, 2.5, 4.5 hours of adsorption and rinsed it well with DI water at least 3 times. Next, we did TGA for each time point using conditions specified above.

3.2.6: Procedure for the Calculation of Polymer Thickness from TGA Data

TGA data can be used to calculate the thickness/amount of polymer bound to the surface of the particulates[3]. The thickness of polymer bound to the surface of the particulates is directly proportional to the amount of weight loss in the TGA experiment and depends on the surface area of the particulates. It was assumed that the polymer is

uniformly distributed across the surface of the GO particulates. Equation 3.1 was used to calculate the thickness (t) of the polymer attached to the planar GO nanoparticulates. This equation is derived from geometrical considerations:

$$h_p = h_{GO} \cdot \frac{m_p \rho_{GO}}{m_{GO} \rho_p} \tag{3.1}$$

where h_{GO} is the thickness of the pristine GO (whisker or nanoparticle), ρ_{GO} and ρ_p are the densities of the bulk GO and polymer, m_p and m_{GO} are the weight fractions for the polymer and nanoparticulates as indicated by TGA, respectively.

3.2.7: Formation of GO-P1 Monolayer

Preparation of SiO_2/Si substrates

Highly polished, single-crystal, undoped non-conductive silicon wafers, cut to ~2 × 4 cm size, (University Wafer: <100>, 10000–20000 Ohm·cm, 500 um) were used as substrates. Before deposition of the GO-P1 monolayer the wafers were first cut using diamond cutter and cleaned in an ultrasonic bath for 30 min, placed in a hot "piranha" solution (3:1 concentrated sulfuric acid 30% hydrogen peroxide) for 1 h, and then rinsed several times with high-purity DI water (18MΩ,cm, Nanopure). After being rinsed, the substrates were dried under a stream of ultra-high purity nitrogen (purchased from Airgas).

GO-P deposition via adsorption

In order to study the possibility of GO-P1 monolayer formation via adsorption deposition clean wafer of SiO_2/Si was placed into a 40 ml test-tube with 0.025 wt. % water solution of GO-P1 and left there for 12 and 24 hours (**Figure 3.3A**). During that time the solution was subject to gentle shaking. Next, the sample was taken out from the test-tube

and placed in DI water for 1 hour. Water in the test-tube was replaced at least three times. After being rinsed, the sample was dried under a stream of ultra-high purity nitrogen and then scanned with AFM. The same procedure was repeated for reference wafer in pristine GO solution. From **Figure 3.3** (**B and C**) we can see that no layers were formed by adsorption for both pristine GO (**B**) and GO-P1 (**C**).

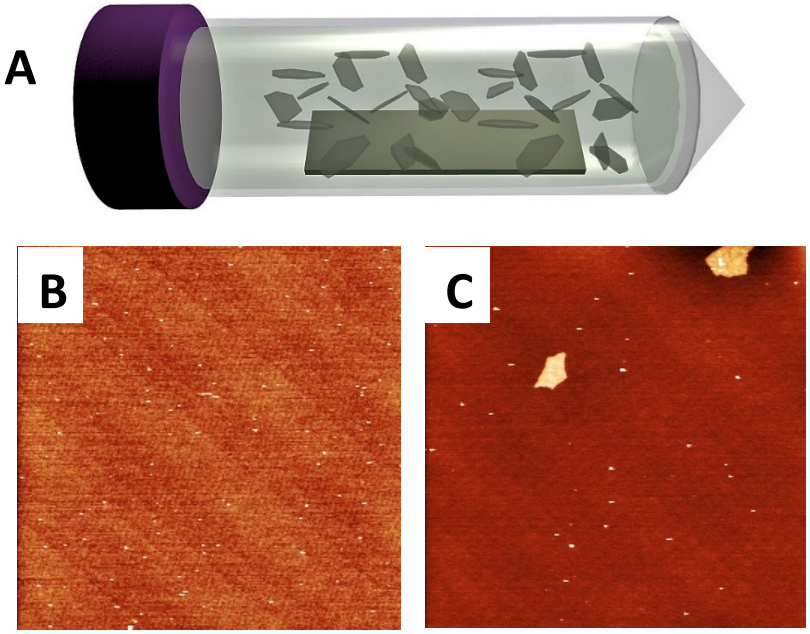

Figure 3.3: (A): Schematic representation of GO adsorption on bare SiO_2/Si. (B): Adsorption of pristine GO. (C): Adsorption of GO-P1.

GO-1P deposition via dip-coating

The GO-P1 mononolayer was deposited on clean SiO_2/Si substrate by dip-coating (**Figures 3.1A**) from 0.025 wt. % GO-P1 suspension at a 300 mm/min withdrawal speed (Mayer Feintechnik dip coater, model D-3400).

3.2.8: Formation of GO-P1 Multilayer

Adsorption deposition of polymer linker layer on GO-P1 monolayer

Two SiO_2/Si samples (labeled as #1 and #2) with the deposited GO-P1 monolayers were immersed in a 2 wt. % solution of polyacrylic acid (PAA) with a pH of 2.5–2.8 (35 wt. % water solution obtained from Sigma-Aldrich, Mw = 100 kDa) and kept there for 20 min. To remove unattached PAA from the surface, samples were rinsed at least three times each with different solvent for 15 minutes: sample #1 was rinsed with methanol and sample #2 - with DI water. After the rinsing procedure samples were dried in ambient conditions. It was revealed by AFM imaging that methanol is a better candidate for rinsing purposes as water completely removed adsorbed PAA layer from sample #2 (**Figure 3.4B**). Therefore, in all our next experiments we only used methanol as a solvent to rinse PAA layers.

Deposition of second GO-P1 monolayer

A second layer of GO-P1 was deposited over the first one modified with PAA by dip-coating using at least 300 mm/min withdrawal speed (**Figure 3.1C and D**). To emphasize on the importance of PAA as a linker layer dip-coating was performed on both samples #1(**Figure 3.16**) and #2 (**Figure 3.4**). In contrast to sample #1 sample #2 showed no bilayer presence after second GO-P1 deposition (**Figure 3.4**).

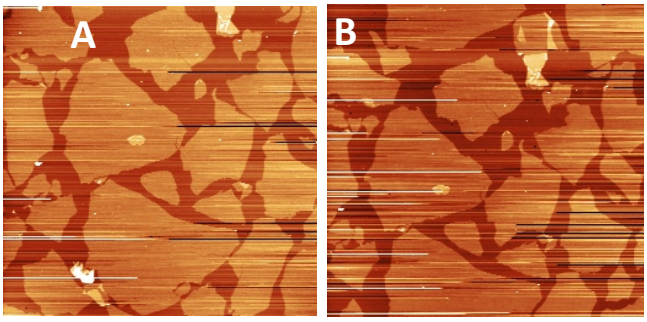

Figure 3.4: Sample #2. AFM images showing (A): dip-coated GO-P1 monolayer with adsorbed PAA and (B): the same spot of GO-P1/PAA monolayer after being rinsed with Methanol and second dip-coating in GO solution (vertical scale: 20 nm for 30x30 μm^2).

3.2.9: Surface Morphology of GO-P1 Films

Morphological studies

Morphology, microstructure and changes in thickness of individual GO sheet after modification with the polymers were studied with a Dimension 3100 (Veeco Digital Instruments, Inc.) in the tapping mode. Silicon tips with a spring constant of 50 N m^{-1} were used for all scans at 1 Hz. Analysis of AFM images was carried out using Gwyddion version 2.45 with the assistance of Dr. Ruslan Burtovyy.

Optical and Scanning Electron Microscopy

Scanning electron microscope (SEM) (Hitachi S-4800, acceleration voltage of 0.5 - 1 kV) and optical microscope (HUVITZ HRM-300) were used as means to further investigate morphology and microstructure of GO-P1 layers on silicon substrate.

3.3: Results and Discussion

3.3.1: Modification of GO Sheets with P1 Copolymer

The statistical copolymer (P1)[4] used for the GO modification consists of two different methacrylic monomeric units (reactive via epoxy group and hydrophobic glycidyl methacrylate [GMA] and the polar oligoethylene glycol methyl ether methacrylate [OE] responsible for solubility of the P1 in water). We hypothesized, that during the modification of GO with P1, GMA epoxy groups react with (hydroxyl, carboxyl, and epoxy) GO functional groups via non-condensation reactions (**Figure 3.5**)[5-6].

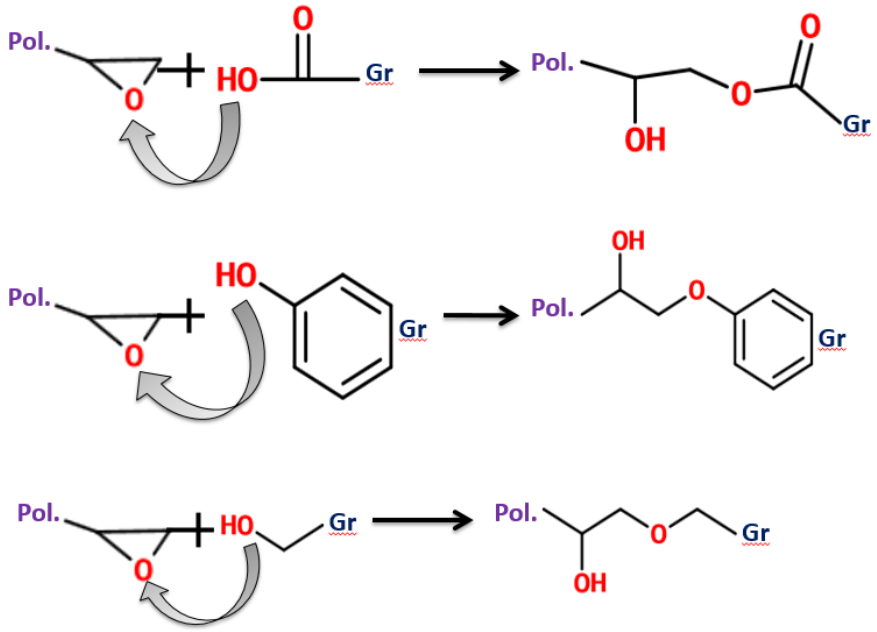

Figure 3.5: Reactions of GMA epoxy groups with functional groups of GO.

The presence of multiple reactive groups along the polymer chain is needed to ensure that every macromolecule will form multiple connections with GO surface to form the thin polymer coating enveloping the sheets. It is necessary to highlight that the suspension of the GO sheets modified with P1 is stable for a long time. In fact, we used the same suspension for the formation of GO layers for up to 6 months. This observation

indicates that the copolymer chains anchored to the GO surface provide an effective steric stabilization of the colloidal suspension.

Chemical, structural and morphological properties of the GO-P1 particulates were comprehensively investigated by means of various characterization techniques: AFM, FTIR, XPS, DSC, TGA and Raman.

3.3.2: Chemical Analysis of GO-P1

The attachment of P1 on pristine GO surfaces was attested by Fourier transform infrared spectroscopy (FTIR). **Figure 3.6** illustrates the FTIR spectra of Pristine GO, P1, and GO-P1 respectively. The results of FTIR spectra were analyzed using readily available spectral databases for organic compounds [7]. The broad peak at 3400 cm^{-1} is from O-H groups, and two narrow peaks assigned to the carbonyl group (C=O stretching) and the skeletal vibration of unoxidized graphitic domains on GO sheets (aromatic C=C) can be observed at 1740 and 1620 cm^{-1} (**Figure 3.6a**). The range of 1000-1280 cm^{-1} corresponds to ethers and/or epoxide groups. For P1 (**Figure 3.6b**), the C-H stretching group is represented by the peak at 2870 cm^{-1}.

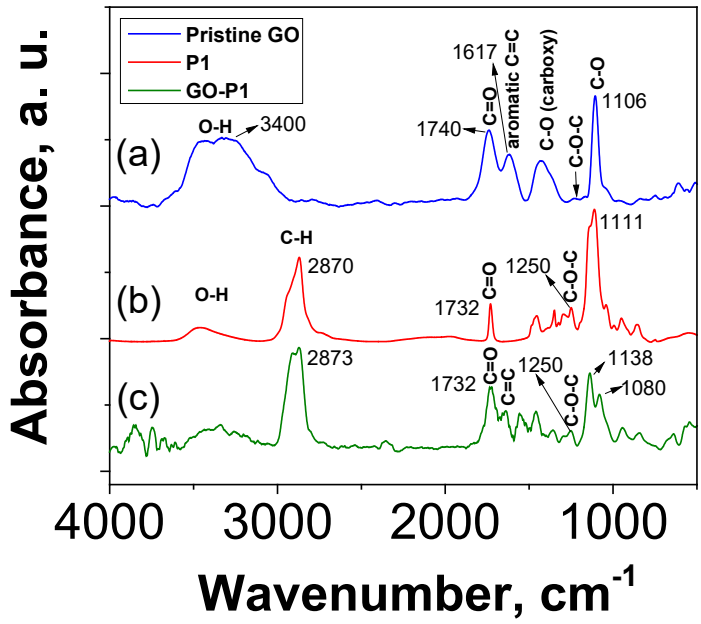

Figure 3.6: FTIR spectra for: (a) pristine GO, (b) P1, and (c) GO-P1.

The absorbance peaks at 1732, 1250, 1111 cm^{-1} can be attributed to carbonyl (C=O), epoxy (C-O-C) and ether (C-O) stretching vibrations. In the spectrum of GO-P (**Figure 3.6c**) the absorption bands detected at 2873, 1732 and 1250 cm^{-1} are the characteristic of the C-H, C=O and C-O-C groups of the grafted P1, respectively [8]. As evidenced from the spectra of P1 the intensities of epoxy at 1138 cm^{-1} decreased (relatively to CH peak) after modification of GO with P1, which implies possible chemical reaction between two compounds (consumption of epoxy via esterification reactions).

In order to further study the chemical composition of GO films and find C/O ratio of GO before and after modification we used XPS. Curve fitting of C_{1s} XPS spectra of each sample was performed using the Gaussian-Lorentzian distribution. It is reported elsewhere [9-13] that the values of chemical shifts are normally assigned at 284.5-285.0 eV for C-C/C=C and the rest of the peaks reveal the following chemical shift from the latter one: +1.3 - +1.7

eV for C-OH, +2.5 - +3.0 eV for C=O/C-O-C and +4.0 - +4.5 eV for COOH. Since our films are less than 10 nm in thickness, we could not reliably define C/O ratio from the survey spectrum due to the presence of SiO_2 layer on silicon wafer which significantly contributes to O_{1s} peak. Therefore, the C/O ratio was estimated by **Equation 3.2** based on the deconvoluted C_{1s} peak:

$$C/O = A_{C_{1s}}/(0.57 \times A_{C-OH} + 0.5 \times 0.57 \times A_{C=O/C-O-C} + 0.5 \times 0.4 \times A_{C=O/C-O-C} + 0.72 \times A_{COOH}) \quad (3.2)$$

where A_{C-OH}, $A_{C=O/C-O-C}A_{COOH}$ correspond to the area of each peak in the C_{1s} spectrum and $A_{C_{1s}}$is total peak area.

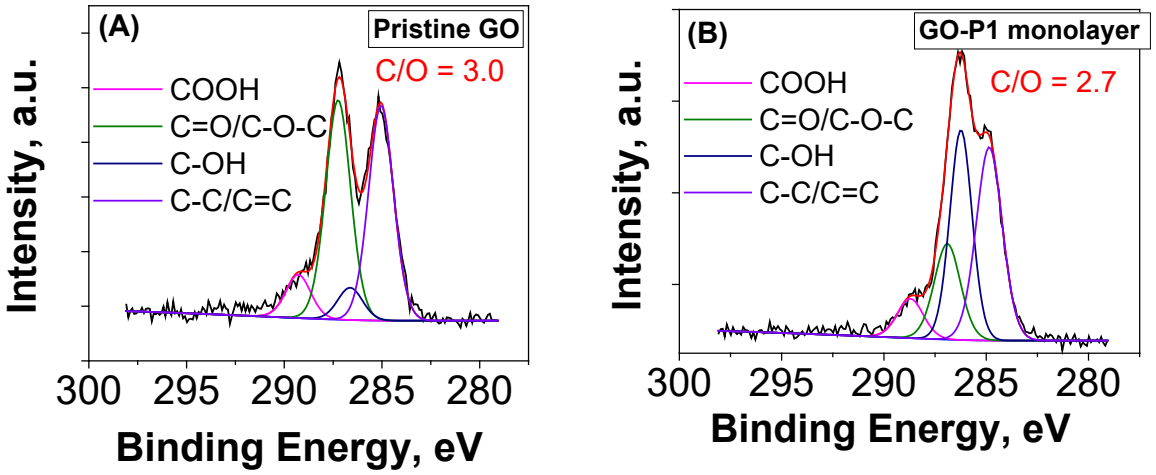

Figure 3.7: High resolution C1s spectra of (A) pristine GO and (B) GO-P1 monolayer.

The atomic % for different O related functional groups is calculated with respect to the total area of the C1s spectrum as a sum of the areas of each component weighted by the corresponding stoichiometric ratio. As seen from the **Figure 3.7A** C=O/C-OC at 287.5 eV

(epoxy) peak is of comparable intensity to C=C at 284. 5 eV. In contrast, P1-modified GO showed significant decrease in epoxy peak relatively to C=C at the expense of C-OH increase at 286 eV as shown in **Figure 3.7B**. These results align well with the FTIR results, suggesting effective grafting of P1 polymer chains to GO sheets mediated by chemical reactions of epoxy functional groups shown in **Figure 3.5**.

3.3.3: Thermal Properties of GO-P1

Next, thermogravimetric analysis (TGA) and dynamic scanning calorimetry (DSC) were used to further investigate the process of GO modification with P1 copolymers: (i) to study the thermal stability of pristine GO, P1 and GO-P1 (ii) to study the kinetics of copolymer adsorption and (iii) to find out the weight ratio between copolymer and GO material after adsorption process is completed.

Thermal stability of GO-P1

To study the thermal stability of pristine GO, P1, GO-P1 and PAA the samples were heated to 700 ^{o}C at a rate of 15 ^{o}C /min in a nitrogen atmosphere. From **Figure 3.10**, it can be observed that pristine GO is not thermostable: mass loss of GO started below 100 ^{o}C, which is attributed to the volatilization of stored water in its π-stacked structure [14]. The main weight loss of GO around 200 ^{o}C is caused by the decomposition of labile oxygen-containing functional groups yielding CO, CO_2 and H_2O steam [15]. The overall weight loss of pristine GO is 44%. The curve of P1 shows a fast weight reduction at 415 ^{o}C. The reduction is caused by the decomposition of P1 polymer, leaving about 6% of carbon. As for GO-P1, about 70% weight fraction loss is observed from 200 to 500 ^{o}C, which is due

to the decomposition of P1 and some oxygen functional groups of GO sheets. The peak analysis was done by taking first derivative of the GO-P1 curve with respect to temperature, then subsequent fit deconvolution and was done using Pseudo Voigt I function in Origin 9.0 (2016). From this, the ratio of the GO to polymer can be found. Based on TGA curves we found that P1 constituted about 50% of total mass of GO-P1 being decomposed. Taking the bulk density of GO as 1800 kg/m^3 [1617] and assuming the density of P1 to be close to that of PEG 1200 kg/m^3 [18], and knowing that 56% of total mass of P1 corresponds to polymer, total thickness of P1 was estimated – 1.78 nm according to **Equation 3.1** (~0.9 nm of polymer on each side of GO). Also, TGA curve for PAA showed that approximately 15 % of carbon is left after PAA decomposition.

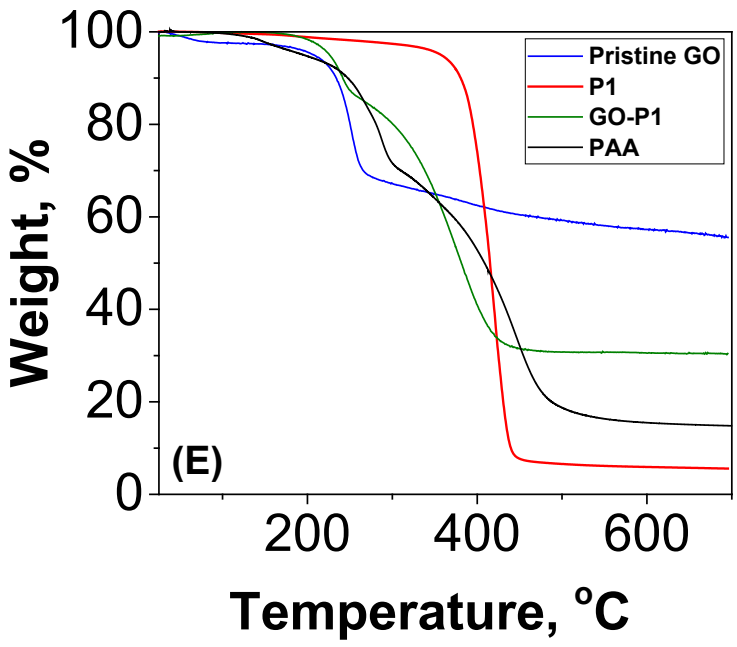

Figure 3.8: Thermogravimetric analysis of pristine GO, P1, GO-P1 and poly acrylic acid (PAA).

Kinetics of copolymer adsorption

TGA curves for GO-P1 and the resulting kinetic isotherm for P1 adsorption onto GO surface are presented in **Figure. 3.9**. We found that adsorption equilibrium was reached within about 20 minutes and the grafted copolymer weight content was equal to 53%. It suggests that grafting process is very fast at initial stage and is similar to the observed grafting from melt [4].

In order to further analyze the adsorption process we used appropriate kinetic models. According to the literature, two kinetic models, namely the pseudo-first order (PFO) and pseudo-second-order (PSO) equations, are commonly used to describe adsorption process under non-equilibrium conditions [19-20]. In this study, the non-linear form of PFO was used to fit the experimental kinetic data for the adsorption of P1 copolymer to the surface of GO in water. The PFO (3.3) and PSO (3.4) kinetic equations for adsorption analysis can be expressed as follows:

$$A_t = A_\infty(1 - e^{-k_1 t}) \tag{3.3}$$

$$A_t = \frac{k_2 A_\infty^2 t}{1 + k_2 A_\infty t} \tag{3.4}$$

where k_1 and k_2 are the rate constants of corresponding models, A_t is the amount of solute (P1) adsorbed on the adsorbent (GO) at time t, and A_∞ is the amount at equilibrium. In this study, we used the R^2 values to determine the relationship between the experimental data and the kinetic models [19]. The kinetic parameters obtained from the non-linear fittings by **Equation 3.3** and **3.4** are shown in **Figure 3.11A.** The value of (R^2) show that the PSO

model was better than the PFO model in the simulation of kinetics of P1 adsorption on pristine GO in water. Therefore, the adsorption process of P1 on GOs was probably controlled by the chemical adsorption process as suggested in ref. [21-22]. The above conclusion may prove the hypothesis (see **Section 3.3.1**) that P1 chains get chemically attached to GO sheets via covalent interactions between GMA epoxy groups and (hydroxyl, carboxyl, and epoxy) GO functional groups. The software, Origin 9.0 (2016), was used to fit the experimental data.

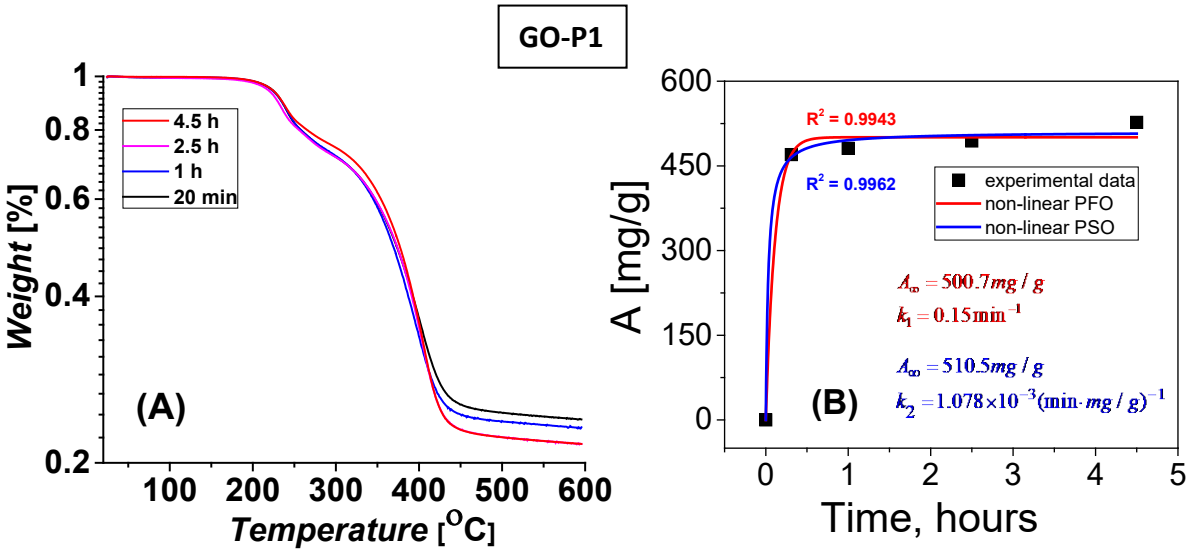

Figure 3.9: (A) TGA thermograms of GO grafted with P1 as a function of grafting time; (B) Grafted amount of copolymer to GO from water as a function of time.

DSC studies of the interaction between the GO and P1

Figure 3.10 shows the DSC curves of GOs before and after P1 introduction to the GOs. The obtained results clearly demonstrate the following: (1) the melting point depression of P1 from ~34.5 ºC to 29.3 ºC and (2) a notable suppression in the intensity of endothermic peak associated with melting.

According to previous research results [23-24] it is the interaction between the GO surface and stabilizing polymer that decides the shift direction of the melting point. The observed 5 ºC decrease in the melting point of primary peak is due to the significant interaction between the GO sheets and P1 chains. By contrast, an increased phase change temperature will occur when the interaction between polymer chains becomes highly attractive which is through hydrogen bonding between side OEGMA units in free P1 chains.

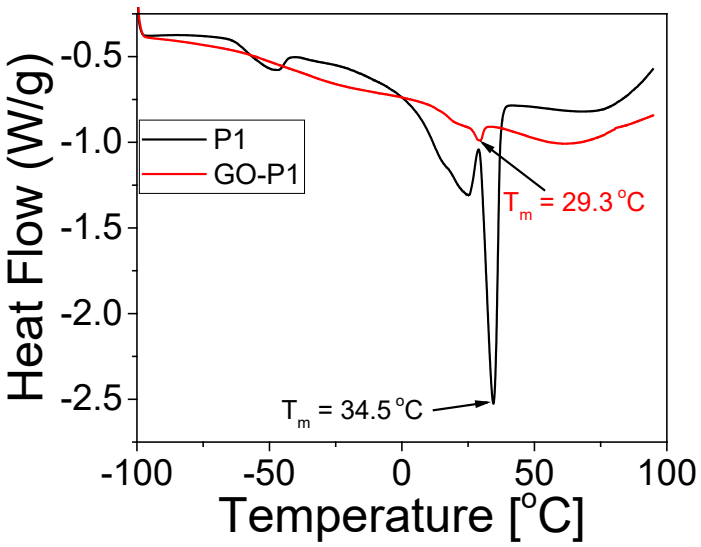

Figure 3.10: DSC thermograms for P1 and GO-P1.

Next, a notable suppression in endothermic peak indicates that most OEGMA segments are amorphous, which in turn suggests that most of mobility of the OEGMA side segments is restricted by the surface anchoring.

3.3.4: Colloidal Stability of GO-P1

Influence of molecular weight of P1 on colloidal stability of GO

It is expected that when P1 polymer is adsorbed on GO surface there will be a repulsive steric entropic force generated with a range determined by the radius of gyration of the polymer (R_g) [25]. However, at distances less than R_g attractive dispersion forces start to dominate resulting in GO flocculation and bridging. Thus, it was hypothesized that aggregation/flocculation of GO increases with the decrease in P1/GO ratio (by count) which negatively impacts the quality of a monolayer after deposition. **Figure 3.11** presents AFM images of GO modified with P1 of different molecular weight: M_{w1} = 500 kDa and M_{w2} = 2000 kDa. Mixing of $P1_{500\ kDa}$ (0.5 wt%) and GO (0.15 wt%) at mass ratio of 1:1 resulted in dense and uniform GO-P1 monolayer formed after dipcoating. On the other hand, when $P1_{2\ MDa}$ (0.5 wt%) was mixed with GO (0.15 wt%) flocculates or aggregates GO-P1 were present on top of GO-P1 layer, as shown in **Figure 3.11C**. This aggregation of GO sheets is ascribed to the bridging effect [26-27]. Specifically, larger R_g of $P1_{Mw\ =\ 2\ MDa}$ enhances attractive dispersion forces, causing polymer-bridging induced aggregation of GO sheets (polymer chains are long enough to adsorb onto more than one GO particle [28]). Therefore, shorter polymer chains of $P1_{Mw\ =\ 500kDa}$ are better choice for obtaining uniform and well-defined GO-P1 monolayer.

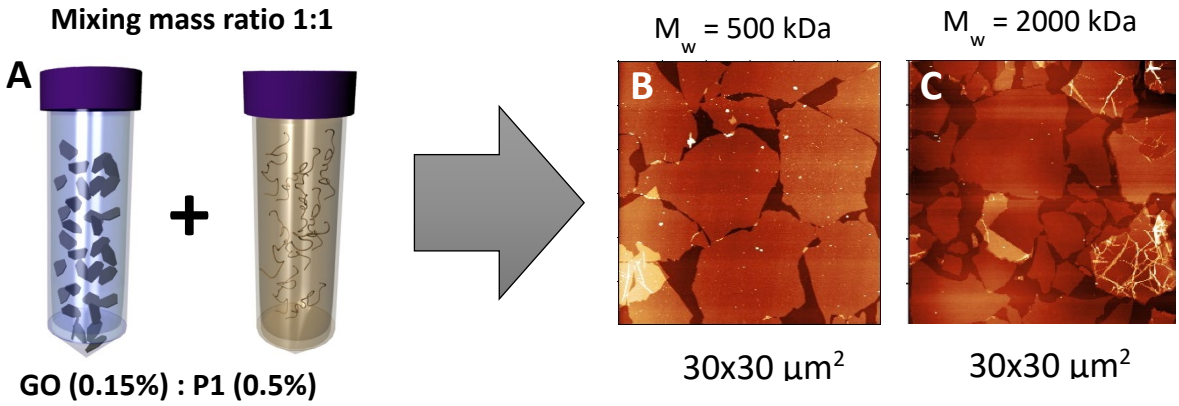

Figure 3.11: (A): Schematic representation of pristine GO and P1 copolymer in water before mixing. (B) and (C): representative AFM images of GO-P1(500 kDa) and GO-P1 (2 MDa).

Colloidal stability of GO as a function of mixing ratio between P1 and GO

To investigate what concentrations of GO and P1 (M_w = 2 MDa) would be the most efficient to form stable GO-P1 suspension, as this is predicted to play a large role in a deposition of good quality monolayer on a targeted substrate, we prepared 4 water solutions of GO and P1 at different mixing mass ratios (m_{GO}/m_{P1}): 1:1, 1:3, 1:6, 1:12.

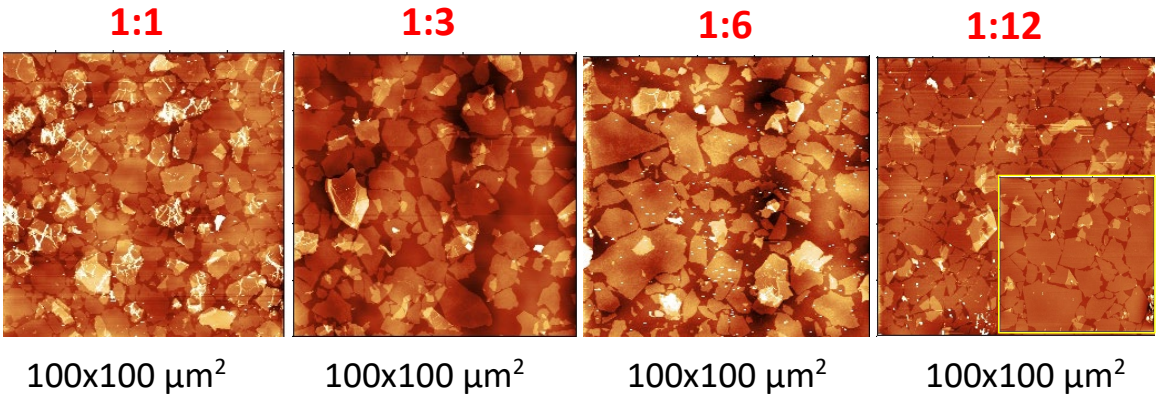

Figure 3.12: AFM images of GO sheets modified with P1 (M_w = 2 MDa) at different mixing mass ratios of GO and polymer P1. m_{GO}/m_{P1}: 1:1, 1:3, 1:6, 1:12.

AFM images, shown in **Figure 3.12**, clearly demonstrate that the quality of a monolayer becomes better with lesser bridging effect as the concentration of P1 increases.

In summary, our results confirm literature findings [29] that very long polymer ($P1_{Mw = 2\ MDa}$) chains and their low concentrations contribute to bridging flocculation. Therefore, the mixing ration used in all our next experiments was at least 1:6.

3.3.5: Formation of GO-P1 Monolayer

Thickness of adsorbed copolymer layer

To determine the thickness of the individual GO sheets modified with P1, we used atomic AFM. As indicated by the cross-sectional analysis (**Figure 3.13A**), the thickness of the pristine GO sheet was on the level of 1 nm, which is comparable to the value typically reported for the GO sheets obtained via Hummers method [30-32].

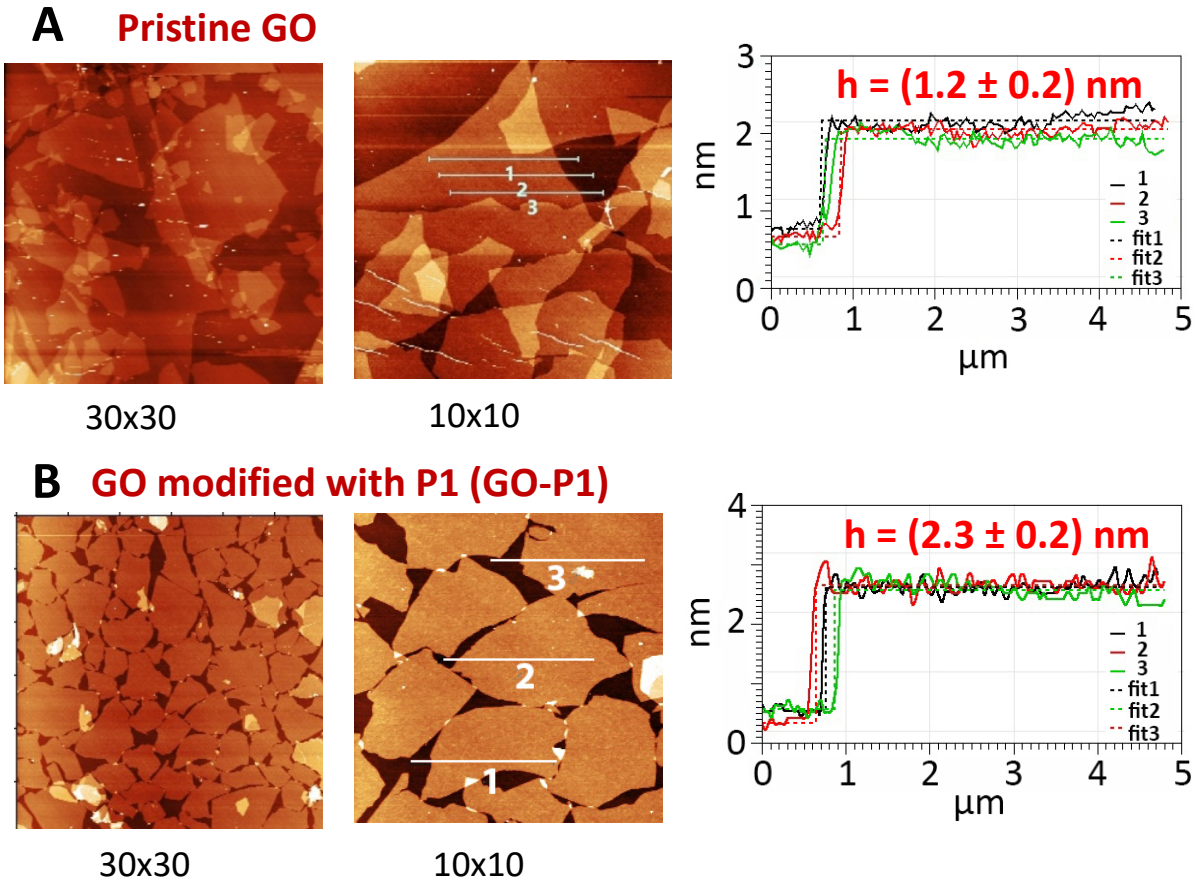

Figure 3.13: AFM images and corresponding cross-sectional profiles showing (A): a pristine GO layer obtained by dip-coating (vertical scale: 10 and 5 nm for 30x30 μm^2 and 10x10μm^2 images, respectively) and (B): GO-P1 monolayer obtained by dip-coating (vertical scale: 10 and 5 nm for 30x30 μm^2 and 10x10μm^2 images, respectively).

However, the thickness increased more than twofold to ~2.5 nm (**Figure 3.13B**) upon the GO modification with copolymer. This implies that the P1monolayer was indeed anchored to the GO surface. Also, the height profile of GO-P1 sheets (**Figure 3.13B**) suggested that the P1 chains formed even and dense coating encapsulating the sheets. The above result is in good agreement with TGA-found total thickness of ≈2 nm as reported in **Section 3.3.3**.

3.3.6: Morphology of GO-P1 Monolayer

In our initial experiments with pristine (unmodified with P1) GO sheets, we found that it was impossible to obtain a GO dense monolayer via dip-coating. We obtained either scarce coverage (40-50%) in the first layer or random multilayered/aggregated deposition with local wrinkles when concentration of the GO suspension was increased (**Figure 3.13A**). On the contrary, the GO-P1 sheets formed a dense monolayer (surface coverage more than 90%) as a result of the dip-coating at a quite high (300 mm/min) withdrawing speed (**Figure 3.13B**). The virtual absence of the second layer was observed by AFM as well. It is evident that the P1 coating sterically stabilized the GO sheets and prevented the interaction between the sheets during the deposition. At the same time, the P1 layer offered strong adhesion to the silicon oxide surface and the modified GO due to reaction between epoxy functional groups of GMA and silanol groups present on the surface of silicon wafer.[33] In fact, a dried GO-P1 monolayer does not delaminate from the surface in water even after an intensive one-hour ultra-sonication treatment (**Figure 3.14**).

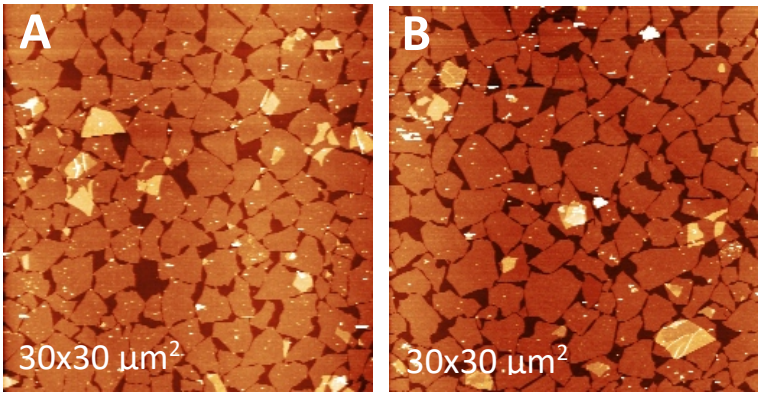

Figure 3.14: Stability of GO-P1 monolayers. AFM images of GO-P1 monolayer on Si wafer before (A) and after 1hour ultra-sonication in water (B). Vertical scale 10 nm.

Since GO reveals size-dependent amphiphilicity [34-35] we used flakes with large (~1600 µm^2), medium (~100 µm^2), and small (~9 µm^2) average areas to investigate how the quality of monolayer coverage is affected by the lateral sheet size. We concluded that the quality of deposited monolayers on hydrophilic silicon substrate does not depend on the initial size of pristine GO flakes, which was manifested through the AFM measurements shown in **Figure 3.15(A, B, C)**.

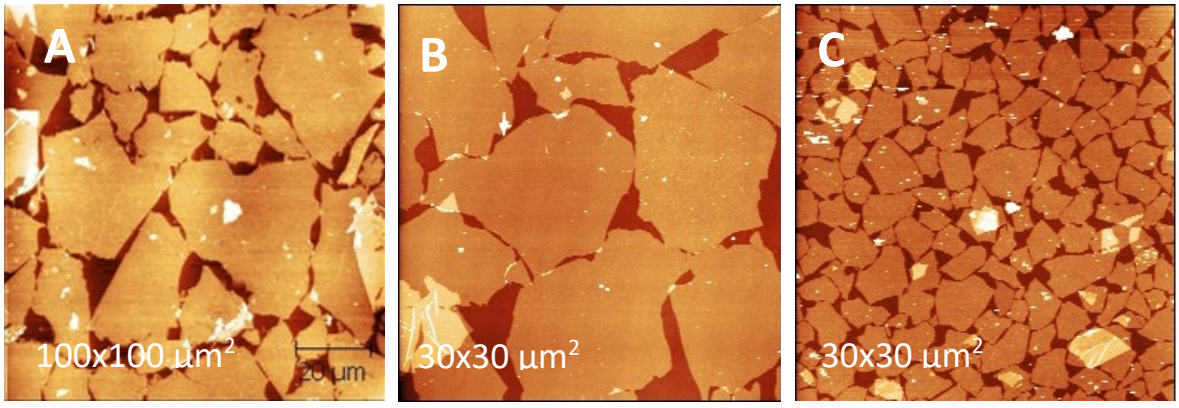

Figure 3.15: Hydrophilic Si wafer. (A-C) modified GO-P1 of different average sheet sizes (~ 40 µm, ~ 10 µm, ~ 3 µm). Height scale (0-10 nm) for all images.

3.3.7: Formation of GO-P1 Multilayers

We have hypothesized that high level of conductivity will be associated with a decrease in the inter-sheet resistance via the addition of a second GO-P1 monolayer above the first one. We had foreseen that the bi-layered structure, where sheets from the top layer are placed over the sheet-to-sheet contact of the bottom layer, will decrease layer resistivity. In addition, we used a polymer linker between the sheets, PAA, which during thermal reduction can serve as a carbon source for the defect "healing"[32, 36-37] and "welding" of the sheets. In fact, TGA measurements showed that during heating in an inert atmosphere, PAA material produced a significant amount of carbon, 15% by the polymer weight, which is significantly larger than the 5% produced during P1decomposition **(Figure 3.8)**. Therefore, external supply of carbon can saturate carbon vacancies forming as a result of CO/CO_2 dissociation during the thermal treatment.

The PAA linker layer was adsorbed on the dip-coated GO-P1 monolayer (**Figure 3.1B and Figure 3.16A-B**) using the approach previously employed for the L-b-L deposition of hydrogen-bonded multilayers[38-39]. Namely, we utilized the complex formation between polyethylene glycol side chains of P1 and PAA at pH values below 3[40]. AFM imaging confirmed the successful deposition of the PAA layer, as indicated by changes in morphology as well as increase in the roughness and thickness of the individual GO-P1 sheets (**Figure 3.16D-E)**. The result of the AFM cross-section measurements indicated that a PAA layer of about 2.5–3 nm was anchored to the GO-P1 sheets. The employment of PAA did not require any additional modification of the GO-P1 material, and the same suspension of GO-P1 in water was used for the formation of the

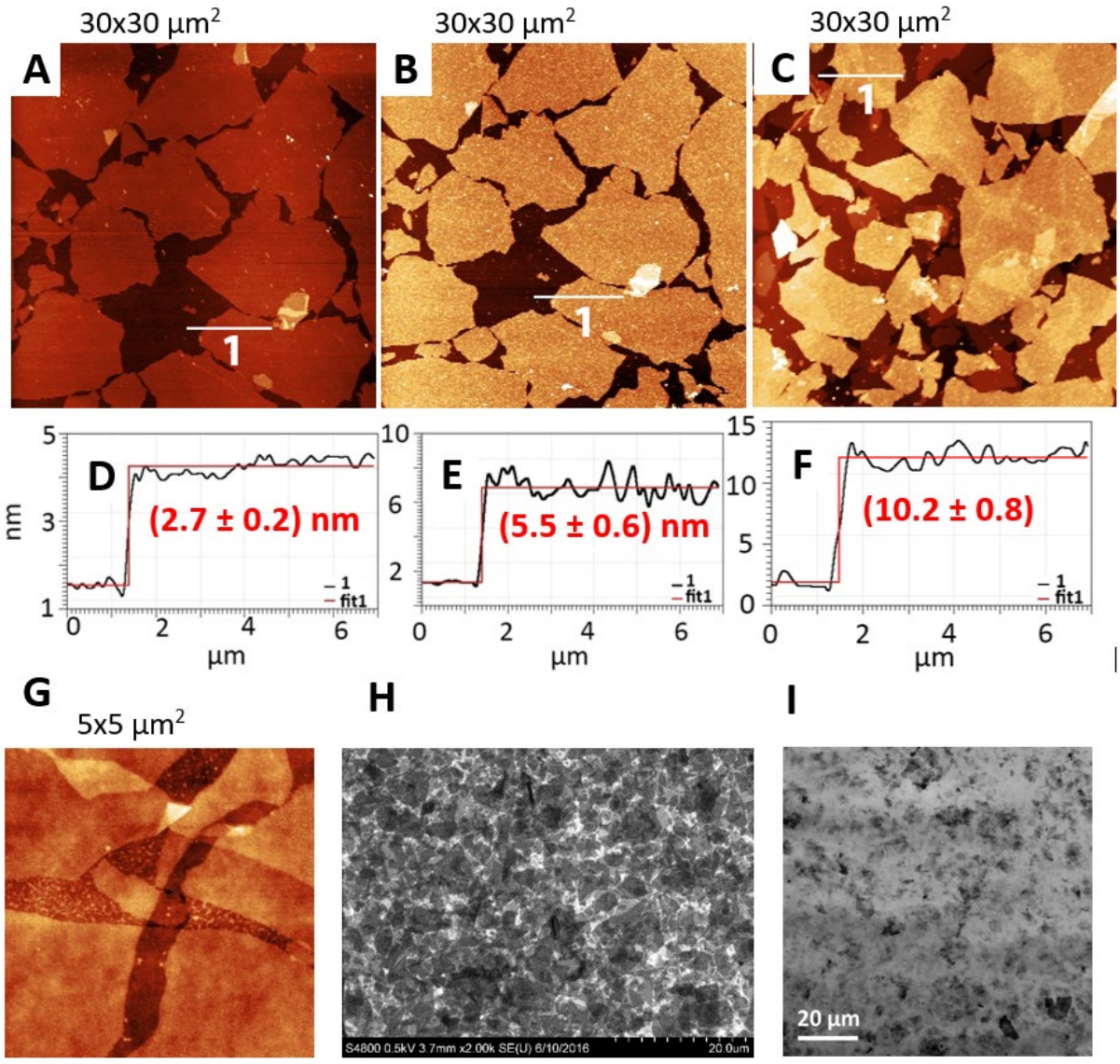

Figure 3.16: AFM topography images of a GO-P1 monolayer (A) (vertical scale: 12 nm), GO-P1 with adsorbed PAA layer on top (B) (vertical scale: 12 nm) and GO-P1 bi-layer (C, G) (vertical scale: 20 and 12 nm for 30x30 µm^2 and 5x5 µm^2 images, respectively) and corresponding cross-sectional profiles (D-F). SEM (H) and optical (I) images of GO-P1 bi-layer film. All films were deposited on undoped SiO_2/Si substrate. From the image (G) we can clearly see two overlapping layers of GO-P1 (second top layer) and GO-P 1/PAA (first bottom layer).

second GO-P1 monolayer. The second GO-P1 layer was readily deposited over the first one modified with PAA by dip-coating using the same experimental parameters as for the

first layer's deposition (**Figure 3.16C, F**). The virtually uniform double-layer structure with total thickness of ~ 10 nm was fabricated this way (**Figure 3.13AC, F-I)**. It should be noted that the second GO-P1 layer "heals" the empty areas not covered by the first layer joining individual GO-P1 sheets and forming a monolithic coherent bi-layer structure. It is very important that the surface was found to be virtually free of the extra third-layer presence. We found that without the PAA layer a complete second GO-P1 layer could not be obtained via dip-coating. We associate this phenomenon with steric repulsion (caused by P1 chains) between the GO-P1 sheets already deposited on the surface and the sheets being deposited later.

3.4: Conclusions

The following conclusions can be derived as a result of our study reported in Chapter 3:

- Using XPS, TGA and DSC it was confirmed that P1 copolymer can be readily grafted to GO surface through the non-condensation reactions of epoxy functional groups with (hydroxyl, carboxy, and epoxy) functional groups located on the GO surface.
- Steric stabilization of individual GO sheets was achieved through its surface modification with P1 copolymer.
- High molecular weight polymer P1 (M_w = 2MDa) can be used for steric stabilization of GO only at high enough concentrations to avoid polymer-bridging effect.

- Straightforward and technology-friendly dip-coating method allows obtaining uniform monolayers of different-sized GO on the level of 10 cm^2.
- The method allowed to control the thickness GO-P1 film with single-layer precision.
- GO-P1 monolayer showed strong adhesion to the SIO_2/Si substrate.
- The presence of PAA was necessary to achieve 2^{nd} complete monolayer to form uniform GO-P1 bilayer.

3.5: References

1. Hummers, W. S.; Offeman, R. E., Preparation of graphitic oxide. *J. Am. Chem. Soc.* **1958,** *80* (6), 1339-1339.

2. Tsyalkovsky, V.; Klep, V.; Ramaratnam, K.; Lupitskyy, R.; Minko, S.; Luzinov, I., Fluorescent reactive core-shell composite nanoparticles with a high surface concentration of epoxy functionalities. *Chemistry of Materials* **2008,** *20* (1), 317-325.

3. Townsend, James, "Fabrication and Characterization of Silicon Carbide Epoxy Composites" (2017). All Dissertations. 1948.

https://tigerprints.clemson.edu/all_dissertations/1948

4. Borodinov, N.; Gil, D.; Savchak, M.; Gross, C. E.; Yadavalli, N. S.; Ma, R.; Tsukruk, V. V.; Minko, S.; Vertegel, A.; Luzinov, I., En Route to Practicality of the Polymer Grafting Technology: One-Step Interfacial Modification with Amphiphilic Molecular Brushes. A*CS Applied Materials & Interfaces 2***018,** 1*0* (16), 13941-13952.

5. Roghani-Mamaqani, H.; Khezri, K., Polystyrene-attached graphene nanolayers by reversible addition-fragmentation chain transfer polymerization: a grafting from epoxy groups with various densities. J*ournal of Polymer Research 2***016,** 2*3* (9).

6. Zdyrko, B.; Luzinov, I., Polymer Brushes by the "Grafting to" Method. M*acromol. Rapid Commun. 2***011,** 3*2* (12), 859-869.

7. Pretsch, E.; Bühlmann, P.; Badertscher, M., S*tructure Determination of Organic Compounds : Tables of Spectral Data.* Springer: Berlin, 2009.

8. Wu, X.; Li, S.; Zhao, Y.; Tang, Y.; Liu, J.; Guo, X.; Wu, D.; He, G., Using a layer-by-layer assembly method to fabricate a uniform and conductive nitrogen-doped graphene anode for indium-tin oxide-free organic light-emitting diodes. A*CS Appl Mater Interfaces 2***014,** 6 (18), 15753-9.

9. Yumitori, S., Correlation of C1s chemical state intensities with the O1s intensity in the XPS analysis of anodically oxidized glass-like carbon samples. J*ournal of Materials Science 2***000,** 3*5* (1), 139-146.

10. Shi, H. F.; Wang, C.; Sun, Z. P.; Zhou, Y. L.; Jin, K. J.; Yang, G. Z., Transparent conductive reduced graphene oxide thin films produced by spray coating. S*cience China-Physics Mechanics & Astronomy 2***015,** 5*8* (1), 5.

11. Yang, D.; Velamakanni, A.; Bozoklu, G.; Park, S.; Stoller, M.; Piner, R. D.; Stankovich, S.; Jung, I.; Field, D. A.; Ventrice, C. A.; Ruoff, R. S., Chemical analysis of

graphene oxide films after heat and chemical treatments by X-ray photoelectron and Micro-Raman spectroscopy. C*arbon 2***009,** 4*7* (1), 145-152.

12. Sutar, D. S.; Narayanam, P. K.; Singh, G.; Botcha, V. D.; Talwar, S. S.; Srinivasa, R. S.; Major, S. S., Spectroscopic studies of large sheets of graphene oxide and reduced graphene oxide monolayers prepared by Langmuir-Blodgett technique. T*hin Solid Films 2***012,** 5*20* (18), 5991-5996.

13. Becerril, H. A.; Mao, J.; Liu, Z.; Stoltenberg, R. M.; Bao, Z.; Chen, Y., Evaluation of solution-processed reduced graphene oxide films as transparent conductors. A*CS Nano 2***008,** 2 (3), 463-470.

14. Jung, I.; Dikin, D.; Park, S.; Cai, W.; Mielke, S. L.; Ruoff, R. S., Effect of Water Vapor on Electrical Properties of Individual Reduced Graphene Oxide Sheets. J. *Phys. Chem. C 2***008,** 1*12* (51), 20264-20268.

15. Stankovich, S.; Dikin, D. A.; Piner, R. D.; Kohlhaas, K. A.; Kleinhammes, A.; Jia, Y.; Wu, Y.; Nguyen, S. T.; Ruoff, R. S., Synthesis of graphene-based nanosheets via chemical reduction of exfoliated graphite oxide. C*arbon 2***007,** 4*5* (7), 1558-1565.

16. https://www.sigmaaldrich.com/catalog/product/aldrich/796034?lang=en&region=US

17. Williams, C. D.; Carbone, P.; Siperstein, F. R., Computational characterisation of dried and hydrated graphene oxide membranes. N*anoscale 2***018,** 1*0* (4), 1946-1956.

18. https://www.sigmaaldrich.com/catalog/product/aldrich/202444?lang=en&region=US

19. Lin, J.; Wang, L., Comparison between linear and non-linear forms of pseudo-first-order and pseudo-second-order adsorption kinetic models for the removal of methylene blue by activated carbon. F*rontiers of Environmental Science & Engineering in China 2***009,** 3 (3), 320-324.

20. Ho, Y. S.; McKay, G., A Comparison of Chemisorption Kinetic Models Applied to Pollutant Removal on Various Sorbents. P*rocess Safety and Environmental Protection 1***998,** 7*6* (4), 332-340.

21. Mu, B.; Tang, J.; Zhang, L.; Wang, A., Facile fabrication of superparamagnetic graphene/polyaniline/Fe3O4 nanocomposites for fast magnetic separation and efficient removal of dye. S*cientific Reports 2***017,** 7 (1), 5347.

22. Zhu, Y.; Zheng, Y.; Wang, F.; Wang, A., Monolithic supermacroporous hydrogel prepared from high internal phase emulsions (HIPEs) for fast removal of Cu2+ and Pb2+. C*hemical Engineering Journal 2***016,** 2*84,* 422-430.

23. Wang, C. Y.; Feng, L. L.; Yang, H. Z.; Xin, G. B.; Li, W.; Zheng, J.; Tian, W. H.; Li, X. G., Graphene oxide stabilized polyethylene glycol for heat storage. P*hys. Chem. Chem. Phys. 2***012,** 1*4* (38), 13233-13238.

24. Min, X.; Fang, M.; Huang, Z.; Liu, Y. g.; Huang, Y.; Wen, R.; Qian, T.; Wu, X., Enhanced thermal properties of novel shape-stabilized PEG composite phase change materials with radial mesoporous silica sphere for thermal energy storage. S*cientific Reports 2***015,** 5*,* 12964.

25. Evans, D.F., H. Wennerström, The Colloidal Domain : Where Physics, Chemistry, Biology, and Technology Meet, 2nd Edition. 1999: p. 406-416

26. Chen, K.; Li, H.-s.; Zhang, B.-k.; Li, J.; Tian, W.-d., A New Self-Consistent Field Model of Polymer/Nanoparticle Mixture. S*cientific Reports 2***016,** 6*,* 20355.

27. Gregory, J.; Barany, S., Adsorption and flocculation by polymers and polymer mixtures. A*dvances in Colloid and Interface Science 2***011,** 1*69* (1), 1-12.

28. Schwuger, M. J., Surfactants and Interfacial Phenomena. Von M. J. Rosen. John Wiley & Sons, New York 1978. 1. Aufl., XIV, 304 S., geb. $ 30.45. A*ngewandte Chemie 1***979,** 9*1* (5), 451-451.

29. Hogg, R., Bridging Flocculation by Polymers. K*ONA Powder and Particle Journal 2***013,** 3*0,* 3-14.

30. Kulkarni, D. D.; Kim, S.; Chyasnavichyus, M.; Hu, K.; Fedorov, A. G.; Tsukruk, V. V., Chemical Reduction of Individual Graphene Oxide Sheets as Revealed by Electrostatic Force Microscopy. J. *Am. Chem. Soc. 2***014,** 1*36* (18), 6546-6549.

31. Zhao, J. P.; Pei, S. F.; Ren, W. C.; Gao, L. B.; Cheng, H. M., Efficient preparation of large-area graphene oxide sheets for transparent conductive films. A*CS Nano 2***010,** 4 (9), 5245-5252.

32. Rozada, R.; Paredes, J. I.; Lopez, M. J.; Villar-Rodil, S.; Cabria, I.; Alonso, J. A.; Martinez-Alonso, A.; Tascon, J. M. D., From graphene oxide to pristine graphene: revealing the inner workings of the full structural restoration. N*anoscale 2***015,** 7 (6), 2374-2390.

33. Hoy, O.; Zdyrko, B.; Lupitskyy, R.; Sheparovych, R.; Aulich, D.; Wang, J. F.; Bittrich, E.; Eichhorn, K. J.; Uhlmann, P.; Hinrichs, K.; Muller, M.; Stamm, M.; Minko,

S.; Luzinov, I., Synthetic hydrophilic materials with tunable strength and a range of hydrophobic interactions. A*dv. Funct. Mater. 2***010,** 2*0* (14), 2240-2247.

34. Kim, J.; Cote, L. J.; Huang, J. X., Two Dimensional Soft Material: New Faces of Graphene Oxide. A*ccounts of Chemical Research 2***012,** 4*5* (8), 1356-1364.

35. Kim, J.; Cote, L. J.; Kim, F.; Yuan, W.; Shull, K. R.; Huang, J. X., Graphene Oxide Sheets at Interfaces. J*ournal of the American Chemical Society 2***010,** 1*32* (23), 8180-8186.

36. López, V.; Sundaram, R. S.; Gómez-Navarro, C.; Olea, D.; Burghard, M.; Gómez-Herrero, J.; Zamora, F.; Kern, K., Chemical vapor deposition repair of graphene oxide: a route to highly-conductive graphene monolayers. A*dv. Mater. 2***009,** 2*1* (46), 4683-4686.

37. Dai, B.; Fu, L.; Liao, L.; Liu, N.; Yan, K.; Chen, Y.; Liu, Z., High-quality single-layer graphene via reparative reduction of graphene oxide. N*ano Research 2***011,** 4 (5), 434-439.

38. Erel-Unal, I.; Sukhishvili, S. A., Hydrogen-bonded multilayers of a neutral polymer and a polyphenol. M*acromolecules 2***008,** 4*1* (11), 3962-3970.

39. Sukhishvili, S. A.; Granick, S., Layered, erasable polymer multilayers formed by hydrogen-bonded sequential self-assembly. M*acromolecules 2***002,** 3*5* (1), 301-310.

40. Khutoryanskiy, V. V.; Dubolazov, A. V.; Nurkeeva, Z. S.; Mun, G. A., pH effects in the complex formation and blending of poly(acrylic acid) with poly(ethylene oxide). L*angmuir 2***004,** 2*0* (9), 3785-3790.

CHAPTER FOUR

CHARACTERIZATION OF THERMALLY REDUCED GO FILMS

4.1: Introduction

As discussed in the previous chapter, the GOs can be encapsulated in a nanometer-thick copolymer layer allowing for the nearly perfect formation of the GO layers via dip coating from water on hydrophilic SiO_2/Si substrate. In this chapter, the results on the study of opto-electrical properties of thermally reduced GO-P1 monolayers and bi-layers are presented. Specifically, this chapter focuses on the relationship between the morphology, chemical composition and electrical conductivity of GO-P1 nanoscale films. Additionally, mechanism of electrical conductivity, charge carrier properties and electronic band gap in rGO-P1 bilayer films were investigated using Hall mobility and thermoelectric methods.

4.2: Experimental

4.2.1: Thermal Reduction

Thermal reduction

The reduction of GO films on silicon substrates was done in a quartz tube using Across International STF1200 furnace, as schematically shown in **Figure 4.1**.

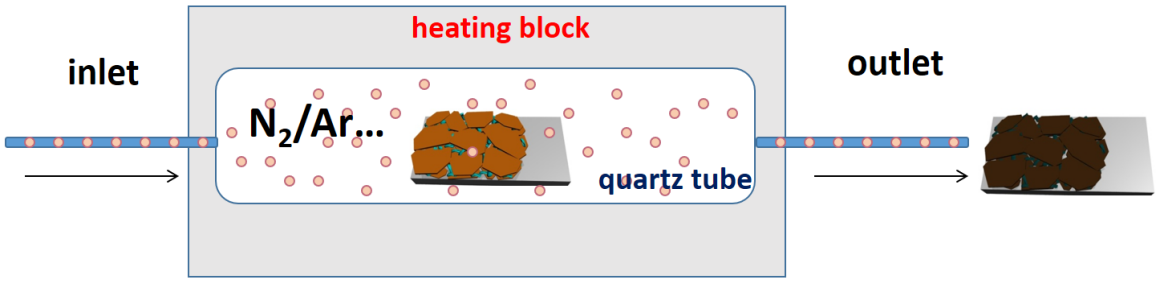

Figure 4.1: Schematic representation of the thermal reduction process.

The heating program used involved blowing the oven chamber with ultra-high purity argon (Ar) or nitrogen (N) gas for 10 minutes, heating from room temperature to 1000 °C within 115 min (10ºC/min), maintaining that temperature for 60 min, and then cooling to room temperature within 360 min.

GO-P films on quartz substrate

At first, we were not able to obtain stable rGO-P1 films on quartz thus to determine optical transparency of our reduced films due to significant crumpling effect and disintegration of GO-P1 sheets after thermal treatment (**Figure 4.2A-B**) at 10°C/min heating rate.

Heating and cooling rate - **10°C/min**

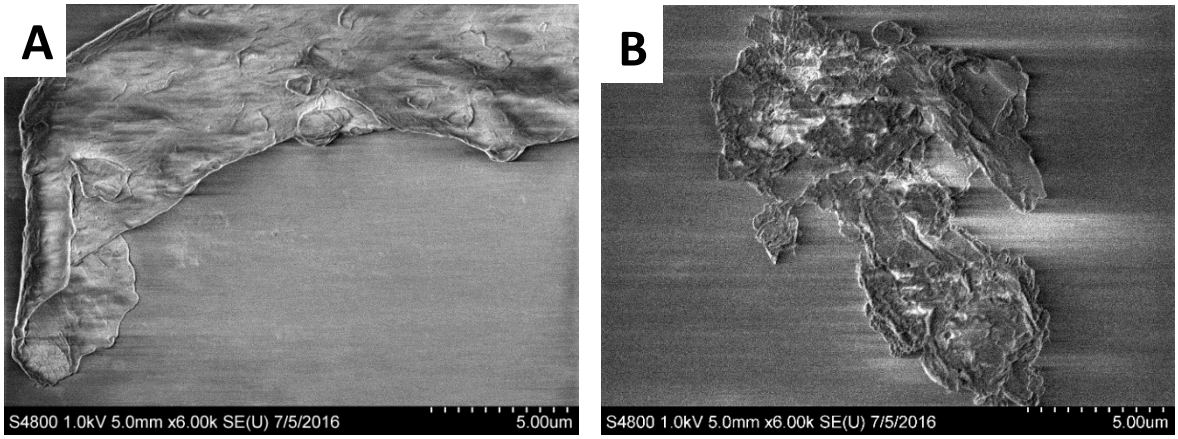

Heating and cooling rate - **3°C/min**

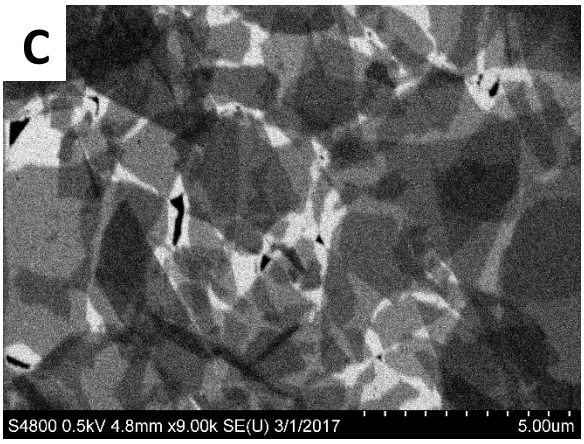

Figure 4.2: SEM images of rGO-P1 bi-layers on quartz after thermal reduction was carried out at (A, B) 10°C/min and (C) 3°C/min of heating/cooling rate.

According to Ref. [1] the heating/cooling rate plays an important role in the structure of the thermally treated graphene oxide films. Especially when treated at higher heating rate (10°C/min) GO-P1 was decomposed to into very light soot containing lots of pores of various sizes [1]. Therefore, when we reduced heating/cooling rate down to 3°C/min rGO-P1/PAA/rGO-P1 films maintained their integrity with ≈ 95% transparency at 550 nm (**Figure 4.2C**). Such behavior of rGO-P1 bilayer films can be due to the opposite thermal deformation of GO-P1 and quartz as quartz is known to have very low positive coefficient of expansion while for graphene and graphene oxide it is reported as highly negative [2-4]. Therefore, in all our next thermal reduction experiments we used below 3°C/min heating/cooling rate for films deposited on a quartz substrate.

4.2.2: Materials Characterization

Optical microscopy was performed using an Olympus LEXT OLS 4000 confocal laser microscope. Scanning electron microscopy (SEM) was performed using Hitachi S-4800 with accelerating voltages of ~0.5 - 1.0kV.

Raman spectra were recorded directly from the samples (quartz and/or undoped Si were used as substrates) using a spectrograph (SPEX, Triplemate 1377) interfaced to a thermoelectrically cooled CCD detector (Andor Technology, Model DU420A-BV) operating at -60 °C. The spectra were excited with 514.5 nm radiation from an Innova 100 (Coherent) argon ion laser. The diameter of 514.5 nm laser beam in our Raman experiment was ~1 mm. Thus, the area it covers is quite large ~3.1 mm^2 (for circular cross-section of

laser spot). Such spot size is more than enough to ensure that we probe material as a whole: the average area of single GO sheet is $\sim 3.1 \times 10^{-4}$ mm^2. At 80% of coverage the number of sheets that are probed within the laser spot is equivalent to: $N = 0.8 \times \frac{3.1}{3.1 \times 10^{-4}} = 8000$. The laser power was between 0.1–0.5 W at the sample with a total acquisition time of 100 s for each measurement. The scattered light was collected in a backscattering geometry, and the instrument was calibrated using a cyclohexane/toluene, indene or chloroform/bromoform standard depending on the desired spectral region. Raman data and spectra were processed using Origin 2016 and freeware Spekwin32 version 1.7. Raman spectra acquisition was conducted by Drs. Daniel Willett and Emay Wen under the guidance of Prof. G. Chumanov.

To measure the conductivity of the rGO-P1 films, we placed a mask with rectangular cutouts made from aluminum foil and Kapton tape on the wafers and sputtered 100-nm thick gold contacts through physical vapor deposition (PVD). Current-voltage (I-V) curves were produced using an HP 4156B Precision Semiconductor Parameter Analyzer and The Micromanipulator Co., Inc. (VLSI Reliability LAB) probe station. One probe was set to provide a sweep of voltages from -4V to +4 volts in 0.1V increments and the other probe as an ammeter to monitor the current. The slope of the I-V curves correlated to R^{-1}, which was used in the same manner as with the multi-meter measurements through the equation $\rho = R\,h\,d/L$ (where R - resistance, ρ - resistivity, L - length between contact points, h - the thickness of the graphene layer(s), and d- the average width of the two contact points). The sheet resistance was measured by the two-point probe technique. The average thickness h of the films found from the AFM was used in converting the resistance into

conductivity. We used $\sigma = 1/\rho$ to convert the resistance measurements obtained to the values of conductivity [5]. An optical microscope at low magnification was used to precisely measure the lengths between the contacts and the width of contacts. All current-voltage measurements were carried out by Daniel Cutshall in Dr. W. Harrell laboratory at Clemson University. I-V data were processed and analyzed using Origin 2016.

Carrier mobility was measured using Van der Pauw Ecopia HMS-3000 Hall measurement system. A square shaped masked (~7.5 × 7.5 mm^2) was used to form a metal electrodes on top of rGO-P1 film deposited on undoped SiO_2/Si (2 nm oxide layer) substrate to get Van Der Pauw configuration [6]. Ti/Ni (30/150 nm) metal stack were deposited as the electrodes using E-beam evaporator with shadow mask (**Figure 4.3)**. Then, prepared Hall sample was mounted on a PCB holder, four electrodes were connected through gold coated needles to the Hall Effect measurement system. A HMS 3000 (Ecopia) system was used, in which a 0.55 T magnet was utilized to apply magnetic field perpendicular to the sample surface. The Hall effect is the production of a voltage difference, namely, the Hall voltage (VH), across a conductor in a direction transverse to the current flux (I) in the conductor in the presence of a magnetic field (B) that is perpendicular to the current [7]. In the Hall Effect measurement, we get the conductivity (σ) and Hall coefficient ($R_H = V_H t/I_x B_z$, where t – is the thickness of the sample) from the measurement then extract Hall mobility (μ_{Hall}) and Hall carrier concentration (n_{Hall}) from $\mu_{Hall} = \sigma \cdot R_H$ and $n_{Hall} = q^{-1} R_H^{-1}$ [8]. Since our SiO_2 layer is quite thin, we also performed Hall mobility tests on thermally treated bare SiO_2/Si and we didn't see any detectable response, which means Si substrate should not contribute to the measured values of mobilities. PVD

and Hall mobility measurements have been conducted by Hongmei Li in Dr. G. Koley's laboratory at Clemson University.

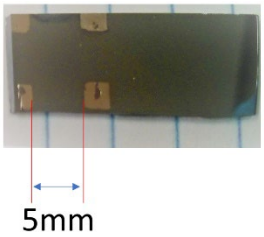

Figure 4.3: rGO-P1 bilayer film on deposited on SiO_2/Si substrate with 4 Ni/Ti contacts for Hall mobility measurements.

The transparency of the reduced double-layer film was measured using UV/vis spectroscopy (Shimadzu UV3600). We used 1/8-inch-thick quartz polished plates purchased from Quartz Scientific Inc as substrate. We used a diamond cutter to achieve the desired size of the plate: 1 cm by 3 cm slides. All quartz substrates were initially cleaned with the piranha solution according to the same procedure as that for Si wafers. The spectra of original cleaned plate were used as baseline in our measurements. We used the following expression (conductivity ratio) to evaluate opto-electrical performance of rGO-P films [9].

$$\frac{\sigma_{DC}}{\sigma_{Op}} = \frac{Z_0}{2R_s\left(T^{-\frac{1}{2}} - 1\right)} \tag{4.1}$$

where σ_{DC} is DC conductivity, σ_{Op} is optical conductivity, and $Z_0 = 377\,\Omega$ is the impedance of free space. One can expect high opto-electrical properties (high transmittance and low sheet resistance) of rGO-P1 layers if high σ_{DC}/σ_{Op} is achieved.

4.2.3: Electronic Band Gap of rGO-P1 Bilayer Film

The band gap is most often determined by measuring the resistance of semiconductor as a function of temperature [10]. The dependency of the resistance (R) upon temperature (T) for semiconductors is defined by the following expression [11]:

$$R = R_0 e^{\frac{\Delta E}{2kT}} \tag{4.2}$$

where, T is the absolute temperature in *K,* ΔE is the energy difference between the valence and conducting bands (band gap), k is Boltzman's constant and R_0 is a constant which corresponds to the resistance at $T \to \infty$. After applying logarithm to both sides of the equation (4.2) we obtain the following expression:

$$Ln(R) = Ln(R_0) + \Delta E/2kT \tag{4.3}$$

Next, the Equation 4.3 was plotted on a semi-log plot as *Ln(R)* versus *(1/2kT)*. Then, the band gap (ΔE) will correspond to the linear portion of the curve.

GO-P1 bi-layers (see **Chapter 3**) were prepared onto piranha-cleaned quartz substrate (3 cm × 1 cm) by dip-coating and then subject to thermal reduction at 1000-1150 °C in Argon or Nitrogen atmosphere. Next, silver paste was used to prepare two contacts (**Figure 4.4A).** The experimental setup [12] used for measurement is illustrated schematically in **Figure 4.4B**. One part of the diagram includes an electrical furnace (R4) and thermostat used to heat rGO-P1 sample (R3), an ammeter (AM1) used to measure current which passes through R3 thermistor, voltmeter (VM1) to measure voltage drop across R3 and base-emitter (p-n) junction of transistor (VT1). The other part of the schematics represents current regulator, which consists of Zener diode (VD), transistor (VT) and two resistors

(R2, R3). The purpose of a current regulator is to provide a constant current regardless of changes in the input voltage or load current. Therefore, with the regulated current output (I) and measured voltage drop (V) on R3 the resistance can be defined from Ohm's law as follows:

$$R = V/I \tag{4.4}$$

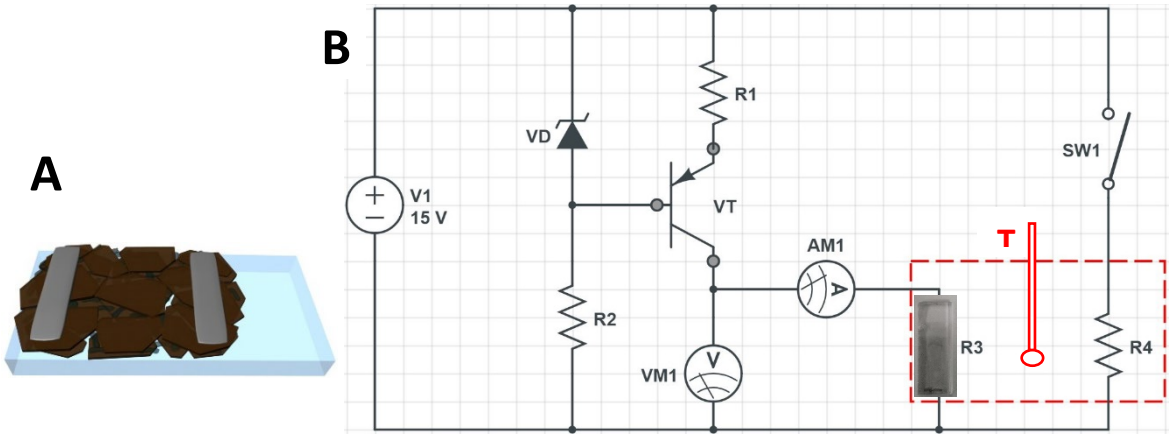

Figure 4.4: (A) Schematic representation of rGO-P1 bilayer deposited on quartz with indium contacts on top used for Band Gap measurement. (B) Schematic circuit diagram for Band Gap measurement.

4.3: Results and Discussion

4.3.1: Reduced GO-P1 Monolayer

We examined properties of the reduced GO-P1 (rGO-P1) monolayer obtained with the aid of P1modification. For this purpose the monolayer was deposited on an undoped (non-conductive) Si wafer. GO-P thermal reduction was conducted at 1000 °C–1150 °C in inert atmosphere. This process is reported to enable removal of oxygen-containing functional groups via dissociation of CO/CO_2 molecules.[13] The dissociation process is accompanied with formation of atomic vacancies in the carbon lattice, which are

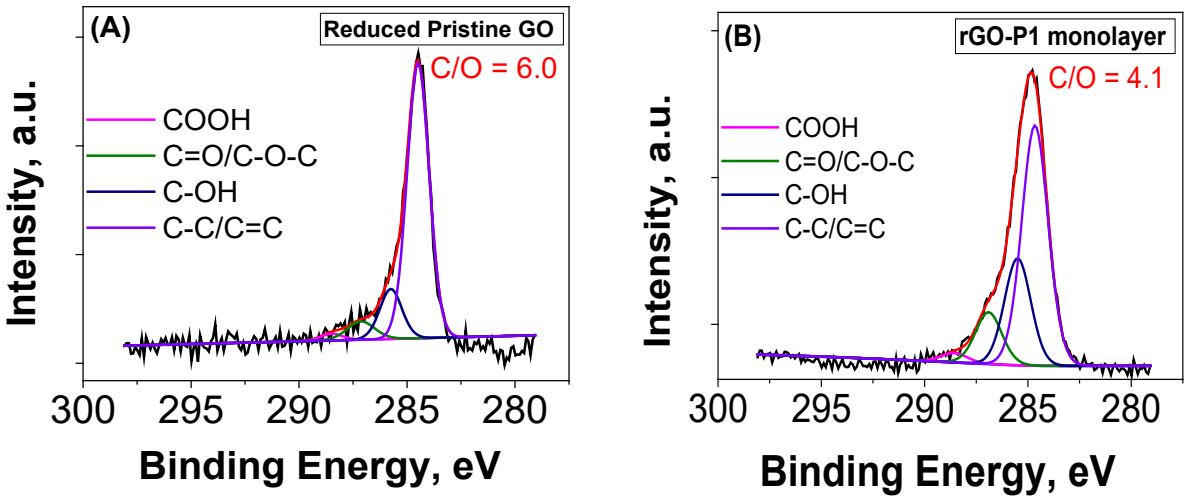

Figure 4.5: High resolution C1s spectra of (A) reduced pristine GO and (B) reduced GO-P1 monolayer.

rapidly saturated with residual oxygen to form quite temperature stable carbonyl and/or ether groups. In our model experiment with pristine GO sheets (no modification with P1) XPS spectra **(Figure 4.5A)**, indeed, showed significant presence of carbonyl/ether groups in the reduced GO sheets. The result also indicated that thermal reduction process applied is quite effective, since significant amount of oxygen is removed from the sheets. C/O ratio (**Equation 3.2**) is increased from 3 to 6 (or to about 86% of carbon content), which is comparable to the value typically reported for the thermal reduction of GO sheets at the temperatures used.[13]

For rGO-P1 monolayer obtained at the same conditions from GO modified with P1 XPS spectra showed an increase of the C/O ratio (**Equation 3.2**) from 2.7 to only 4.1 **(Figure 4.5B).** XPS results also indicate that significant amount of other than carbonyl/ether oxygen containing groups are present in the rGO-P1 monolayer. We

associate this phenomenon with the P1 polymer (enveloping GO sheets) that contains a significant concentration of oxygen in its structure **(Figure 3.2 and Figure 3.7B)** and, therefore, changes chemical pathways of the reduction process. AFM, scanning electron microscopy (SEM) and optical microscopy (**Figure 4.6A-B)** show that rGO-P monolayers preserved their integrity and structure. AFM cross-sectional measurements indicated that the obtained rGO-P1 sheets are 1.5–1.7 nm in thickness **(Figure 4.7).**

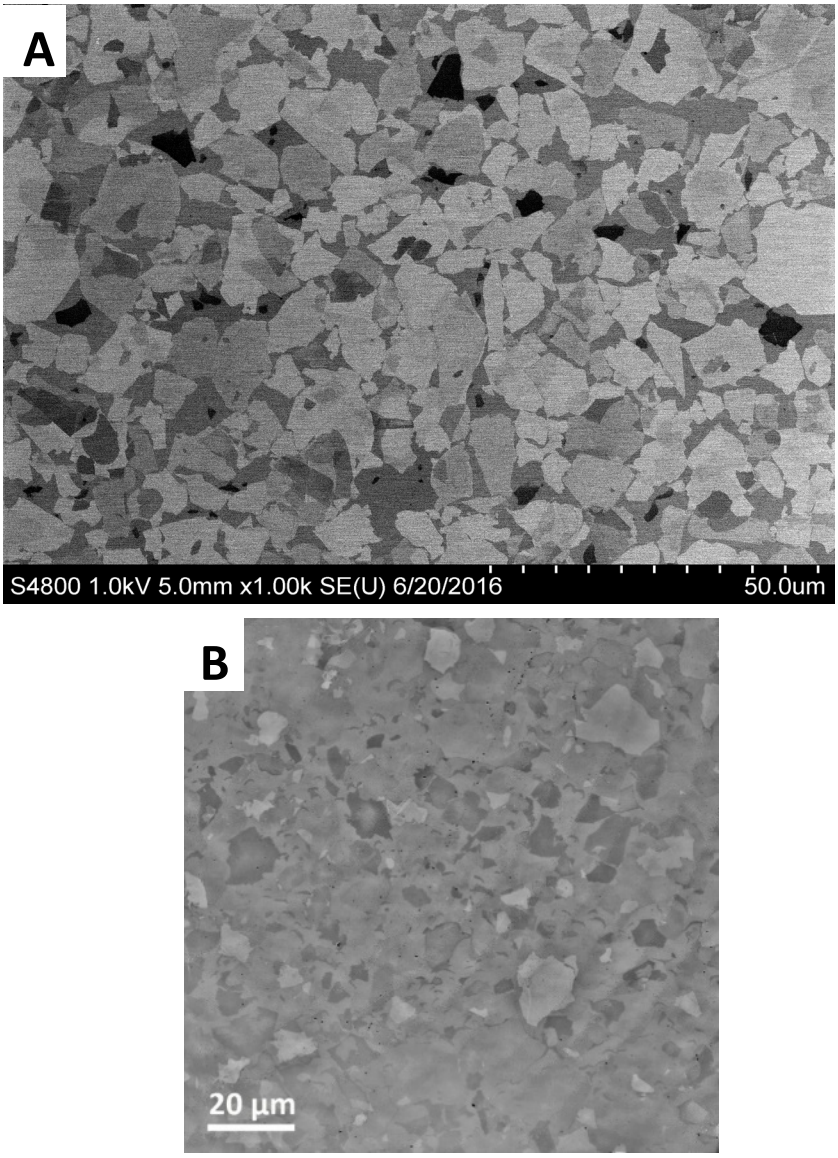

Figure 4.6: (A): SEM image and (B): optical image. All samples were thermally reduced at 1000 ºC-1100 ºC in the presence of Argon gas.

This thickness is higher than the one typically observed for rGO sheets.[14] We attribute the higher thickness after the thermal treatment to presence of carbon/oxygen containing material incorporated in the rGO sheets, which originated during pyrolysis of P1 copolymer.

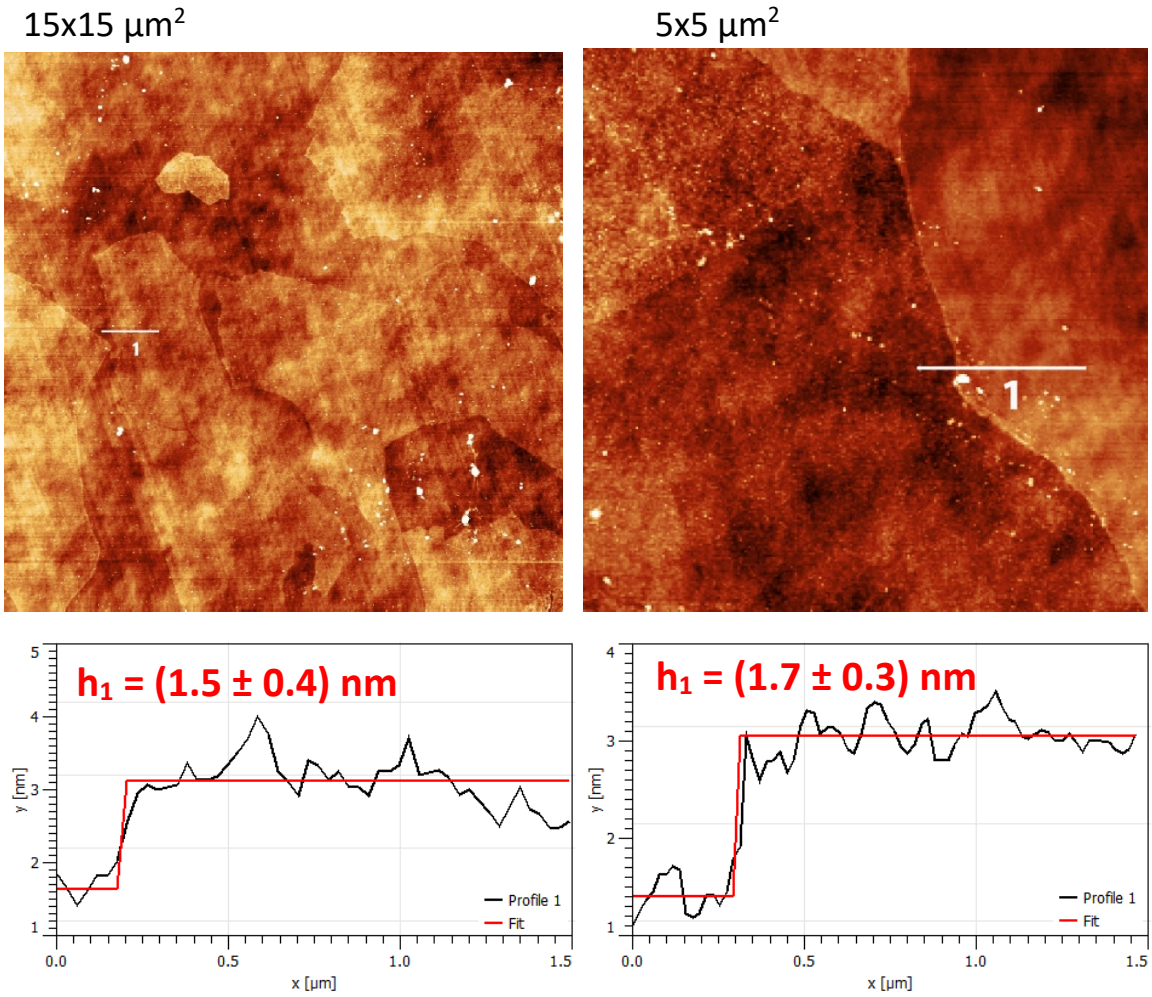

Figure 4.7: AFM images of rGO-P1 monolayer reduced at 1100 ºC in the presence of argon gas and corresponding cross-sectional profile measurements.

To assess the rearrangement of the carbon atoms in the basal plane during the thermal annealing, we used Raman spectroscopy[15-20].

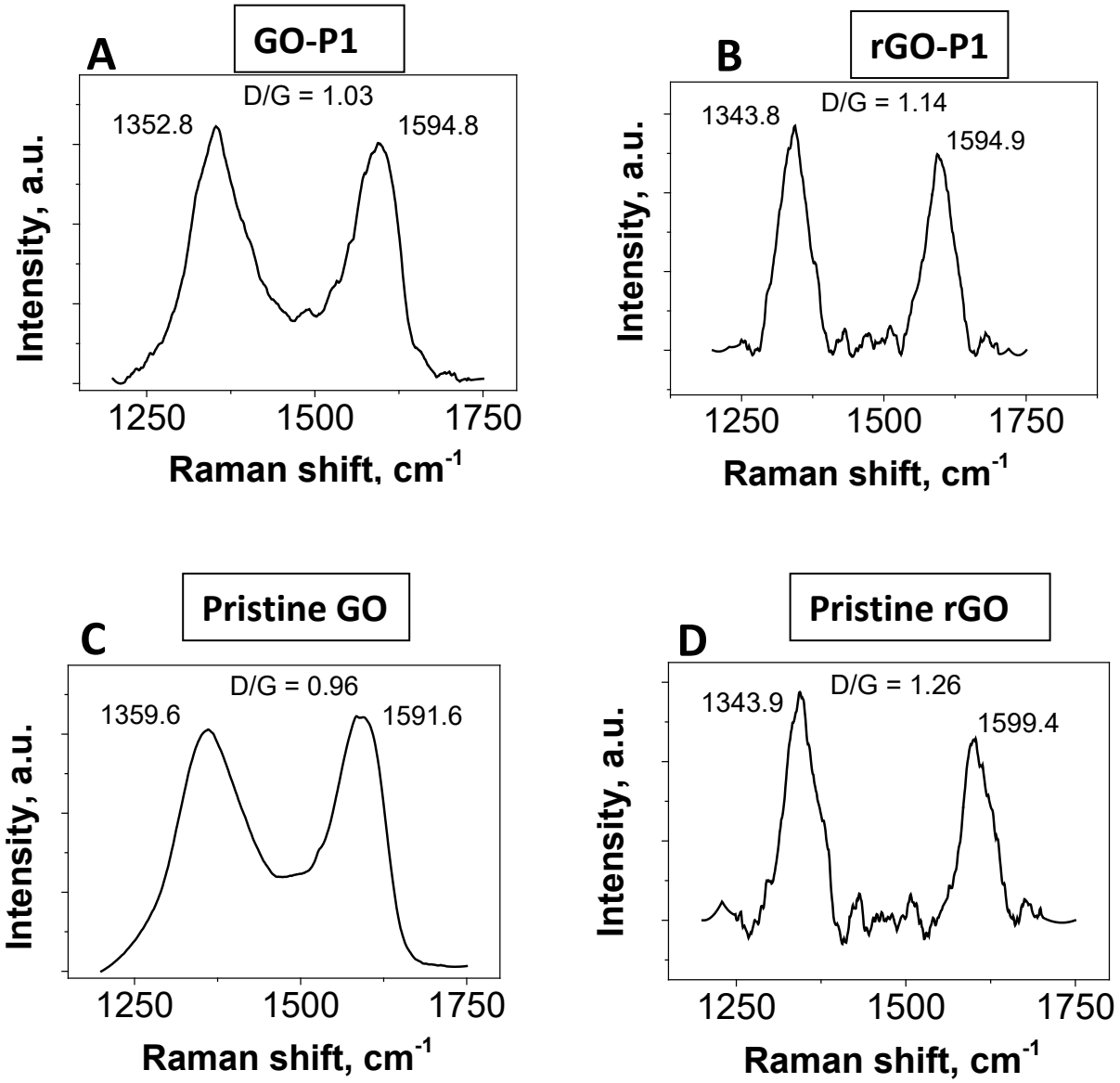

Figure 4.8: The Raman spectrum of the prepared GO-P1 monolayer and pristine GO on undoped Si wafer before (A and C) and after thermal reduction (B and D) at 1100 ºC in the presence of argon gas.

The Raman spectrum of the prepared GO-P1 monolayer displays the typical for GO materials carbon D (breathing modes of sp^2 rings) and G (the first order scattering of the

E_{2g} mode for sp^2 carbon lattice) band peaks at ~1353 and ~1595 cm^{-1}, respectively (**Figure 4.8A-B)**. As a result of thermal reduction the peaks become narrower due to sp^2 ordering of carbon atoms.[19] The ratio of the peak intensities, D/G is related to the degree of disorder and dimensions/concentration of sp^2 ring clusters. It is frequently observed for GO materials that the ratio is increased in course of the reduction and formation of sp^2 structures[15, 18]. The increase is suggested to be associated with a decrease in the average size of domains but with a growth in the number of sp^2 domains upon reduction[16-17]. Simultaneously the D band redshifted by ~9 cm^{-1}, which we associate with bond disorder increase (aromatic clusters become smaller), as suggested by Ferrari et al.[16]. For the pristine GO reduced at the same conditions (**Figure 4.8C-D)** D/G ratio is increased to a higher degree (from 0.96 to 1.26) and higher redshift was observed.

To assess the electrical properties of the rGO-P1 monolayers, we conducted two-point I-V measurements. The distance between electrodes was between 0.5 and 0.8 cm. We report an average of three parallel samples here. The I-V curves for rGO-P1 monolayers **(Figure 4.9)** revealed a non-linear and somewhat asymmetric behavior, indicating the Schottky barrier between the contact and the film[21]. This behavior can be associated with a number of defects/traps in the material previously reported for rGO materials, such as the Poole-Frenkel effect[22], Fowler-Nordheim tunneling [23] and a space-charge-limited emission[24-25]. We also note that the samples prepared from pristine GO (no prior P1 modification, **Figure 3.13A**) and having higher C/O ratio demonstrate much lower value of conductivity **(Figure 4.9)**. From the linear portion of the I-V curve (between -0.5 and +0.5 V) we estimated the sheet resistance values for rGO-P1 monolayers to be 23.8 kΩ/sq,

and then, taking into account the thickness of individual rGO-P1 sheets, we found the average conductivity to be only 580 S/cm (**Table 4.1**).

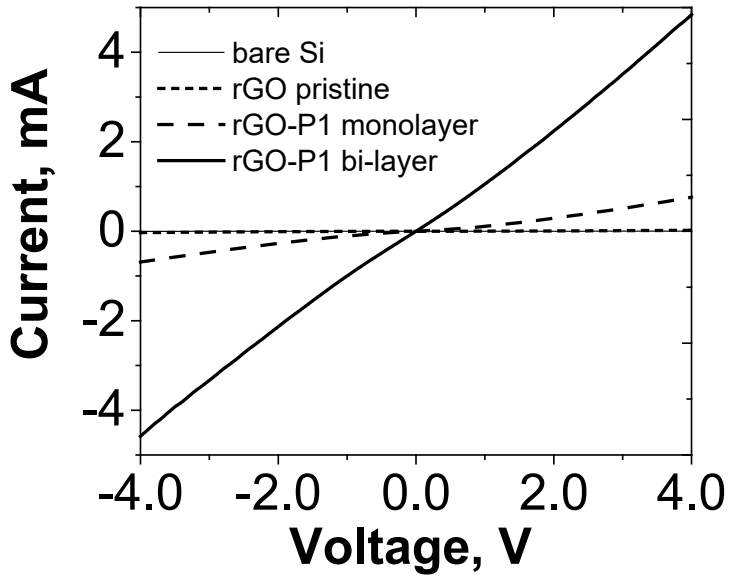

Figure 4.9: I-V curves acquired under ambient conditions for bare silicon and rGO samples. All samples were thermally reduced at 1000 ºC-1100 ºC in the presence of Argon gas.

Table 4.1: Electrical conductivity of rGO monolayer on undoped SiO_2/Si wafer obtained from I-V measurements for ± 0.5V.

Sample	Electrodes	Distance between electrodes, mm	Conductivity, S/cm	Sheet resistance (Ohm/sq)
1	1-2	8.2	632	10500
2	1-2	4.5	123	54100
3	1-2	6.7	984	6780
Average	**-**	**6.4**	**580**	**23800**
Standard Dev.			**433**	**26300**

These results are in line with most literature reports for rGO materials[26-31]. We also carried out van der Pauw Hall effect measurements[32] to extract charge carrier mobility values for our samples. The value for the rGO-P1 monolayer was estimated to be 65 $cm^2 V^{-1} s^{-1}$. This value is significantly (order of magnitude) lower than the highest mobility values reported for rGO[33-34]. It is obvious that the presence of the large number of trap states caused by the defects significantly diminishes the carrier mobility. The rGO-P1 monolayer fabricated on quartz plate had a quite high transparency of 93% in the UV-VIS region **(Figure 4.10)**, which yields an optical conductivity ratio (σ_{DC}/σ_{OP}) on the level of 0.2.

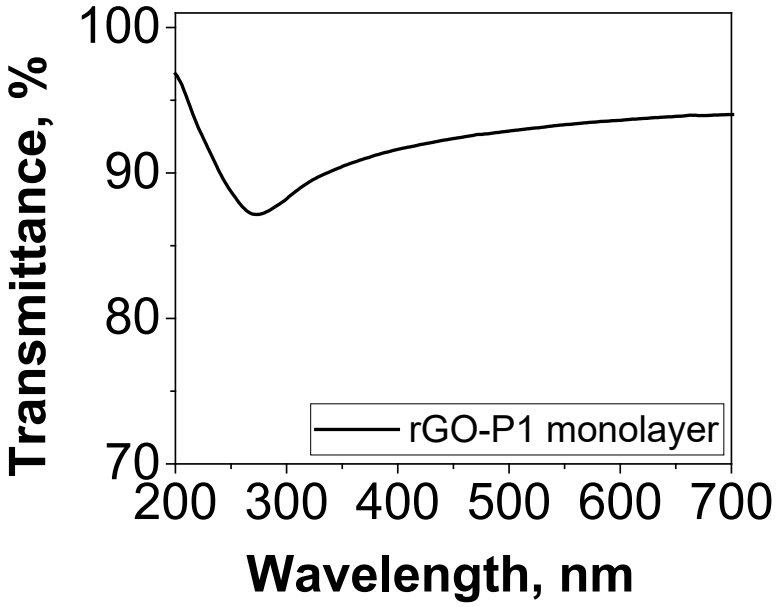

Figure 4.10: UV-Vis spectrum of rGO-P1 monolayer deposited on quartz plate.

4.3.2: Reduced GO-P1 Bilayer

The reduction of GO bilayer was conducted at the same conditions as for the GO-P1 monolayer. AFM (**Figure 4.11A-B** and **E(insets)**) imaging clearly showed that that the structure of the bi-layer is preserved after the high temperature reduction. It is necessary to

note that residual carbon originating from the PAA (bright dots on the surface of the rGO-P1 sheets) is located in-between the top and bottom layers, creating a "welded" joint between them (**Figure 4.11A, B**). The sheets of the second top layer did not contain PAA.

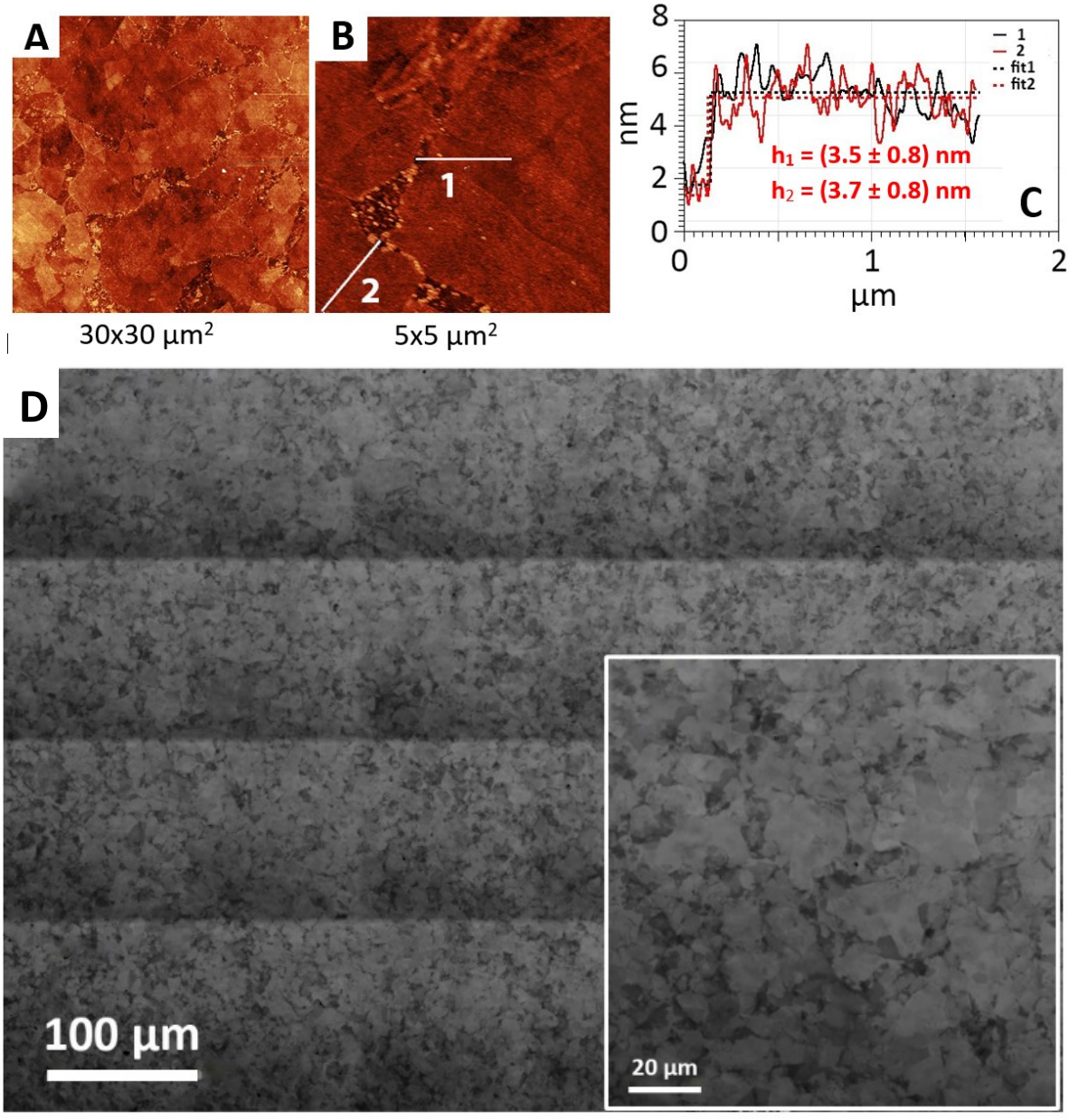

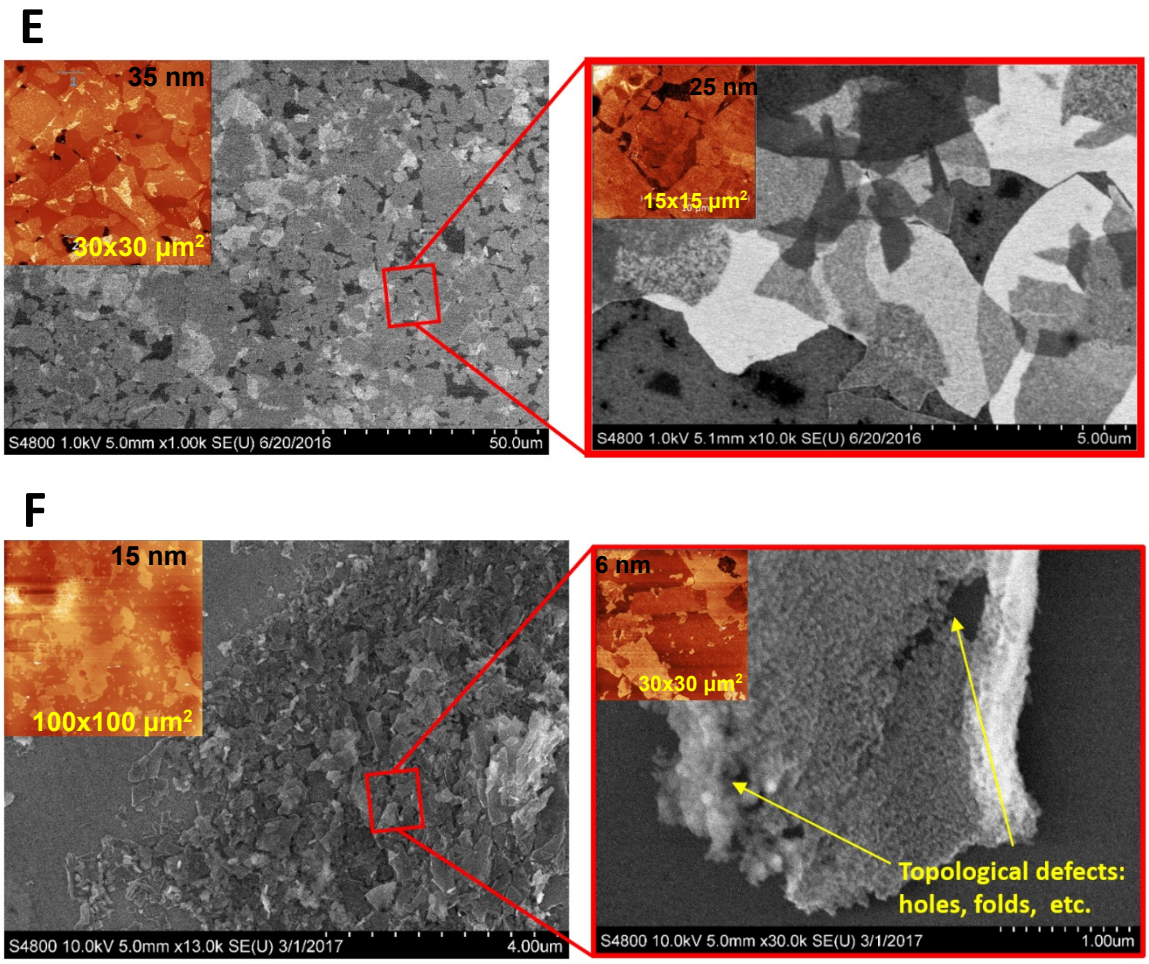

Figure 4.11: (A-C) AFM topographical (30x30 µm^2 and 5x5µm^2 images of rGO-P1 bi-layers deposited on undoped Si wafer and AFM corresponding cross-sectional profiles. Vertical scale: 20 nm. Optical (D) and SEM (E) images of rGO-P1 bi-layer film deposited on undoped Si wafer. (F) SEM images of reduced pristine GO on undoped Si wafer. Insets: corresponding AFM images. Lines of the optical 700x 475 µm^2 image are artefact originated from the software stitching of the consecutive optical images.

Therefore, their surface looks smooth and uniform for the part of the layer that has no direct plane contact with the first layer. We suggest that the numerous "welding" points play a dual role. First, they cement the entire structure, making it more robust and coherent. Second, they create multiple conduction routes for the electrons allowing the omission of

non-conducting or poorly conducting regions, thus, significantly improving the conductivity. In addition, from AFM images it appears that the border between the neighboring rGO sheets is smoothed out (**Figure 3.16C and Figure 4.11A, B**). We suggest that this is a result of "welding" of the sheets by the carbon originated from PAA linker layer. From AFM cross-sectional profiles we estimated that the thickness of rGO-P1 bi-layer is on the level of 3.5 nm. This value of the thickness was used in our estimation of the conductivity. Lower-magnification SEM and optical images confirmed that a nearly perfect rGO-P1 bi-layer was formed on the surface of the silicon wafer **(Figure 4.11D, E)**. In contrast, reduced pristine GO showed highly damaged and disintegrated structure with topological defects/irregularities in form of holes, folds etc. as evidenced from **Figure 4.11F**.

The XPS results (**Figure 4.12A-B**) showed that after the thermal reduction the intensities of all the related oxygen peaks were sharply decreased. The C:O ratio of the bi-layer rGO-P1 film was greatly improved to approximately 17:1 (or to about 94% of carbon content), and the C-C/C=C peak downshifted from 284.9 to 284.3 eV, indicating that the delocalized π conjugation was restored to a significant extent[35-36]. The C/O ratio is more than two times higher than the one determined for pristine rGO sheets obtained from pristine GO. It is also 3.5 times higher than the ratio found for rGO-P1 monolayer. We associate the significant increase in the C/O ratio with the carbon originating from the PAA linker layer. Raman spectroscopy confirmed efficient reduction of GO-P1 bi-layer as well **(Figure 4.12C-D)**. The D and G peaks become sharper and D/G intensity ratio significantly increased from ∼1.00 to ∼1.46, which indicates increase in number of the

conductive sp^2 domains[16-17, 37]. Simultaneously, a blue shift of ~10 cm^{-1} and ~7 cm^{-1} was observed for the D and G bands, respectively. Moreover, a 2D band of around 2700 cm^{-1} was readily detectable.

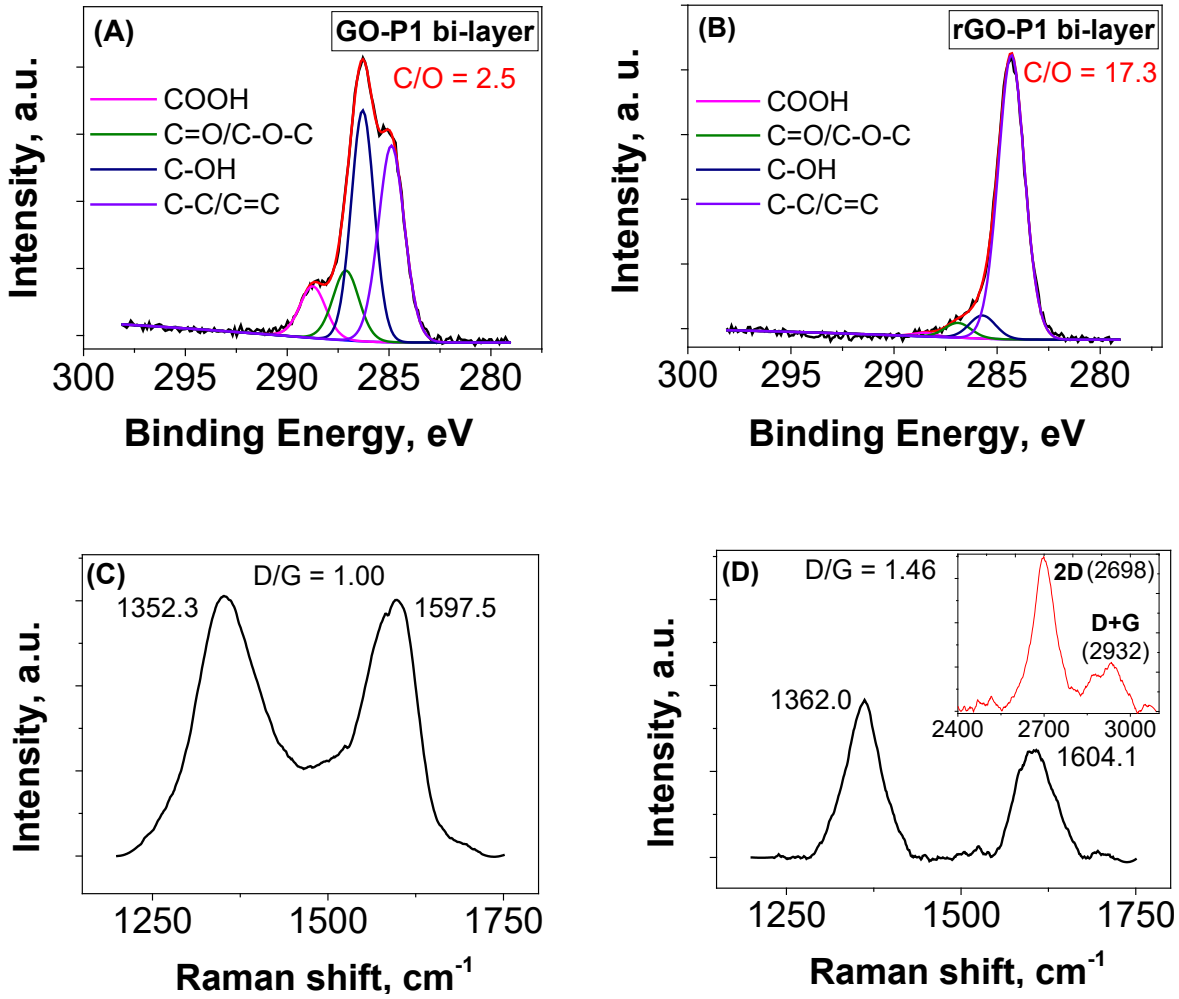

Figure 4.12: High resolution C1s spectra of GO-P1 bi-layer film (A) and rGO-P1 bi-layer film (B). Raman spectra of GO-P1 bi-layer film (C) and rGO-P1 bi-layer film

These characteristics are indicative of the change in electron bands [16, 19-20] caused by the transition from amorphous carbon to nanocrystalline graphite or sp^2 clustering and conjugation recovery (graphitization)[16, 38].

To assess the electrical properties of the rGO-P1 bi-layers, we conducted two-point I-V measurements. The distance between electrodes was between 0.5 and 1.5 cm. We report an average of 13 independent measurements on 9 different bi-layer samples.

Table 4.2: Electrical conductivity of rGO-P1 bi-layer deposited on undoped Si wafer obtained from I-V measurements for ± 4V.

Sample	Electrodes	Distance between electrodes, mm	Conductivity, S/cm	Sheet resistance, Ohm/sq
1	1-2	10.4	1984	1440
	2-3	6.7	1808	1580
2	1-2	7.7	2341	1220
	2-3	7.1	1944	1470
3	1-2	5	1892	1510
	2-3	4.9	2100	1360
4	1-2	8.5	10240	279
5	1-2	14.5	5310	538
6	1-2	14.2	1764	1620
7	1-2	10.4	1552	1840
8	1-2	11.3	4430	645
	2-3	9.4	3715	769
9	1-2	10.0	3171	901
Average		**9.2**	**3250**	**1167**
Standard Dev.			**2375**	**487**

We found a virtually metallic property (close-to-linear *I-V* curve) for the bi-layer film in contrast to the rGO-P1 monolayer **(Figure 4.9)**. The electrical properties for all samples are listed in **Table 4.2.** The two-point transport measurements indicated an average sheet resistance of 1.170 ± 0.487 kΩ/sq, which resulted in average conductivities of 3250 ± 2376 S/cm. We associate the relatively high standard deviation for our samples with manual handling of each sample (e.g. positioning of the samples in dip-coater grip). We expect that the consistency of the samples can be greatly improved with more precise automatic/robotic sample handling/alignment. In this respect for the three best samples the sheet resistance and conductivity are 0.490±0.150 kΩ/sq and 0.7±0.26 $*10^4$ S/cm, respectively. Our measurements indicated that, to the best of our knowledge, we obtained rGO nanoscale films with the highest conductivity ever reported. It is also necessary to note that the rGO-P bi-layer conductivity is fairly close to the conductivity of indium tin oxide, which is ~10^4 S/cm [39-40].

We conducted van der Pauw Hall effect measurements [32] to extract charge carrier mobility values for our samples. We obtained an average value of ~ 500 $cm^2 V^{-1} s^{-1}$ for the rGO-P1 bi-layer, which is in good agreement with the highest mobility values reported for rGO [34, 41]. Increased value of Hall mobility could be explained by nearest neighbor hopping (NNH) transport mechanism which is dominated at room and higher temperatures [42-43]. According to this theory several factors may be responsible for improved mobility: (1) lower hopping energy, (2) longer localization length, (3) smaller hopping distance, and (4) minimal defect density. For example, the reported by Feng et al. [41] in (123 $cm^2 V^{-1} s^{-1}$) mobility was measured on and individual rGO sheet which is in direct contact with the

substrate. In our case we have at least two layers and charge carriers have better pathways for tunneling. Similarly, for the graphene samples in direct contact with substrates, the carrier mobilities are typically in the ~10^3 cm^2 V^{-1} s^{-1} range [44].

We prepared the rGO-P1 bi-layers on the surface of a quartz plate to determine their optical properties. AFM imaging confirmed the formation of the rGO-P1 bi-layer film on the quartz slide with the similar structure as that for the one fabricated on the silicon wafer **(Figure 4.13A-B)**.

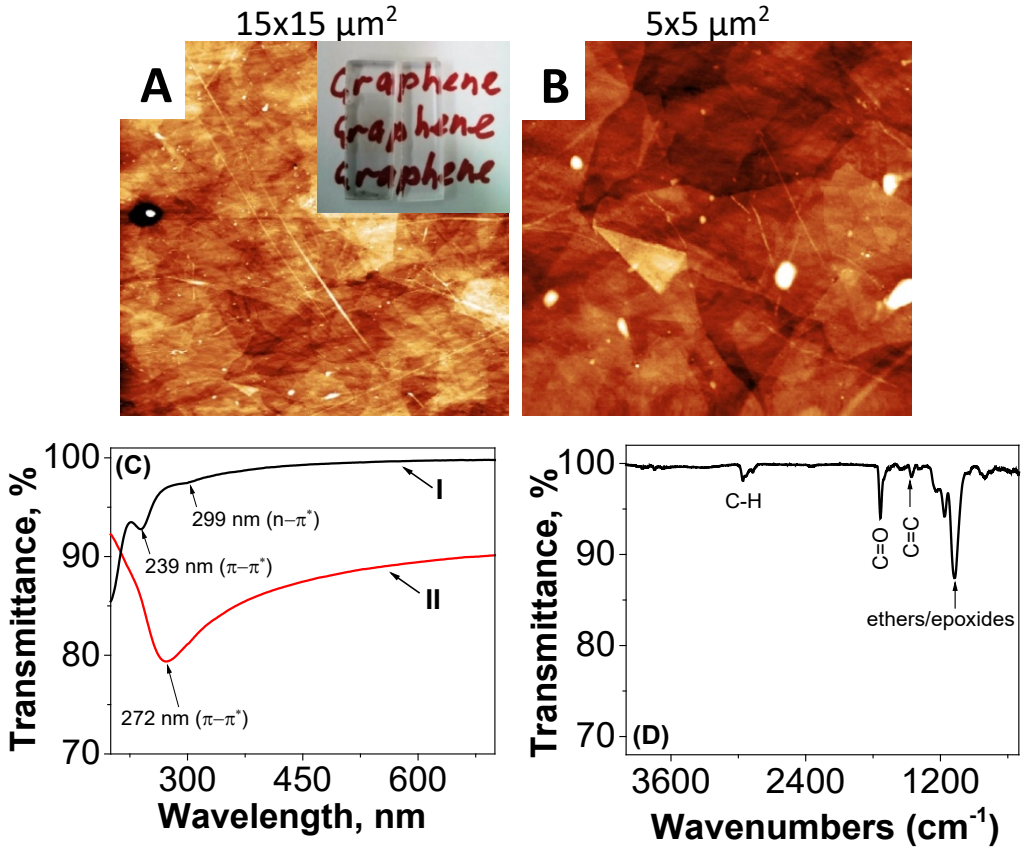

Figure 4.13: (A-B): AFM images of rGO-P1 bilayer film fabricated on quartz plate. Vertical scale: 60 and 10 nm for 15x15 µm² and 5x5 µm² images, respectively. Inset: optical image of quartz plate covered with rGO-P1 (*left*) and original quartz plate (*right*). (C): UV-Vis transmittance spectra of GO-P1 bi-layer film (I) and rGO-P1 bi-layer film (II). (D): FTIR spectrum of rGO-P1 bi-layer film.

The sheet resistance and conductivity of the film were also comparable to the parameters of the rGO-P1 film deposited on the silicon wafer **(Table 4.3)**.

Table 4.3. Electrical conductivity of rGO-P1 bi-layer deposited on quartz plate obtained from multimeter measurements at 1V.

	Electrodes	Distance between electrodes, mm	Conductivity, S/cm	Sheet resistance, Ohm/sq	Conductivity ratio, σ_{DC}/σ_{OP}
	1-2	6.0	2100	1362	2.31
	3-4	6.0	3650	783	4.45
	1-4	8.6	1764	1619	1.94
	1-3	10.4	1680	1700	1.85
Average		**7.8**	**2300**	**1366**	**2.6**
Standard Dev.			**796**	**414**	**1.2**

The UV-VIS spectra for the film is presented in **Figure 4.13C**. It is shown that the rGO-P1 bi-layer has an average transparency of ~89% at 550 nm in comparison with bare quartz. It is reported [45] that unreduced GO-P1 exhibits a maximum of adsorption at 231 nm (which corresponds to the $\pi \rightarrow \pi^*$ transitions of aromatic C=C bonds) and a shoulder at ~300 nm (ascribed to the $n \rightarrow \pi^*$ transitions of C=O bonds). After reduction, the maximum redshifts to about 272 nm (as observed in our case), which is indicative of the restored electronic conjugation within the carbon framework [46]. The calculated σ_{DC}/σ_{OP} value for the rGO-P1 bi-layers deposited on the quartz plate was between 2 and 4.5 **(Table 4.3)**. A comparison with the data in the literature clearly indicates that our σ_{DC}/σ_{OP} ratio is one of the highest reported for rGO-P1 films [29, 47-48]. We also carried out Fourier Transform Infrared measurements (**Figure 4.13D**) for the rGO-P1 bi-layer film deposited on silicon wafer and observed that the rGO-P1 bi-layer is > 94% transparent over the range of 6667–

2500 nm (4000–1500 cm^{-1}). For the significant IR spectra regions the transparency is on the level of 99%. This level of IR transparency for the rGO-P1 bi-layer is similar to the transparency of graphene sheets[49-50]. It is also important to point that conductive ITO films have very low transparency in IR spectral region[51]. Therefore, rGO-P1 bi-layer films reported here have definite advantage in the applications requiring IR transparency of conductive coatings.

4.3.3: Electronic Band Gap of rGO-P1 Bilayer Film

Mechanism of electrical conductivity in rGO-P1 bilayer films

One of the parameters that determines the potential usefulness of any new semiconductor material is its energy gap. It is a major factor determining the electrical conductivity and optical properties of a solid. Thus, the precise determination of electronic band gap is important for device design and performance projections. The basic theory of direct and indirect transitions in semiconductros was formulated by Bardeen et al. [52].

Here, we used thermoelectric method described in experimental **Section 4.2.3** to determine electronic band gap of rGO-P1 bilayer film. Before exploring the temperature dependence of electrical conductivity, it is important to define the predominant type of primary charge carriers (electrons or holes) as it influences the band gap structure [53]. Another important parameter to consider is the level and type of impurities or defects in rGO-P1 film. It has been shown in literature [54] that the type of conductivity of rGO (p-type or n-type) can be tuned by changing the type and the amount of functional groups present on it via thermal reduction [55]. Namely, an electron-donating groups (sp^2-bonded hydroxyl,

ether, and epoxide groups) will give rGO n-type conductivity whereas an electron-withdrawing groups (carboxyl, carbonyl, and sp^3-bonded hydroxyl, ether and epoxide groups) will make it a p-type [54].

Therefore, it is possible to qualitatively predict the type of conductivity in rGO-P1 using XPS results. **Table A1** in **Appendix** shows the ratio of the area of corresponding oxygen-containing functional group and the total carbons. From these data we concluded that our rGO-P1 bilayer film must have n-type conductivity as the sp^2-hydroxyl (C-OH% ≈ 7%) and sp^2 ether groups (C-O-C% ≈ 5%) became predominant after almost complete removal of carboxyl groups (COOH% < 1%). This finding is in good agreement with the reported results in Ref. [54].

For more quantitative verification of the above conclusion we relied on the Hall effect measurements to determine the carrier concentrations and mobilities in the rGO-P1 bilayer films (**Sections 4.2.1**). The sign of the Hall coefficient (R_H) indicates whether the primary charge carriers are holes or electrons [54]. Based on the results shown in (**Appendix, Table A2** (reduced GO-P1 bilayer)) we confirmed that both rGO-P1 monolayer and bilayer possess n-type characteristics.

Next, we determined the band gap of rGO-P1 bilayer film using the procedure described in **Section 4.2.3**. All measurements were carried out by Dr. Borys Turko in Dr. Kapustianyk's laboratory at Ivan Franko National University of Lviv, Ukraine. The results shown in **Figure 4.14A** demonstrate three regions of temperature dependence of the current. These regions are denoted as extrinsic range (256 K to ~ 333 K), exhaustion range

(333 K to ~ 378 K) and intrinsic range (378 K to ~ 450 K) [56]. In the extrinsic region (blue curve) the conductivity depends on the dopants, electrons of which populate the donor level (E_d). As the temperature increases more and more of these donor electrons get excited into the conduction band until a temperature is reached such that donor level becomes emptied. This is referred to as exhaustion region (black curve). Conductivity in this region is constant. As the temperature proceeds into the intrinsic region the lattice scattering mechanisms due to thermal agitation start to play dominant role, which is why we observe a slight decrease in current flow around 378 K.

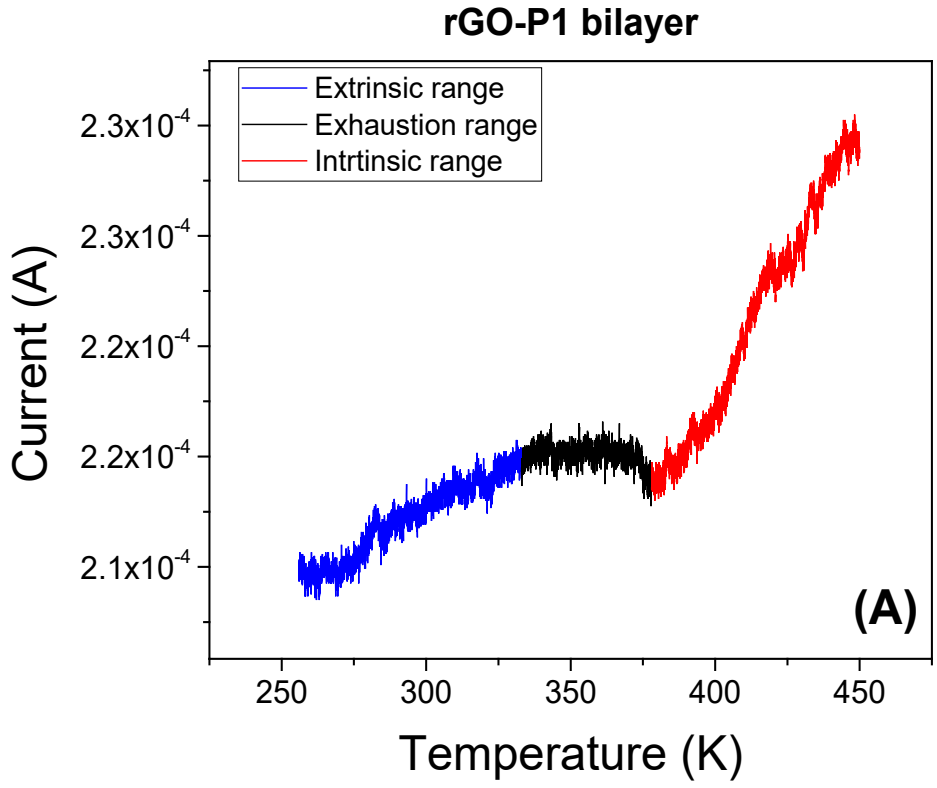

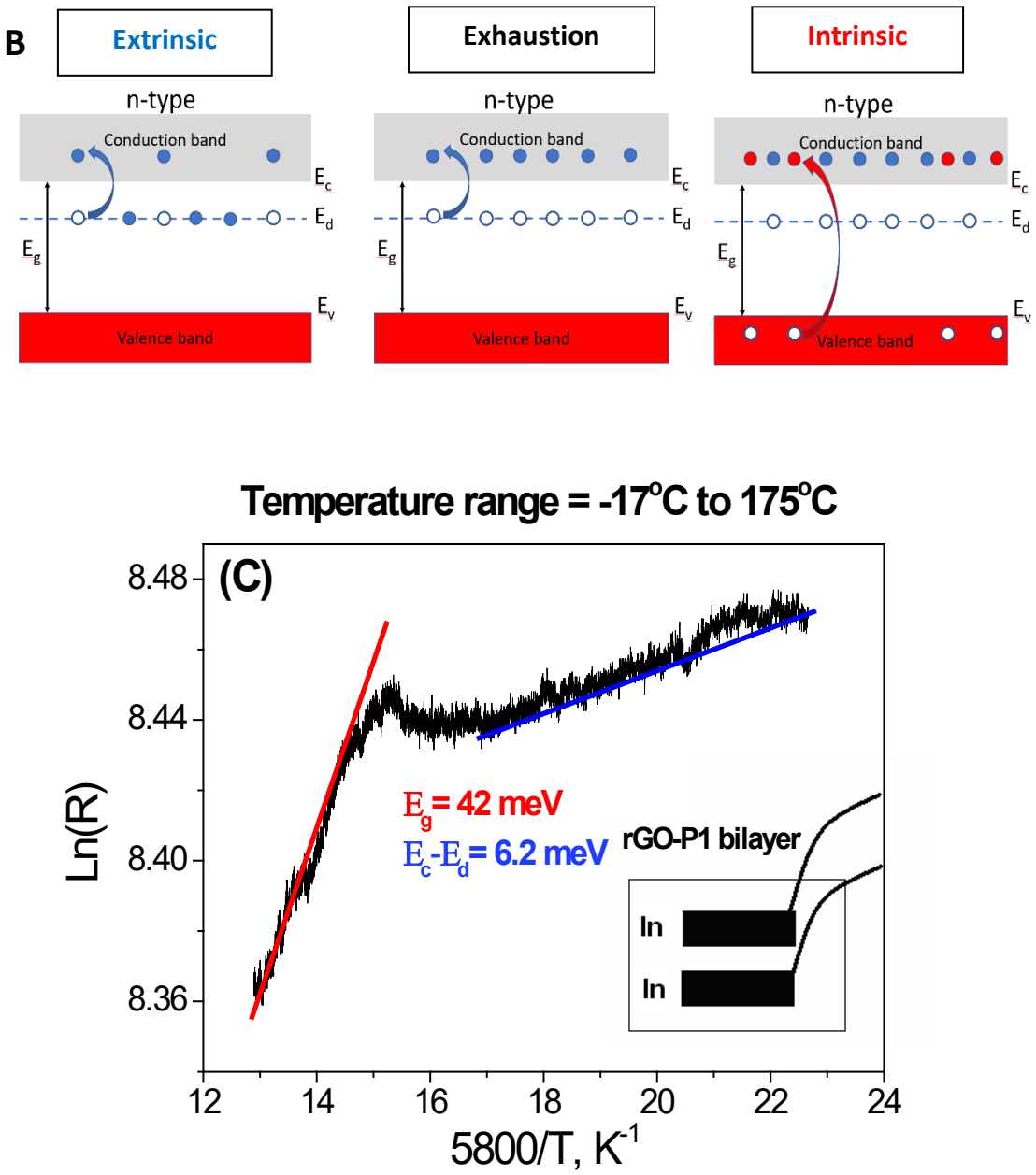

Figure 4.14: (A): Temperature dependence of the current in rGO-P1 bilayer film. (B): Energy band gap diagram for rGO-P1 film. (C): Plot of *R(T)* data in the form of Equation 4.3. E_g = 42 meV and $E_c - E_d$ = 6 meV correspond to an activation energy needed to promote electron from valence and donor energy level to a conduction band respectively. Inset: schematic of rGO-P1/quartz sample with two indium contacts.

After that, as temperature increases above 378 K, there is enough thermal energy to induce the transition of electrons from the valence band into the conduction band (intrinsic range). As this continues, the concentration of valence electrons in the conduction band rapidly increases while mobility decreases due to significant lattice thermal vibrations and scattering effects. Nevertheless, the current linearly increases as there are now so many more electrons in the conduction band. Based on the above results and discussion presented in **Section 2.9** we suggest that obtained value of band gap (E_g = 42 meV), which is rather small, corresponds to K-point in the electronic band gap shown in **Figure 2.11.** For comparison, the value of E_g = 29 meV was reported in Ref. [57] for CVD deposited graphene films. The non-zero band gap, E_g, between the conduction and valence band is an indicative of the possible break up of lattice symmetry at the Dirac points (K) of the rGO film due to the presence of defects and/or moisture, as discussed in the **Section 2.9**.

4.4: Conclusions

The following conclusions can be drawn as a result of the study reported in Chapter 4:

- Highly conductive (up to 10^4 S/cm) and transparent (~ 90%) rGO-P1 monolayers and bi-layers on non-conductive substrates were produced.
- In contrast to pristine rGO, rGO-P1 double layer film revealed nearly defect-free morphology with high coherency and preserved integrity.
- GO-P1 flakes showed higher level of reduction and carbonization/graphitization in the presence of PAA carbon residue as evidenced from XPS and AFM.

- Low heating and cooling rate plays a crucial role for preventing GO-P1 sheets from buckling and decomposing on rough surfaces like quartz.
- Electronic energy band gap of rGO-P1 bilayer was calculated to be ~29 meV at K-point on electronic band diagram of graphene.

4.5: References

1. Xiao, M.; Du, X. S.; Meng, Y. Z.; Gong, K. C., The influence of thermal treatment conditions on the structures and electrical conductivities of graphite oxide. *New Carbon Materials* **2004,** *19* (2), 92-96.

2. Bao, W.; Miao, F.; Chen, Z.; Zhang, H.; Jang, W.; Dames, C.; Lau, C. N., Controlled ripple texturing of suspended graphene and ultrathin graphite membranes. *Nature Nanotechnology* **2009,** *4*, 562.

3. Deng, S.; Berry, V., Wrinkled, rippled and crumpled graphene: an overview of formation mechanism, electronic properties, and applications. *Materials Today* **2016,** *19* (4), 197-212.

4. Zhu, J.; Andres, C. M.; Xu, J.; Ramamoorthy, A.; Tsotsis, T.; Kotov, N. A., Pseudonegative Thermal Expansion and the State of Water in Graphene Oxide Layered Assemblies. *ACS Nano* **2012,** *6* (9), 8357-8365.

5. Schroder, Dieter K. (1998). Semiconductor Material and Device Characterization. New York: J Wiley & Sons. pp. 1–55. ISBN 0-471-24139-3.

6. L. J. van der Pauw, "A Method of Measuring Specific Resistivity and Hall Effect of Discs of Arbitrary Shape," Philips Research Reports, Vol. 13, February 1958, pp. 1-9.

7. Laughlin, R. B., Quantized Hall conductivity in two dimensions. *Physical Review B* **1981,** *23* (10), 5632-5633.

8. Colinge, J.-P., & Colinge, C. A. (2002). Physics of semiconductor devices. Boston: Kluwer Academic Publishers.

9. Shi, L. F.; Yang, J. H.; Yang, T.; Hanxun, Q.; Li, J.; Zheng, Q. B., Molecular level controlled fabrication of highly transparent conductive reduced graphene oxide/silver nanowire hybrid films. *Rsc Advances* **2014,** *4* (81), 43270-43277.

10. Collings, P. J., Simple measurement of the band gap in silicon and germanium. *American Journal of Physics* **1980,** *48* (3), 197-199.

11. Kittel, C., *Introduction to Solid State Physics*. Wiley: 2004.

12. http://www.tpub.com/neets/book7/27l.htm

13. Rozada, R.; Paredes, J. I.; Lopez, M. J.; Villar-Rodil, S.; Cabria, I.; Alonso, J. A.; Martinez-Alonso, A.; Tascon, J. M. D., From graphene oxide to pristine graphene:

revealing the inner workings of the full structural restoration. *Nanoscale* **2015,** *7* (6), 2374-2390.

14. Kulkarni, D. D.; Kim, S.; Chyasnavichyus, M.; Hu, K.; Fedorov, A. G.; Tsukruk, V. V., Chemical Reduction of Individual Graphene Oxide Sheets as Revealed by Electrostatic Force Microscopy. *J. Am. Chem. Soc.* **2014,** *136* (18), 6546-6549.

15. Mattevi, C.; Eda, G.; Agnoli, S.; Miller, S.; Mkhoyan, K. A.; Celik, O.; Mastrogiovanni, D.; Granozzi, G.; Garfunkel, E.; Chhowalla, M., Evolution of Electrical, Chemical, and Structural Properties of Transparent and Conducting Chemically Derived Graphene Thin Films. *Advanced Functional Materials* **2009,** *19* (16), 2577-2583.

16. Ferrari, A. C.; Robertson, J., Interpretation of Raman spectra of disordered and amorphous carbon. *Phys. Rev. B* **2000,** *61* (20), 14095-14107.

17. Pei, S. F.; Cheng, H. M., The reduction of graphene oxide. *Carbon* **2012,** *50* (9), 3210-3228.

18. Mohan, V. B.; Jayaraman, K.; Stamm, M.; Bhattacharyya, D., Physical and chemical mechanisms affecting electrical conductivity in reduced graphene oxide films. *Thin Solid Films* **2016,** *616*, 172-182.

19. Ferrari, A. C., Raman spectroscopy of graphene and graphite: Disorder, electron-phonon coupling, doping and nonadiabatic effects. *Solid State Communications* **2007,** *143* (1-2), 47-57.

20. Lespade, P.; Marchand, A.; Couzi, M.; Cruege, F., Characterization of carbon materials with raman microspectrometry. *Carbon* **1984,** *22* (4-5), 375-385.

21. Di Bartolomeo, A., Graphene Schottky diodes: an experimental review of the rectifying graphene/semiconductor heterojunction. *Phys. Rep.-Rev. Sec. Phys. Lett.* **2016,** *606*, 1-58.

22. Kajen, R. S.; Chandrasekhar, N.; Pey, K. L.; Vijila, C.; Jaiswal, M.; Saravanan, S.; Ng, A. M. H.; Wong, C. P.; Loh, K. P., Charge transport in lightly reduced graphene oxide: A transport energy perspective. *J. Appl. Phys.* **2013,** *113* (6), 7.

23. Pandey, S.; Biswas, C.; Ghosh, T.; Bae, J. J.; Rai, P.; Kim, G. H.; Thomas, K. J.; Lee, Y. H.; Nikolaev, P.; Arepalli, S., Transition from direct to Fowler-Nordheim tunneling in chemically reduced graphene oxide film. *Nanoscale* **2014,** *6* (6), 3410-3417.

24. Li, Y. M.; Ni, X. Y.; Ding, S. J., High performance resistive switching memory organic films prepared through PPy growing on graphene oxide substrate. *J. Mater. Sci.-Mater. Electron.* **2015,** *26* (11), 9001-9009.

25. Joung, D.; Chunder, A.; Zhai, L.; Khondaker, S. I., Space charge limited conduction with exponential trap distribution in reduced graphene oxide sheets. *Appl. Phys. Lett.* **2010,** *97* (9), 3.

26. Garg, R.; Elmas, S.; Nann, T.; Andersson, M. R., Deposition methods of graphene as electrode material for organic solar cells. *Adv. Energy Mater.* **2017,** *7* (10).

27. Ferrari, A. C.; Bonaccorso, F.; Fal'ko, V.; Novoselov, K. S.; Roche, S.; Boggild, P.; Borini, S.; Koppens, F. H. L.; Palermo, V.; Pugno, N.; Garrido, J. A.; Sordan, R.; Bianco, A.; Ballerini, L.; Prato, M.; Lidorikis, E.; Kivioja, J.; Marinelli, C.; Ryhanen, T.; Morpurgo, A.; Coleman, J. N.; Nicolosi, V.; Colombo, L.; Fert, A.; Garcia-Hernandez, M.; Bachtold, A.; Schneider, G. F.; Guinea, F.; Dekker, C.; Barbone, M.; Sun, Z. P.; Galiotis, C.; Grigorenko, A. N.; Konstantatos, G.; Kis, A.; Katsnelson, M.; Vandersypen, L.; Loiseau, A.; Morandi, V.; Neumaier, D.; Treossi, E.; Pellegrini, V.; Polini, M.; Tredicucci, A.; Williams, G. M.; Hong, B. H.; Ahn, J. H.; Kim, J. M.; Zirath, H.; van Wees, B. J.; van der Zant, H.; Occhipinti, L.; Di Matteo, A.; Kinloch, I. A.; Seyller, T.; Quesnel, E.; Feng, X. L.; Teo, K.; Rupesinghe, N.; Hakonen, P.; Neil, S. R. T.; Tannock, Q.; Lofwandera, T.; Kinaret, J., Science and technology roadmap for graphene, related two-dimensional crystals, and hybrid systems. *Nanoscale* **2015,** *7* (11), 4598-4810.

28. Pang, S. P.; Hernandez, Y.; Feng, X. L.; Mullen, K., Graphene as transparent electrode material for organic electronics. *Adv. Mater.* **2011,** *23* (25), 2779-2795.

29. Zheng, Q. B.; Li, Z. G.; Yang, J. H.; Kim, J. K., Graphene oxide-based transparent conductive films. *Prog. Mater Sci.* **2014,** *64*, 200-247.

30. Lopez-Naranjo, E. J.; Gonzalez-Ortiz, L. J.; Apatiga, L. M.; Rivera-Munoz, E. M.; Manzano-Ramirez, A., Transparent electrodes: a review of the use of carbon-based nanomaterials. *J. Nanomater.* **2016**, 12.

31. Huang, X.; Yin, Z. Y.; Wu, S. X.; Qi, X. Y.; He, Q. Y.; Zhang, Q. C.; Yan, Q. Y.; Boey, F.; Zhang, H., Graphene-based materials: synthesis, characterization, properties, and applications. *Small* **2011,** *7* (14), 1876-1902.

32. Li, X. S.; Cai, W. W.; Jung, I. H.; An, J. H.; Yang, D. X.; Velamakanni, A.; Piner, R.; Colombo, L.; Ruoff, R. S., Synthesis, characterization, and properties of large-area graphene films. In *Graphene and Emerging Materials for Post-Cmos Applications*, Obeng, Y.; DeGendt, S.; Srinivasan, P.; Misra, D.; Iwai, H.; Karim, Z.; Hess, D. W.; Grebel, H., Eds. Electrochemical Society Inc: Pennington, 2009; Vol. 19, pp 41-52.

33. Feng, H. B.; Cheng, R.; Zhao, X.; Duan, X. F.; Li, J. H., A low-temperature method to produce highly reduced graphene oxide. *Nat. Commun.* **2013,** *4*, 7.

34. Eigler, S.; Hu, Y. C.; Ishii, Y.; Hirsch, A., Controlled functionalization of graphene oxide with sodium azide. *Nanoscale* **2013,** *5* (24), 12136-12139.

35. Stankovich, S.; Dikin, D. A.; Piner, R. D.; Kohlhaas, K. A.; Kleinhammes, A.; Jia, Y.; Wu, Y.; Nguyen, S. T.; Ruoff, R. S., Synthesis of graphene-based nanosheets via chemical reduction of exfoliated graphite oxide. *Carbon* **2007,** *45* (7), 1558-1565.

36. Some, S.; Kim, Y.; Yoon, Y.; Yoo, H.; Lee, S.; Park, Y.; Lee, H., High-Quality Reduced Graphene Oxide by a Dual-Function Chemical Reduction and Healing Process. *Sci Rep* **2013,** *3*, 5.

37. Furio, A.; Landi, G.; Altavilla, C.; Sofia, D.; Iannace, S.; Sorrentino, A.; Neitzert, H. C., Light irradiation tuning of surface wettability, optical, and electric properties of graphene oxide thin films. *Nanotechnology* **2017,** *28* (5), 10.

38. Dai, B.; Fu, L.; Liao, L.; Liu, N.; Yan, K.; Chen, Y.; Liu, Z., High-quality single-layer graphene via reparative reduction of graphene oxide. *Nano Research* **2011,** *4* (5), 434-439.

39. Granqvist, C. G.; Hultåker, A., Transparent and conducting ITO films: new developments and applications. *Thin Solid Films* **2002,** *411* (1), 1-5.

40. Hosono, H.; Ohta, H.; Orita, M.; Ueda, K.; Hirano, M., Frontier of transparent conductive oxide thin films. *Vacuum* **2002,** *66* (3), 419-425.

41. Feng, H.; Cheng, R.; Zhao, X.; Duan, X.; Li, J., A low-temperature method to produce highly reduced graphene oxide. *Nature Communications* **2013,** *4*, 1539.

42. Abdullah, Y.; Necmi, S.; Tülay, S.; Mehmet, K., Crossover from Nearest-Neighbor Hopping Conduction to Efros–Shklovskii Variable-Range Hopping Conduction in Hydrogenated Amorphous Silicon Films. *Japanese Journal of Applied Physics* **2009,** *48* (11R), 111203.

43. Bae, J. J.; Yoon, J. H.; Jeong, S.; Moon, B. H.; Han, J. T.; Jeong, H. J.; Lee, G.-W.; Hwang, H. R.; Lee, Y. H.; Jeong, S. Y.; Lim, S. C., Sensitive photo-thermal response of graphene oxide for mid-infrared detection. *Nanoscale* **2015,** *7* (38), 15695-15700.

44. Farmer, D. B.; Chiu, H. Y.; Lin, Y. M.; Jenkins, K. A.; Xia, F. N.; Avouris, P., Utilization of a buffered dielectric to achieve high field-effect carrier mobility in graphene transistors. *Nano Lett.* **2009,** *9* (12), 4474-4478.

45. Paredes, J. I.; Villar-Rodil, S.; Solis-Fernandez, P.; Martinez-Alonso, A.; Tascon, J. M. D., Atomic force and scanning tunneling microscopy imaging of graphene nanosheets derived from graphite oxide. *Langmuir* **2009,** *25* (10), 5957-5968.

46. Li, D.; Muller, M. B.; Gilje, S.; Kaner, R. B.; Wallace, G. G., Processable aqueous dispersions of graphene nanosheets. *Nat. Nanotechnol.* **2008,** *3* (2), 101--5.

47. Zhao, J. P.; Pei, S. F.; Ren, W. C.; Gao, L. B.; Cheng, H. M., Efficient preparation of large-area graphene oxide sheets for transparent conductive films. *ACS Nano* **2010,** *4* (9), 5245-5252.

48. Zheng, Q. B.; Ip, W. H.; Lin, X. Y.; Yousefi, N.; Yeung, K. K.; Li, Z. G.; Kim, J. K., Transparent conductive films consisting of ultra large graphene sheets produced by Langmuir-Blodgett assembly. *ACS Nano* **2011,** *5* (7), 6039-6051.

49. De, S.; King, P. J.; Lotya, M.; O'Neill, A.; Doherty, E. M.; Hernandez, Y.; Duesberg, G. S.; Coleman, J. N., Flexible, Transparent, Conducting Films of Randomly Stacked Graphene from Surfactant-Stabilized, Oxide-Free Graphene Dispersions. *Small* **2010,** *6* (3), 458-464.

50. Li, X. L.; Zhang, G. Y.; Bai, X. D.; Sun, X. M.; Wang, X. R.; Wang, E.; Dai, H. J., Highly conducting graphene sheets and Langmuir-Blodgett films. *Nat. Nanotechnol.* **2008,** *3* (9), 538-542.

51. Taylor, R. A.; Hewakuruppu, Y.; DeJarnette, D.; Otanicar, T. P., Fabrication and Comparison of Selective, Transparent Optics for Concentrating Solar Systems. In *High and Low Concentrator Systems for Solar Energy Applications X*, Plesniak, A. P.; Prescod, A. J., Eds. Spie-Int Soc Optical Engineering: Bellingham, 2015; Vol. 9559.

52. J. Barden, H. Hall and F. J. Balatt : proceeding of the Conference on photoconductivity, New York (1965) 146.

53. Mousavi, H., Electronic properties of doped gapped graphene. *Physica B: Condensed Matter* **2013,** *414*, 78-82.

54. Tu, N. D. K.; Choi, J.; Park, C. R.; Kim, H., Remarkable Conversion Between n- and p-Type Reduced Graphene Oxide on Varying the Thermal Annealing Temperature. *Chemistry of Materials* **2015,** *27* (21), 7362-7369.

55. Bagri, A.; Mattevi, C.; Acik, M.; Chabal, Y. J.; Chhowalla, M.; Shenoy, V. B., Structural evolution during the reduction of chemically derived graphene oxide. *Nat. Chem.* **2010,** *2* (7), 581-587.

56. Neamen, Donald A. (2003). Semiconductor Physics and Devices: Basic Principles (3rd ed.). McGraw-Hill Higher Education. ISBN 0-07-232107-5.

57. Indrani, B.; Tsegie, F.; Zlatka, S.; Paul, G. H.; Chen, J.; Ashwani, K. S.; Asim, K. R., Graphene films printable on flexible substrates for sensor applications. *2D Materials* **2017,** *4* (1), 015036.

CHAPTER FIVE

GO LAYERS ON HYDROPHOBIC SUBSTRATES

5.1: Introduction

As mentioned in **Section 2.8** polymeric films are widely employed in flexible electronics as flexible substrates. However, these films are often hydrophobic by nature and have poor adhesive properties, which inhibit the deposition quality of GO layers from water-based solutions. Therefore, it raises the need for surface modification to these substrates to reduce their inherent surface hydrophobicity. As an alternative, the surface of GO can be made more hydrophobic to enable stronger interaction with the hydrophobic substrate. In both cases, it is important to understand the influence of the hydrophobic substrate on morphology of deposited GO layers.

In general, the results of this chapter demonstrated that it is difficult to obtain a stable and uniform monolayer of GO modified with P1 on hydrophobic surfaces. Specifically, heavy wrinkling, crumpling and scrolling of GO-P1 sheets was observed after dipcoating/deposition from water solution. We suggest, these events are directly related to the lack of hydrophobic interaction between the surface of the substrate and GO-P1 individual flake. Additionally, as discussed in **Chapter 3** the presence of polymer linker layer (PLL) was necessary to fabricate a bi-layer of GO-P1, which makes it inconvenient from the manufacturing point of view.

To this end, this chapter reports on the development of fundamental and practical approach to the deposition of sub-nanometer GO films directly on hydrophobic polymeric

substrates via scalable water-based dip-coating. Our final successful approach relies on the enveloping GOs into especially designed (1-2 nm thick) amphiphilic copolymer shell poly(Oligo Ethylene Glycol methyl ether Methacrylate [OEGMA]- Glycidyl Methacrylate [GMA]- Lauryl Methacrylate [LMA]) (P2) that allows controlled formation of monolayer and/or multilayer upon single dipcoating procedure/step, thus eliminating the need of PLL.

Spectroscopic and thermal methods, such as XPS, FTIR, TGA and DSC were used to confirm covalent attachment/grafting of copolymer to GO and to study any compositional changes in GO during modification. Like in **Chapter 3**, the kinetics of copolymer grafting to GO sheets was investigated using thermogravimetric analysis (TGA), which also helped us to evaluate the level of grafting of copolymer to the GOs after copolymer adsorption saturation.

In addition, the surface properties, such as the morphology and the surface energy of GO-modified layers, were investigated using atomic force microscopy (AFM), Quartz crystal microbalance with dissipation monitoring (QCM-D) and contact angle measurements. The thickness of copolymer bound to the surface of the GO particulates was also defined from AFM images of GO-copolymer monolayers on SiO_2/Si.

5.2: Experimental

5.2.1. Quartz Crystal Microbalance with Dissipation Monitoring (QCM-D)

In QCM-D [1] experiments, a quartz crystal is driven by applying and alternating electric field at one of its resonance frequencies: 5, 15, 25, ..., 65 MHz. QCM-D measures changes in resonance frequency, ΔF, and dissipation, ΔD, of a sensor crystal upon

interaction of (soft) matter with its surface (**Figure 5.1**). The QCM-D response is sensitive to the mass (including hydrodynamically coupled water) and the mechanical properties of the surface-bound layer [1]. As a first approximation, a decrease in ΔF indicates a mass increase, while high (low) values of ΔD indicate a soft (rigid) film. All QCM-D measurements were performed with a Q-Sense E1 system (Biolin Scientific AB).

5.2.2. Surface Functionalization of QCM-D Sensor with P1 Copolymer Layer

Substrate Preparation

The surface of the SiO_2-coated AT-cut quartz crystals (4.95 MHz, QSX 303, Q-Sense AB) was functionalized with P1 copolymer following the procedure described in the next section. The quartz crystal was cleaned by plasma treatment using O_2-plasma etcher (the generator power switch was set at 12 W at 0.2-torr atmospheric pressure) for 15 min followed by immersion in 2 vol % sodium dodecyl sulfate (SDS) solution in high purity MilliQ water (18 MΩ·cm) for 30 min, rinsing with Milli-Q water, drying with ultra-high-purity nitrogen, and a final O_2-plasma treatment for 15 min.

Deposition of P1 film

The P1 layer was then deposited by dipcoating at 5 mm/sec from 2% solution of P1 in 2-butanone (MEK). The resulting film was allowed to dry under ambient conditions for 24 hours. Then, unattached copolymer chains were removed by rinsing the sample in water and MEK three times for 30 min each.

The thickness of P1 film before and after the rinsing was monitored using single-wavelength ellipsometry (COMPEL automatic ellipsometer, InOmTech, Inc.) at 70º angle

of incidence. Based on the five measurements the thickness of the as-deposited film and after rinsing was (40 ± 8 nm) and (38 ± 8 nm) respectively.

Swelling Experiments

The temperature for QCM-D experiments was held at 25 ºC. The flow rate for all water-ethanol solutions (0%, 10%, 50%, 70% and 100% of ethanol content) was kept at 100 μL/min using a peristaltic pump (ISMATEC, IPC-N). A baseline for each measurement was established by flowing all solutions over bare quartz crystal in sequential manner until stable signal was achieved. Then, after the crystal was removed from the measuring chamber, thoroughly cleaned with O_2-plasma and dried with nitrogen, P1 layer was grafted to the activated surface of SiO_2 followed by drying under ambient conditions overnight. Next, the swelling experiments were run on grafted copolymer layer with the same water-ethanol solutions as for bare crystal. The collected raw data on P1 swelling was corrected using the $\Delta F/n$ and ΔD values from bare quartz crystal. This allowed us to accurately determine viscoelastic properties of hydrated copolymer layer and to account for any changes in the viscoelastic properties of the surrounding fluid.

5.2.3. Modeling of the QCM-D Response for Swelling of Nanoscale P1 film in Water-Ethanol Mixtures

QCM-D data for P1 swelling in water ethanol mixtures was collected using Q-Sense E1 instrument. Adsorbed mass of thin and nondissipative layers can be calculated using Sauerbrey model [2]:

$$\Delta m = - C\Delta F/n \quad (5.1)$$

where n = 1, 3, … is the overtone number, ΔF is the frequency change, and C = 17.7 ng/(cm^{2}Hz) at 5 MHz - sensitivity constant of quartz crystal. However, the Sauerbrey equation is not applicable for highly hydrated and highly viscous polymer films which result in high dissipation shifts ($\Delta D_n/(-\Delta F_n/n) > 0.4 \times 10^{-6}$ Hz^{-1}).

The Voigt viscoelastic model, in turn, has been successfully used previously [3] to calculate the adsorbed mass and viscoelastic properties of highly dissipative polymer brushes [4-5] and adsorbed proteins layers [6-7]. In summary, the adsorbed/swollen layer can be described by four parameters: effective density (ρ), shear viscosity (η), shear elastic modulus (μ), and thickness (h). Since each harmonic acoustic frequency has different penetration depth at least three overtones need to be simultaneously fitted using the Voigt model to obtain values of ρ, η, μ and h of viscous layers [8].

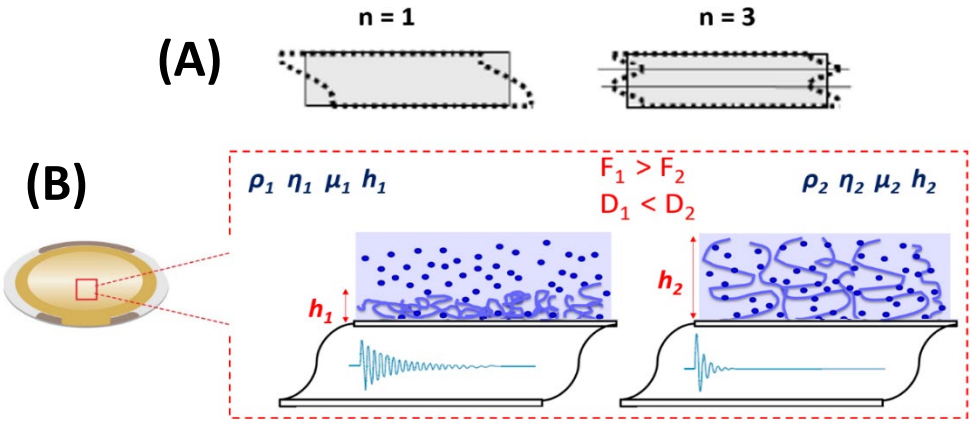

Figure 5.1: (A, B) QCM-D sensing mechanism.

We used Voigt viscoelastic model embedded in Smartfit algorithm of QSense Dfind and QTools software packages [9] to fit our experimental QCM-D response in form of frequency (ΔF) and dissipation shifts (ΔD). Three overtones (third, fifth, seventh) were

used to fit the following parameters: layer viscosity, layer shear (elasticity) and layer thickness, while the value of layer density (ρ_{wet}), fluid density (ρ_{fluid}), and fluid viscosity (η_{fluid}) was fixed. The density of solvated P1 layer was estimated from the relative weighting of the densities of the dry polymer film (ρ_{dry}) and the solvent (ρ_{fluid}) using the ellipsometry and QCM-D mass measurements [10],

$$\rho_{wet} = \rho_{dry}\left(\frac{m_{dry}}{m_{wet}}\right) + \rho_{fluid}\left(\frac{m_{wet}-m_{dry}}{m_{wet}}\right) \quad (5.2)$$

The effective solvated film thickness (h_{wet}), can be determined from the mechanical coupling of the 'wet' mass of the solvated polymer with the quartz crystal resonator in QCM-D [11] using the following relationship,

$$h_{wet}[nm] = \frac{m_{wet}\,[ng/cm^2]}{\rho_{wet}\,[g/cm^3]} * 10^{-2} \quad (5.3)$$

The mass per unit area for wet/solvated film (m_{wet}) is the mass of polymer plus the mass of adsorbed solvent molecules and it was found directly from the QCM-D data using Voigt model [12]. Effective density of the swollen polymer film (ρ_{wet}) was estimated from the **Equation 5.2**. Unlike h_{wet}, m_{wet} does not depend on the choice of the input parameter ρ_{wet}. The mass per unit area for dry film ($m_d = \rho_{dry} \cdot h_d$) was calculated by multiplying the thickness of dry polymer film which was measured using ellipsometry with the assumed density of the dry P1 film (1150 ± 100 kg/m^3) [13]. The values of ρ_{fluid} and η_{fluid} were taken from the reference [14] for 0%, 10%, 50% and 100% of ethanol content.

5.2.4: Formation of Hydrophobic Test Surface with Self-Assembled Monolayers (SAMs) on SiO_2/Si substrates

To prepare hydrophobic model-surface on silicon, chlorosilane-based self-assembled monolayers (SAMs) were obtained on SiO_2/Si substrate via a vapor-phase coating process [15], as shown in **Figure 5.2**. A silicon wafer (**step 1**) was cleaned using "piranha" solution and washed with DI water. Then, the cleaned silicon wafer was placed in tightly closed vial with 3-4 droplets of chlorosilane compound (**step 2**). Over-night vapor deposition of chlorosilane took place through the condensation reaction with the hydroxyl groups of activated silicon substrate [1617]. After the deposition was complete, the modified substrate (**step 3**) was removed from vial and rinsed with MEK three times for 10 minutes to remove unbound deposited materials. The thickness and surface morphology of the silane films were determined using ellipsometry and AFM, respectively.

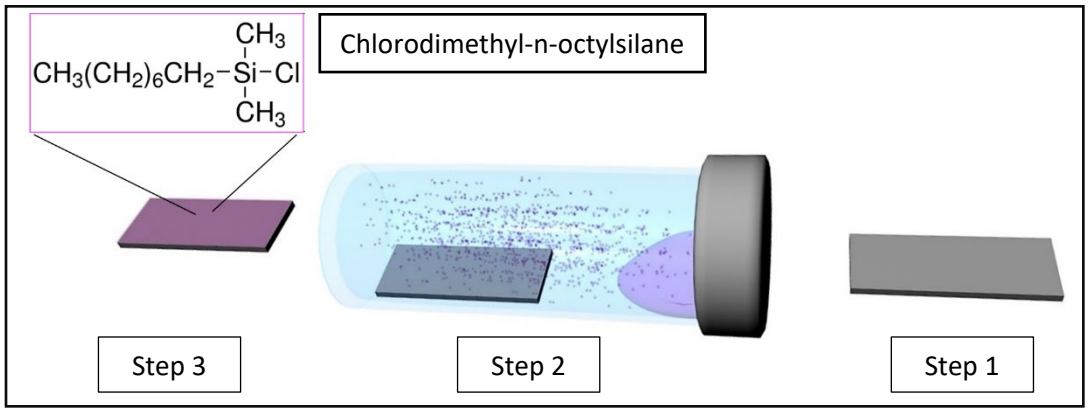

Figure 5.2: Schematic representation of the method for self-assembly of hydrophobic monolayers on silicon substrate. Water contact angle on silane-modified silicon was 100º.

5.2.5: Modification of GO Sheets with P2

Copolymer P2 was synthesized by solution free-radical polymerization [18]. For the modification (**Figure 5.12**), an aqueous suspension of GO (~ 0.75-1.5 mg/ml) was mixed

with an aqueous solution of P2 (~ 3-4 mg/ml) in a mass ratio of 1:6 according to the procedure described in **Section 3.2.3**.

5.2.6. QCM-D Investigation of Viscoelastic Properties of Adsorbed GO-P1 and GO-P2 layers on Hydrophobic Surfaces

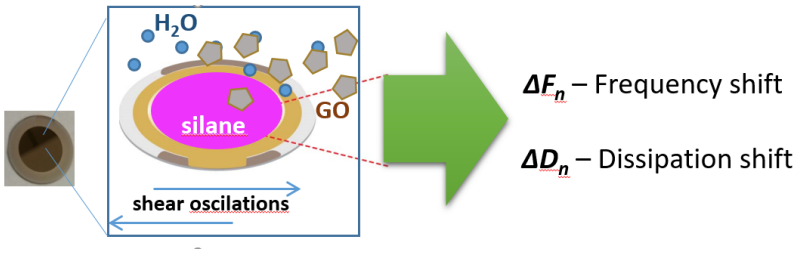

Figure 5.3: Schematic of adsorption of GO-P1/2 onto silane-modified quartz crystal.

Pristine GO, GO-P1 and GO-P2 adsorption to silane-coated crystals was performed using QCM-D at 25 ºC under 200 µL/min flow rate (**Figure 5.3**). Three aqueous suspensions were used at the same concentration of 0.016 wt.%.

All adsorbed materials were modeled as homogeneous single viscoelastic layers with acoustic thickness d, density ρ, storage modulus $G'(f)$, and loss modulus $G''(f)$. The storage modulus is a measure for the elasticity of the film. The loss modulus is related to the film's viscosity $\eta(f)$ by $G''(f) = 2\pi f\eta(f)$. Both G' and G'' (and η) are frequency-dependent. If $G' \gg G''$ - material is predominantly elastic, and if $G' \ll G''$ - material is predominantly viscous, and in case of $G' \approx G''$ it is viscoelastic. The viscoelastic properties are represented by the loss and storage modulus as the frequency dependent complex shear moduli, G_f of the layer.

$$G_f = \mu_f + i2\pi f\eta_f = G'_f + iG''_f \tag{5.4}$$

where f is frequency of oscillation and μ_f is shear elastic modulus.

The relationship between G''/G' gives a measure of the stiffness of the film and is called the loss tangent or loss angle, tan(δ_L). For soft and dissipative films loss angle is higher than for rigid non-dissipative ones [19].

$$\tan(\delta_L) = \frac{G''}{G'} = \frac{J''}{J'} \tag{5.5}$$

5.2.7. Deposition of GO-P2 multilayers on polymeric substrate

In this particular work we selected to focus on manufacturing of the GO layers on four polymer films possessing different surface energy, mechanical properties, thermal transitions, and internal structure. Specifically, in our research we will employ Kapton (polyimide, 25 μm, DuPont), PP (6 μm, Chemplex), PC (125 μm, MacMaster) and UHWPE (125 μm, MacMaster). Characteristics of those polymers are well known [20-21] and films of different thicknesses are commercially available. The following water contact angles were measured: Kapton – (80 ± 6)º, PP - (94 ± 3)º, PC - (76 ± 1)º and UHWPE - (92 ± 3)º. Sharp razor-blade was used to cut films into stripes of 1x4 cm^2. Kapton, PP, UHWPE samples were thoroughly rinsed with acetone, chloroform and

Figure 5.4: Deposition of a monolayer of GO-P2 on flexible polymeric substrate.

methanol for 10 min each to remove contaminants. Hexane was used for PC. Then, each sample was sandwiched between 2 magnetic frames with cut-out windows. Finally, dip-coating was performed (**Figure 5.4**). After the deposition, polymer films were allowed to dry under ambient conditions.

5.2.8. Estimation of surface energy for GO-P1 and GO-P2

We obtain the contact angles of two different liquids on solid surface by drop shape analysis Kruss, Germany at room temperature, and use the results to calculate the surface energy of the solid substrate by the Owens-Wendt method (**Equation 5.6**) [22].

$$\gamma_{l1}(1+cos\theta_1) = 2\sqrt{(\gamma_s^d \gamma_{l1}^d} + 2\sqrt{(\gamma_s^p \gamma_{l1}^p}$$

$$\gamma_{l2}(1+cos\theta_2) = 2\sqrt{(\gamma_s^d \gamma_{l2}^d} + 2\sqrt{(\gamma_s^p \gamma_{l2}^p} \quad (5.6)$$

$$\gamma_s = \gamma_s^d + \gamma_s^p$$

where γ_s and γ_l are the surface tensions of the solid and liquid, respectively. The subscripts *d* and *p* correspond to dispersion and polar components of the surface tension, respectively. Surface free energy (γ_s) and its polar (γ_s^p) and dispersion (γ_s^d) components of the GO surfaces were determined using two sets of contact angle measurements of water and hexadecane. The γ_l^p and γ_l^d components of liquids shown in **Table 5.1** were used in the calculations.

Table 5.1. Water and hexadecane contact angles for P1, P2, GO-P1 and GO-P2. γ_l^p and γ_l^d components of liquids are taken from reference [23].

	γ_l^d (mJ m^{-2})	γ_l^p (mJ m^{-2})	γ_l (mJ m^{-2})	P1	P2	GO-P1	GO-P2	GO
Hexadecane (1)	26.35	0	26.35	(15 ± 6)°	0°	0°	0°	0°
Water (2)	21.8	51	72.8	(38 ± 4)°	(94 ± 3)°	0°	(51 ± 2)°	0°
Surface Energy (mJ m^{-2})	-	-	-	59.3	28.3	73.1	50.8	73.1

Thus, using WCA and HCA values derived from the experiment and **Equation 5.6** the surface energy of the GO-P1 and GO-P2 films were found to be ~73 mJ m^{-2} and ~51 mJ m^{-2} respectively (**Table 5.1**). Analysis of water and hexadecane contact angles (HCAs) was done in Dr. Kornev's laboratory using a KRUSS DSA10 drop shape analyzer at 20 s after droplet deposition on the grafted copolymer surface.

5.3: Results and Discussion

5.3.1: GO-P1 Layers on Hydrophobic Substrates Deposited from Aqueous Solution by Dipcoating

In this section of the dissertation we investigate whether the pristine GO (unmodified with the copolymer) and GO-P1 can uniformly coat the hydrophobic Silane-SiO_2/Si substrates. Specifically, we investigated the effect of GO sheet sizes on the quality of monolayer formation on hydrophobic substrates.

In our initial experiments with pristine (unmodified with the copolymers) GO sheets we found that it was impossible to obtain a GO monolayer via dip-coating on hydrophobic surfaces (**Figure 5.5A**). Image presented in **Figure 5.5B** reveals that

deposition of GO-P1 on hydrophobic surface resulted in non-uniform coverage and crumpling of GO-P1 flakes. Furthermore, the data shown in **Figure 5.6** shows that the quality of deposited GO-P1 layers on hydrophobic surface is strongly size-dependent. For example, GO-P1 < 5 μm could not be deposited on hydrophobic surface by the dipcoating (**Figure 5.6A**) while the largest GO-P1 flakes (~80 μm, **Figure 5.6G**) resulted in highly non-uniform and crumpled/scrolled particulates and a monolayer with only slightly wrinkled ~5 μm GO-P1 sheets (**Figure 5.6B**). Similar scrolling and wrinkling phenomenon has been already reported in literature [24-28], although it is still not well understood. We associate this observation with poor adhesion of hydrophilic/polar OEGMA units to the hydrophobic surface and capillary forces originated from solvent evaporation [29-30]. The development of sharp wrinkles/atomic scale corrugations and folds in GO is the direct result of significant local stresses as suggested elsewhere [31] and extreme flexibility of individual GO flake (low bending modulus) [32]. The formation of such features is also energy-favorable because it can reduce the number of interaction contacts between two unlike surfaces - hydrophilic OEGMA units and hydrophobic Si substrate. The thickness of the wrinkled and scrolled GO-P1 sheets ranged from 3 to 500 nm as determined from AFM profiles (**Figure 5.6(C, F, H)**).

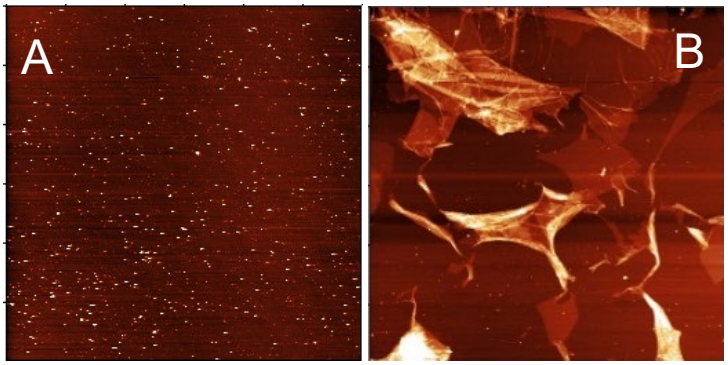

Figure 5.5: Atomic force microscopy of pristine graphene oxide (A) and GO-P1 (B) deposited on hydrophobic substrate. The size of the scans is 30x30 μm^2, vertical scale is: 2 nm (A), 70 nm (B, inset). GO was deposited by dip-coating.

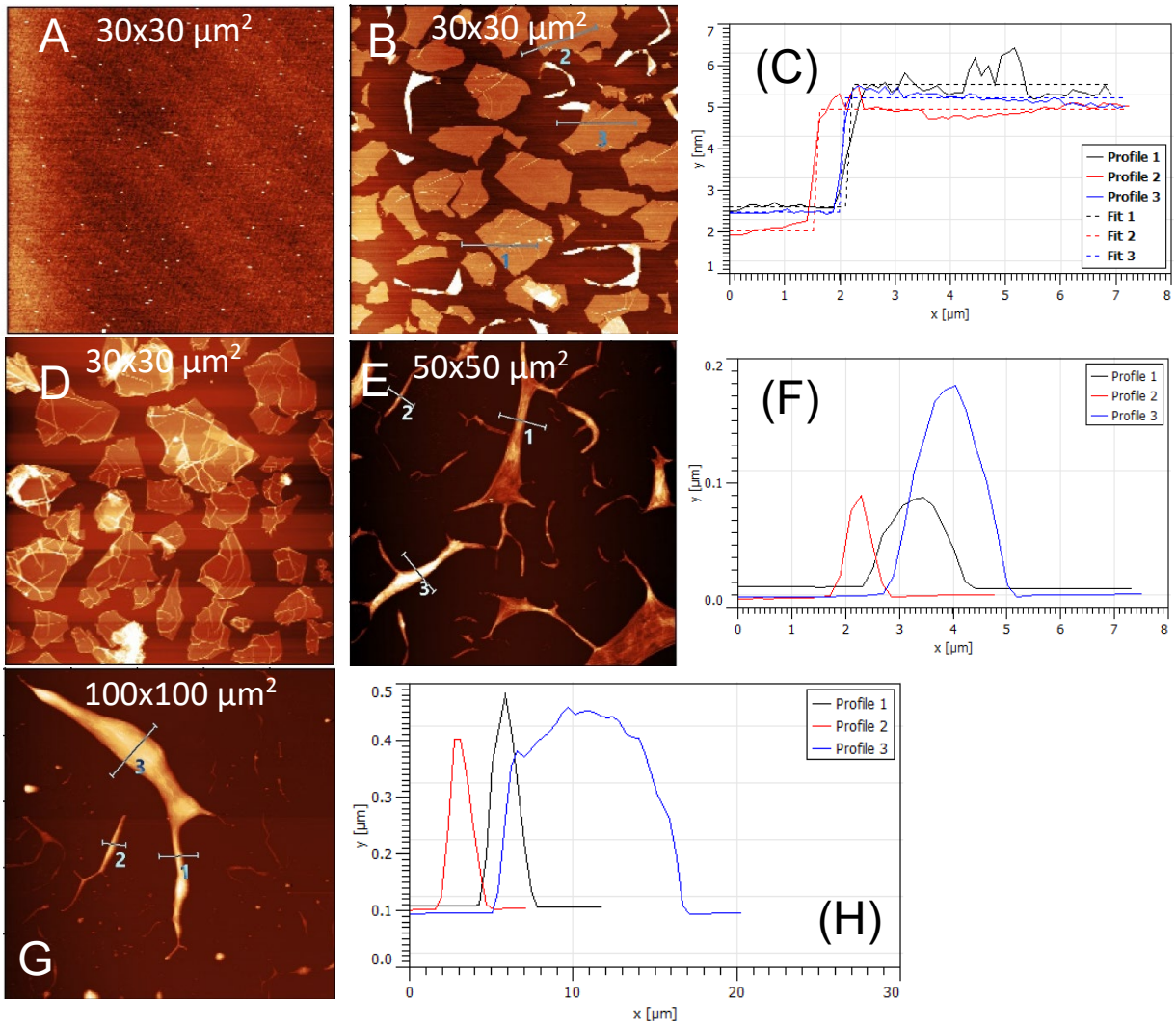

Figure 5.6: AFM images showing GO-P1 with different average flake sizes deposited on hydrophobic substrates: ~3 µm (A); ~5 µm (B); ~7 µm (D); ~30 µm (E); ~95 µm (G); (vertical scale: 2 nm (A), 10 nm (B), 25 nm (D), 150 nm (E), 600 nm (G)). Corresponding cross-sectional profiles (C, F, H).

Therefore, an extra efforts were made to obtain GO-P1 with well defined morphology on hydrophobic surfaces (see **Section 5.3.3**).

5.3.2: Theoretical Aspect of Crumpling/Scrolling: Folding Griteria of GO-P1 Sheets

The present section discusses the possible formation mechanism of GO-P1 curled-up structures and nanoscrolls. Previously, capillary interaction between water and GO is reported to be liable for the formation of folded GO nanostructures on hydrophobic substrates during "molecular combing" [28, 33].

Similarly, in this dissertation, there are several actions which may lead to the formation of GO nanoscrolls. Firstly, hydrophobic interaction [34] between GO sheets and hydrophobic substrates contributed to the pinning of some GO sheets to the surface. Secondly, substrate-enhanced dewetting of liquid film allowed the capillary force to induce the folding or scrolling of GO sheet [31].

In the next step of our discussion, the theoretical assessment of folding criteria of GO-P1 sheet is carried out. According to the scientific literature, the folding/bending in unconstrained submicron solid films (few hundred nanometers) or carbon nanotubes could be modeled using the classical Bernoulli-Euler beam theory [35-37]. However, it was proven to fail for nanometer scale monolayer of graphene/graphene oxide sheets since the physical thickness becomes close to the size of constituent particles (carbon atoms, bonds) and particle-scale features need to be accounted for [38-39]. In contrast to bi- and multilayered systems the bending rigidity of atomic monolayers involves much different mechanisms. The bending behavior of such sheets is expected to be affected by strain and torsional gradients accompanied by changes of atomic bond and dihedral angles [40-41]. In conventional theory, the resistance of a thin sheet to elastic deformation is defined by the

Young's modulus E and the out-of-plane bending modulus (bending spring constant), D_0, respectively. These two parameters are related by the following Euler equation [36]:

$$D_0 = \frac{EH^3}{12(1-\nu^2)} \tag{5.6}$$

where H is the GO thickness, $\nu \approx 0.07$ – Poisson ratio [42] (for 0.18 degree of oxidation), $E \approx 200$ GPa - elastic modulus of GO [43]. To account for the size-dependent bending rigidity due to non-local effects in GO-P1 flake, we used a correction to the bending modulus given by [40]:

$$D = D_0 \left[1 + 6(1-\nu)\left(\frac{l}{H}\right)^2\right] \tag{5.7}$$

where l is the length scale at which classical elasticity breaks down for the specific material. Parameter l becomes important for materials possessing a nonhomogeneous structure like amorphous solids or polymers [38, 44]. Thus, following the ref [38] we assumed $l \approx 60$ nm for GO-P1 system.

Next, using the minimization of total free energy (the sum of surface energy and elastic energy) with respect to in-plane and out-of-plane strains the instability criteria for buckling is obtained as follows [36]:

$$\gamma \geq f_{cr}^{B} = \frac{\pi^2 D}{2L^2} \tag{5.8}$$

where $\gamma \approx 73$ mJ m^{-2} corresponds to the surface energy of GO-P1 layer, calculated in **Section 5.2.8**.

In this work we assumed the contribution of the interaction energy term (interaction between GO-P1 flake and hydrophobic surface) to be negligible. **Equation 5.8** shows that the crumpling of GO is governed by surface free energy and the elastic energy [27]. The

evaluation of the critical surface stress required to induce buckling lead to the conclusion that only GO-P1 sheets with a spring constant higher than f_{cr}^{B}~73 mJ m^{-2} could resist complete scrolling/folding, corresponding to L_{cr} = 6 - 8 μm and H = 2 – 3 nm (**Figure 5.7**). Thus, GO-P1 scrolling will take place only if the surface tension force γ acting at the junction of receding water meniscus - 2D material – air dominates over strain/elastic forces arising from GO-P1 bending [31, 45].

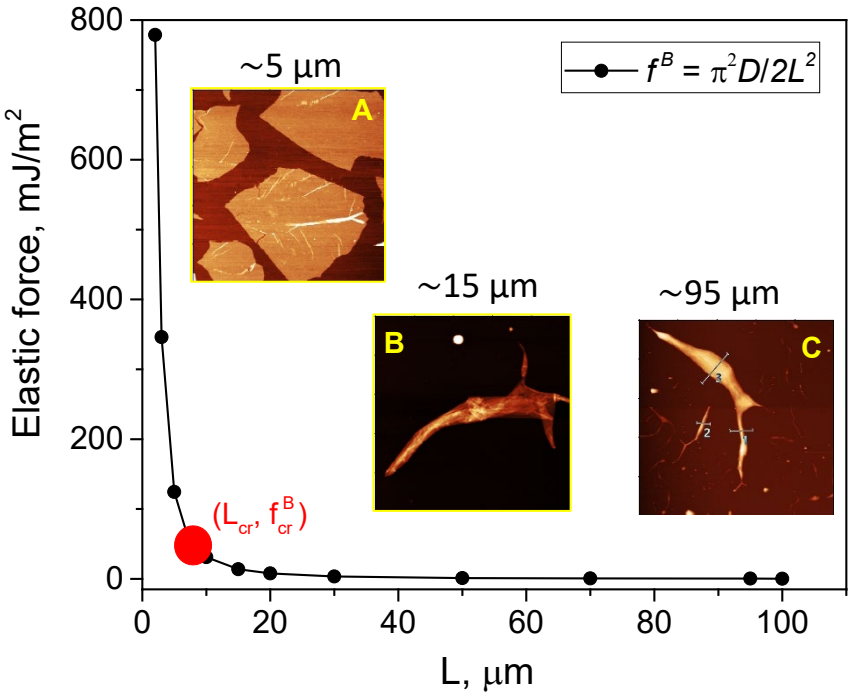

Figure 5.7: Elastic force as function of GO-P1 sheet size based on Equation 5.8. AFM images showing GO-P1 with different average flake sizes deposited on hydrophobic substrates. The size of the scans is 10x10 µm^2 (A, B), 100x100 µm^2 (C); Vertical scale: 10 nm (A), 70 nm (B), 600 nm (C). GO-P1 was deposited by dip-coating from water-ethanol mixtures. Red spot corresponds to critical conditions at which crumpling/folding takes place.

Also, the stability of these crumpled formations was tested in the same manner as for the hydrophilic case, and no detachment was observed after intensive ultrasonic

treatment (sample were left in water on a shaker for an hour then sonicated 3 times for 10 minutes, and no changes were observed in the AFM results). The above results suggest that the nanoscrolls were well fixed in the strained state [34, 46] on the substrate.

Hence, the above results suggest that the scrolling is driven mainly by the capillary forces which depend on the evaporation rate of the solvent [47-49]. The latter one in turn is associated with the rate of dewetting and ambient temperature [50].

5.3.3: GO-P1 Layers on Hydrophobic Substrates from Water-Ethanol Mixtures

Influence of dewetting rate on GO-P1 morphology

The results presented in **Section 5.3.1** suggest that it is challenging to obtain well defined GO-P1 layers directly on hydrophobic substrate. Specifically, GO-P1 sheets tend to assume crumpled and scrolled conformation when in contact with hydrophobic substrate. As it was shown in previous section, the interplay between surface energies of solvent, GO-P1 sheets and substrate plays a crucial role in crumpling effect. Therefore, another variable to be considered in the formation of GO-monolayers is the solvent in which GO-P1 flakes were dissolved in. In this part of dissertation we investigated the influence of solvent's conditions (surface tension and temperature) on the ability of GO-P1 sheets to form a monolayer on hydrophobic substrates.

Based on the **Equation 5.8** we hypothesized that the addition to water of organic solvents with lower surface tension and much less self-hydrogen-bonding ability (ethanol, methanol or acetone [51]) would promote the interaction between the hydrophobic surface and GO-P1 by diminishing water's free energy of cohesion [52]. Therefore, ethanol was

introduced into GO-P1 in water solution at: 0%, 10%, 50%, 70% and 100%. Then we performed a deposition of GO-P1 layers on hydrophobic and hydrophilic Si substrates via dip-coating at 300-500 mm/min withdrawal speed and the surface of each sample was scanned using AFM as shown in **Figure 5.8**.

The results show that instead of increased coverage, there is a pronounced crumpling/scrolling effect already at 10 weight percent of ethanol added (**Figure 5.8D)**, resulting in loosely folded GO-P1 structures on hydrophobic Si (Figure 4 - 5C, D). Next, we found that even the smallest sized sheets scrolled up such that GO-P1 flake could not maintain its planar structure after a contact with hydrophobic silane-SiO_2/Si substrates. Next, as the ethanol amount was further increased up to 30% and 70%, no further influence was revealed on the scrolling/folding behavior of GO-P1 sheets (**Figure 5.8(D-I)**).

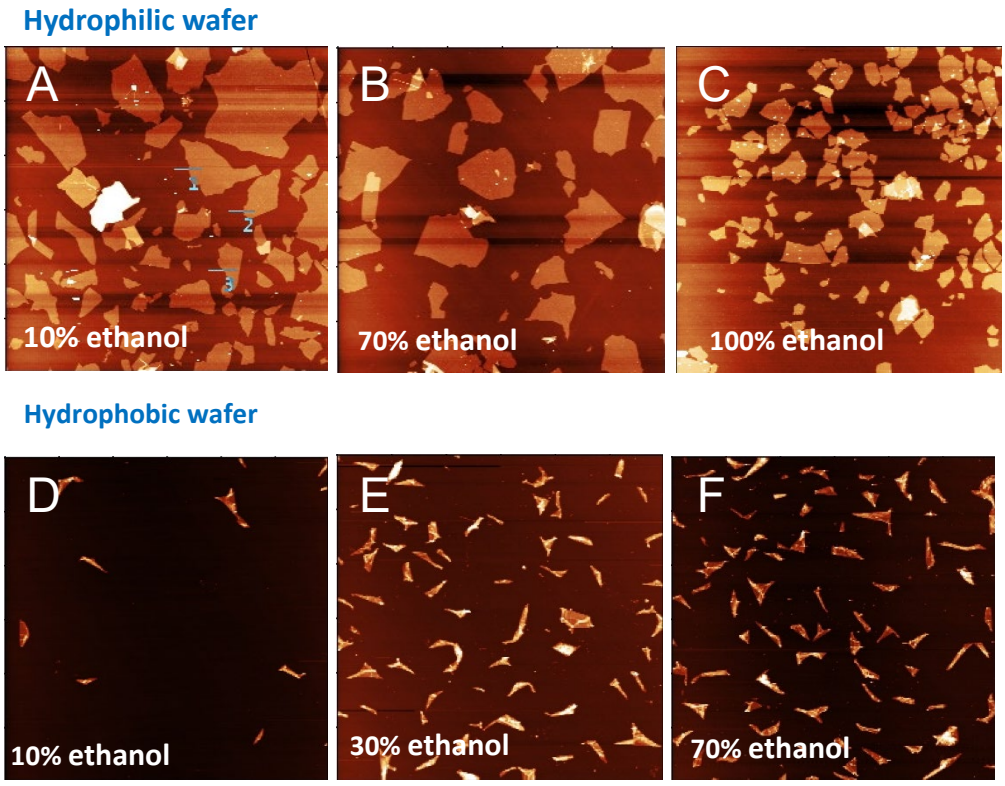

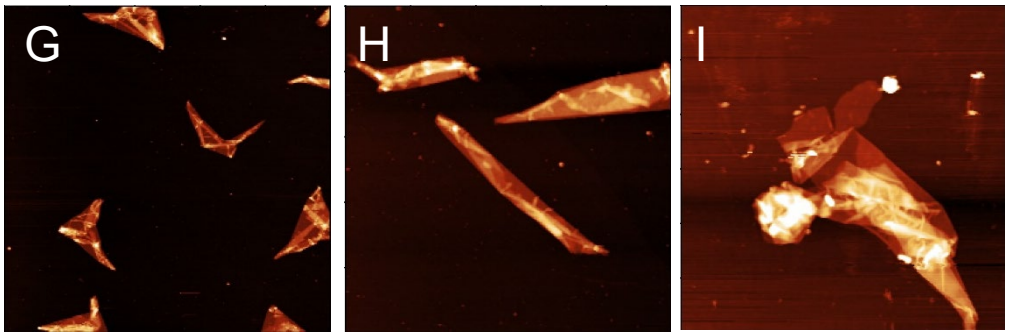

Figure 5.8: AFM images showing GO-P1 with average flake sizes of ~3 μm deposited on hydrophilic (A – C) and hydrophobic substrates (D – I); The size of the scans is 30x30 μm^2 (A – F), 10x10 μm^2 (G), 5x5 μm^2 (H), 3x3 μm^2 (I); Vertical scale: 10 nm (A - C), 35 nm (D – I). GO-P1 was deposited by dip-coating from water-ethanol mixtures.

In contrast, the use of hydrophilic Si substrates prevented GO-P1 from folding (**Figure 5.8(A-C)**). Previously, it has been reported that the hydrophobic substrate is indeed favorable for the formation of crumpled and folded graphene [28, 53].

Swelling of P1 layer in water-ethanol by QCM-D

In order to better understand the mechanism of scrolling of GO-P1 sheets we investigated the responsive behavior of P1 grafted layers in the external environment (water-ethanol mixtures). For this, P1 layer was deposited on SiO_2/Si substrate (**Section 5.2.2**) and QCM-D was employed as a tool to monitor real-time changes in film thickness, mass, and viscoelastic properties of solvated P1 layer. Initial thickness of the dry copolymer layer was $h_{dry} \approx 40$ nm as measured by ellipsometry. The raw data from a typical QCM-D measurement (changes in frequency (ΔF) and dissipation (ΔD)) for the P1-solvent system is displayed in **Figure 5.9**. As can be seen from the graph, overtone-normalized frequency shows overtone-dependent behavior for all harmonics, which together with the fact that $\Delta D > 0$ indicates a viscoelastic nature of the swollen film [54]. Therefore, the above

result imply that the Sauerbrey equation (**Equation 5.1**) would be invalid for such highly hydrated and viscous surface-grafted polymer layers that result in high dissipation shifts.

Therefore, using the viscoelastic Voigt model and **Equation 5.9**, thickness and viscosity of swollen P1 layer as a function of ethanol content were found. The solvent content in P1 film for different ethanol-water mixing ratios was estimated by **Equation 5.9** [8].

$$\% \text{ Solvent Content} = \frac{m_{wet} - m_{dry}}{m_{wet}} \cdot 100\% \qquad (5.9)$$

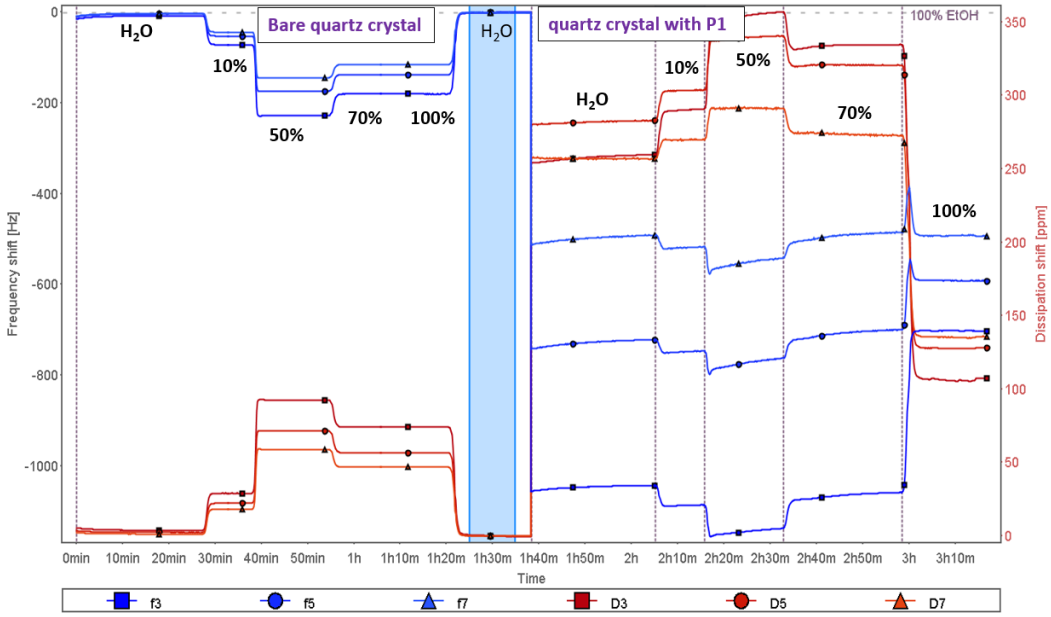

Figure 5.9: GO-P1 swelling in water-ethanol. QCM-D results showing changes in the 3rd, 5th and 7th harmonic frequencies (blue) and dissipations (red).

Table 5.2 summarizes the values of solvation of different solvent/P1 systems. One can see from **Figure 5.10 (A)** that the thickness of grafted P1 layer undergoes its minimum of ~228 nm at 50% ethanol content and then reaches maximum value of 254 nm at 100% ethanol. In contrast, **Figure 5.10 (B)** demonstrates only gradual deswelling of P1 with the

addition of ethanol. We suggest that the following events take place when ethanol is introduced into the system: (i) initial dehydration is caused by water being expelled out of outermost layers of P1 leading to thickness decrease; (ii) hydrated ethanol associates/clusters get hydrodynamically coupled to the polymer layer, thus increasing its shear viscosity (at 50%); (iii) substitution of water molecules with lager ethanol molecules introduces free volume into P1 layer which increases thickness of the layer at the expense of density (ρ_{wet}) decrease.

Table 5.2: QCM-D parameters of solvent/P1 systems.

Amount of ethanol in water	m_{dry} [ng/cm^2]	ρ_{dry} [g/cm^3]	h_{dry} [nm]	ρ_{fluid}^* [g/cm^3]	η_{fluid}^* [mPa·s]	m_{wet} [ng/cm^2]	ρ_{wet} [g/cm^3]
dry film	4600	1.15	40	-	-	4600	-
0%	-	-	-	0.997	0.9	23859	1.026
10%	-	-	-	0.982	1.35	23431	1.015
50%	-	-	-	0.914	2.75	22016	0.963
70%	-	-	-	0.868	2.25	22380	0.926
100%	-	-	-	0.784	1.06	21861	0.861

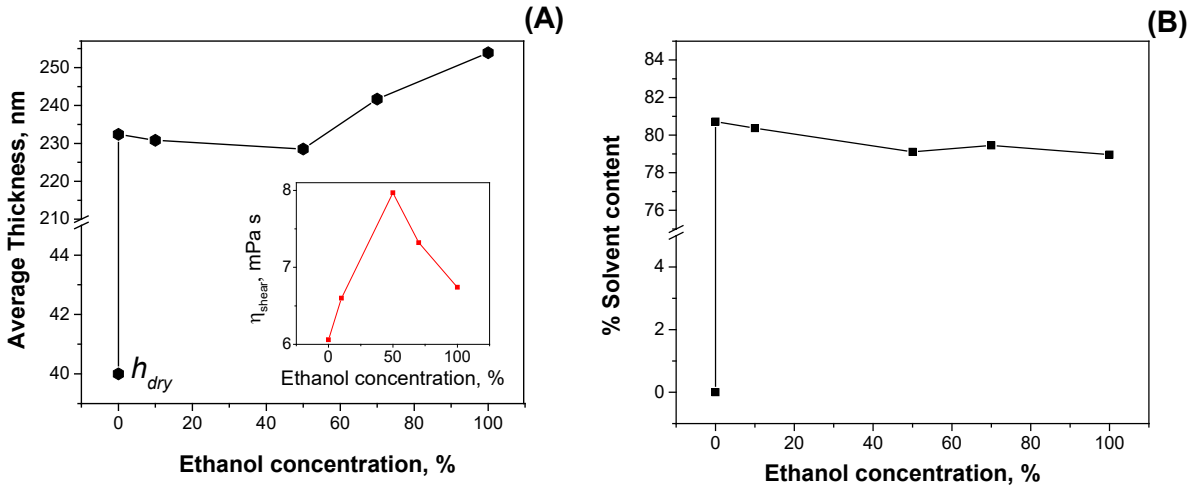

Figure 5.10: QCM-D measurement in **Figure 5.9** modeled using Voigt-based model (A and inset); B: solvent content in P1 film as a function of ethanol concentration.

Another result also shows that shear viscosity (**Figure 5.10**, **inset**), obtained by fitting experimental data from **Figure 5.9** to Voigt model (see **Section 5.2.3**), reaches its maximum at 50% of ethanol concentration, implying highly dissipative nature of copolymer layer. This may result from a strong interaction between molecules of water and ethanol leading to the formation of clusters of the hydrated ethanol micelles [55] coupled with OEGMA units via hydrogen bonding. It is necessary to point out that viscosity measurements using QCM-D captures only local viscosity in the vicinity of the quartz SiO_2/Si crystal being coated with copolymer. Therefore, these events may explain why we observed more pronounced scrolling/folding of GO-P1 sheets in the presence of ethanol-water mixtures. Specifically, as more volume is introduced by ethanol molecules P2 chains assume more "loose" conformation due to ethanol being poorer solvent than water (**Figure 5.10B**). It may lead to higher evaporation rate causing faster dewetting during dipcoating procedure, which in turn creates larger surface stress on GO-P1 sheets, promoting even small size GO-P1 sheets to fold.

To conclude, the addition to water of organic liquids like ethanol creates unfavorable conditions for obtaining a uniform and well-defined GO-P1 monolayer on hydrophobic substrate.

Influence of temperature on GO-P1 morphology

Literature has reported that wrinkles and ripples can be enhanced via thermal manipulation due to the negative thermal expansion coefficient of graphene [56]. To verify this effect of temperature, we performed dipcoating from 80 ºC hot GO-P1 water solution.

The AFM image shown in **Figure 5.11** demonstrates heavily shrunk and compressed/warped GO-P1 sheets suggesting that larger temperature-induced capillary compression has been exerted on GO sheets [57]. Surprisingly, crumpled GO sheets self-assembled into short fiber-like structures similar to porous graphene fibers observed by Li et al. [47], which can be associated with intermolecular hydrogen bonds in OEGMA segments [58] as water becomes poor solvent nearing the LCST point of OEGMA [59].

It is expected that folded graphene oxide structures could constitute a new class of stimuli-responsive materials well suited for drug delivery systems or nanostorage [60].

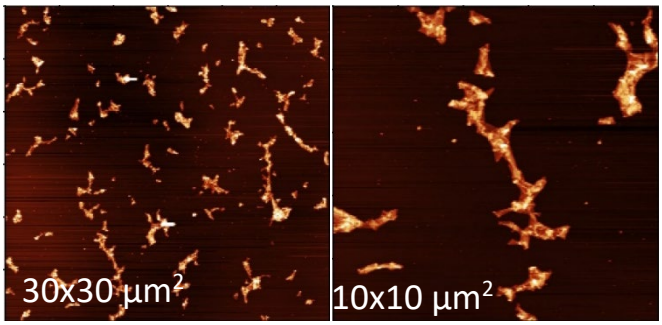

Figure 5.11: GO-P2 sheets on Si wafer deposited from 80 ºC hot GO-P2 water solution. Vertical scale: 35 nm.

5.3.4: Modification of GO Sheets with P2 Copolymer

We showed in the sections above that due to the minor interaction with hydrophobic substrate, flat GO-P1 becomes unstable with increasing lateral dimensions leading to self-fold or scroll. As mechanical structures enter the nanoscale regime, the influence of hydrophobic and van der Waals forces increases [61]. Therefore, there was a need in a new polymer which would improve interaction of GO sheets with hydrophobic surfaces.

In view of this, the statistical copolymer P2 was synthesized in Dr. Luzinov's laboratory by Dr. Nikolay Borodinov [18]. The copolymer consists of

three different methacrylic monomeric units (reactive via epoxy group and hydrophobic glycidyl methacrylate [GMA], polar oligoethylene glycol methyl ether methacrylate [OEGMA]

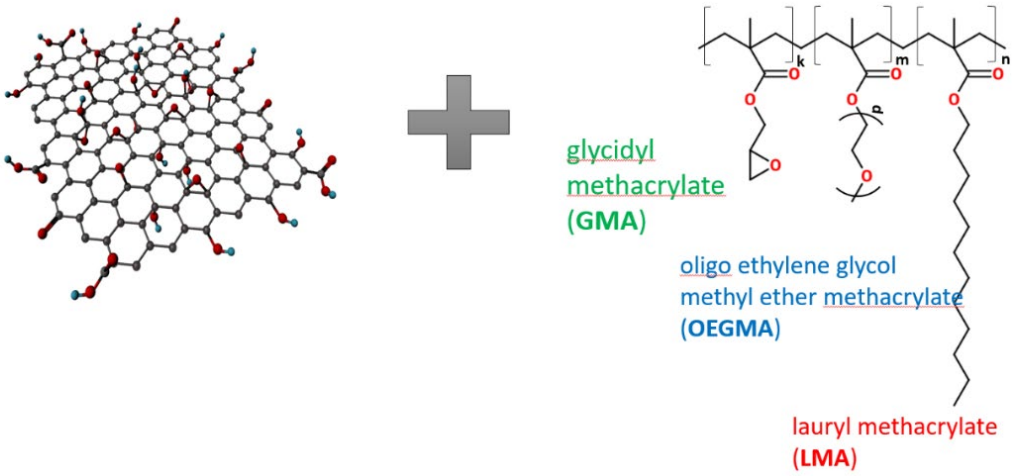

Figure 5.12: Modification of GO sheets with P2 copolymer.

responsible for solubility of the P1 in water and hydrophobic lauryl methacrylate [LMA] responsible for hydrophobic interaction between the polymer and low-energy polymeric substrates [46, 62]) (**Figure 5.12**). It is hypothesized that the hydrophobic (Van der Waals) force, enabled by LMA segment, clamps graphene flakes to substrates, and holds together the individual graphene sheets in multilayer fashion. The ability of P2 copolymer (containing hydrophobic LMA) to dissolve in water is essential to the process of surface modification as it opens venues to reduce the use of potentially environmentally hazardous solvents.

We suggest that during the modification of GO with P2, GMA epoxy groups react with (hydroxyl, carboxyl, and epoxy) GO functional groups [63-64]. The presence of multiple reactive groups along the polymer chain is needed to ensure that every macromolecule will

form multiple connections with GO surface to form the thin polymer coating enveloping the sheets. Similarly to GO-P1 (as discussed in **Chapter 3**) the suspension of the GO sheets modified with P2 is stable for a long time (6-8 months). Following the experimental approach described in **Chapter 3**, structural and morphological properties of the GO-P2 particulates were also thoroughly investigated using AFM, FTIR, XPS, DSC, TGA and Raman.

5.3.5: Chemical Properties of GO-P2

The successful attachment of P2 on pristine GO surfaces was confirmed by Fourier transform infrared spectroscopy (FTIR).

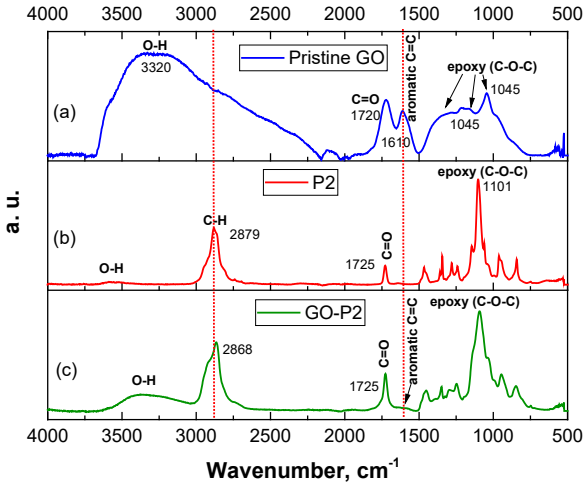

Figure 5.13: FTIR spectra for: (a) pristine GO, (b) P2 and (c) GO-P2.

As shown in **Figure 5.13a**, the broad peak at 3320 cm^{-1} is from O-H groups and two narrow peaks assigned to the carbonyl group (C=O stretching) and the skeletal vibration of unoxidized graphitic domains on GO sheets (aromatic C=C) can be observed at 1720 and 1610 cm^{-1}. The range of 1000-1280 cm^{-1} corresponds to ethers and/or epoxides groups. For P2 (**Figure 5.13b**), the C-H stretching group is shown by the peak at 2868 cm^{-1}. The

absorbance peaks at 1725, 1250, 1111 cm^{-1} can be attributed to carbonyl (C=O), epoxy (C-O-C) and ether (C-O) stretching vibrations. In the spectrum of GO-P2 hybrid (**Figure 5.14c**) the absorption bands detected at 2873, 1732 and 1250 are the characteristic of the C-H, C=O and C-O-C groups of the grafted P2, respectively [65].

We further confirmed the attachment of the copolymer to the GO surface with XPS (**Figure 5.14**). As seen from the **Figure 5.14B** system of GO-P2 showed similar energy peaks to those of GO and GO-P1 (**Figure 5.14A)** and the amount of oxygen-containing groups (OH) significantly increased as the epoxy decreased, suggesting effective grafting of P2 polymer chains to GO sheets. The C/O ratio was estimated by **Equation 3.2** based on the deconvoluted C_{1s} peak.

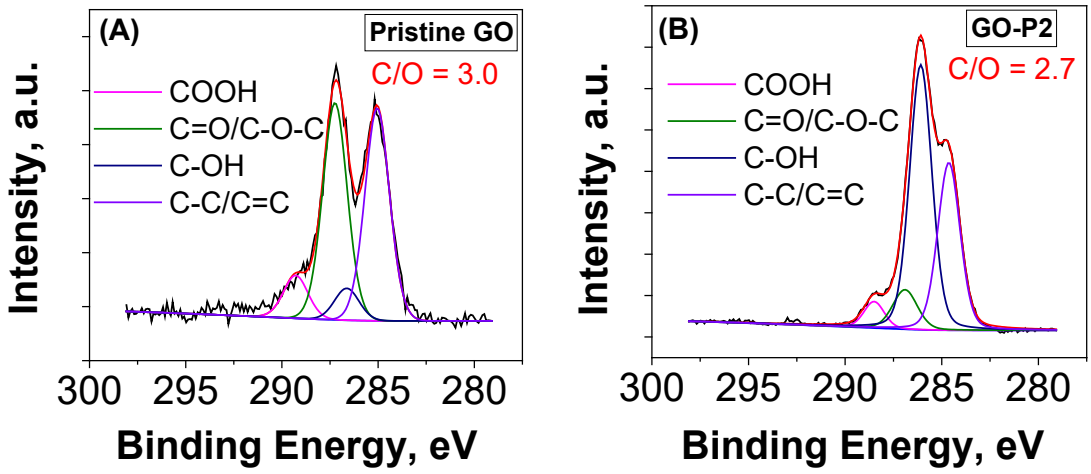

Figure 5.14: High resolution C1s spectra of pristine GO (A) and GO-P2 (B).

5.3.6: Thermal Properties of GO-P2

The process of GO modification using water solution of P2 copolymer has been investigated with thermogravimetric analysis, TGA and dynamic scanning calorimetry (DSC). In this section we show that, like P1 copolymer, the P2 copolymer can be readily

grafted to GO surface through the non-condensation reactions of epoxy functional groups with (hydroxyl, carboxy, and epoxy) functional groups located on the GO surface.

Thermal properties of GO-P2

The samples were heated to 700 ºC at a rate of 15 ºC/min in a nitrogen atmosphere. From **Figure 5.15**, it can be observed that pristine GO is not thermostable: mass loss of GO started below 100 ºC, which is attributed to the volatilization of stored water in its π-stacked structure.[66]

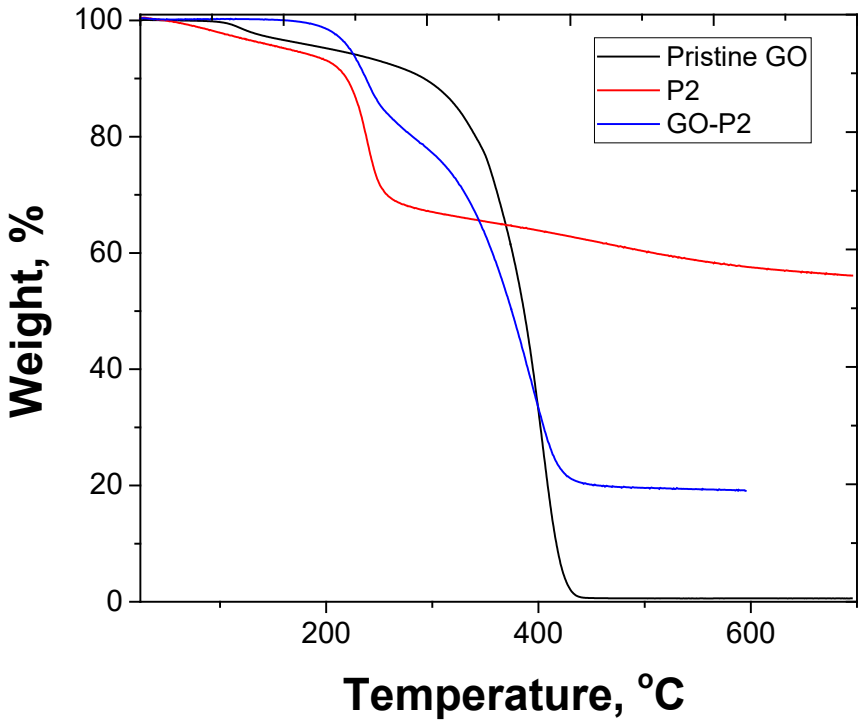

Figure 5.15: TGA analysis of pristine GO, P2 and GO-P2.

The main weight loss of GO around 200 ºC is caused by the decomposition of labile oxygen-containing functional groups yielding CO, CO_2 and H_2O steam [67]. The overall weight loss of pristine GO is 44%. The curve of P2 shows a fast weight reduction at 415

ºC. The reduction is caused by the decomposition of P2 polymer, leaving about <1% of carbon. As for GO-P2, about 80% weight fraction loss is observed from 200 to 500 ºC, which is due to the decomposition of P2 and some oxygen functional groups of GO sheets. From the ratio the GO to P2 and using **Equation 3.1** total thickness of P2 layer was estimated to be around 1.8 – 2.0 nm (0.9 – 1 nm on one side of GO sheet).

Kinetics of copolymer adsorption

The kinetic isotherm for P2 attachment to GO is presented in **Figure 5.16 (right)**. Based on TGA curves we found that the adsorption mechanism of P2 copolymer is fast and similar to what was observed earlier for P1 case. Following the equations (3.3) and (3.4) the kinetic parameters were calculated from the non-linear fittings using PFO and PSO models. Since the PSO model provided better fit to experimental data we concluded that the adsorption of P2 on GOs is also governed mostly by chemisorption (**Figure 5.16 (right)**).

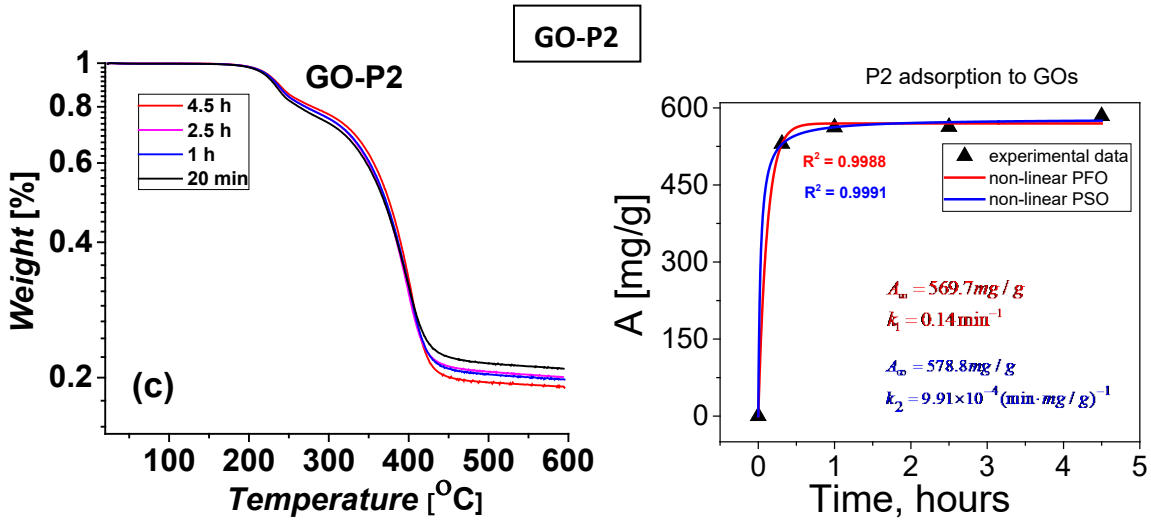

Figure 5.16: (A) TGA thermograms of GO grafted with P2 as a function of grafting time; (B) Grafted amount of P2 copolymer to GO from water as a function of time

DSC studies of the interaction between the GO and P2

The results from DSC (**Figure 5.17)** showed that melting peak is largely suppressed, which indicates that the mobility of OEGMA segments in P2 copolymer are restricted, preventing crystallization [68-69]. Similarly to GO-P1 (see **Section 3.3.3**) the observed ~9 ºC decrease in the melting point of primary peak is due to the significant interaction between the GO sheets and P1 chains. By contrast, an increased phase change temperature will occur when the interaction between polymer chains becomes highly attractive because of hydrogen bonding between side PEG units in free P1 chains.

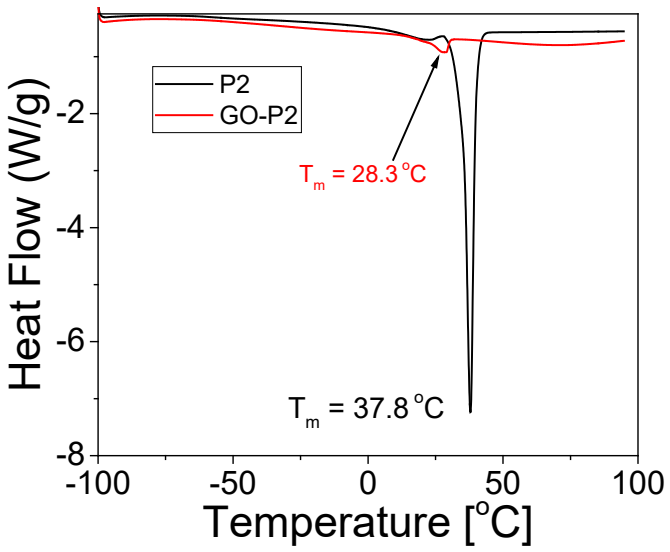

Figure 5.17: DSC thermograms for P2 and GO-P2.

5.3.7: Morphology of GO-P2 films on Hydrophilic and Hydrophobic Surfaces

Next, we found that the grafting of the copolymers to GO surface, indeed, allows formation of GO monolayers on surfaces of various polarity via the conventional dip-coating from water. As a hydrophilic surface we used chemically cleaned SiO_2/Si wafer with 0° water contact angle. In order to mimic the hydrophobic nature of polymeric films and facilitate characterization of GO-P coatings on such surfaces we used Si/SiO_2 substrates covered with ~1 nm layer of chlorodimethyl-n-octylsilane (water contact angle ~ 100°). It allowed us to determine true thickness of GO-P2 layers and reveal the morphology of GO-P2 sheets on substrates. Thus, in experiments with pristine (unmodified with the copolymers) GO sheets, we found that it was impossible to obtain a uniform GO monolayer via dip-coating on hydrophilic and hydrophobic surfaces (**Figure 5.18A, B**). In contrast, individual GO-P2 sheets were uniformly distributed on the surface of both hydrophilic and hydrophobic SiO_2 (**Figure 5.18C, D**). Furthermore, we found that

thickness/structure of GO-P2 layers deposited can be carefully regulated via concentration of the GO sheets in water suspension (**Figure 5.18E)**.

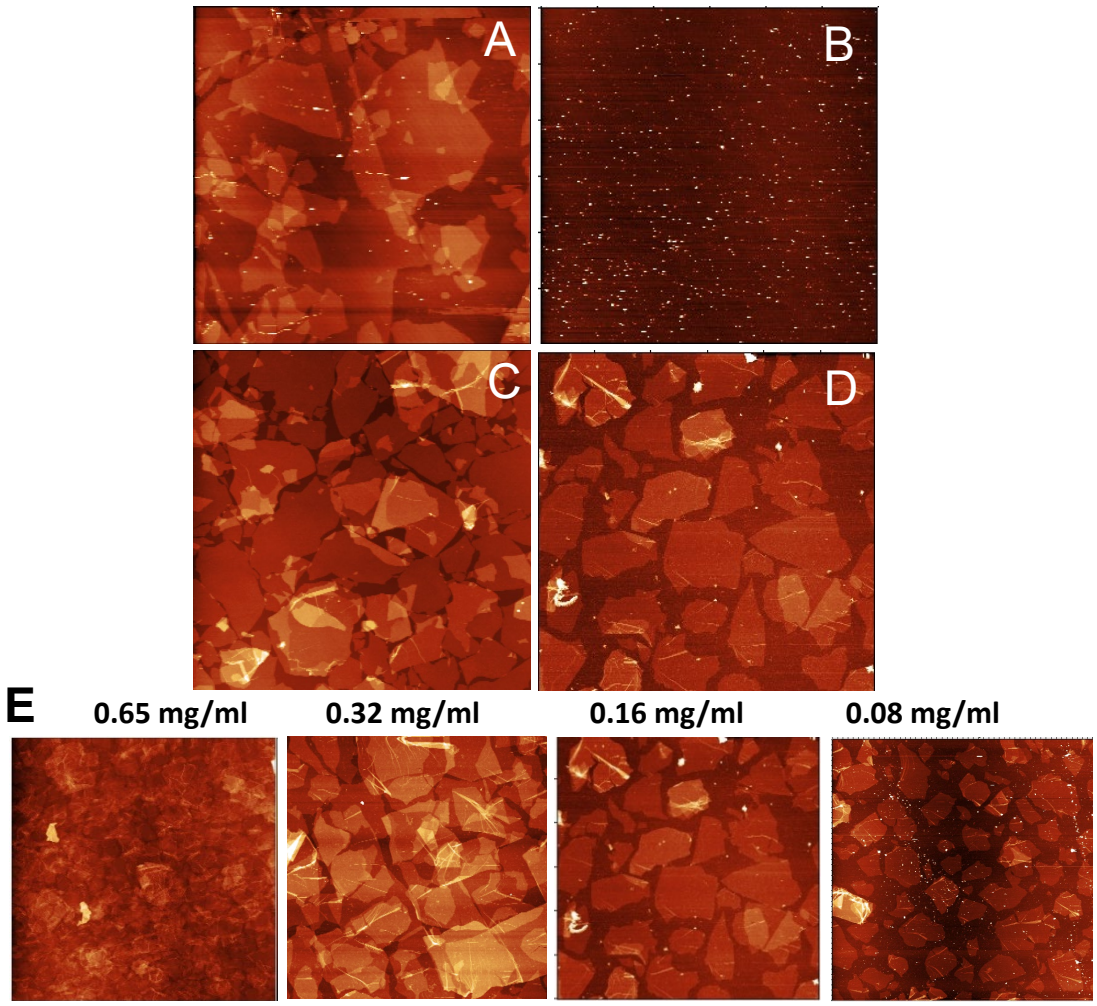

Figure 5.18: Atomic force microscopy of pristine graphene oxide deposited on hydrophilic (A) and hydrophobic (B) surface, and GO-P2 on hydrophilic (C) and hydrophobic (D) surface. (E): Hydrophobic silicon wafer dip-coated with GO-P2 using suspension of different concentrations. The size of the scans is 30x30 μm^2, vertical scale is: 30 nm (A), 2 nm (B), 70 nm (C, D, E). GO was deposited by dip-coating.

Atomic force microscopy has been also used to determine the thickness of individual GO sheet modified with P2.

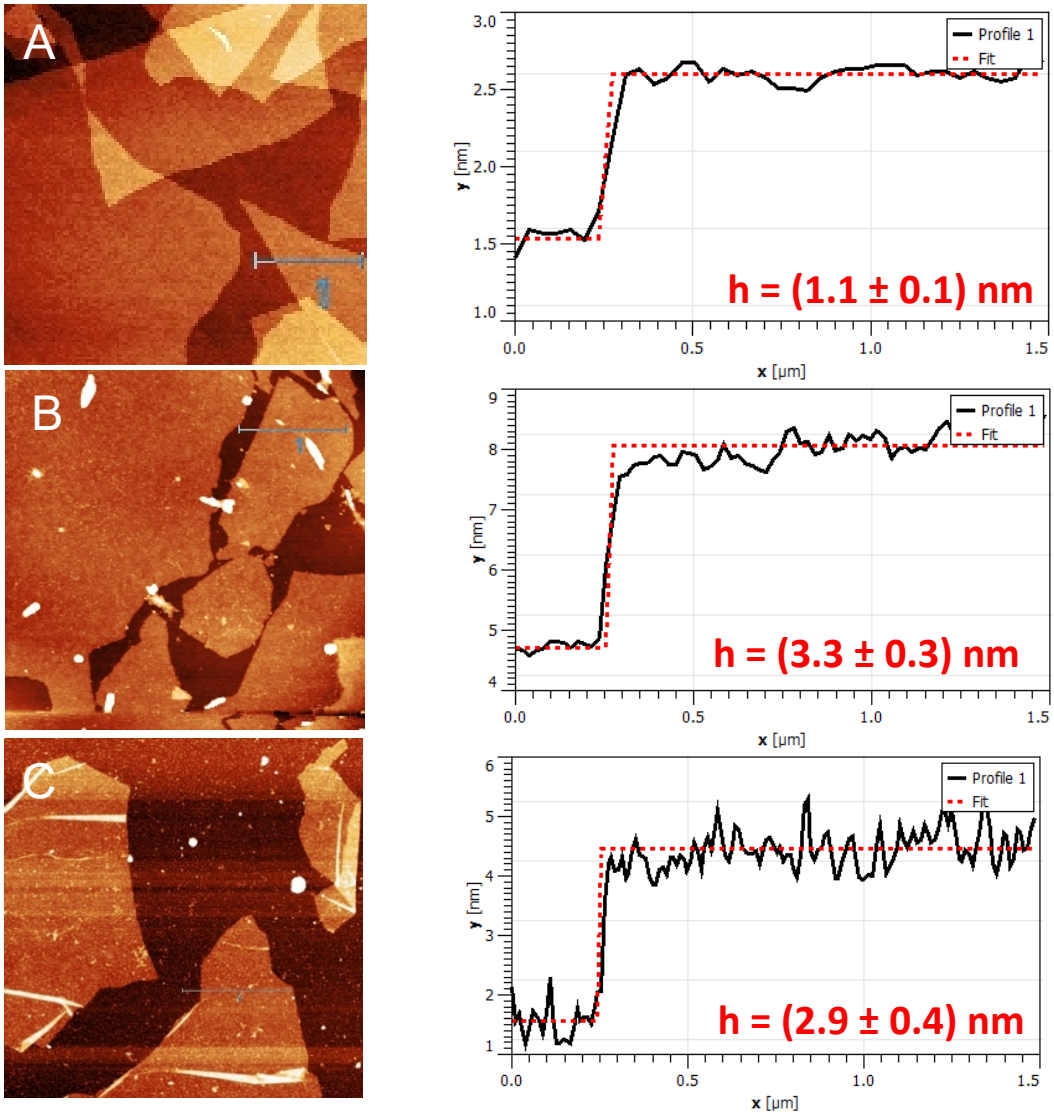

Figure 5.19: AFM images and corresponding cross-sectional profiles showing (A): a pristine GO layer, (B): GO-P2 monolayer on hydrophilic Si substrate and (C): GO-P2 on hydrophobic Si (silane-modified). The size of the scans is 5x5 μm^2, vertical scale is: 5 nm (A), 10 nm (B, C). GO was deposited by dip-coating.

As indicated by the cross-sectional analysis **(Figure 5.19A)**, the thickness of the pristine GO sheet was on the level of 1 nm, which is comparable to the value typically reported for the GO sheets obtained via Hummer's method [70-72]. However, cross-sectional analysis revealed that thickness of pristine GO sheet increased roughly by 1.5 nm **(Figure 5.19B)**. It confirmed that the copolymer layer was indeed anchored to graphene oxide sheets. Also, the height profile of GO-P2 sheets suggested that the P2 polymer chains formed even and dense coating encapsulating the sheets. **Figure 5.19C** shows GO-P2 sheets on a hydrophobic silane-SiO_2/Si substrate with its corresponding height profile. Further analysis of AFM images revealed that GO-P2 on hydrophobic substrate tends to be slightly wrinkled in contrast to GO-P1 on hydrophilic substrate. This is why, the same amount of GO-P1 layers may result in higher average thicknesses on hydrophobic substrate. As shown in **Figure 5.18E**, we can easily control the number of such layers by varying concentration of GO-P2 in water.

5.3.8: Comparative Studies of Interaction of GO-P1 and GO-P2 with the Hydrophobic Interface Using QCM-D

In previous sections we showed that it is possible to obtain a uniform monolayer on hydrophobic substrates using GO modified with P2 copolymer. In contrast, using both pristine GO and GO-P1 we were unable to achieve a well-defined monolayer. Thus, it is important to understand key differences between these materials. The interaction and the subsequent binding of the GO, GO-P1 and GO-P2 flakes to hydrophobic silane-SiO_2/Si surface was analyzed both qualitatively and quantitatively in real time using QCM-D. **Figure 5.20** reports typical change in frequency (ΔF) and dissipation (ΔD) data associated with the adsorption of the above-mentioned substances onto the hydrophobic surface. Specifically, pristine GOs revealed no adsorption to the hydrophobic surface as it is evidenced by the very small shift in ΔF value of less than 5 Hz. In contrast, large ΔF shift of about 20-27 Hz for both GO-P1 and GO-P2 is an indicative of a significant adsorption on the surface of the crystal.

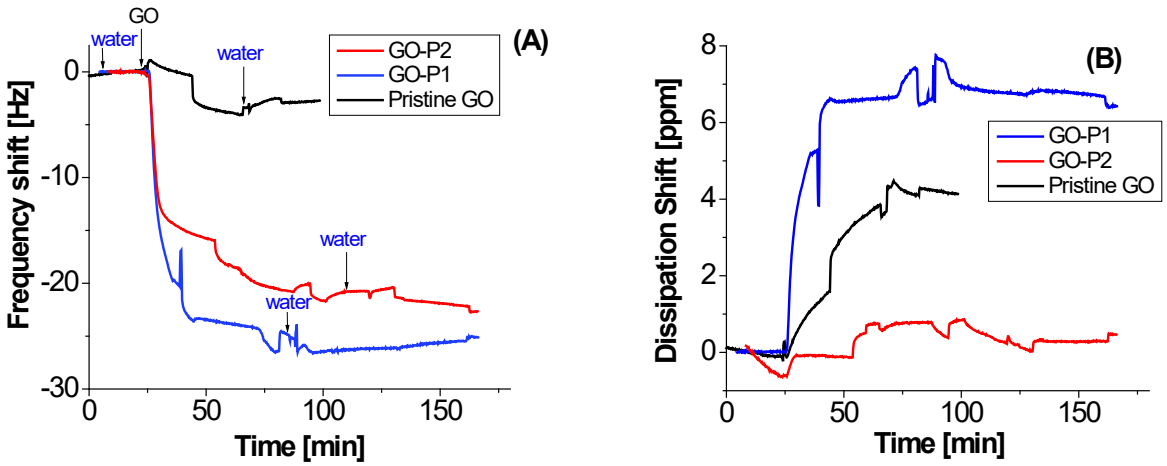

Figure 5.20: Real time QCM-D data of the normalized third overtone. Frequency shifts (A) and dissipation shifts (B) for pristine GO, GO-P1 and GO-P2 adsorption to hydrophobic silane-modified SiO_2/Si substrate.

However, the large dissipation shift seen for the adsorption of GO-P1 is in striking contrast to the lack of dissipation shift for GO-P2. This suggests the intrinsically different structure of the adsorbed layers on the hydrophobic surface.

As stated in **Section 5.2.5**, a reduction in frequency (negative *ΔF* value) provides only rough estimate of the mass of adsorbed material. Therefore, qualitative analysis has been carried out by analyzing time-independent dissipation (*ΔD*) versus frequency (*ΔF*) curves (**Figure 5.21**), known as *ΔD/ΔF or DF* plots [73-74].

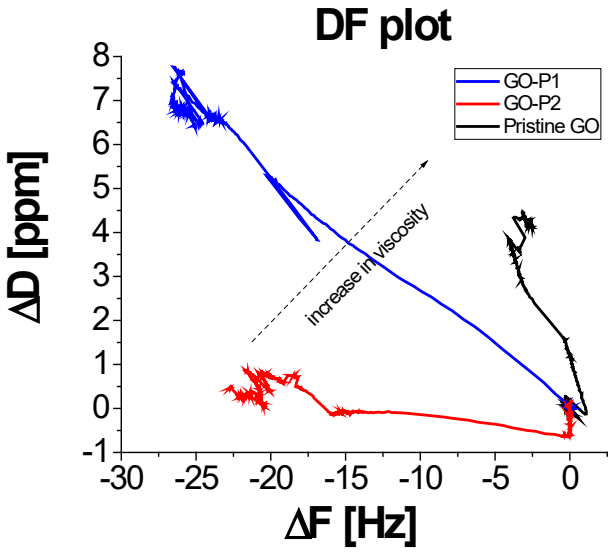

Figure 5.21: Typical ΔD/ΔF plots of adsorbed GO-P1 and GO-P2 layers on a hydrophobic (silane-modified) SiO_2/Si substrate

Changes in *ΔD/ΔF* ratio provided an unambiguous identification of structural differences in surface-adsorbed layers, giving a unique fingerprint of how the conformational state (rigid/nonrigid) of the adsorbed layer evolves with coverage [6, 75]. Consequently, all the above results imply that the GO-P1 forms less compact structure (larger slope in *DF* curve), which via internal friction will cause an increase in the energy dissipation [76]. If to consider the hydrophobic interaction as the primary driving force, such behavior is expected to be

energetically favorable for the adsorption of an amphiphilic molecule/particle onto a hydrophobic surface in an aqueous solution ("hydrophobic effect") [52].

Quantitative analysis of the adsorption

In our next step, we performed a quantitative analysis by applying viscoelastic model to fit *ΔD* and ΔF values for three overtones (3, 5, 7) using SmartFit algorithm in QSense Dfind software (license provided by Biolin Scientific AB [77]). Modeled values of the thickness, shear viscosity and shear elastic modulus for adsorbed GO-P1 and GO-P2 layers were plotted as a function of time and are displayed in **Figure 5.22**.

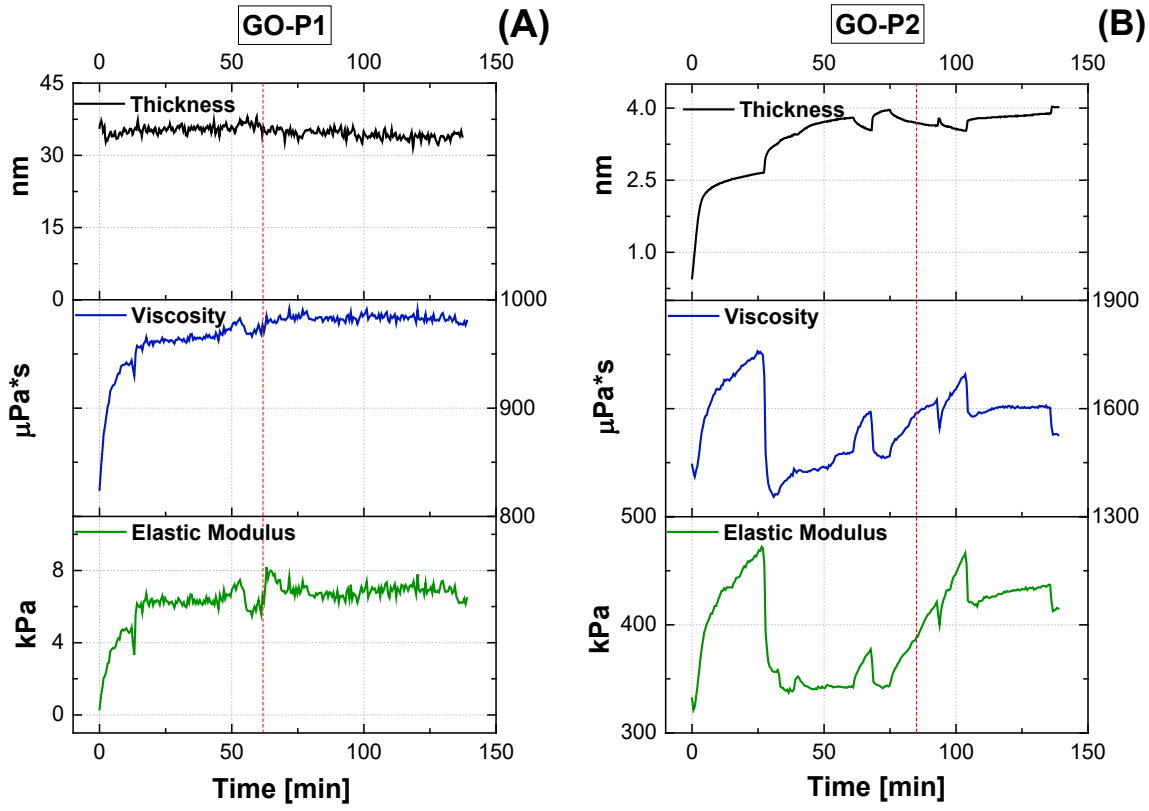

Figure 5.22: Modeled QCM-D results for GO-P1 (A) and GO-P2 (B) adsorbed layers. Red dashed line indicates the time when water was introduced.

We can see from the graphs, QCM-D thickness of adsorbed GO-P1 layer is around 35 nm which is much larger than 3.7 nm of GO-P2 layer. Also, it can be observed that the GO-P2 sheets adsorb in a multilayer fashion which is evident from the step at around 60 minutes. GO-P1 thickness, in contrast, was constant over time of adsorption process.

Equations 5.6, 5.7, and 5.8 were combined and used to estimate the loss angles, $\tan(\delta_L)$, of adsorbed GO-P1 and GO-P2 films at f_0 = 4.95 MHz frequency (**Figure 5.23**). Since $\tan(\delta_l)_{GO-P1} = 4.53 \gg \tan(\delta_l)_{GO-P2} = 0.13$, we can conclude that GO-P1 is loosely attached to the hydrophobic surface and thus reveals predominantly dissipative and viscous mechanical properties while GO-P2 is rigid and stiff.

To complement the QCM-D measurements, AFM was used to investigate and compare the morphology of GO-P1 and GO-P2 sheets after adsorption on hydrophobic QCM-D quartz crystal surface. Obtained images show that GO-P1 is heavily crumpled and scrolled while GO-P2 is just slightly wrinkled. In addition, we can observe multilayer formations of the latter one.

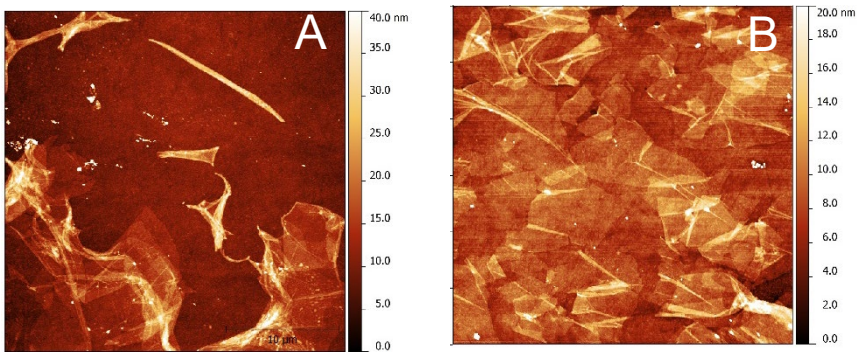

Figure 5.23: GO-P1 (A) and GO-P2 (B) on silane-modified quartz QCM-D crystal.

5.3.9: Morphology of GO-P2 on Polymeric Surfaces

Besides the positive outcome with GO layers deposition on hydrophobic SiO_2/Si substrates we still needed to show that we can achieve the same result on flexible polymeric substrates. As we have hypothesized earlier the formation of GO monolayers on surfaces of various polarity via dip-coating from water will be associated with enhanced hydrophobicity of individual GO flakes through the grafting of amphiphilic P2 copolymer to their surface.

We conducted dip-coating of GO-P2 on pristine Kapton, ultra-high molecular weight polyethylene (UHWPE) and polypropylene films. For instance, it is worth noting that the surface of UHWPE polymer was completely dry after dip-coating step using pristine GO suspension (**Figure 5.24 (left)**). In contrast, after using GO-P2 suspension the entire surface of UHWPE substrate has been uniformly covered ("wetted") with GO-P2-water layer, as shown in **Figure 5.24 (right)**. Herein, it was virtually impossible to obtain a GO film via dip-coating on various polymeric surfaces with pristine GO sheets (unmodified with the copolymer). The AFM images revealed the formation of well-defined GO monolayers on the flexible hydrophobic substrates (**Figure 5.25 (right)**).

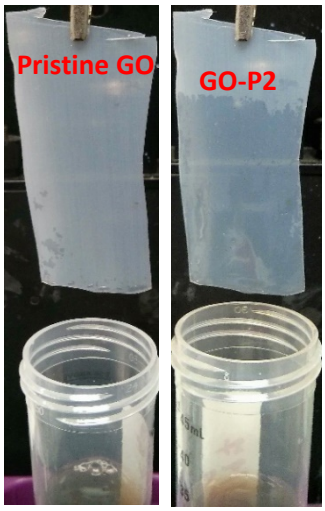

Figure 5.24: Photograph UHWPE (125 µm) film dipcoated in pristine GO solution (left) and GO-P2 solution (right).

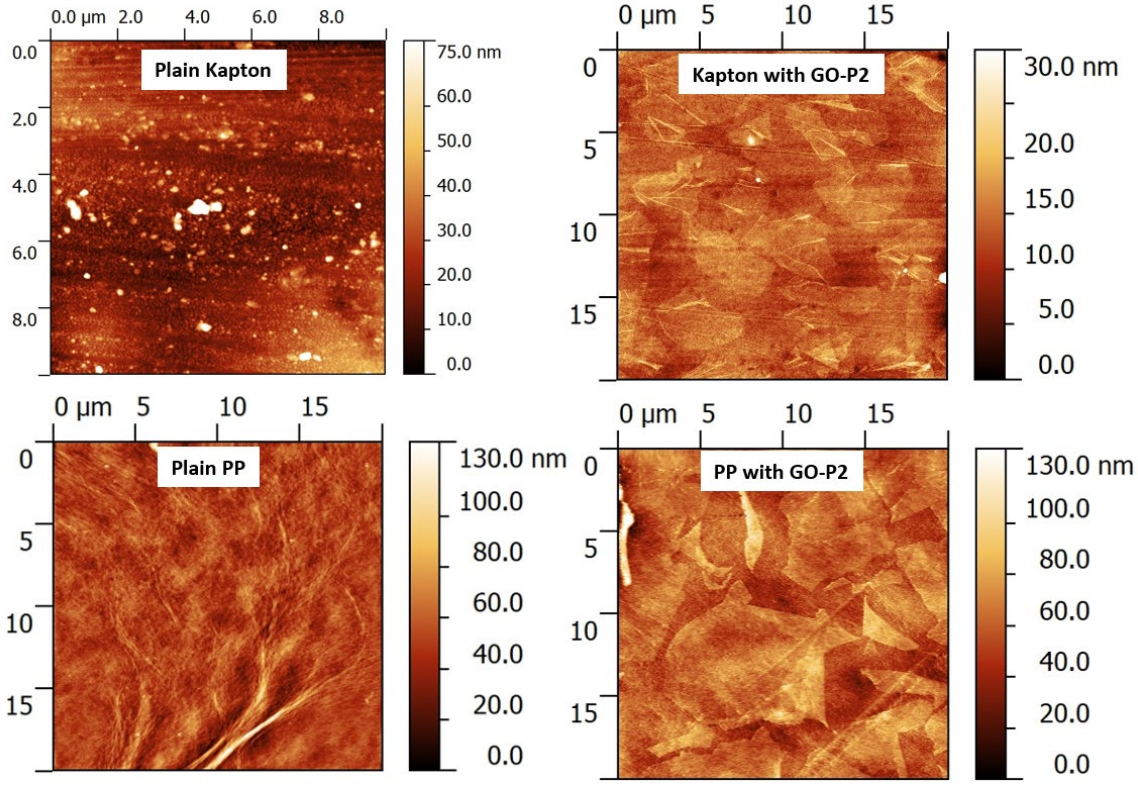

Figure 5.25: AFM images of plain polymeric substrates (left) and polymeric substrates covered with GO-P2 layer (right).

5.4: Conclusions

The following conclusions can be made as a result of the study reported in Chapter 5:

- The weaker van-der Waals attraction between GO-P1 and hydrophobic substrates allowed GO-P1 to fold and scroll due to molecular interactions with water.
- Crumple formations depend on the original size of the sheet and the compression/capillary forces acting on the GO sheet.

- Enhanced hydrophobic-hydrophobic interaction allowed to achieve formation of uniform layers on both hydrophilic and hydrophobic surfaces by using more hydrophobic P2 copolymer.
- It was confirmed experimentally that P2 copolymer can be readily grafted to GO surface through the non-condensation reactions of epoxy functional groups with functional groups located on the GO surface.
- On contrary to GO-P1, GO-P2 formed a dense and well-defined monolayer on the hydrophobic surfaces of various polarity (surface coverage > 85 %) as a result of the dip-coating.
- The attraction of GO-P2 and hydrophobic substrate is too strong which prevented GO-P2 sheets from folding.

5.5: References

1. Liu, G.; Zhang, G., Basic Principles of QCM-D. In *QCM-D Studies on Polymer Behavior at Interfaces*, Liu, G.; Zhang, G., Eds. Springer Berlin Heidelberg: Berlin, Heidelberg, 2013; pp 1-8.

2. Sauerbrey, G., Verwendung von Schwingquarzen zur Wägung dünner Schichten und zur Mikrowägung. *Zeitschrift für Physik* **1959,** *155* (2), 206-222.

3. Hovgaard, M. B.; Dong, M. D.; Otzen, D. E.; Besenbacher, F., Quartz crystal microbalance studies of multilayer glucagon fibrillation at the solid-liquid interface. *Biophysical Journal* **2007,** *93* (6), 2162-2169.

4. Ramos, J. J. I.; Moya, S. E., Water Content of Hydrated Polymer Brushes Measured by an In Situ Combination of a Quartz Crystal Microbalance with Dissipation Monitoring and Spectroscopic Ellipsometry. *Macromol. Rapid Commun.* **2011,** *32* (24), 1972-1978.

5. Yahiro, C.; Annaka, M.; Kikuchi, A.; Okano, T., *Collapse and swelling of thermosensitive poly(N-isopropylacrylamide) brushes monitored by a quartz crystal microbalance*. Materials Research Society Japan-Mrs-J: Tokyo, 2007; Vol. 32, p 807-810.

6. Weber, N.; Pesnell, A.; Bolikal, D.; Zeltinger, J.; Kohn, J., Viscoelastic properties of fibrinogen adsorbed to the surface of biomaterials used in blood-contacting medical devices. *Langmuir* **2007,** *23* (6), 3298-3304.

7. Reimhult, E.; Larsson, C.; Kasemo, B.; Hook, F., Simultaneous surface plasmon resonance and quartz crystal microbalance with dissipation monitoring measurements of biomolecular adsorption events involving structural transformations and variations in coupled water. *Anal. Chem.* **2004,** *76* (24), 7211-7220.

8. Garg, A.; Heflin, J. R.; Gibson, H. W.; Davis, R. M., Study of Film Structure and Adsorption Kinetics of Polyelectrolyte Multilayer Films: Effect of pH and Polymer Concentration. *Langmuir* **2008,** *24* (19), 10887-10894.

9. https://www.biolinscientific.com/qsense/software/

10. Muller, M. T.; Yan, X. P.; Lee, S. W.; Perry, S. S.; Spencer, N. D., Lubrication properties of a brushlike copolymer as a function of the amount of solvent absorbed within the brush. *Macromolecules* **2005,** *38* (13), 5706-5713.

11. Limpoco, F. T. J., *Nanotribology of Polymer Brushes Investigated by Atomic Force Microscopy*. University of Florida: 2009.

12. O'Neal, J. T.; Dai, E. Y.; Zhang, Y.; Clark, K. B.; Wilcox, K. G.; George, I. M.; Ramasamy, N. E.; Enriquez, D.; Batys, P.; Sammalkorpi, M.; Lutkenhaus, J. L., QCM-D Investigation of Swelling Behavior of Layer-by-Layer Thin Films upon Exposure to Monovalent Ions. *Langmuir* **2018,** *34* (3), 999-1009.

13. Vuoriluoto, M.; Orelma, H.; Johansson, L.-S.; Zhu, B.; Poutanen, M.; Walther, A.; Laine, J.; Rojas, O. J., Effect of Molecular Architecture of PDMAEMA–POEGMA Random and Block Copolymers on Their Adsorption on Regenerated and Anionic Nanocelluloses and Evidence of Interfacial Water Expulsion. *The Journal of Physical Chemistry B* **2015,** *119* (49), 15275-15286.

14. González, B.; Calvar, N.; Gómez, E.; Domínguez, Á., Density, dynamic viscosity, and derived properties of binary mixtures of methanol or ethanol with water, ethyl acetate, and methyl acetate at T=(293.15, 298.15, and 303.15)K. *The Journal of Chemical Thermodynamics* **2007,** *39* (12), 1578-1588.

15. Zhong, J.; Chinn, J.; Roberts, C. B.; Ashurst, W. R., Vapor-Phase Deposited Chlorosilane-Based Self-Assembled Monolayers on Various Substrates for Thermal Stability Analysis. *Industrial & Engineering Chemistry Research* **2017,** *56* (18), 5239-5252.

16. Galabura, Yuriy, "SYNTHESIS AND CHARACTERIZATION OF NANOSCALE POLYMER FILMS GRAFTED TO METAL SURFACES" (2014). All Dissertations. 1300.

https://tigerprints.clemson.edu/all_dissertations/1300

17. Luzinov, I.; Julthongpiput, D.; Liebmann-Vinson, A.; Cregger, T.; Foster, M. D.; Tsukruk, V. V., Epoxy-Terminated Self-Assembled Monolayers: Molecular Glues for Polymer Layers. L*angmuir 2***000,** 1*6* (2), 504-516.

18. Borodinov, N.; Gil, D.; Savchak, M.; Gross, C. E.; Yadavalli, N. S.; Ma, R.; Tsukruk, V. V.; Minko, S.; Vertegel, A.; Luzinov, I., En Route to Practicality of the Polymer Grafting Technology: One-Step Interfacial Modification with Amphiphilic Molecular Brushes. A*CS Applied Materials & Interfaces 2***018,** 1*0* (16), 13941-13952.

19. JOHANNSMANN, D. (2015). The quartz crystal microbalance in soft matter research: fundamentals and modeling. http://public.eblib.com/choice/publicfullrecord.aspx?p=1783082.

20. Fried, J. R., P*olymer Science and Technology.* 3rd ed.; Prentice Hall: Upper Saddle River, NJ, 2014; p 663.

21. http://www.dupont.com/content/dam/dupont/products-and-services/membranes-and-films/polyimde-films/documents/DEC-Kapton-summary-of-properties.pdf (accessed 1/16/2018).

22. Owens, D. K.; Wendt, R. C., Estimation of the surface free energy of polymers. J*ournal of Applied Polymer Science 1***969,** 1*3* (8), 1741-1747.

23. Janczuk, B.; Wojcik, W.; Zdziennicka, A.; Bruque, J. M. Components of the surface free energy of low rank coals in the presence of n-alkanes, Powder Technology 1996, 86, 229-238

24. Deng, S.; Berry, V., Wrinkled, rippled and crumpled graphene: an overview of formation mechanism, electronic properties, and applications. M*aterials Today 2***016,** 1*9* (4), 197-212.

25. Mpourmpakis, G.; Tylianakis, E.; Froudakis, G. E., Carbon Nanoscrolls: A Promising Material for Hydrogen Storage. N*ano Letters 2***007,** 7 (7), 1893-1897.

26. Xie, X.; Ju, L.; Feng, X.; Sun, Y.; Zhou, R.; Liu, K.; Fan, S.; Li, Q.; Jiang, K., Controlled Fabrication of High-Quality Carbon Nanoscrolls from Monolayer Graphene. N*ano Letters 2***009,** 9 (7), 2565-2570.

27. Gao, Y.; Chen, X.; Xu, H.; Zou, Y.; Gu, R.; Xu, M.; Jen, A. K. Y.; Chen, H., Highly-efficient fabrication of nanoscrolls from functionalized graphene oxide by Langmuir–Blodgett method. C*arbon 2***010,** 4*8* (15), 4475-4482.

28. Li, H.; Wu, J.; Qi, X.; He, Q.; Liusman, C.; Lu, G.; Zhou, X.; Zhang, H., Graphene Oxide Scrolls on Hydrophobic Substrates Fabricated by Molecular Combing and Their Application in Gas Sensing. S*mall 2***013,** 9 (3), 382-386.

29. Wang, W. N.; Jiang, Y.; Biswas, P., Evaporation-Induced Crumpling of Graphene Oxide Nanosheets in Aerosolized Droplets: Confinement Force Relationship. J*ournal of Physical Chemistry Letters 2***012,** 3 (21), 3228-3233.

30. Becton, M.; Zhang, L. Y.; Wang, X. Q., Mechanics of graphyne crumpling. P*hysical Chemistry Chemical Physics 2***014,** 1*6* (34), 18233-18240.

31. Ko, H.; Peleshanko, S.; Tsukruk, V. V., Combing and Bending of Carbon Nanotube Arrays with Confined Microfluidic Flow on Patterned Surfaces. T*he Journal of Physical Chemistry B 2***004,** 1*08* (14), 4385-4393.

32. Poulin, P.; Jalili, R.; Neri, W.; Nallet, F.; Divoux, T.; Colin, A.; Aboutalebi, S. H.; Wallace, G.; Zakri, C., Superflexibility of graphene oxide. P*roceedings of the National Academy of Sciences of the United States of America 2***016,** 1*13* (40), 11088-11093.

33. Wu, J.; Yang, J.; Huang, Y.; Li, H.; Fan, Z.; Liu, J.; Cao, X.; Huang, X.; Huang, W.; Zhang, H., Graphene Oxide Scroll Meshes Prepared by Molecular Combing for Transparent and Flexible Electrodes. A*dvanced Materials Technologies 2***017,** 2 (2), 1600231-n/a.

34. Meyer, E. E.; Rosenberg, K. J.; Israelachvili, J., Recent progress in understanding hydrophobic interactions. P*roceedings of the National Academy of Sciences 2***006,** 1*03* (43), 15739.

35. Rossi, M. P.; Gogotsi, Y.; Kornev, K. G., Deformation of carbon nanotubes by exposure to water vapor. L*angmuir 2***009,** 2*5* (5), 2804-10.

36. Kornev, K. G.; Srolovitz, D. J., Surface stress-driven instabilities of a free film. A*pplied Physics Letters 2***004,** 8*5* (13), 2487-2489.

37. Park, S. K.; Gao, X. L., Bernoulli–Euler beam model based on a modified couple stress theory. J*ournal of Micromechanics and Microengineering 2***006,** 1*6* (11), 2355-2359.

38. Wang, Y.; Liao, J.; McBride, S. P.; Efrati, E.; Lin, X. M.; Jaeger, H. M., Strong Resistance to Bending Observed for Nanoparticle Membranes. N*ano Lett 2***015,** 1*5* (10), 6732-7.

39. Poulin, P.; Jalili, R.; Neri, W.; Nallet, F.; Divoux, T.; Colin, A.; Aboutalebi, S. H.; Wallace, G.; Zakri, C., Superflexibility of graphene oxide. P*roceedings of the National Academy of Sciences 2***016,** 1*13* (40), 11088-11093.

40. Yang, F.; Chong, A. C. M.; Lam, D. C. C.; Tong, P., Couple stress based strain gradient theory for elasticity. I*nternational Journal of Solids and Structures 2***002,** 3*9* (10), 2731-2743.

41. Lu, Q.; Arroyo, M.; Huang, R., Elastic bending modulus of monolayer graphene. J. *Phys. D-Appl. Phys. 2***009,** 4*2* (10), 6.

42. Wan, J.; Jiang, J.-W.; Park, H. S., Negative Poisson's ratio in graphene oxide. N*anoscale 2***017,** 9 (11), 4007-4012.

43. Suk, J. W.; Piner, R. D.; An, J.; Ruoff, R. S., Mechanical Properties of Monolayer Graphene Oxide. A*CS Nano 2***010,** 4 (11), 6557-6564.

44. Maranganti, R.; Sharma, P., Length Scales at which Classical Elasticity Breaks Down for Various Materials. P*hysical Review Letters 2***007,** 9*8* (19), 195504.

45. Py, C.; Reverdy, P.; Doppler, L.; Bico, J.; Roman, B.; Baroud, C. N., Capillary Origami: Spontaneous Wrapping of a Droplet with an Elastic Sheet. P*hysical Review Letters 2***007,** 9*8* (15), 156103.

46. Lee, J. H.; Kopeckova, P.; Kopecek, J.; Andrade, J. D., Surface properties of copolymers of alkyl methacrylates with, methoxy (polyethylene oxide) metiiacrylates and their application as protein-resistant coatings. B*iomaterials 1***990,** 1*1* (7), 455-464.

47. Li, X.; Zhao, T.; Wang, K.; Yang, Y.; Wei, J.; Kang, F.; Wu, D.; Zhu, H., Directly drawing self-assembled, porous, and monolithic graphene fiber from chemical vapor deposition grown graphene film and its electrochemical properties. L*angmuir 2***011,** 2*7* (19), 12164-71.

48. Wang, W.-N.; Jiang, Y.; Biswas, P., Evaporation-Induced Crumpling of Graphene Oxide Nanosheets in Aerosolized Droplets: Confinement Force Relationship. T*he Journal of Physical Chemistry Letters 2***012,** 3 (21), 3228-3233.

49. Ma, X.; Zachariah, M. R.; Zangmeister, C. D., Crumpled Nanopaper from Graphene Oxide. N*ano Letters 2***012,** 1*2* (1), 486-489.

50. Xu, L.; Shi, T.; Dutta, P. K.; An, L., Rim instability by solvent-induced dewetting. J *Chem Phys 2***007,** 1*27* (14), 144704.

51. Vazquez, G.; Alvarez, E.; Navaza, J. M., SURFACE-TENSION OF ALCOHOL PLUS WATER FROM 20-DEGREES-C TO 50-DEGREES-C. J. *Chem. Eng. Data 1***995,** 4*0* (3), 611-614.

52. van Oss, C. J.; Giese, R. F., Role of the Properties and Structure of Liquid Water in Colloidal and Interfacial Systems. J*ournal of Dispersion Science and Technology 2***005,** 2*5* (5), 631-655.

53. Bellido, E. P.; Seminario, J. M., Molecular Dynamics Simulations of Folding of Supported Graphene. T*he Journal of Physical Chemistry C 2***010,** 1*14* (51), 22472-22477.

54. Craig, M.; Bordes, R.; Holmberg, K., Polypeptide multilayer self-assembly and enzymatic degradation on tailored gold surfaces studied by QCM-D. S*oft Matter 2***012,** 8 (17), 4788-4794.

55. Song, S.; Peng, C., Viscosities of Binary and Ternary Mixtures of Water, Alcohol, Acetone, and Hexane. J*ournal of Dispersion Science and Technology 2***008,** 2*9* (10), 1367-1372.

56. Bao, W.; Miao, F.; Chen, Z.; Zhang, H.; Jang, W.; Dames, C.; Lau, C. N., Controlled ripple texturing of suspended graphene and ultrathin graphite membranes. N*ature Nanotechnology 2***009,** 4*,* 562.

57. Luo, J. Y.; Jang, H. D.; Sun, T.; Xiao, L.; He, Z.; Katsoulidis, A. P.; Kanatzidis, M. G.; Gibson, J. M.; Huang, J. X., Compression and Aggregation-Resistant Particles of Crumpled Soft Sheets. A*cs Nano 2***011,** 5 (11), 8943-8949.

58. Philippova, O. E.; Kuchanov, S. I.; Topchieva, I. N.; Kabanov, V. A., Hydrogen bonds in dilute solutions of poly(ethylene glycol). M*acromolecules 1***985,** 1*8* (8), 1628-1633.

59. Dormidontova, E. E., Role of Competitive PEO−Water and Water−Water Hydrogen Bonding in Aqueous Solution PEO Behavior. M*acromolecules 2***002,** 3*5* (3), 987-1001.

60. Chen, Y.; Guo, F.; Jachak, A.; Kim, S.-P.; Datta, D.; Liu, J.; Kulaots, I.; Vaslet, C.; Jang, H. D.; Huang, J.; Kane, A.; Shenoy, V. B.; Hurt, R. H., Aerosol Synthesis of Cargo-Filled Graphene Nanosacks. N*ano Letters 2***012,** 1*2* (4), 1996-2002.

61. Koenig, S. P.; Boddeti, N. G.; Dunn, M. L.; Bunch, J. S., Ultrastrong adhesion of graphene membranes. N*ature Nanotechnology 2***011,** 6*,* 543.

62. Meyer, E. E.; Rosenberg, K. J.; Israelachvili, J., Recent progress in understanding hydrophobic interactions. P*roc Natl Acad Sci U S A 2***006,** 1*03* (43), 15739-46.

63. Roghani-Mamaqani, H.; Khezri, K., Polystyrene-attached graphene nanolayers by reversible addition-fragmentation chain transfer polymerization: a grafting from epoxy groups with various densities. J*ournal of Polymer Research 2***016,** 2*3* (9).

64. Zdyrko, B.; Luzinov, I., Polymer Brushes by the "Grafting to" Method. M*acromol. Rapid Commun. 2***011,** 3*2* (12), 859-869.

65. Wu, X.; Li, S.; Zhao, Y.; Tang, Y.; Liu, J.; Guo, X.; Wu, D.; He, G., Using a layer-by-layer assembly method to fabricate a uniform and conductive nitrogen-doped graphene anode for indium-tin oxide-free organic light-emitting diodes. A*CS Appl Mater Interfaces 2***014,** 6 (18), 15753-9.

66. Jung, I.; Dikin, D.; Park, S.; Cai, W.; Mielke, S. L.; Ruoff, R. S., Effect of Water Vapor on Electrical Properties of Individual Reduced Graphene Oxide Sheets. J. *Phys. Chem. C 2***008,** 1*12* (51), 20264-20268.

67. Stankovich, S.; Dikin, D. A.; Piner, R. D.; Kohlhaas, K. A.; Kleinhammes, A.; Jia, Y.; Wu, Y.; Nguyen, S. T.; Ruoff, R. S., Synthesis of graphene-based nanosheets via chemical reduction of exfoliated graphite oxide. C*arbon 2***007,** 4*5* (7), 1558-1565.

68. Wang, C. Y.; Feng, L. L.; Yang, H. Z.; Xin, G. B.; Li, W.; Zheng, J.; Tian, W. H.; Li, X. G., Graphene oxide stabilized polyethylene glycol for heat storage. P*hys. Chem. Chem. Phys. 2***012,** 1*4* (38), 13233-13238.

69. Min, X.; Fang, M.; Huang, Z.; Liu, Y. g.; Huang, Y.; Wen, R.; Qian, T.; Wu, X., Enhanced thermal properties of novel shape-stabilized PEG composite phase change

materials with radial mesoporous silica sphere for thermal energy storage. S*cientific Reports 2***015,** 5*,* 12964.

70. Kulkarni, D. D.; Kim, S.; Chyasnavichyus, M.; Hu, K.; Fedorov, A. G.; Tsukruk, V. V., Chemical Reduction of Individual Graphene Oxide Sheets as Revealed by Electrostatic Force Microscopy. J. *Am. Chem. Soc. 2***014,** 1*36* (18), 6546-6549.

71. Zhao, J. P.; Pei, S. F.; Ren, W. C.; Gao, L. B.; Cheng, H. M., Efficient Preparation of Large-Area Graphene Oxide Sheets for Transparent Conductive Films. A*cs Nano 2***010,** 4 (9), 5245-5252.

72. Rozada, R.; Paredes, J. I.; Lopez, M. J.; Villar-Rodil, S.; Cabria, I.; Alonso, J. A.; Martinez-Alonso, A.; Tascon, J. M. D., From graphene oxide to pristine graphene: revealing the inner workings of the full structural restoration. N*anoscale 2***015,** 7 (6), 2374-2390.

73. Fatisson, J.; Azari, F.; Tufenkji, N., Real-time QCM-D monitoring of cellular responses to different cytomorphic agents. B*iosensors and Bioelectronics 2***011,** *26* (7), 3207-3212.

74. Watarai, E.; Matsuno, R.; Konno, T.; Ishihara, K.; Takai, M., QCM-D analysis of material–cell interactions targeting a single cell during initial cell attachment. S*ensors and Actuators B: Chemical 2***012,** 1*71-172,* 1297-1302.

75. Hovgaard, M. B.; Dong, M.; Otzen, D. E.; Besenbacher, F., Quartz Crystal Microbalance Studies of Multilayer Glucagon Fibrillation at the Solid-Liquid Interface. B*iophysical Journal 93* (6), 2162-2169.

76. Keller, C. A.; Kasemo, B., Surface specific kinetics of lipid vesicle adsorption measured with a quartz crystal microbalance. B*iophysical journal 1***998,** 7*5* (3), 1397-1402.

77. https://www.biolinscientific.com/qsense/software/

CHAPTER SIX

FABRICATION AND CHARACTERIZATION OF ELECTRICALLY CONDUCTIVE rGO FILMS ON FLEXIBLE POLYMERIC SUBSTRATES

6.1: Introduction

It was demonstrated (**Chapter 5**) that GO-P2 layers can be directly deposited on hydrophobic Si (modified with silane) and polymeric substrates (UHWPE, PP, Kapton). The next question arises: Is it possible to make such GO-covered polymer films electrically conductive? In this part of the work, the results on the study of opto-electrical and mechanical properties of chemically reduced GO-P2 nanoscale multilayers deposited on polymer films are presented. Specifically, we have used the acidic agent, hydroiodic (HI) acid, to efficiently reduce GO-P2 films following the procedure described in Ref. [1]. This chapter mainly consists of the two parts: (1) chemically reduced rGO-P2 layers on model hydrophobic Si substrate and (2) rGO-P2 layers on various polymeric substrates.

First, the morphology, structure and composition of rGO-P2 films on model hydrophobic Si substrates were investigated by Raman spectroscopy, XPS, X-ray diffraction (XRD), optical microscopy, SEM and AFM. Second, the morphological properties of rGO-P2 films on flexible substrates were studied by means of optical microscopy, SEM and AFM. In brief, optical microscopy and scanning electron microscopy confirmed that rGO-P2 layers had preserved their integrity and structure on a larger scale upon chemical treatment. In addition, we studied the influence of GO-P2 solution concentration (final layer thickness) on electrical conductivity. We have shown that obtained rGO-P2 films can achieve relatively high electrical conductivity of ~60 S/cm

after chemical reduction by hydrogen iodine acid [1] on both model hydrophobic Si and polymeric substrates.

In our next step, we investigated the electro-mechanical response and life-cycle durability of rGO-P2 films deposited on various polymeric substrates. To better understand the electro-mechanical behavior of rGO-P2 layers on polymer films we performed bending stress analysis with different radii of curvature based on the Finite Element Analysis (FEA) approach. Finally, we demonstrated the operation of a light emitting diode (LED) in a circuit with a bent and suspended transparent UHWPE film coated with rGO-P2 (rGO/UHWPE) as part of the conductive circuit wiring [2].

6.2: Experimental

6.2.1. Chemical Reduction of GO-P2 layers

The reduction of GO-P2 layers deposited on Si wafer and polymeric substrates was performed by immersion GO films into a 57% HI acid solution for 1 hour in a beaker that

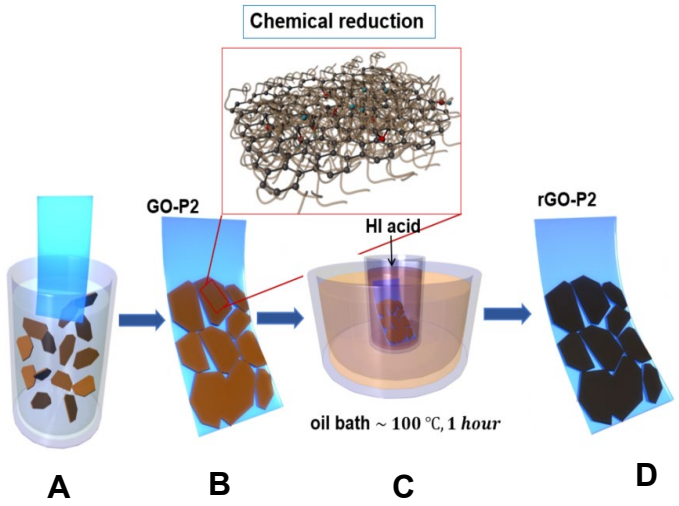

Figure 6.1. Schematic representation of the proposed workflow for fabrication of conductive GO-based flexible films. **A):** deposition of a monolayer of GO sheets enveloped with P2 polymer layer by dip-coating. **B):** final GO layer on polymeric substrate. **C):** chemical reduction process. **D):** rGO-P2 film after chemical reduction.

was placed in a thermostatted oil bath (**Figure 6.1**).

The temperature of HI acid was maintained at 100 ºC. Next, the samples were placed in saturated water solution of sodium bicarbonate to neutralize the residue of acid followed by thorough rinsing with DI water. Finally, stream of ultra-high purity nitrogen has been used to dry samples. It is worth pointing out that HI treated rGO-P2 films partially delaminated from the hydrophobic silicon while their integrity was intact when deposited on polymeric substrates.

6.2.2: Materials Characterization

Raman and XPS (see **Sections 3.2.4** and **4.2.2** for more details) were used to study the change in microstructure and chemical composition of rGO-P2 layers after HI reduction. An undoped Si with 2 nm SiO_2 was used as a substrate.

The crystal structure of HI-reduced rGO-P2 film was determined using an Ultima IV, Rigaku Corp. XRD. The diffraction pattern was collected from 10^{o} to 70^{o} at 40 kV beam intensity and scan speed of 1 deg./min. The measurement was conducted by Colin McMillen from Department of Chemistry at Clemson University.

AFM, UV/Vis spectrometer (see **Sections 3.2.9** and **4.2.2** for more details), variable pressure scanning electron microscope (SEM) (Hitachi SU-6600, acceleration voltage of 10 kV) and optical microscope (HUVITZ HRM-300) were used as means to investigate morphology, microstructure and measure transparency of rGO-P2 layers. To characterize rGO-P2 layers on polymeric substrates with AFM we used silicon substrate with a thin

adhesive layer as a support to which the specimen was attached. The roughness and thickness of rGO-P2 layers on plastics were analyzed using Gwyddion 2.37 software.

To measure conductivity of the rGO-P2 films on plastics, we used silver paste to form two contacts. Then, the sample with silver paste on top was subject to temperature treatment at 80 ºC in ambient for at least 1 hour. For 6 μm thin polypropylene substrate both ends needed to be fixated in order to prevent buckling of the film when silver paste was drying. Current-voltage (I-V) curves were produced using two-point probe configuration described in **Section 4.2.1**.

6.2.3. Electro-Mechanical Response under Compression/Bending

The electro-mechanical responses and life-cycle durability of all fabricated samples were measured by a home-made testing platform (**Figure 6.2**). Computer-1 was connected to single-axis microstep motion controller (SMC-series Pollux ^{3}) to program movements of the motion platform. The electrical signals of film under compressive bending were recorded using a digital source meter (BK Precision 5492) and saved into Excel on computer-2. Digital camera has been used to record profile images of bent film.

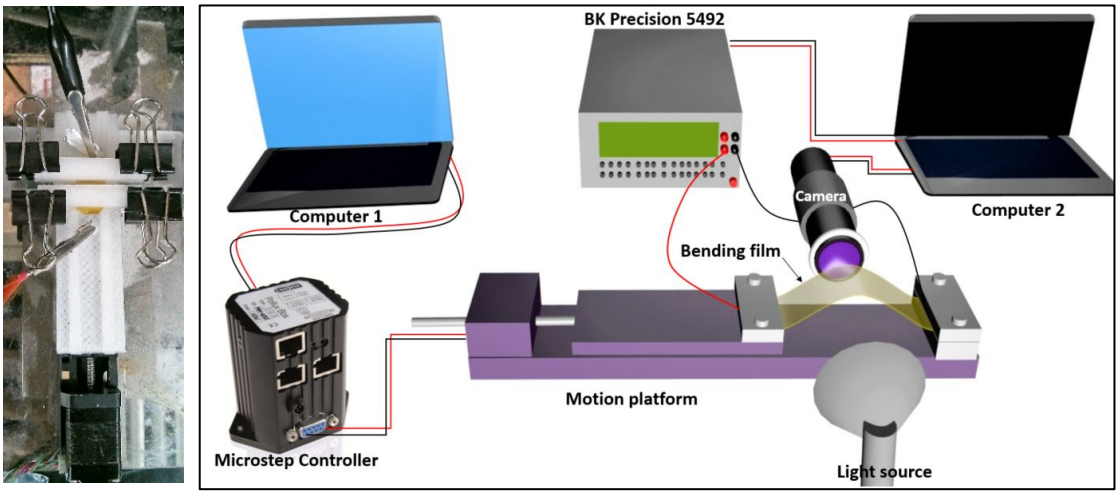

Figure 6.2. Home-made testing platform (left) and schematic of the compressive/bending setup (right).

All measurements were conducted in Dr. Kornev's laboratory with the help of Dr. Chengzi Zhang and Mark Anayee.

The radius of the film profile at a particular point of bending was defined as the radius of the approximating circle using "Three-Point-Circular ROI" plugin [4] in ImageJ software, as shown in **Figure 6.3 (right)**. In addition, film profile calculations based on Euler-Bernoulli model for beams were conducted by Dr. Arthur Salamatin under the guidance of Prof. K. Kornev. The results of the calculations are described in detail in the **Appendix (Figure A13** and **Table A4)**.

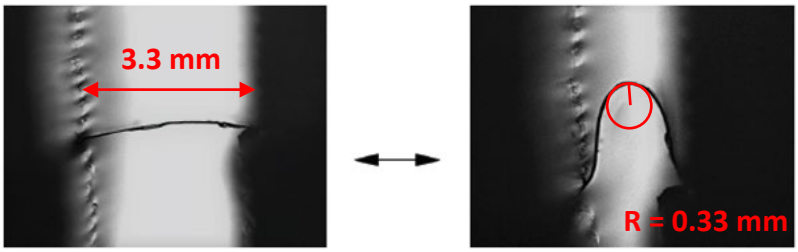

Figure 6.3. Photograph of rGO/Kapton film in flat (left) and bent (right) state.

6.2.4. Electro-Mechanical Response under Tensile Strain

The setup for electromechanical tensile testing is shown in **Figure 6.4**. The two-point probe measurement configuration was used. Many previous studies emphasized that the geometry of the resistance measurement setup may contribute to the measured resistance[5-6].

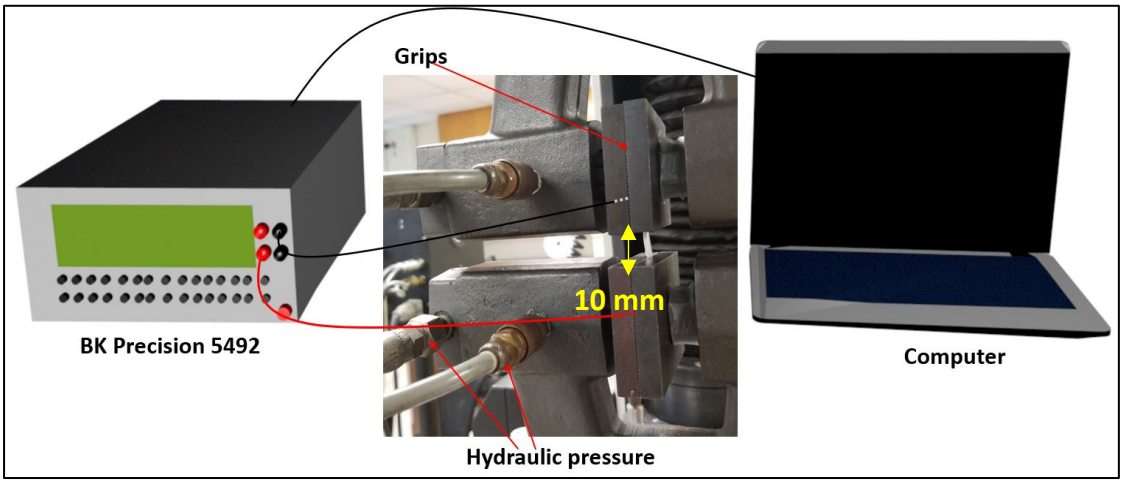

Figure 6.4. Schematic of the tensile strain measurement system.

Specifically, contacts should be introduced into the clamps or grips that hold the sample during straining [5]. Tensiometer (Instron 1125) with 5000 N load cell has been used.

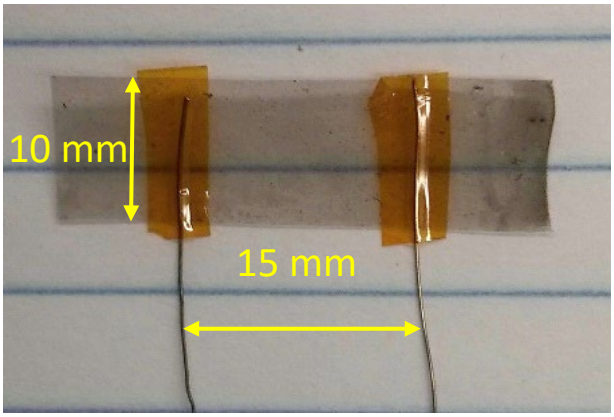

Figure 6.5. Photograph of a transparent double-sided rGO/UHWPE film.

In addition, hydraulic grips (15000 psi) with rubberized inner faces were used to prevent slippage of the sample. UHWPE sample with rGO-P2 (~6 nm) film on top and sheet resistance of 2.3 MΩ/sq was selected. Razor-blade was used to cut a rectangular sample with a length of 33 mm and a width of 10 mm (**Figure 6.5**). Two nickel-plated copper wires were directly attached to the film with the help of Kapton tape at 15 mm separation distance. The initial distance between two Instron's jaws was 10 mm (gage length), as illustrated in **Figure 6.4**. The experiment was performed at strain rate of 0.05 $(mm/mm)min^{-1}$.

It is important to note that all conductive films were coated with rGO on both sides, therefore each specimen has been trimmed from all four sides to make sure that electrical signal is acquired on one side only.

6.2.5. Simulation of Mechanical Stresses using Finite Element Analysis (FEA)

To provide additional insight into the mechanical properties of rGO-P2 layers on polymeric substrates, we performed a finite element analysis of the film/substrate system. The purpose of this study was twofold: (1) to investigate the effect of curvature and substrate thickness on the bending stresses generated in uniform films of rGO-P2 films deposited on PP/Kapton/UHWPE substrates and (2) to find the correlation between the resistance change and bending stresses.

Since our bent films assume very complex meander-like/sine-generated shape upon deformation it becomes increasingly difficult to find the reliable analytical formulae to describe such mechanical behavior [7]. Thus, the finite element analysis (FEA) [8] was used

for mapping field variables such stresses and strains that originate when simulated forces or deformations (compression, bending, stretching, etc.) are applied to modeled system. For this we used commercially available ANSYS APDL 15.0 [9]. Each FEA model is discretized into many small pieces – "elements". Each element has several nodes with finite degree of freedom and analysis is performed for every node. In every case FEA analysis procedure involves several steps: (1) defining the type of problem and choosing appropriate type of element, (2) meshing the analysis model, (3) applying the boundary conditions and loads, (5) solving the problem, and (6) results postprocessing and interpretation.

The element used in the bending stress analysis is Shell 181, which is well suitable for thin-wall structure materials (2D materials) [1011]. In our virtual model we used one shell with two layers: polymeric substrate as layer one and rGO as layer two. The polymeric substrate was modeled as isotropic material, whereas rGO film was considered as orthotropic. As the rGO film conforms with the substrate the Poisson's ratio of the substrate was taken for stress simulations in rGO films. All sample dimensions were the same as in experiment. We used the following parameters for the Kapton film: Young's modulus of (2.9 ± 0.2) GPa, Poisson ratio of 0.34 and thickness of 25 μm [12]; UHWPE: Young's modulus – (0.6 ± 0.1) GPa, Poisson ratio - 0.46 and thickness - 125 μm [13]. For rGO layer the following parameters were used: $E_x = E_y = 600$ GPa, $E_z = 80$ GPa, where E_x, E_y and E_z – is in-plane and out-of-plane Young's moduli. Young's moduli values for substrates were found from slopes of linear portion of stress-strain curves following the AATCC D-882 procedure, as shown in the **Appendix** (**Figure A14**). The rGO moduli were estimated basing on Ref.[14] from (using XRD diffractometer) interlayer distance in our rGO films

(0.41 nm) (**Section 6.3.1, Figure 6.11**). Poisson ratio was considered to be the same as for graphene (~0.21[15]).

Figure 6.6 shows the example of FEA simulations for rGO-P2/Kapton (rGO/Kapton) film. According to the simulations, the highest stresses developed in the

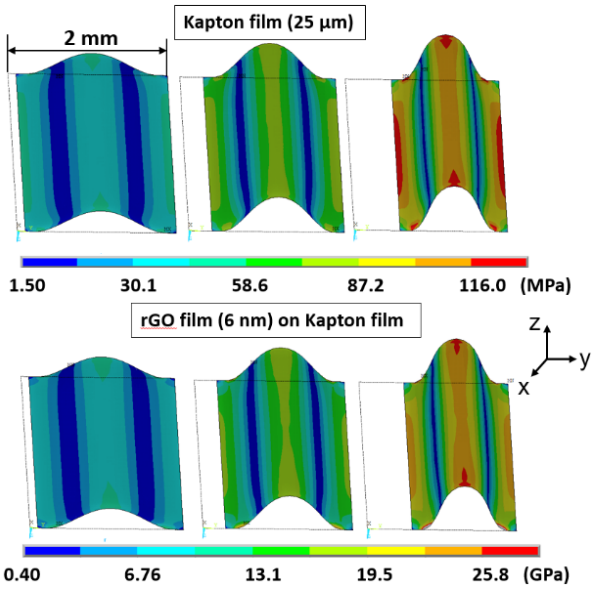

Figure 6.6. The example of FEA simulation. The von Mises stress distribution in rGO-P2/Kapton (rGO/Kapton) film versus curvature.

Kapton film are on the level of 100 MPa which is significantly lower than its tensile strength, 231 MPa [12]. For rGO-P2 on Kapton stresses are in the range of 0.4-20GPa.

6.2.6. Estimation of Young's Modulus of rGO-P2 Film

In order to analyze the stresses in rGO films we need to estimate its elastic modulus. As demonstrated elsewhere[16], the ideal graphene sheet has its Young's modulus around 1 TPa. However, this value drastically decreases as graphene gets converted to GO.

Numerous research has been done to determine the elastic properties of GO and rGO layered films. For example, Rioboo et al [14] quantified the anisotropic behavior of the elastic modulus of thermally reduced GO few-layer films and confirmed that both out-of-plane/transverse and in-plane/longitudinal elastic moduli are strongly dependent on interlayer GO-GO distances, orientation of GO stacks, film thickness as well as the amount of sp^3/oxygen content. As shown in [14], an in-plane component of Young's modulus increases from ~268 GPa to ~620 GPa as the amount of interlayer spacing decreases from 0.8 to 0.5 nm. Based on our XRD results (**Section 6.3.1**) and using the approach from Ref. [14] the Young's modulus was evaluated to be ~600 GPa.

6.3: Results and Discussion

6.3.1: Characterization of Chemically Reduced GO-P2 Films on Hydrophobic Si Substrates

First, we prepared GO-P2 films of different thicknesses on hydrophobic Si wafers with ≈300 nm SiO_2 using dip-coating deposition method. For this we used solutions with various concentrations of GO-P2 sheets. In our next step, we treated all samples (covered with GO-P2 sheets) with 57% concentrated HI acid for 1 hour to make them electrically conductive (**Section 6.2.1**). Treatment of GO with HI causes an enormous structural change with the recovery of the conjugated system, through the removal of oxygen containing groups (**Section 2.6**).

Optical Properties

Optical microscopy offers the potential for rapid, non-destructive characterization of large-area samples. Since Gr is much more conductive than GO it is expected their

optical properties will differ markedly from each other at a certain frequency of light [17]. As a general statement, electrical conductors transmit visible light poorly, while an optically transparent substance cannot be a good conductor of electricity [18]. Typically, graphene and other 2D materials are optically detected and inspected by exploiting the interferometrically enhanced optical contrast obtained on Si substrates containing a submicron layer of silicon dioxide (SiO_2) [17, 19-20]. The total amplitude of the reflected light is affected by the thicknesses and the optical constants of the GO layer, the dielectric layer and the silicon layer.

Here GO monolayers and multilayers, formed on hydrophobic (silane-modified) Si wafer with an intermediate 300 nm thick SiO_2 layer, were qualitatively identified under white light illumination. We could resolve individual GO flakes much easier when they are deposited on such thick SiO_2 as compare to 2 nm thin SiO_2. **Figure 6.7** shows rGO-P2 layers, prepared from different concentrations of GO-P2 solutions, after chemical reduction with HI. It is evident that rGO-P2 layers are formed by well-overlapped and uniform network of rGO-P2 sheets, with slightly wrinkled morphology. Additionally, the density and thus the thickness of rGO-P2 network could be controlled by solution concentration.

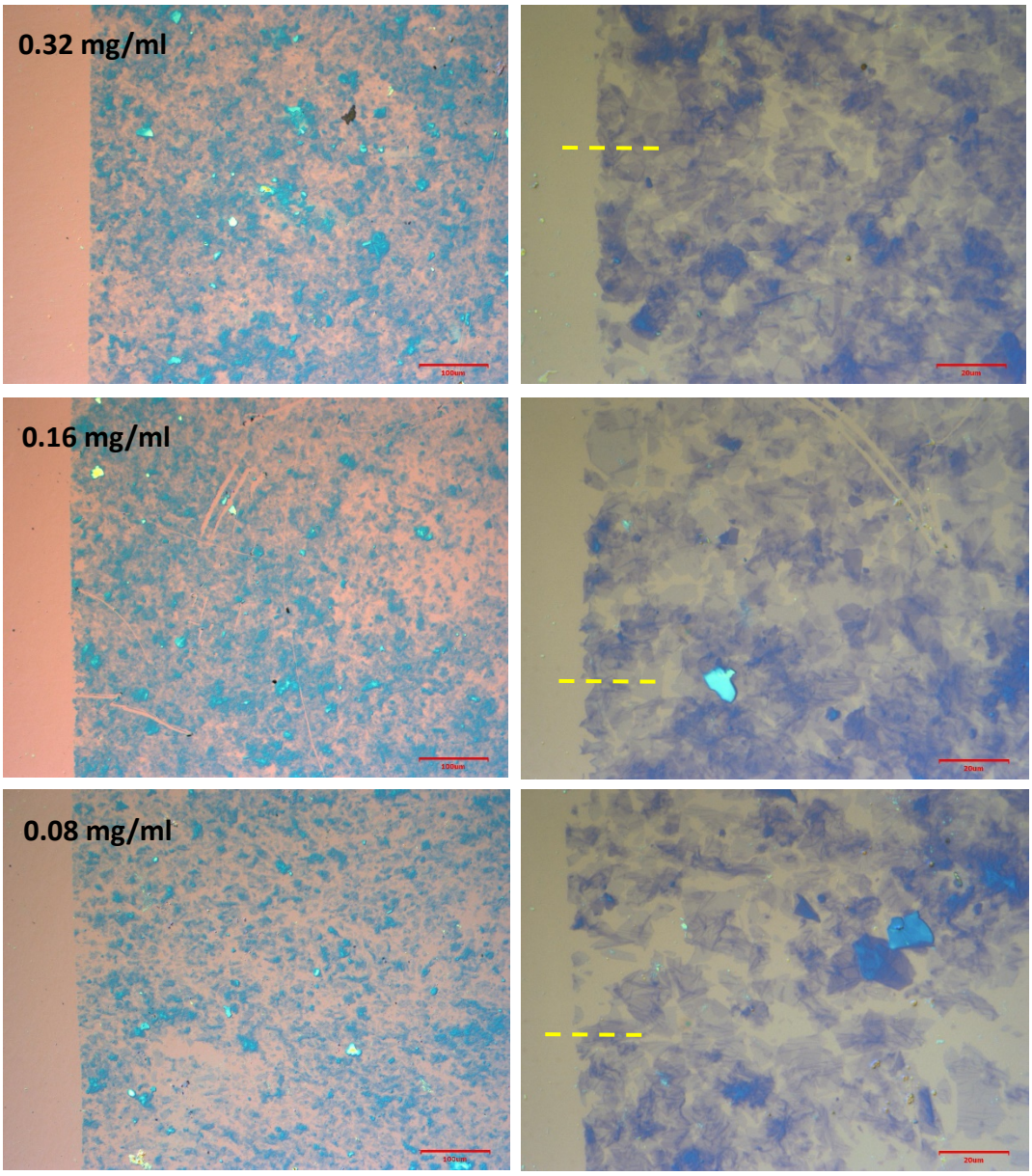

Figure 6.7. Optical images of rGO-P2 films deposited on 300 nm SiO_2/Si wafer. Red scale bar corresponds to 100 µm (left side) and 20 µm (right side)

Thickness of rGO-P2 films

From AFM cross-sectional profiles, measured across the film edges (**Figure 6.5**, dashed line), we estimated that the thicknesses of rGO-P2 films on Si are on the level of

6.5 nm, 5.5 nm, 3.5 and 2 nm for corresponding concentrations of GO-P2 solutions: 0.65, 0.32, 0.16, 0.08 mg/ml, (**Figure 6.8**). These values were used for electrical conductivity

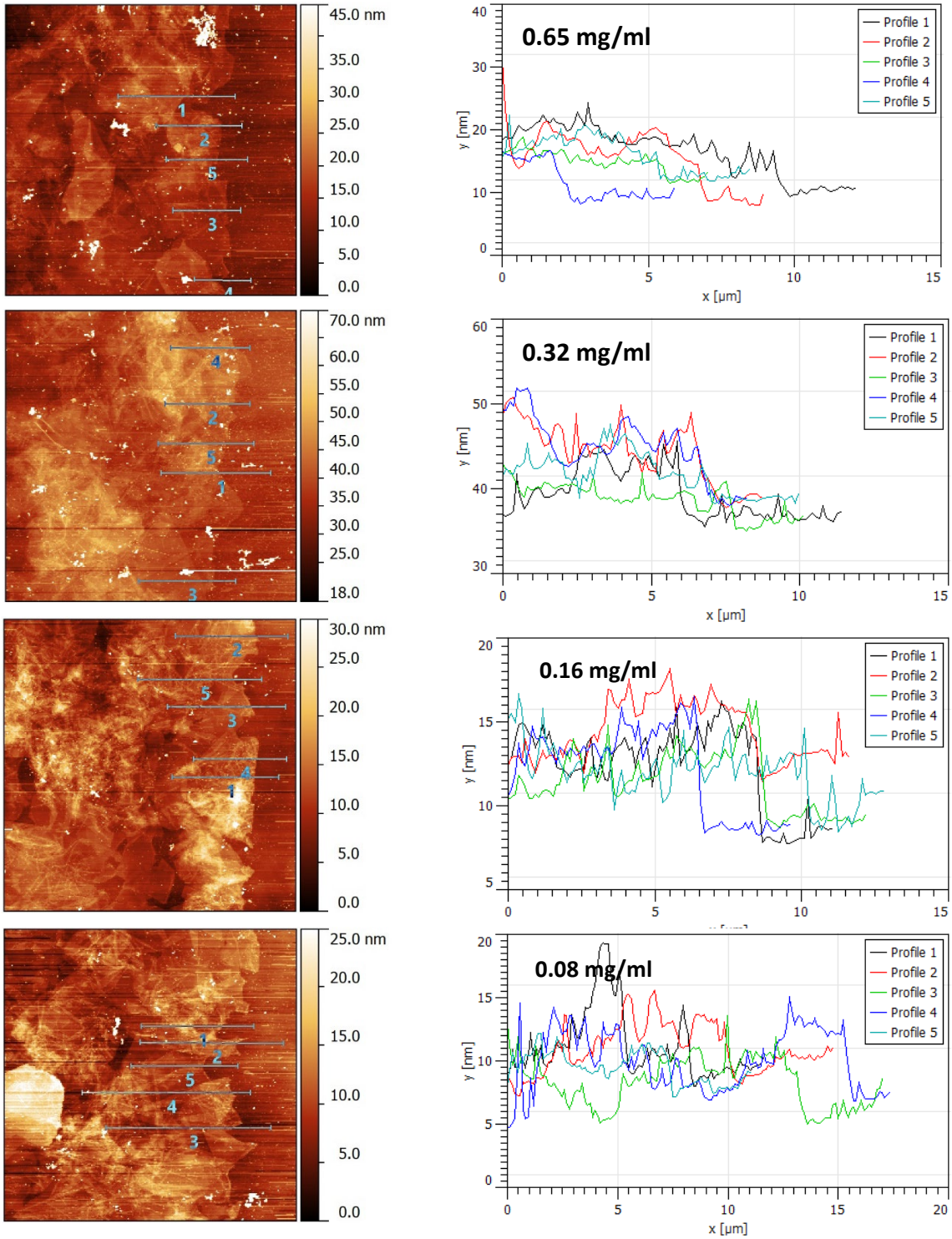

Figure 6.8: AFM images and corresponding cross-sectional profiles.

It is worth mentioning that we could not reliably measure thickness of rGO-P2 layers by forming a scratch on the surface as it produced significant amount of debris on the borders, as shown in **Figure 6.9A**.

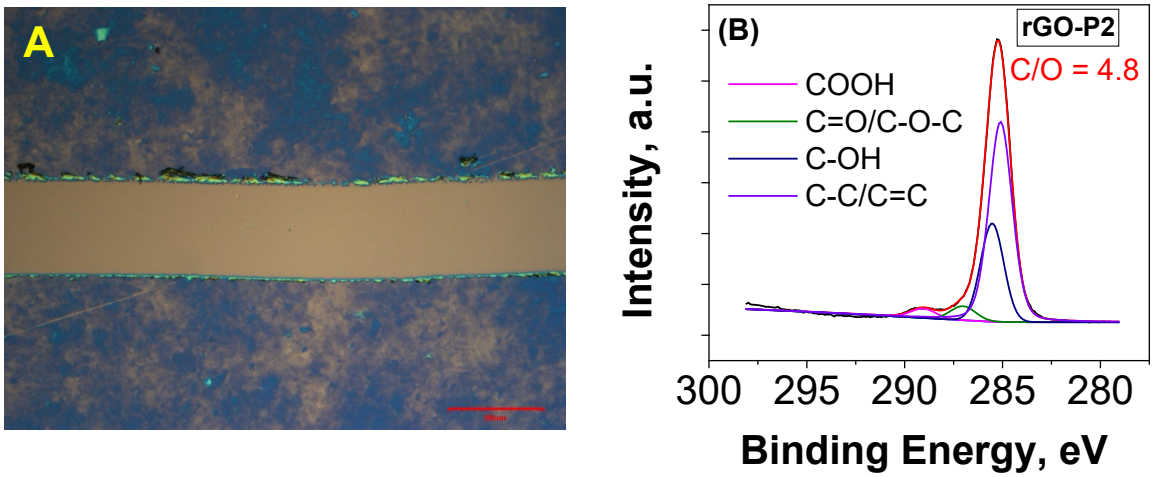

Figure 6.9. A: Optical image of the scratch made on rGO-P2 film deposited on 300 nm SiO_2/Si wafer. Red scale bar corresponds to 50 µm. B: High resolution C1s spectrum of HI reduced rGO-P2 film deposited on silicon.

Microstructural and compositional analysis of rGO-P2 films by XPS and Raman spectroscopy

In order to study the chemical composition of GO films and to assess the extent of deoxygenation for films after chemical reduction we carried out the XPS analysis. The XPS C1s detailed spectra and calculated C:O ratios for reduced sample (rGO-P2) is presented in **Figure 6.9B**. It shows that after the chemical reduction the intensities of all the related oxygen peaks were sharply decreased. The C:O ratio of rGO-P2 film was greatly improved

to approximately 4.8, indicating that the delocalized π conjugation was restored to a significant extent [21-22].

Raman spectroscopy is a powerful technique for detecting defects [23-24] and the amount of dopants in graphene [25]. In **Chapter 4** we demonstrated that Raman can provide insights into the quality of graphene material. In particular, the I_D/I_G ratio along with the positions of D and G bands were used as a measure of aromaticity or crystallite size in rGO-P1 films. However, some studies have shown that traditional methods, which rely upon an apparent G and D peaks, are unreliable for a highly defected Gr and rGO [26]. Consequently, a new Raman metric for the characterization of graphene oxide and its derivatives has been proposed [26-27]. Herein we interpreted the Raman by fitting spectra of rGO-P2 layers to four functions ascribed to D, D', D'' and G bands [23]. Nonlinear Fit was done in Origin 9.3 (2016) using Lorentzian functions. **Figure 6.10** shows the Raman spectra of pristine GO **(A)**, GO-P2 **(B)**, chemically reduced rGO-P2 **(C)** and thermally reduced rGO-P1 bilayer **(D)**. The D' peak at ~1620 cm^{-1} has been reported for defective graphene (with Csp^3 and structural defects) and its intensity is proportional to the amount of defects and crystallite size. D'' peak at ~1500 cm^{-1} - ~1550 cm^{-1} indicates the presence of amorphous phase and its intensity decreases when the crystallinity increases. The blueshift of the maximum position of the D" to 1537 cm^{-1} for GO-P2 after HI reduction is an indicative of oxygen decrease in the system.

To analyze the types of defects (vacancies or sp^3 defects) in rGO-P2 layers the ratio of integrated areas, $A_{D'}/A_D$, has been used [23-24]. The relative area values are collected in **Table 6.1**. Calculations showed the $A_{D'}/A_D$ value of 0.14 and $A_{D'}/A_D = 0.4$ for HI-reduced

rGO-P2 and thermally reduced rGO-P1 layers respectively. Consequently, our results seem to indicate that sp^3 defects predominate in rGO-P2 while vacancies are favored in rGO-P1.

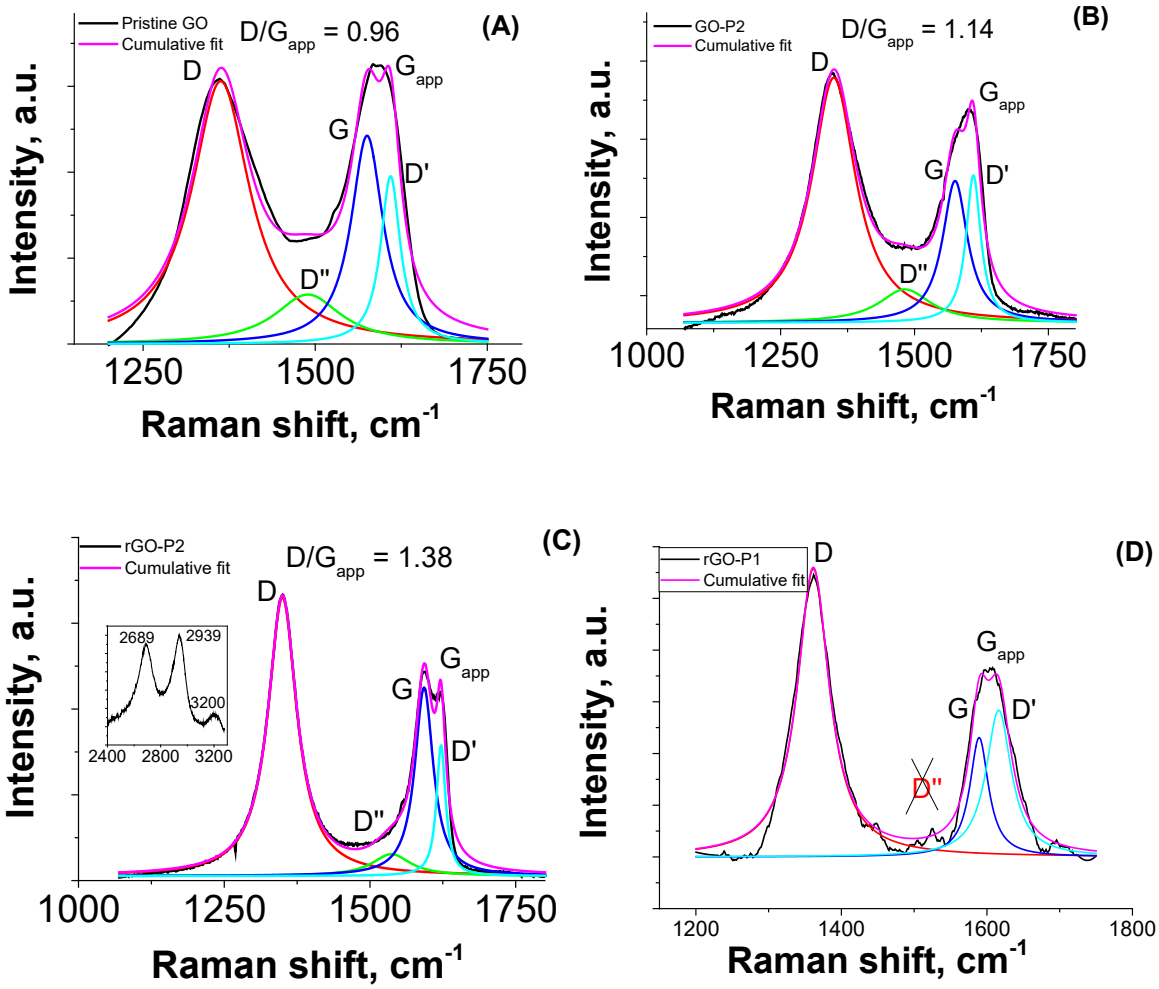

Figure 6.10. Examples of deconvoluted Raman spectra of pristine GO film (A), GO-P2 film (B), HI-reduced rGO-P2 film (C) and thermally reduced rGO-P1 bi-layer film (D). All films were made on undoped Si wafer using drop-casting technique.

Table 6.1. Spectral features from a four-peak fit of the Raman spectra from Figure 6.10.

	D (cm^{-1})	D'' (cm^{-1})	G (cm^{-1})	D' (cm^{-1})	$A_{D'}/A_D$
Pristine GO	1360	1489	1575	1609	0.22
GO-P2	1349	1482	1576	1610	0.20
rGO-P2	1350	1537	1593	1622	0.14
rGO-P1 bilayer	1361	N/A	1589	1616	0.40

Crystallographic properties of rGO-P2 layers

The crystallographic structure of the rGO-P2 films was studied by X-ray diffraction (XRD) (**Section 6.2.2**). The XRD pattern of the sample (**Figure 6.11**) shows a single broad peak at 2θ = 21.5º, corresponding to the (002) diffraction plane[28-29]. Using Bragg's law we determined an interlayer distance d_{002} = 0.41 nm, while for Gr layers it is 0.34 nm [30].

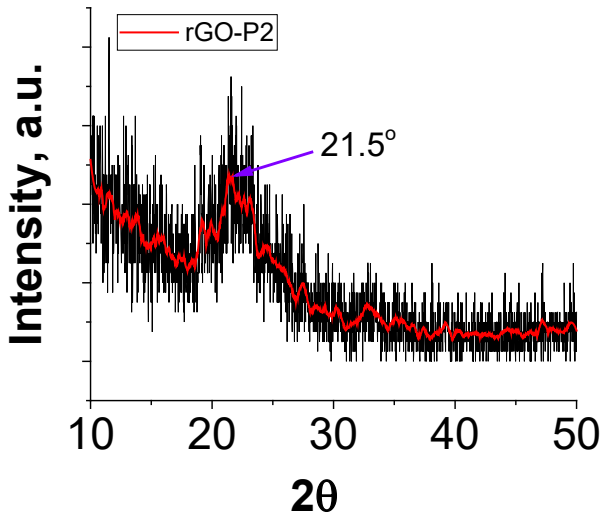

Figure 6.11. XRD diffractogram of HI-reduced rGO-P2 film.

6.3.2: Characterization of Chemically Reduced GO-P2 Films on Polymeric Substrates

Film surface structure and morphology: AFM and SEM studies

The results of chemical reduction of GO-P2 layers deposited on UHWPE, PP and Kapton are shown in **Figure 6.12** and **Figure 6.15** respectively. It is important to investigate the morphology and surface structure of HI reduced GO polymer samples since the morphology of GO sheets/layers on a nanoscale strongly influences its electronic characteristics [31-32]. The equilibrium morphology of the rGO film is governed mainly by two competing factors which contribute to the minimization of total free energy: (1) graphene-substrate interaction energy (characterized by van der Waals forces) [33] and (2) graphene strain energy [34-35]. If GO is fully conformal to the substrate (tight binding with the surface of the substrate or high adhesion energy) those two parameters significantly increase as the surface of the substrate becomes more corrugated [36] (high roughness) since the GO sheet will also corrugate to closely follow the substrate surface morphology [35]. On the other hand, when the graphene film is non-conformal the adhesive interaction with the substrate will be very low (low adhesion energy), which is usually the case for multilayer graphene membranes ($N \gg 1$) [34]. Therefore, the equilibrium rGO morphology can be determined at the minimum of the total free energy of the system (sum of the rGO strain energy and the rGO-substrate interaction energy) [35].

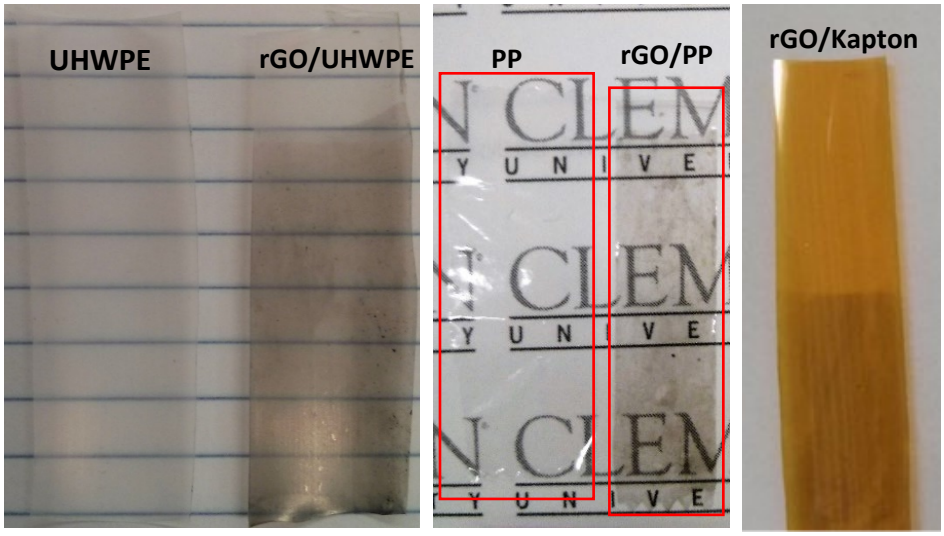

Figure 6.12. Photograph of HI-reduced rGO-P2 film deposited on both sides of UHWPE (left), PP (middle) and Kapton (right) substrates.

Thus, we measured RMS roughness for polymer substrates with and without rGO-P2 from AFM images of 15x15 mkm size. **Figure 6.13** presents AFM images of plain (left) and rGO-P2--covered polymer substrates (right).

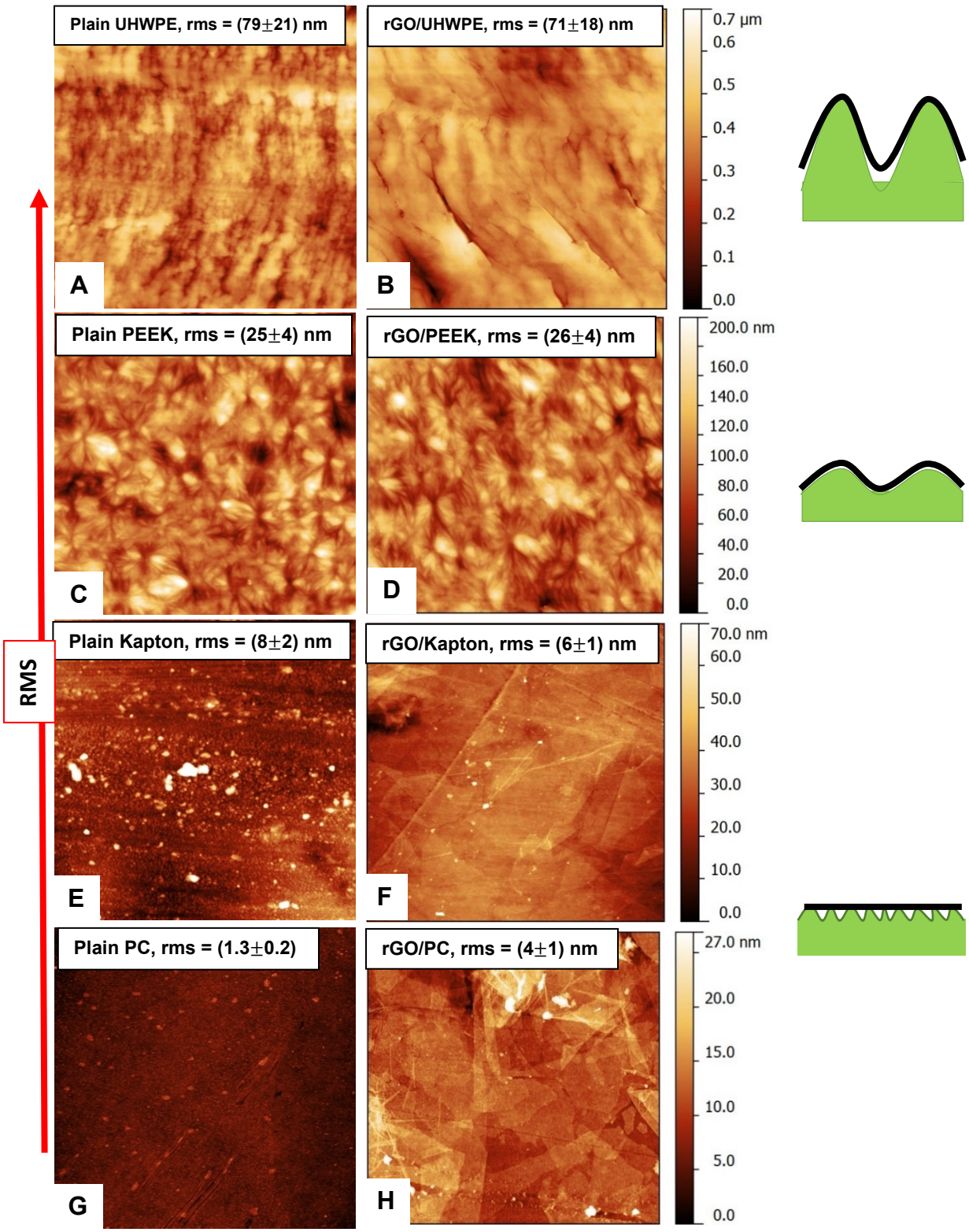
Plain UHWPE, rms = (79±21) nm
rGO/UHWPE, rms = (71±18) nm
0.7 µm
0.6
0.5
0.4
0.3
0.2
0.1
0.0
A
B
Plain PEEK, rms = (25±4) nm
rGO/PEEK, rms = (26±4) nm
200.0 nm
160.0
140.0
120.0
100.0
80.0
60.0
40.0
20.0
0.0
C
D
RMS
Plain Kapton, rms = (8±2) nm
rGO/Kapton, rms = (6±1) nm
70.0 nm
60.0
50.0
40.0
30.0
20.0
10.0
0.0
E
F
Plain PC, rms = (1.3±0.2)
rGO/PC, rms = (4±1) nm
27.0 nm
20.0
15.0
10.0
5.0
0.0
G
H

Figure 6.13. AFM images of plain polymeric substrates (all on the left) and polymeric substrates covered with HI-reduced rGO-P2 layer (all on the right). The size of the scans is 15x15 μm^2, and for Kapton – 10x10 μm^2. Approximate rGO-P2 layer thickness is ≈ 6 nm (0.65 mg/ml GO-P2 solution was used for dip-coating).

As seen from AFM images the rGO morphology revealed two distinct states: closely conforming to the substrate surface and remaining nearly flat on the substrate surface as the substrate surface roughness decreases. The above results indicate that our GO-P2 films still retain extreme flexibility allowing it to follow the morphology of the substrates to a large degree, as seen from **Figure 6.13(D)** ($RMS_{rGO/PEEK} \approx 26$ nm). However, we observed from **Figure 6.13(B)** that rGO film partially conformed to the surface of UHWPE with initial RMS of (79 ± 21) nm, assuming a corrugated morphology similar to the substrate surface grooves but with a slightly smaller amplitude with RMS = (71 ± 18) nm. Our experimental results are in good correlation with theoretical calculations presented in Ref. [35]. There, authors showed that, if the surface roughness is too large the graphene bending energy increases, leading to an increase in total free energy of the system. In contrast, by partially conforming to the substrate the graphene-substrate interaction energy decreases.

We also used SEM and optical microscopy to characterize the physical properties of rGO-P2 layers at the large scale > (50 × 50) μm^2. **Figure 6.14 (A – L)** shows SEM and optical images of rGO-P2 (~ 6 nm) on various polymeric substrates. It can be seen, that rGO-P2 films exhibit good film-forming ability and homogeneous smooth surface on polymer substrates with low surface roughness (PC, Kapton, PP). In addition, rGO-P2 layers are well conformed to the underlying substrate with high roughness (PEEK, UHWPE), which is consistent with the results obtained from AFM studies.

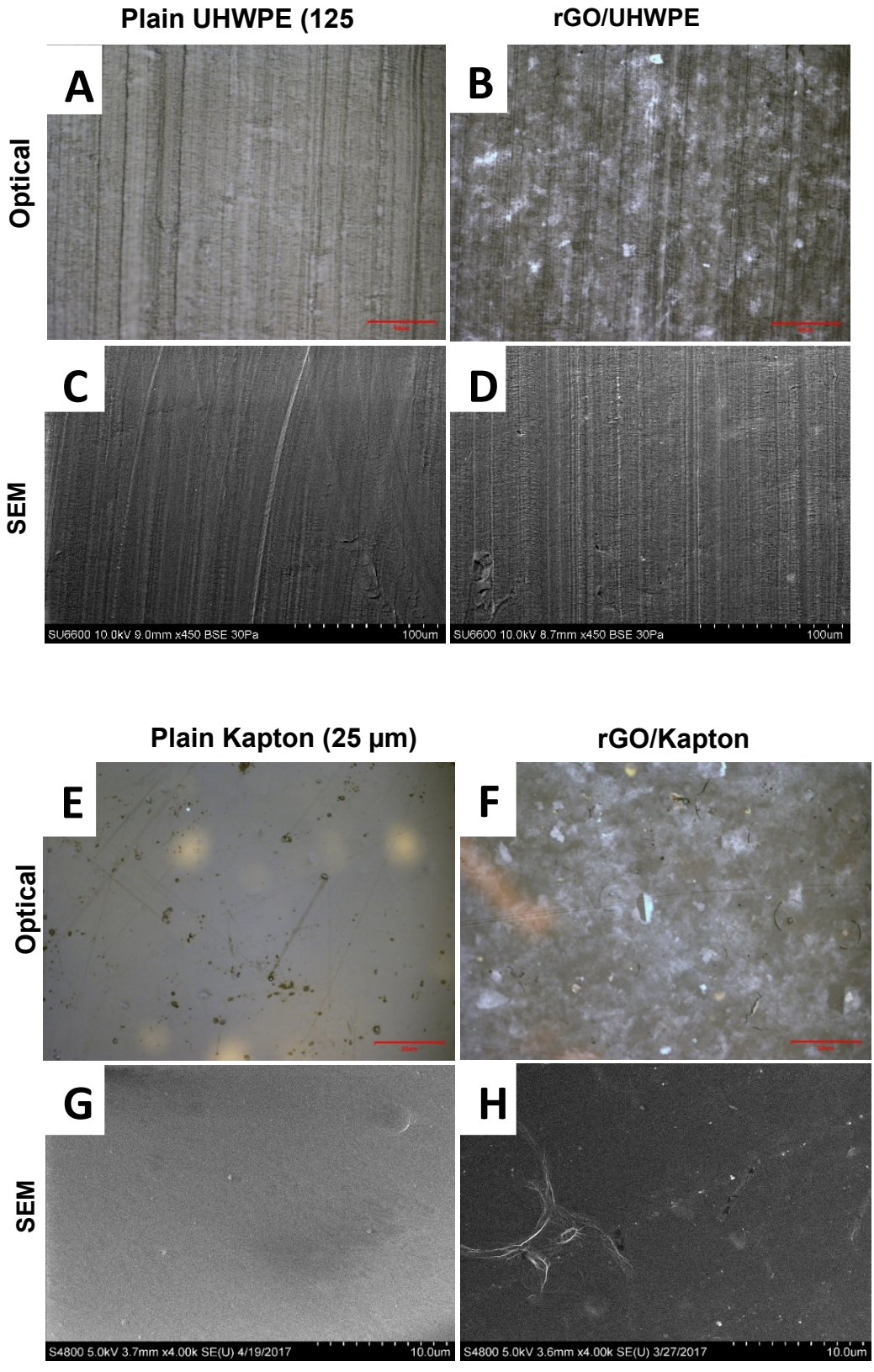
Plain UHWPE (125
rGO/UHWPE
A
B
Optical
C
D
SEM
SU6600 10.0kV 9.0mm x450 BSE 30Pa
100um
SU6600 10.0kV 8.7mm x450 BSE 30Pa
100um
Plain Kapton (25 μm)
rGO/Kapton
E
F
Optical
G
H
SEM
S4800 5.0kV 3.7mm x4.00k SE(U) 4/19/2017
10.0um
S4800 5.0kV 3.6mm x4.00k SE(U) 3/27/2017
10.0um

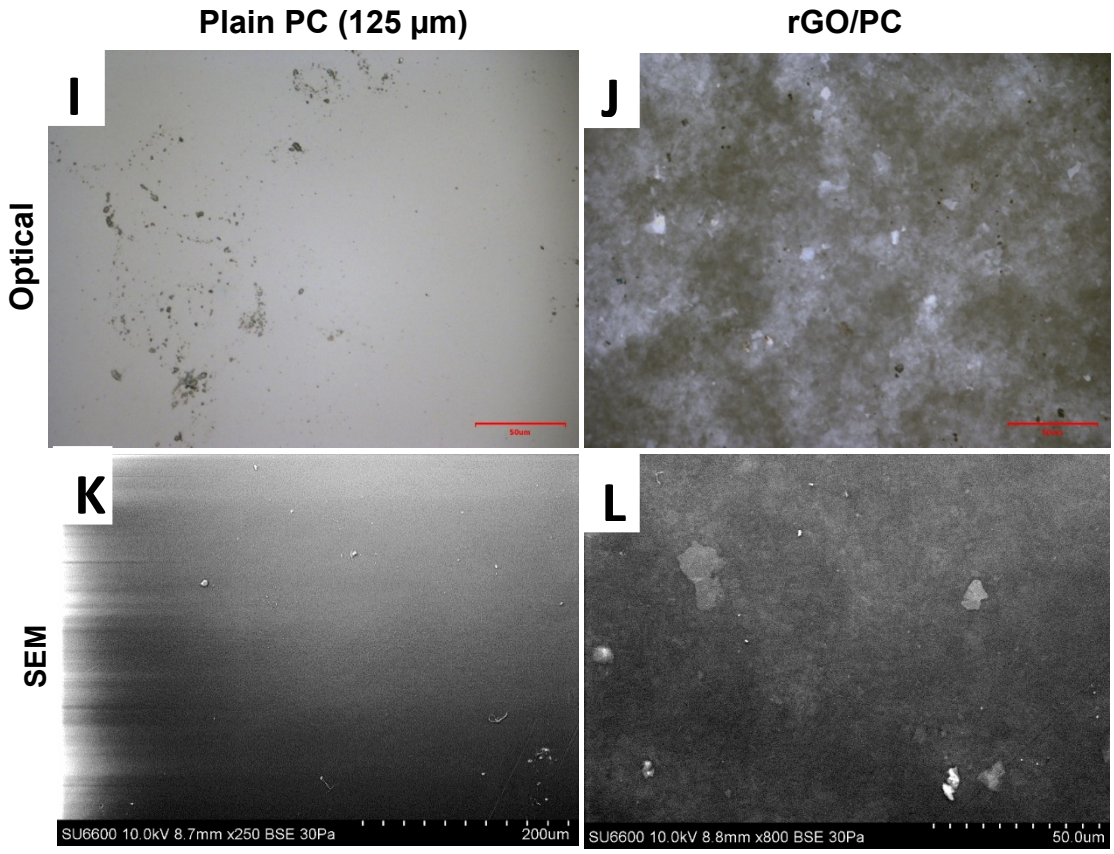

Figure 6.14. Optical and SEM micrographs of HI reduced rGO-P2 layers on different polymeric substrates. Approximate rGO-P2 layer thickness is ≈ 6 nm (0.65 mg/ml GO-P2 solution was used for dip-coating).

Electrical properties of rGO-P2 layers on polymeric substrate

To assess the electrical properties of the chemically reduced rGO-P2 films, we fabricated rGO-P2 films of varying thickness on Kapton polymeric substrate (**Figure 6.15**). Silver electrodes were made for electrical contact according to the procedure described in **Section 6.2.2**. **Figure 6.16(A)** shows the representative I-V characteristics at room temperature for HI-reduced rGO/Kapton samples prepared from different GO-P2 concentrations. At least two different samples have been used to acquire I-V curves. The linear I-V characteristics suggest a good electrical contact between adjacent interconnects

[37], since, otherwise the I-V curve would have an exponential shape. This result clearly indicates that the sheet resistance/conductivity of rGO-P2 films is easily controlled by varying the film thickness which in turn is defined by GO-P2 concentration in water. As shown in **Figure 6.16(B)**, the surface resistance/electrical conductivity decreases/increases rapidly with rGO-P2 layer thickness.

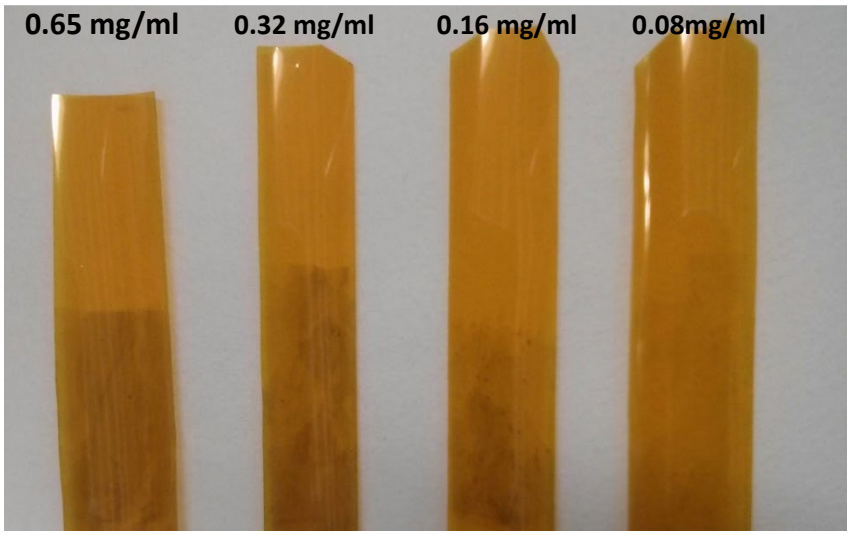

Figure 6.15. Photograph of HI-reduced rGO-P2 films deposited on both sides of Kapton substrate.

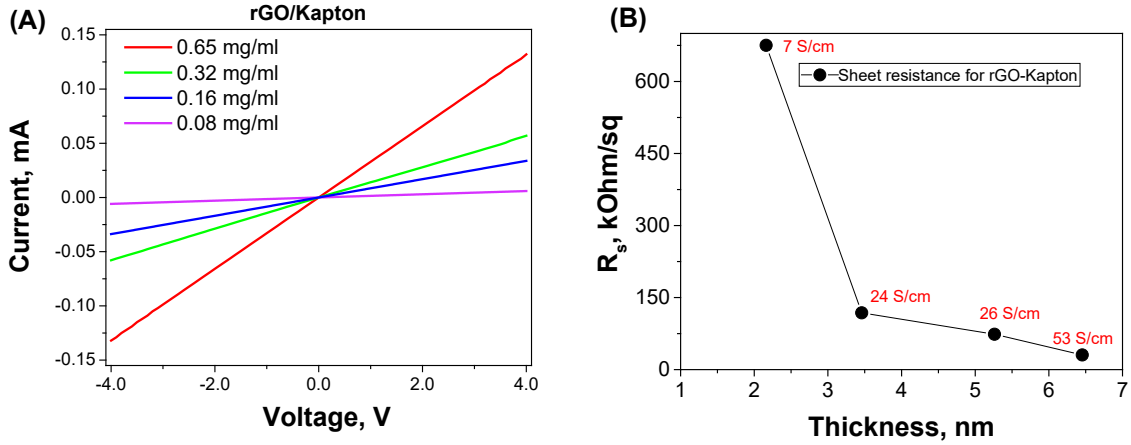

Figure 6.16: (A): I-V curves acquired under ambient conditions for rGO/Kapton samples. (B): Surface electrical conductivity of rGO-P2 layers on Kapton as a function of thickness. I-V curves represent the average of at least two measurements.

Next, we carried out I-V measurements of rGO-P2 deposited on various polymeric substrates from 0.65 mg/ml GO-P2 solution as shown in **Figure 6.17**. The distance between electrodes was between 1 and 3 cm. Using thickness values found by means of AFM (**Section 6.3.1, Figure 6.8**) and sheet resistances calculated from I-V slopes we could estimate the electrical conductivities of rGO-P2 layers (≈ 6 nm) on plastics. The electrical properties for all samples are listed in **Table 6.1**.

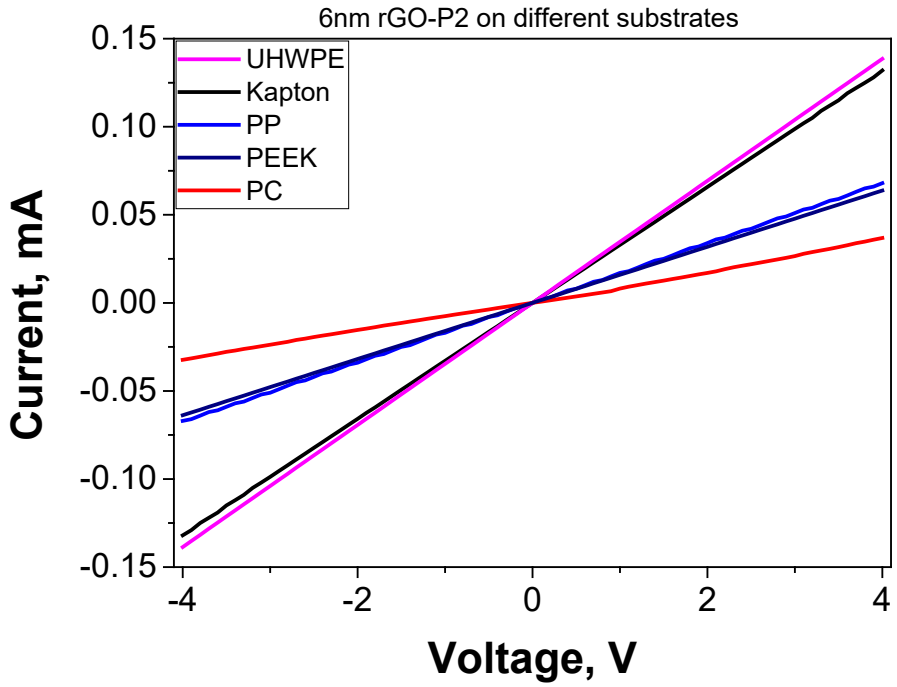

Figure 6.17: I-V curves acquired under ambient conditions for rGO-P2 layers on different polymeric films

For all the different substrates investigated here, the values of sheet resistance measured in air are typically lower than 135 kΩ/sq, with the best values reaching as low as 28.9 kΩ/sq. Various macroscopic and microscopic defects such as wrinkles, folds, tears, cracks, missing carbon atoms can adversely influence the electric conductivity [38-39]. However, we

observe that even if the polymer films have a rough surface morphology (**Figure 6.12** and **6.13** (UHWPE)) the electrical conductance of rGO-P2 layer remains relatively large and the current *vs.* voltage characteristics reveal linear behavior as expected for Ohmic conduction or metallic property of rGO-P2 sheets [2, 40].

Table 6.2. Electrical conductivity of rGO-P2 layers deposited on various polymeric films obtained from I-V measurements for ± 4V.

Sample	**Distance between electrodes, mm**	**Normalized Slope** *Ohm^{-1}*	**Sheet resistance,** *Ohm/sq*	**Conductivity,** *S/cm*
UHWPE	41.7	3.46e-5	28900	58
Kapton	20	3.29e-5	30400	55
PP	20.4	1.67e-5	59900	28
PEEK	34.3	1.59e-5	62900	27
PC	30.8	7.41e-6	135000	12

Optical Properties of rGO-P2 layers on polymeric substrates: UV-Vis measurements

To investigate optical properties of rGO-coated polymer films we used UV-Vis spectrometry. The transmittance data T(%) as a function of wavelength for three films are presented in **Figure 6.18**.

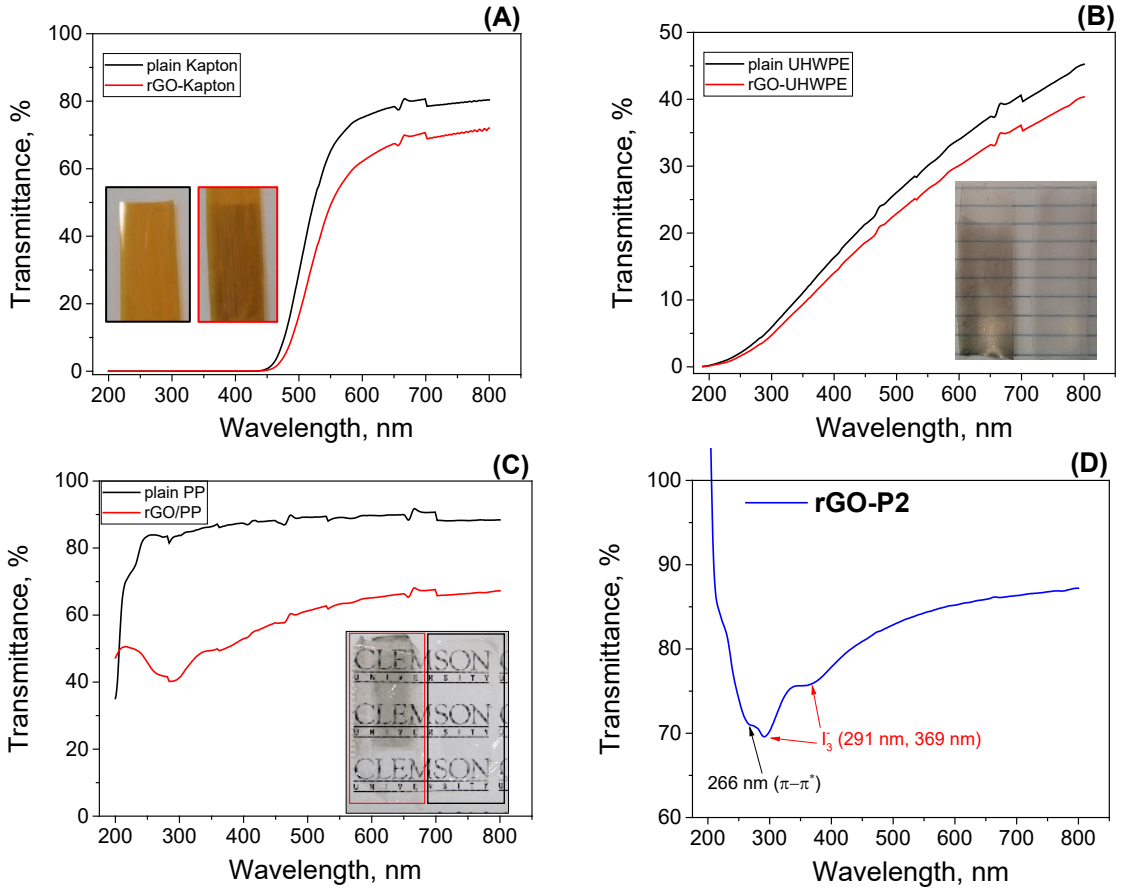

Figure 6.18: UV-Vis spectra of double-sided rGO/Kapton (A), rGO/UHWPE (B), rGO/PP (C) and spectrum of single rGO-P2 (6 nm) found as a difference between plain PP and rGO/PP.

It is shown that the produced films were also optically transparent in the visible range. PP, UHWPE and Kapton films with rGO-P2 coatings on both sides demonstrated transmittance of 63 %, 27 % and 50 % respectively (measured at 550 nm), whereas the corresponding

transmittance values for bare films are 89 %, 30 % and 65 %. After subtraction of plain PP absorption spectrum from rGO/PP one, the transmittance of single rGO-PP2 layer (≈ 6 nm) was measured at 84 % at 550 nm. Additionally, we could detect the presence of iodine anions (I_3^-) (with adsorption at 291 nm and 369 nm)[41] besides usual $\pi \rightarrow \pi^*$ transitions of aromatic C=C bonds at 266 nm. In order to quantitatively describe the amount of the residual iodine within the rGO-P2 film we measured XPS $I3d_{5/2}$ spectra (**Figure A15** in the **Appendix**). The results show that the atomic ratio of iodine to carbon (I/C) is less than 0.0022.

6.3.3. Electro-Mechanical Response under Compression/Tensile Bending

Besides electrical conductivity and optical transparency, flexible electrode should possess two important properties – durability and reliability in order to be suitable for practical applications. The devices made of flexible electrodes often work under mechanical stresses caused by tension, bending and twisting. Two parameters should be taken into account when subjecting thin films to mechanical deformations: (i) the maximum strain that thin film can withstand with single loading before failure and (ii) the maximum strain that it can withstand with cyclic loading before failure [2, 42]. Thus, the effect of bending on the electrical resistance of the rGO-coated polymer films was studied.

Electrical properties under bending stress

Flexural stability of the rGO-P2 (≈ 6 nm) deposited on a commercially available Kapton, UHWPE and PP was tested by measuring the dynamic response of normalized electrical resistance variation $((R - R_0)/R_0)$ under both extension (tensile strain) and

compression (compressive strain) conditions of bending (**Figure 6.19**). The latter ones could be controlled by both the radii of curvature and the thickness of polymeric substrate. FEA simulations were used to determine the value of strain and stress (see **Sections 6.2.5** and **Figure 6.21** for more details). For both rGO/Kapton and rGO/UHWPE the relative resistance ($\Delta R/R_0$) is found to increase with increasing radius of curvature under tensile strain (**Figure 6.19**(A, B), black curve), while it decreased under compression (**Figure 6.19**(A), red curve). Similar behavior was previously reported on graphene-coated PET films and CVD grown graphene layers [29]. The maximum bending strain of rGO-P2 film on Kapton was 3 % at radius of curvature R = 0.36 mm while on UHWPE the bending strain reached 10 % at slightly larger R = 0.56 mm. It is worth noting that $((R - R_0)/R_0$ for rGO-P2 film on UHWPE did not return to its original value at the end of experiment. For rGO-P2 film deposited on PP we could not achieve any significant signal response due to low PP thickness (≈ 6 μm) which produced strains much lower than 1%.

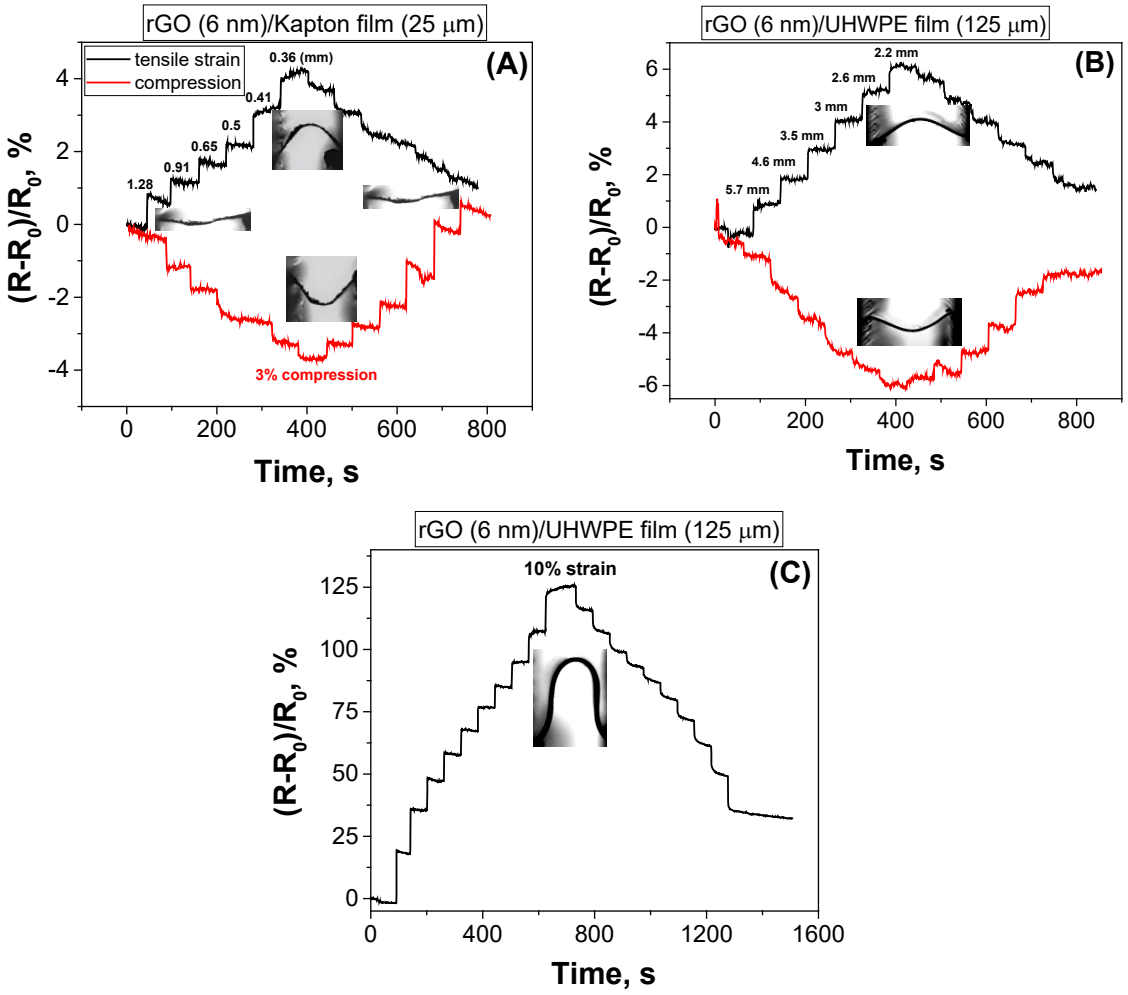

Figure 6.19: Relative resistance change as a function of time for rGO-P2 film deposited on Kapton (25 μm) (A) and UHWPE (125 μm) (B). "Time steps" correspond to different bending radii.

Two factors may lead to the increase/decrease in the resistance: (a) dimensional change in thickness (decrease/increase) on stretching/compression [29] and (b) non-geometrical effects such as sliding between adjacent flakes which disrupt the overlap areas of GO sheets as discussed in [43].

Thus, the results of this section demonstrated that the electrical response (relative resistance change) of rGO-P2 can be precisely modulated by varying the radius of bending and/or underlying substrate's properties (modulus, thickness). Furthermore, the ability to distinguish between different types of deformations (tensile or compressive) is attractive and promising for practical applications in wearable electronics [44].

rGO/Kapton as a strain sensor

The above results imply that rGO/Kapton film can be used as a strain sensor to reflect both tensile and compressive deformations. Strain sensors are attractive and promising for practical applications in wearable electronics such as the detection of acoustic vibration, electronic skins, wearable monitoring systems [45].

Herein, we investigated the responses in the resistance of rGO/Kapton as a strain sensor at different tensile bending frequencies (0.017 Hz and 0.2 Hz), as shown in **Figure 6.20A**. The measurements were repeated on the same rGO/Kapton sample under compression over the same strain range and the results are also illustrated in **Figure 6.20B**.

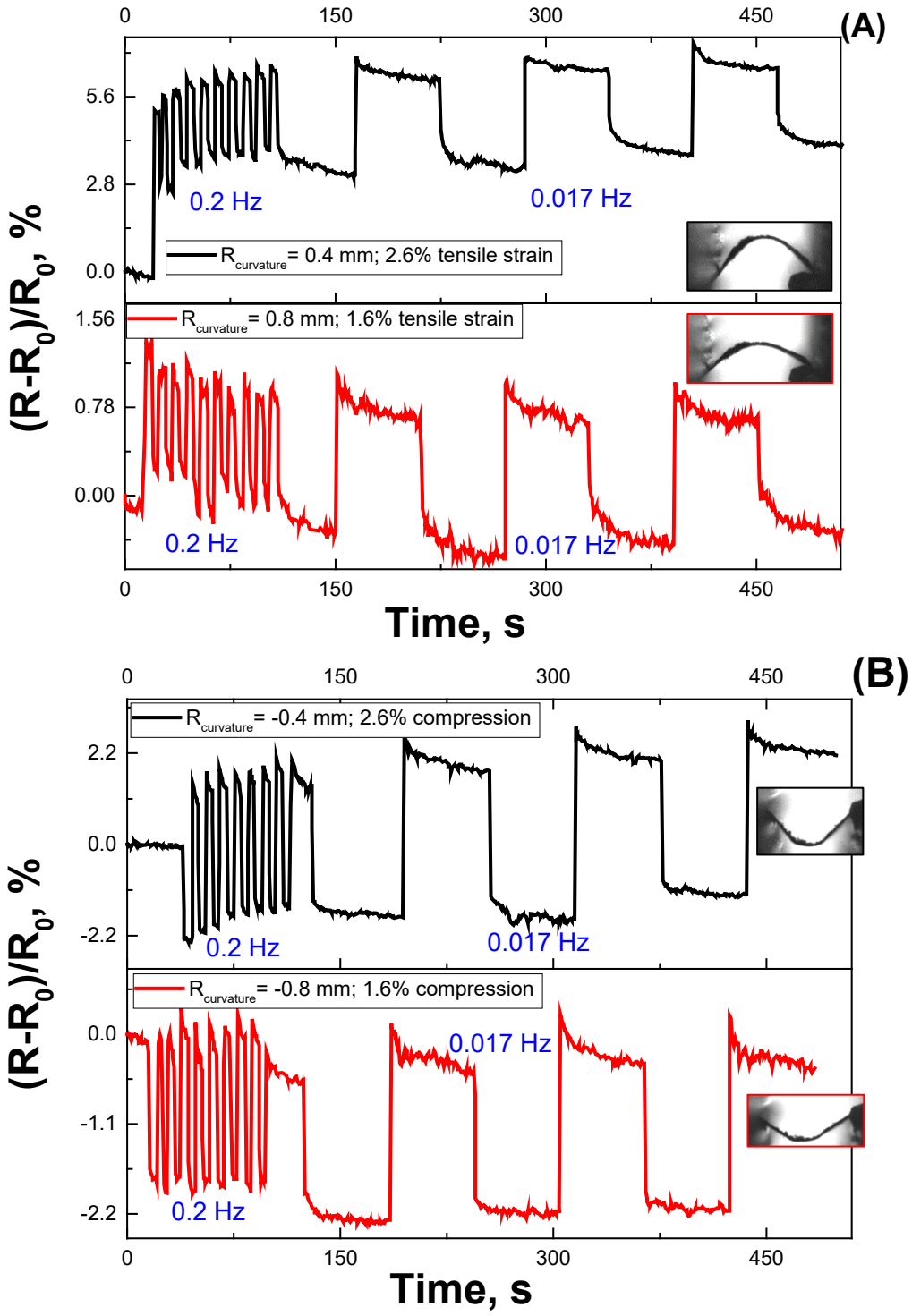

Figure 6.20: Dynamic response curves of rGO/Kapton film under tensile strain (A) and compressive strain (B).

Similarly to [43, 46], gauge factor was used to evaluate the sensing performance of the rGO/Kapton sensor and it is defined as GF = $\delta(\Delta R/R_0)/\delta\varepsilon$, where ε is the strain. The GF was found from the slope of the relative resistance-strain curve shown in **Figure 6.21B**. Thus, the GF of rGO/Kapton sensor was calculated to be ~3.6 within 1% - 3 % strain, which is in accord with recently reported data in [44]. As a result, this strain sensor can be used to detect both stretching and compressing deformations with high sensitivity and excellent repeatability.

Simulation of mechanical stresses and strains using finite element analysis (FEA)

The stress distributions and strain values in rGO-P2 films deposited on UHWPE and Kapton were estimated with the help of FEA (**Figure 6.6**). Finally, we obtained a "master-curve" of R/R_0 plotted against the strains and von Mises stresses generated in rGO-P2 upon bending (**Figure 6.21(B)**). The critical/minimal stress in rGO of at least 15 GPa is required to cause 3% signal change. More details about FEA can be found in **Section 6.2.5**. Mathematically, the dependence of the relative resistance (R/R_0) of the applied strain (ϵ) can be approximated with the following expression:

$$\frac{R}{R_0} = e^{4\epsilon + 42.5\epsilon^2} \tag{6.1}$$

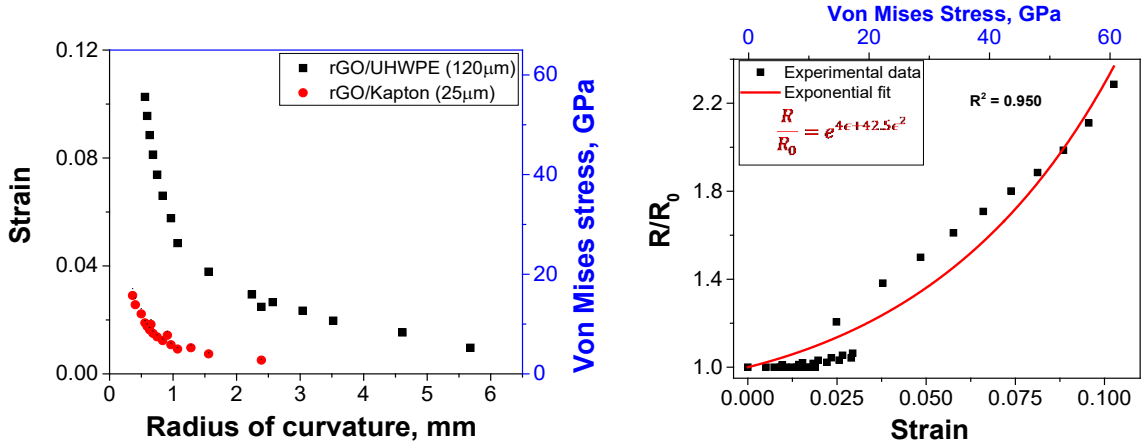

Figure 6.21: A: strain as a function radius of curvature. B: "master-curve" showing the exponential dependency of relative resistance of strain. Axis marked in blue color specify Von Mises stress (found from FEA simulation) developed in rGO layer upon bending.

Thus, using the **Equation 6.1** one can predictively estimate the expected signal response of rGO-P2-based sensor provided the information about strain or stress is given.

6.3.4. Electro-mechanical response under tensile strain

It is important for flexible electronic device to not only withstand repetitive flexing/bending but also demonstrate high stability during one-time mechanical stretching. In this section, the maximum strain that chemically reduced rGO-P2 on UHWPE (rGO/UHWPE) can withstand under tensile load has been investigated *in situ* (in a two-point probe geometry). The schematic and details of the two-point probe resistance measurement setup are presented in **Section 6.2.4**.

In the elastic regime the growth of the resistance is directly proportional to the strain. When a film starts to deform plastically the ideal curve for the relative electrical resistance satisfies the following equation [5-6]:

$$\frac{R}{R_0} = \left(\frac{L}{L_0}\right)^2 \equiv (1+\epsilon)^2 \qquad (6.2)$$

Here R is the electrical resistance of rGO-P2 film stretched to length L. R_0 and L_0 are respectively the initial resistance and distance between the contacts, and ϵ is the applied strain. However, the **Equation 6.2** becomes invalid when film exhibits substantial structural modifications (cracks, tears) which lead to resistivity or volume changes during the experiment. The failure strain is generally defined as the strain at which the experimental curve deviates from the theoretical curve (**Equation 6.2**) by more than 5% [6, 47].

Figure 6.22 displays the change of stress **(bottom)** and resistance **(top)** of rGO/UHWPE film as a function of uniaxial tensile strain. From **Figure 6.22(top)** two stages of resistance-

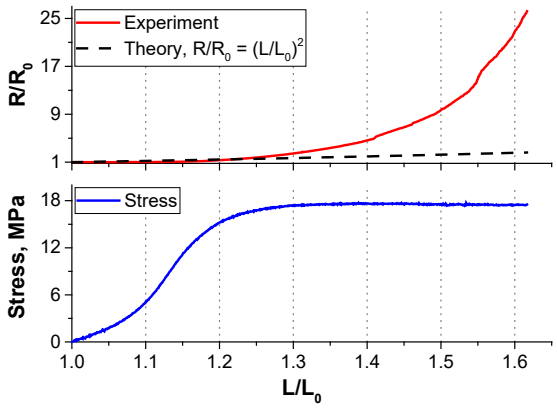

Figure 6.22: Relative resistance versus relative elongation (top) and stress versus relative elongation (bottom).

strain dependency can be identified. In the stage I, the resistance at strains lower than 15% hardly showed any change with respect to applied tensile stress. This could be due to the flattening of wrinkles within rGO/UHWPE film and sliding between adjacent flakes [48]. However, further stretching of the sample over 10-15% (stage II) shows dramatic increase of resistance, which may originate from significant separation distances between individual rGO sheets. A maximum failure strain of 23 % was obtained.

The fact that the resistance starts to deviate from theoretical curve at 10-15 % tensile strain suggests the initiation of plastic deformation of rGO-P2 film due to loss of its integrity. Therefore, the strains of rGO-P2 larger than ~10% should be avoided in any wearable sensing applications where durable stability is of primary importance.

6.3.5. Life-Cycle Testing

In this section of the dissertation we tested the durability of ~6 nm rGO-P2 layers deposited on three different substrates: UHWPE (thickness of 120 μm), Kapton (25 μm) and PP (6 μm). The samples were subjected to at least 40000 bending cycles with frequencies ranging from 0.5 Hz to 2 Hz and radii of curvature ~0.3-0.5 mm. Using FEA in **Section 6** the following tensile strain/strength values ($\Delta L/L_0$) for films bent to the above-mentioned radii of curvature were estimated: 0.6%, 3% and 10% for PP, Kapton and UHWPE respectively.

Figure 6.23 presents the dynamic response curves for three samples during cyclic deformations. We observed very unstable signal with less than 5% change during first 30000 bending cycles for 6 nm rGO-P2 deposited on 6 μm PP (**Figure 6.23A**). For

rGO/Kapton sample (**Figure 6.23C**) bent up to 30000 times the relative resistance increased only by 8% with almost complete recovery in about 20 minutes (with 4 % loss in conductivity) (**Figure 6.23D**). Recent studies have revealed similar trend where the resistance of rGO-P2 recovers to the original value after cyclic deformations due to the reconnection of rGO-P2 sheets upon stress relaxation in polymer substrate.[43, 49] Meanwhile, the resistance of rGO-P2 deposited on 120 μm UHWPE changed by more than 200 % (**Figure 6.23E)** with only 20 % recovery, as shown in **Figure 6.23F**. Such low recovery may be due to the fact that our rGO/UHWPE film was underwent permanent plastic deformation upon 100000 repetitive bending (**Figure 6.23F, inset)**.

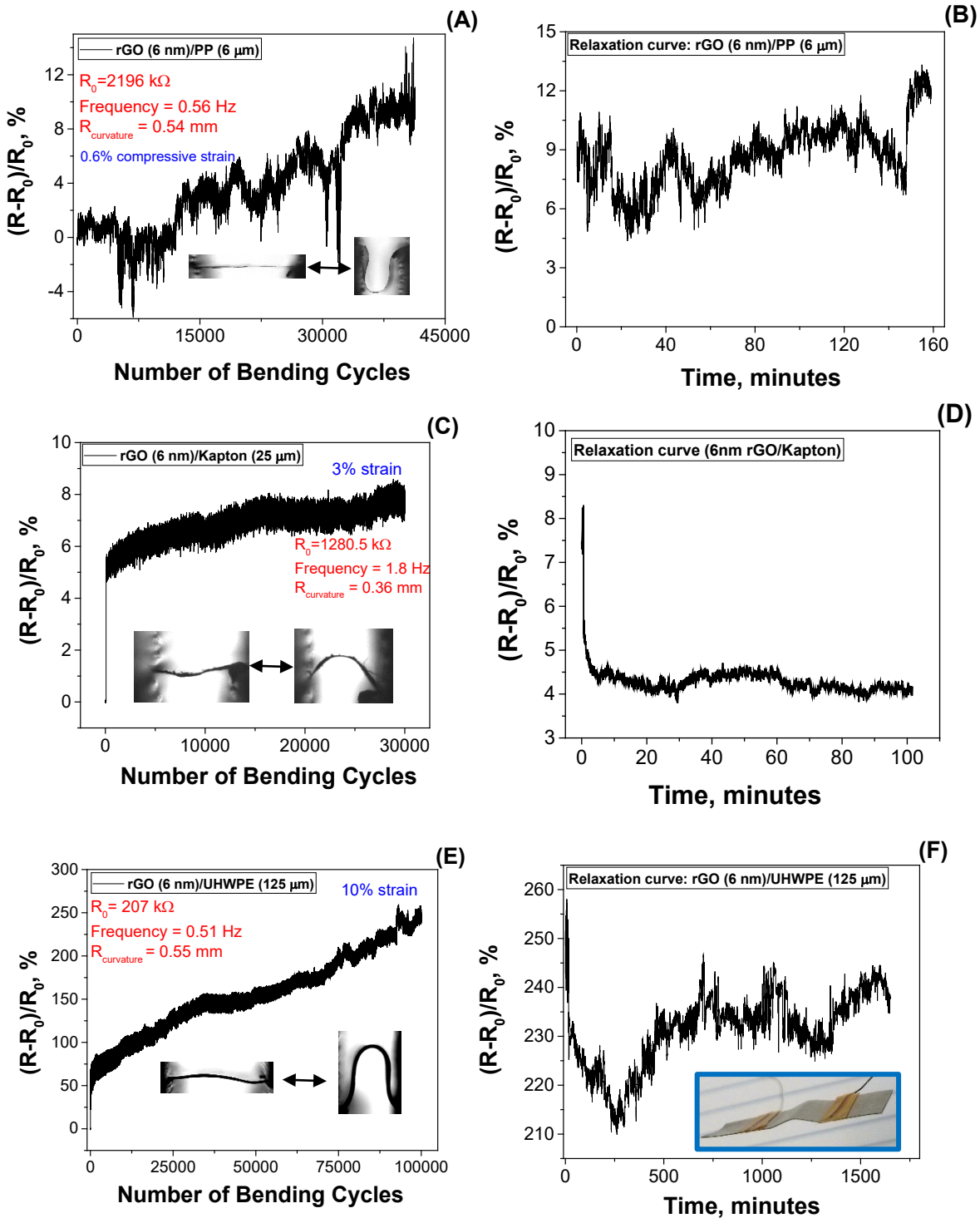

Figure 6.23: Dynamic response curves for three different samples under cyclic bending. rGO/PP (A, B), rGO/Kapton (C, D) and rGO/UHWPE (E, F).

It is obvious that as the applied strain increases up to 10% due to substrate being thicker the contact area of graphene sheets gets significantly reduced leading to a decreased number of conductive pathways and thus an increase in resistance is observed [48]. It is necessary to highlight that these testing conditions are quite severe, since the typical radius into which a circuit can be bent is several millimeters.[50-51]

Our results indicated that at more practical lower bending frequency and radius of curvature even better performance could be expected for such materials. Nevertheless, in terms of durability our electrically conductive rGO-P2 films are still in the range acceptable for highly flexed devices [52], as they were able to withstand 100000 bending cycles at 10 % tensile load without complete loss of its integrity.

6.3.6. The Overview of Other Potential Applications of Transparent Conductive Films

Flexible and transparent conductive films (TCFs) have broad range of potential applications such as biomedical sensors, electronic paper, displays, photovoltaic cells, electronic textiles [53-54], [55-56], electrochemical devices [57], [58], super capacitors, wiring. Flexible electronic devices built on such films are more comfortable and cost effective due to being bendable, lighter and smaller. Many of the above applications require electrical conductivities higher than 1000 S/cm, which means our rGO films on polymeric substrates with conductivities in the range of 1 – 100 S/cm do not meet that requirement. However, such types of films may become very effective in lightweight transparent electromagnetic interference (EMI) shields for the radio frequency range in defense and aerospace

applications [59]. For EMI shielding the conductivity should be at least 10^{-3} - 10^{-1} S/cm [59-60]. The EMI shielding is particularly important and very difficult to attain in the areas of visual observation - observation windows [61], electronic displays [62]. Various transparent materials [63-64] have been investigated for this role, but the promising and low cost are carbon-based materials [63, 65-67], especially in applications where mass should be as low as possible. The fabrication method of EMI shields is based on two approaches the introduction of the conductive material into the polymer matrix or the deposition of conductive coatings to the surface of polymeric substrate [68], [69]. For example, Kim et. al [68] demonstrated that 20 nm thick and 73% transparent (in visible range) rGO film with conductivity of only 12 S/cm exhibited ~ 50 % shielding of incident waves. Thus, we expect that our rGO films can be practically used in the above-mentioned applications.

6.3.7. rGO/UHWPE as Flexible Transparent Conductor

To further demonstrate the potential usage of rGO-coated polymer substrate as flexible conductor we integrated it in a circuit with light emitting diode (LED) **(Figure 6.24)**. The LED operates well at the same voltage when rGO/UPWPE is in bent or unbent state. The radius of bending was ≈ 5-7 mm.

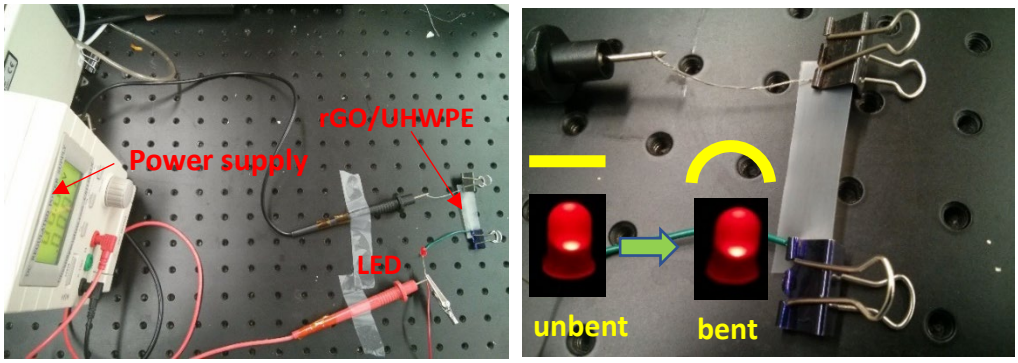

Figure 6.24: Photograph of an electric circuit with LED light, closed with rGO/UHWPE. At least 4V was necessary to light up the LED.

Therefore, our rGO-P2-covered polymer films could be used as lightweight electrode materials where good mechanical stability and transparency are important.

6.3.8. Towards Conductive Textiles: Coating PP Mesh with rGO-P2

Surface structure and morphology of rGO-PP mesh

In this section of the dissertation we demonstrate that our rGO-P2 nanoscale layers can be integrated into textiles to make porous conductors. For this, we used melt-blown polypropylene mesh (PP-mesh) fabric with 160 kg/m^3 density or ~83% porosity. Conductive rGO-PP-mesh material was prepared by dip-coating from 0.65 mg/ml GO-P2 solution and subsequent HI reduction. For practicality, the PP-mesh was not subject to any pretreatment or preliminary rinse with solvents.

The SEM and optical images of PP mesh covered with rGO-P2 sheets (rGO-PP-mesh) are shown in **Figure 6.25(A-F)**. In **Figure 6.25(A, B)** shows the control PP-mesh with clearly visible interlace fibers whose surface is clean and smooth. After the dip-coating and chemical reduction process, rGO-P2 sheets could be detected, as shown in **Figure 6.25(C, F)**. They appear to be well-deposited on the surface of PP mesh with no visible aggregation. Enlarging to the higher magnification the spiderweb-like structure of rGO-P2 nanosheets attached to the PP fibers can be observed from **Figure 6(E, F)**. These results suggest, that the network of well-overlapped rGO-P2 sheets could result in

electrically conductive PP textile fabric. In the next section we studied the electrical conductivity of rGO-PP-mesh using two-point probe method.

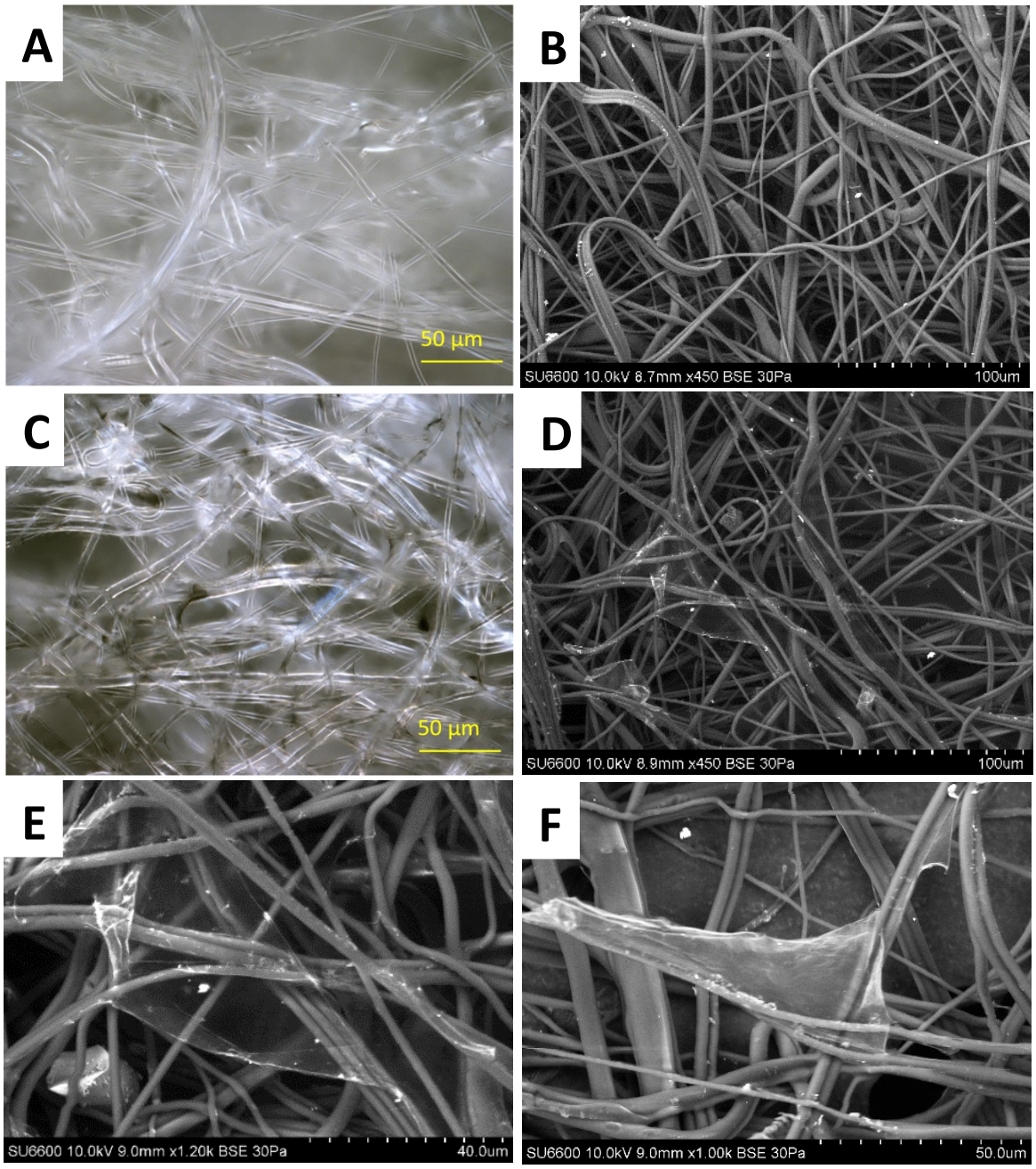

Figure 6.25: Optical (A) and SEM (B) images of plain PP-mesh. Optical (C) and SEM (D – F) images of PP-mesh coated with rGO-P2 on the mesh fiber surface.

Electrical conductivity of rGO-PP mesh

Figure 6.26A shows a conductive fabric rGO-PP-mesh with two contacts made of silver paste. Current *vs.* voltage (*I-V* curve) of the rGO-PP-mesh fabric is shown in **Figure 6.26B.** The I-V curve was measured within the bias voltage range -4 to 4 V at 0.1 V intervals. The electrical conduction conforms to Ohm's law, as the *I-V* curve reveals linear behavior. The sheet resistance R_s of ≈ 1.27 MΩ/sq. was found as an inverse slope (slope = $1/R_s$) of *I-V* curve normalized by (W/L) ratio, were W and L are termed as width and length of conductive channel.

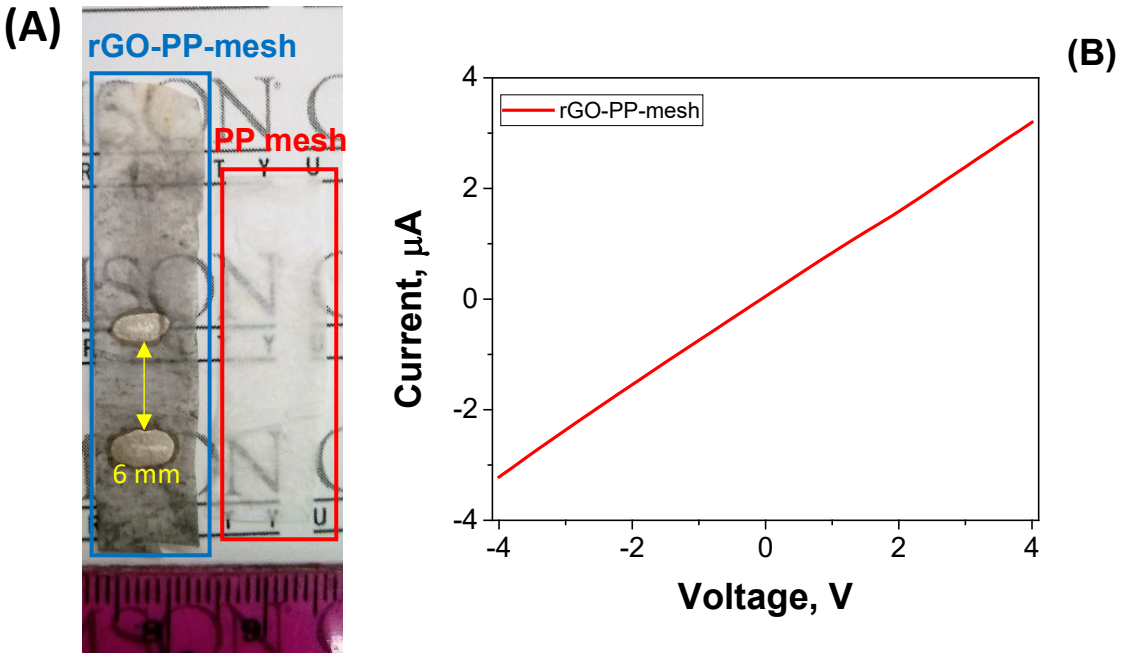

Figure 6.26: Plain PP mesh next to conductive rGO-PP-mesh with two silver contacts (A) and *I-V* curve acquired under ambient conditions (B).

The obtained results indicated that rGO-PP-mesh could be used in applications of electromagnetic interference (EMI) shielding, as shown in Ref. [70]. Furthermore, it was

revealed in the next section that rGO-PP-mesh fabric possesses efficient electro-mechanical properties suitable for truly wearable electronics, where repetitive bending/wrinkling often takes place.

Life-cycle testing

To test the electro-mechanical stability of rGO-PP-mesh we performed bending test (**Figure 6.27)**. According to the bending results shown in **Figure 6.27 (inset)** the relative resistance of rGO-PP-mesh started to decrease rapidly during first ~2000 bending cycles, which can result from tighter overlap/compression between rGO-covered fibers due to tensile strain. However, more research is needed to be done to further understand the linear decrease in signal during 100000 bending cycles.

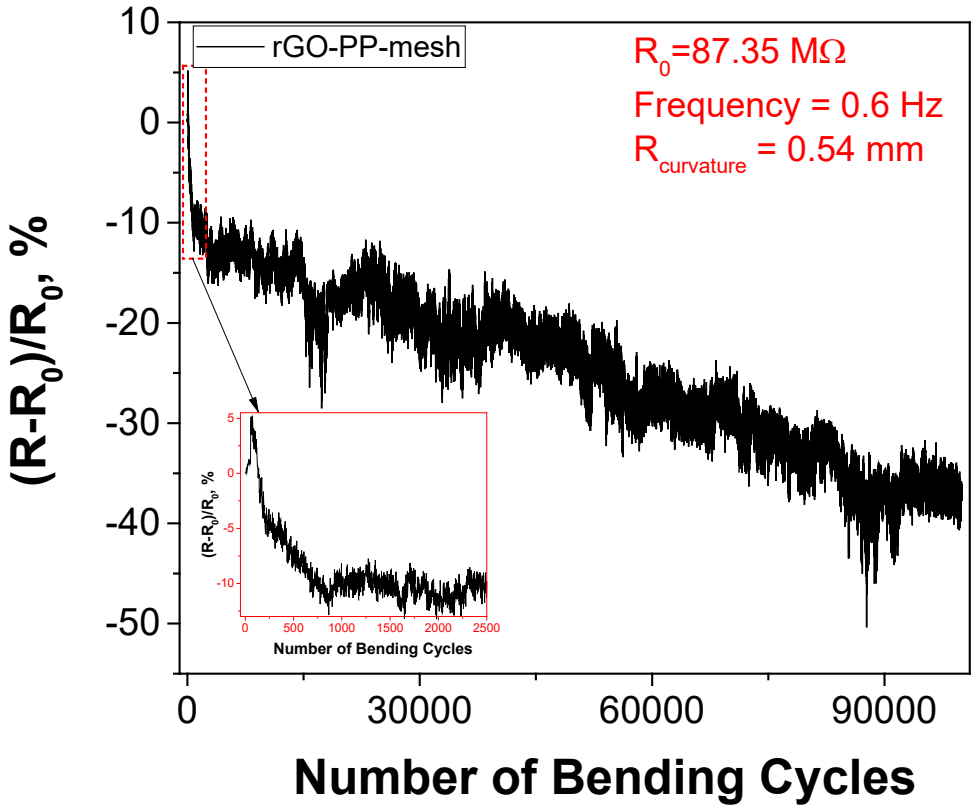

Figure 6.27: Electrical resistance change of the rGO-PP-mesh with repeated cycles of bending.

6.4: Conclusions

The following conclusions can be determined as a result of our study reported in Chapter 6:

- Owing to the van der Waals forces and strong interactions between the films and the plastic substrates, the GO-P2 films were not damaged or detached from the polymeric substrates during the chemical reduction process.
- When rGO-P2 is on the “rough” polymer surface it does not lie flat on top of the target surface, instead it conforms to the morphological features on the surface.

- Reduced GO-P2 films on thin Kapton and PP substrates exhibited ohmic behavior and high tolerance to flexural deformations.
- The electrical and optical properties of rGO-P2 films can be modulated by varying the concentration of GO-P2 solution during dip-coating step.
- The results demonstrated that our fabricated rGO/Kapton and rGO/PP films had long cycling stability even if bent to extreme radii of curvature.
- New approach for Raman spectra analysis showed a great promise for differentiating the nature of defects in graphene oxide material.

6.5: References

1. Pei, S.; Zhao, J.; Du, J.; Ren, W.; Cheng, H.-M., Direct reduction of graphene oxide films into highly conductive and flexible graphene films by hydrohalic acids. *Carbon* **2010,** *48* (15), 4466-4474.

2. Neves, A. I. S.; Bointon, T. H.; Melo, L. V.; Russo, S.; de Schrijver, I.; Craciun, M. F.; Alves, H., Transparent conductive graphene textile fibers. *Scientific Reports* **2015,** *5*, 9866.

3. http://www.micosusa.com/old/Con_5018.html

4. http://www.mecourse.com/landinig/software/software.html

5. Glushko, O.; Cordill, M. J., Electrical Resistance of Metal Films on Polymer Substrates Under Tension. *Experimental Techniques* **2014,** *0* (0).

6. Sanghyeok, K.; Sejeong, W.; Gi-Dong, S.; Inkyu, P.; Soon-Bok, L., Tensile characteristics of metal nanoparticle films on flexible polymer substrates for printed electronics applications. *Nanotechnology* **2013,** *24* (8), 085701.

7. Hathout, D., Sine-Generated Curves: Theoretical and Empirical Notes. *Advances in Pure Mathematics* **2015,** *Vol.05No.11*, 14.

8. Zienkiewicz OC, Taylor RL, Zhu JZ (2013) The finite element

method: its basis and fundamentals. Elsevier, Oxford

9. ANSYS Release 12.1, ANSYS, Inc., PA, 2013.

10. http://ansoft.com/staticassets/ANSYS/staticassets/resourcelibrary/confpaper/2006-Int-ANSYS-Conf-22.pdf

11. Schicker, J.; Khan, W. A.; Arnold, T.; Hirschl, C., Simulating the warping of thin coated Si wafers using Ansys layered shell elements. C*omposite Structures 2***016,** 1*40* (Supplement C), 668-674.

12. http://www.dupont.com/content/dam/dupont/products-and-services/membranes-and-films/polyimde-films/documents/DEC-Kapton-summary-of-properties.pdf (accessed 1/16/2018).

13. Kurtz, S. M.; Pruitt, L.; Jewett, C. W.; Paul Crawford, R.; Crane, D. J.; Edidin, A. A., The yielding, plastic flow, and fracture behavior of ultra-high molecular weight polyethylene used in total joint replacements. B*iomaterials 1***998,** 1*9* (21), 1989-2003.

14. Jimenez Rioboo, R. J.; Climent-Pascual, E.; Diez-Betriu, X.; Jimenez-Villacorta, F.; Prieto, C.; de Andres, A., Elastic constants of graphene oxide few-layer films: correlations with interlayer stacking and bonding. J*ournal of Materials Chemistry C 2***015,** 3 (19), 4868-4875.

15. Paradee, G.; Martin, T.; Christou, A., Fatigue Properties of ITO and Graphene on Flexible Substrates. I*EEE Trans. Device Mater. Reliab. 2***015,** 1*5* (3), 423-428.

16. Memarian, F.; Fereidoon, A.; Darvish Ganji, M., Graphene Young's modulus: Molecular mechanics and DFT treatments. S*uperlattices and Microstructures 2***015,** 8*5,* 348-356.

17. Jung, I.; Pelton, M.; Piner, R.; Dikin, D. A.; Stankovich, S.; Watcharotone, S.; Hausner, M.; Ruoff, R. S., Simple approach for high-contrast optical imaging and characterization of graphene-based sheets. N*ano Letters 2***007,** 7 (12), 3569-3575.

18. Semat, H.; Katz, R., P*hysics.* Rinehart: 1958.

19. Blake, P.; Hill, E. W.; Castro Neto, A. H.; Novoselov, K. S.; Jiang, D.; Yang, R.; Booth, T. J.; Geim, A. K., Making graphene visible. A*pplied Physics Letters 2***007,** 9*1* (6).

20. Romagnoli, P.; Rosa, H. G.; Lopez-Cortes, D.; Souza, E. A. T.; Viana-Gomes, J. C.; Margulis, W.; de Matos, C. J. S., Making graphene visible on transparent dielectric substrates: Brewster angle imaging. 2*d Materials 2***015,** 2 (3).

21. Stankovich, S.; Dikin, D. A.; Piner, R. D.; Kohlhaas, K. A.; Kleinhammes, A.; Jia, Y.; Wu, Y.; Nguyen, S. T.; Ruoff, R. S., Synthesis of graphene-based nanosheets via chemical reduction of exfoliated graphite oxide. C*arbon 2***007,** 4*5* (7), 1558-1565.

22. Some, S.; Kim, Y.; Yoon, Y.; Yoo, H.; Lee, S.; Park, Y.; Lee, H., High-Quality Reduced Graphene Oxide by a Dual-Function Chemical Reduction and Healing Process. S*cientific Reports 2***013,** 3*,* 5.

23. López-Díaz, D.; López Holgado, M.; García-Fierro, J. L.; Velázquez, M. M., Evolution of the Raman Spectrum with the Chemical Composition of Graphene Oxide. T*he Journal of Physical Chemistry C 2***017,** 1*21* (37), 20489-20497.

24. Eckmann, A.; Felten, A.; Mishchenko, A.; Britnell, L.; Krupke, R.; Novoselov, K. S.; Casiraghi, C., Probing the Nature of Defects in Graphene by Raman Spectroscopy. N*ano Letters 2***012,** 1*2* (8), 3925-3930.

25. Bruna, M.; Ott, A. K.; Ijäs, M.; Yoon, D.; Sassi, U.; Ferrari, A. C., Doping Dependence of the Raman Spectrum of Defected Graphene. A*CS Nano 2***014,** 8 (7), 7432-7441.

26. King, A. A. K.; Davies, B. R.; Noorbehesht, N.; Newman, P.; Church, T. L.; Harris, A. T.; Razal, J. M.; Minett, A. I., A New Raman Metric for the Characterisation of Graphene oxide and its Derivatives. S*cientific Reports 2***016,** 6*,* 19491.

27. Hui, L. S.; Whiteway, E.; Hilke, M.; Turak, A., Synergistic oxidation of CVD graphene on Cu by oxygen plasma etching. C*arbon 2***017,** 1*25,* 500-508.

28. Carotenuto, G.; Nicola, S. D.; Ausanio, G.; Massarotti, D.; Nicolais, L.; Pepe, G. P., Synthesis and characterization of electrically conductive polyethylene-supported graphene films. N*anoscale Research Letters 2***014,** 9 (1), 475-475.

29. Banerjee, I.; Faris, T.; Stoeva, Z.; Harris, P. G.; Chen, J.; Sharma, A. K.; Ray, A. K., Graphene films printable on flexible substrates for sensor applications. 2*d Materials 2***017,** 4 (1), 12.

30. Chen, H.; Müller, M. B.; Gilmore, K. J.; Wallace, G. G.; Li, D., Mechanically Strong, Electrically Conductive, and Biocompatible Graphene Paper. A*dv. Mater. 2***008,** 2*0* (18), 3557-3561.

31. Gerardo, G. N.; Salvador, B.-L.; Maurice, O.-L.; Humberto, T., Electronic and optical properties of strained graphene and other strained 2D materials: a review. R*eports on Progress in Physics 2***017,** 8*0* (9), 096501.

32. Atanasov, V.; Saxena, A., Tuning the electronic properties of corrugated graphene: Confinement, curvature, and band-gap opening. P*hysical Review B 2***010,** 8*1* (20), 205409.

33. Bunch, J. S.; Verbridge, S. S.; Alden, J. S.; van der Zande, A. M.; Parpia, J. M.; Craighead, H. G.; McEuen, P. L., Impermeable Atomic Membranes from Graphene Sheets. N*ano Letters 2***008,** 8 (8), 2458-2462.

34. Koenig, S. P.; Boddeti, N. G.; Dunn, M. L.; Bunch, J. S., Ultrastrong adhesion of graphene membranes. N*ature Nanotechnology 2***011,** 6*,* 543.

35. Teng, L.; Zhao, Z., Substrate-regulated morphology of graphene. J*ournal of Physics D: Applied Physics 2***010,** 4*3* (7), 075303.

36. Aitken, Z. H.; Huang, R., Effects of mismatch strain and substrate surface corrugation on morphology of supported monolayer graphene. J*ournal of Applied Physics 2***010,** 1*07* (12), 123531.

37. Zhang, L.; Shi, Z.; Wang, Y.; Yang, R.; Shi, D.; Zhang, G., Catalyst-free growth of nanographene films on various substrates. N*ano Research 2***011,** 4 (3), 315-321.

38. Joung, D.; Chunder, A.; Zhai, L.; Khondaker, S. I., Space charge limited conduction with exponential trap distribution in reduced graphene oxide sheets. A*pplied Physics Letters 2*0**10,** 9*7* (9), 3.

39. Chen, J.-H.; Jang, C.; Xiao, S.; Ishigami, M.; Fuhrer, M. S., Intrinsic and extrinsic performance limits of graphene devices on SiO2. N*ature Nanotechnology 2*0**08,** 3*,* 206.

40. Gomez-Navarro, C.; Weitz, R. T.; Bittner, A. M.; Scolari, M.; Mews, A.; Burghard, M.; Kern, K., Electronic transport properties of individual chemically reduced graphene oxide sheets. N*ano Letters 2*0**07,** 7 (11), 3499-3503.

41. Tan, Kim S.; Grimsdale, A. C.; Yazami, R., A room-temperature refuelable lithium, iodine and air battery. S*cientific Reports 2*0**17,** 7 (1), 6502.

42. Alkhazali, A. S.; Hamasha, M. M.; Lu, S.; Westgate, C. R., A Comparative Study on Electrical and Mechanical Behavior of Indium Tin Oxide and Poly (3, 4-Ethylenedioxythiophene) Thin Films Under Tensile Loads. I*EEE Transactions on Device and Materials Reliability 2*0**15,** 1*5* (2), 174-180.

43. Ye, X.; Yuan, Z.; Tai, H.; Li, W.; Du, X.; Jiang, Y., A wearable and highly sensitive strain sensor based on a polyethylenimine-rGO layered nanocomposite thin film. J*ournal of Materials Chemistry C 2*0**17,** 5 (31), 7746-7752.

44. Xu, M.; Qi, J.; Li, F.; Zhang, Y., Highly stretchable strain sensors with reduced graphene oxide sensing liquids for wearable electronics. N*anoscale 2*0**18,** 1*0* (11), 5264-5271.

45. Tanmoy, D.; Bhupendra, K. S.; Ajit, K. K.; Jong-Hyun, A., Graphene-based flexible and wearable electronics. J*ournal of Semiconductors 2*0**18,** 3*9* (1), 011007.

46. Liu, Q.; Zhang, M.; Huang, L.; Li, Y.; Chen, J.; Li, C.; Shi, G., High-Quality Graphene Ribbons Prepared from Graphene Oxide Hydrogels and Their Application for Strain Sensors. A*CS Nano 2*0**15,** 9 (12), 12320-12326.

47. Lu, N.; Suo, Z.; Vlassak, J. J., The effect of film thickness on the failure strain of polymer-supported metal films. A*cta Materialia 2*0**10,** 5*8* (5), 1679-1687.

48. Ye, X.; Yuan, Z.; Tai, H.; Li, W.; Du, X.; Jiang, Y., A wearable and highly sensitive strain sensor based on a polyethylenimine–rGO layered nanocomposite thin film. J*ournal of Materials Chemistry C 2*0**17,** 5 (31), 7746-7752.

49. Li, X.; Yang, T.; Yang, Y.; Zhu, J.; Li, L.; Alam, F. E.; Li, X.; Wang, K.; Cheng, H.; Lin, C.-T.; Fang, Y.; Zhu, H., Large-Area Ultrathin Graphene Films by Single-Step Marangoni Self-Assembly for Highly Sensitive Strain Sensing Application. A*dvanced Functional Materials 2*0**16,** 2*6* (9), 1322-1329.

50. Huitema, E.; Gelinck, G.; Van Lieshout, P.; Van Veenendaal, E.; Touwslager, F., Flexible electronic-paper active-matrix displays. J*ournal of the Society for Information Display 2***005,** 1*3* (3), 181-185.

51. Han, T.-H.; Kim, H.; Kwon, S.-J.; Lee, T.-W., Graphene-based flexible electronic devices. M*aterials Science and Engineering: R: Reports 2***017,** 1*18,* 1-43.

52. Han, S.; Liu, C.; Xu, H.; Yao, D.; Yan, K.; Zheng, H.; Chen, H.-J.; Gui, X.; Chu, S.; Liu, C., Multiscale nanowire-microfluidic hybrid strain sensors with high sensitivity and stretchability. n*pj Flexible Electronics 2***018,** 2 (1), 16.

53. Molina, J., Graphene-based fabrics and their applications: a review. R*sc Advances 2***016,** 6 (72), 68261-68291.

54. Yetisen, A. K.; Qu, H.; Manbachi, A.; Butt, H.; Dokmeci, M. R.; Hinestroza, J. P.; Skorobogatiy, M.; Khademhosseini, A.; Yun, S. H., Nanotechnology in Textiles. A*CS Nano 2***016,** 1*0* (3), 3042-3068.

55. Alaferdov, A. V.; Savu, R.; Rackauskas, S.; Rackauskas, T.; Canesqui, M. A.; Moshkalev, S., G*raphene nanobelts films for highly sensitive, transparent and flexible pressure and strain resistive sensors.* 2015.

56. Yao, S.; Zhu, Y., W*earable multifunctional sensors using printed stretchable conductors made of silver nanowires.* 2014; Vol. 6.

57. Han, T.-H.; Kim, H.; Kwon, S.-J.; Lee, T. W., G*raphene-based flexible electronic devices.* 2017; Vol. 118, p 1-43.

58. Fang, Y. N.; Hester, J. G. D.; deGlee, B.; Tuan, C. C.; Brooke, P. D.; Le, T. R.; Wong, C. P.; Tentzeris, M. M.; Sandhage, K. H., A novel, facile, layer-by-layer substrate surface modification for the fabrication of all-inkjet-printed flexible electronic devices on Kapton. J*ournal of Materials Chemistry C 2***016,** 4 (29), 7052-7060.

59. Chauhan, S. S.; Abraham, M.; Choudhary, V., Electromagnetic shielding and mechanical properties of thermally stable poly(ether ketone)/multi-walled carbon nanotube composites prepared using a twin-screw extruder equipped with novel fractional mixing elements. R*SC Adv. 2***016,** 6 (114), 113781-113790.

60. Anh Son, H., Electrical conductivity and electromagnetic interference shielding characteristics of multiwalled carbon nanotube filled polyurethane composite films. A*dvances in Natural Sciences: Nanoscience and Nanotechnology 2***011,** 2 (2), 025007.

61. Hu, M. J.; Gao, J. F.; Dong, Y. C.; Li, K.; Shan, G. C.; Yang, S. L.; Li, R. K. Y., Flexible Transparent PES/Silver Nanowires/PET Sandwich-Structured Film for High-Efficiency Electromagnetic Interference Shielding. L*angmuir 2***012,** 2*8* (18), 7101-7106.

62. Bright, C. I.; Le, J. D.; Fitzer, R. C.; Maki, S. P., Ultrathin transparent EMI shielding film comprising a polymer basecoat and crosslinked polymer transparent dielectric layer. Google Patents: 2013.

63. Chaudhary, A.; Kumar, R.; Teotia, S.; Dhawan, S. K.; Dhakate, S. R.; Kumari, S., Integration of MCMBs/MWCNTs with Fe3O4 in a flexible and light weight composite paper for promising EMI shielding applications. J*ournal of Materials Chemistry C 2***017,** 5 (2), 322-332.

64. Gulrez, S. K. H.; Ali Mohsin, M. E.; Shaikh, H.; Anis, A.; Pulose, A. M.; Yadav, M. K.; Qua, E. H. P.; Al-Zahrani, S. M., A review on electrically conductive polypropylene and polyethylene. P*olymer Composites 2***014,** 3*5* (5), 900-914.

65. Hong, S. K.; Kim, K. Y.; Kim, T. Y.; Kim, J. H.; Park, S. W.; Kim, J. H.; Cho, B. J., Electromagnetic interference shielding effectiveness of monolayer graphene. N*anotechnology 2***012,** 2*3* (45), 5.

66. Wu, Z. P.; Cheng, D. M.; Ma, W. J.; Hu, J. W.; Yin, Y. H.; Hu, Y. Y.; Li, Y. S.; Yang, J. G.; Xu, Q. F., Electromagnetic interference shielding effectiveness of composite carbon nanotube macro-film at a high frequency range of 40 GHz to 60 GHz. A*IP Advances 2***015,** 5 (6), 067130.

67. Wei, C.; Jun, W.; Bin, Z.; Qilei, W.; Xiaogang, S., Enhanced electromagnetic interference shielding properties of carbon fiber veil/Fe 3 O 4 nanoparticles/epoxy multiscale composites. M*aterials Research Express 2***017,** 4 (12), 126303.

68. Kim, S.; Oh, J.-S.; Kim, M.-G.; Jang, W.; Wang, M.; Kim, Y.; Seo, H. W.; Kim, Y. C.; Lee, J.-H.; Lee, Y.; Nam, J.-D., Electromagnetic Interference (EMI) Transparent Shielding of Reduced Graphene Oxide (RGO) Interleaved Structure Fabricated by Electrophoretic Deposition. A*CS Applied Materials & Interfaces 2***014,** 6 (20), 17647-17653.

69. Sarto, F.; Sarto, M. S.; Larciprete, M. C.; Sibilia, C., TRANSPARENT FILMS FOR ELECTROMAGNETIC SHIELDING OF PLASTICS. R*ev. Adv. Mater. Sci. 2***003,** 5 (4), 329-336.

70. Tian, M.; Du, M.; Qu, L.; Chen, S.; Zhu, S.; Han, G., Electromagnetic interference shielding cotton fabrics with high electrical conductivity and electrical heating behavior via layer-by-layer self-assembly route. R*SC Advances 2***017,** 7 (68), 42641-42652.

CHAPTER SEVEN

CONCLUSIONS

This chapter is devoted to concluding body of work presented in this dissertation. The study of transparent conductive films based on polymer-encapsulated GO resulted in a number of observations about transparent conductive films. The following major conclusions can be drawn:

- Steric stabilization of individual GO sheets was achieved through its surface modification with P1 copolymer.
- GO-P1 monolayer showed strong adhesion to the SIO_2/Si substrate.
- Highly conductive (up to 10^4 S/cm) and transparent (~ 90%) rGO-P1 monolayers and bi-layers on non-conductive substrates were produced.
- GO-P1 flakes showed higher level of reduction and carbonization/graphitization in the presence of PAA carbon residue as evidenced from XPS and AFM.
- Enhanced hydrophobic-hydrophobic interaction allowed to achieve formation of uniform layers on both hydrophilic and hydrophobic surfaces by using more hydrophobic P2 copolymer.
- The electrical and optical properties of rGO-P2 films can be modulated by varying the concentration of GO-P2 solution during dip-coating step.
- Reduced GO-P2 films on thin Kapton and PP substrates exhibited ohmic behavior and high tolerance to flexural deformations.

Appendix A

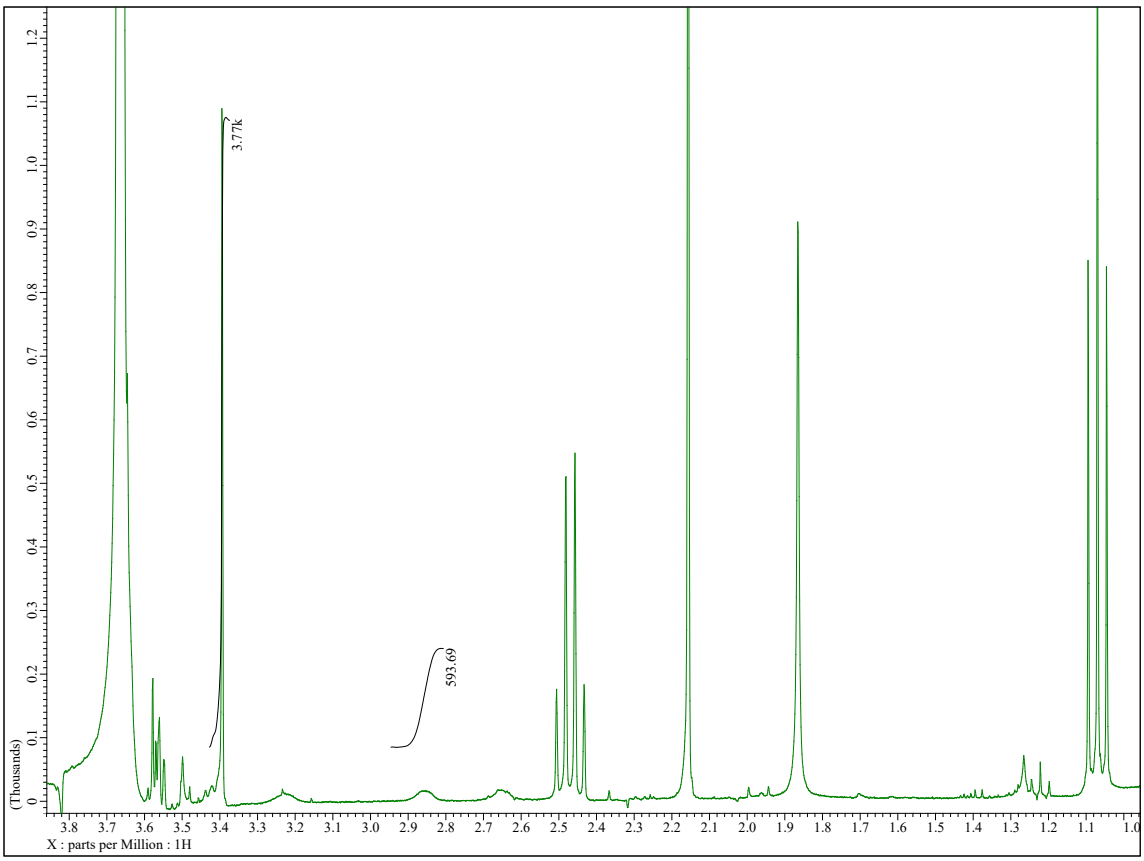

Figure A1. ^{1}HNMR spectra of P1 copolymer as received.

NMR has been done by Dr. Nikolay Borodinov.

Surface morphology of GO-P1 and GO-P2 by high resolution AFM studies

To further investigate surface morphology of polymer modified GO flakes we performed a high-resolution AFM of a single GO-P1 and GO-P2 deposited on hydrophilic SiO_2 wafer from water and water-methanol mixture in 1:1 ratio using dip-coating and spin-coating. **Figure A2 (C, D)**) shows that polymer extension or corona of spindles was only observed for films spun from solutions with at least 1:1 water-methanol ratio, while it has not been so for GO-P1/P2 flakes dispersed in water (**Figure A2 (E, F)**).We could clearly distinguish the individual strands of copolymer protruding out of edges of GO-P1/P2 sheets (**Figure A2(C, D)**) after spin-coating but not dip-coating. It was demonstrated in **Section 5.3.3** that POEGMA copolymer tends to extend in water-alcohol mixtures containing more than 50% alcohol, leading to an increase in apparent thickness.

High resolution AFM imaging has been done by Anise Grant under the guidance of Dr. Tsukruk from Georgia Institute of Technology. The images were captured using a Dimension Icon (Veeco Digital Instruments, Inc.) atomic force microscope in the tapping mode. Silicon tips with a spring constant of 45 N m^{-1}, a tip radius of approximately 8 nm, and resonance frequency of 350 kHz that was operated at scanning speed of 1 Hz. The analysis of AFM images was carried out using Nanoscope 1.40r1.

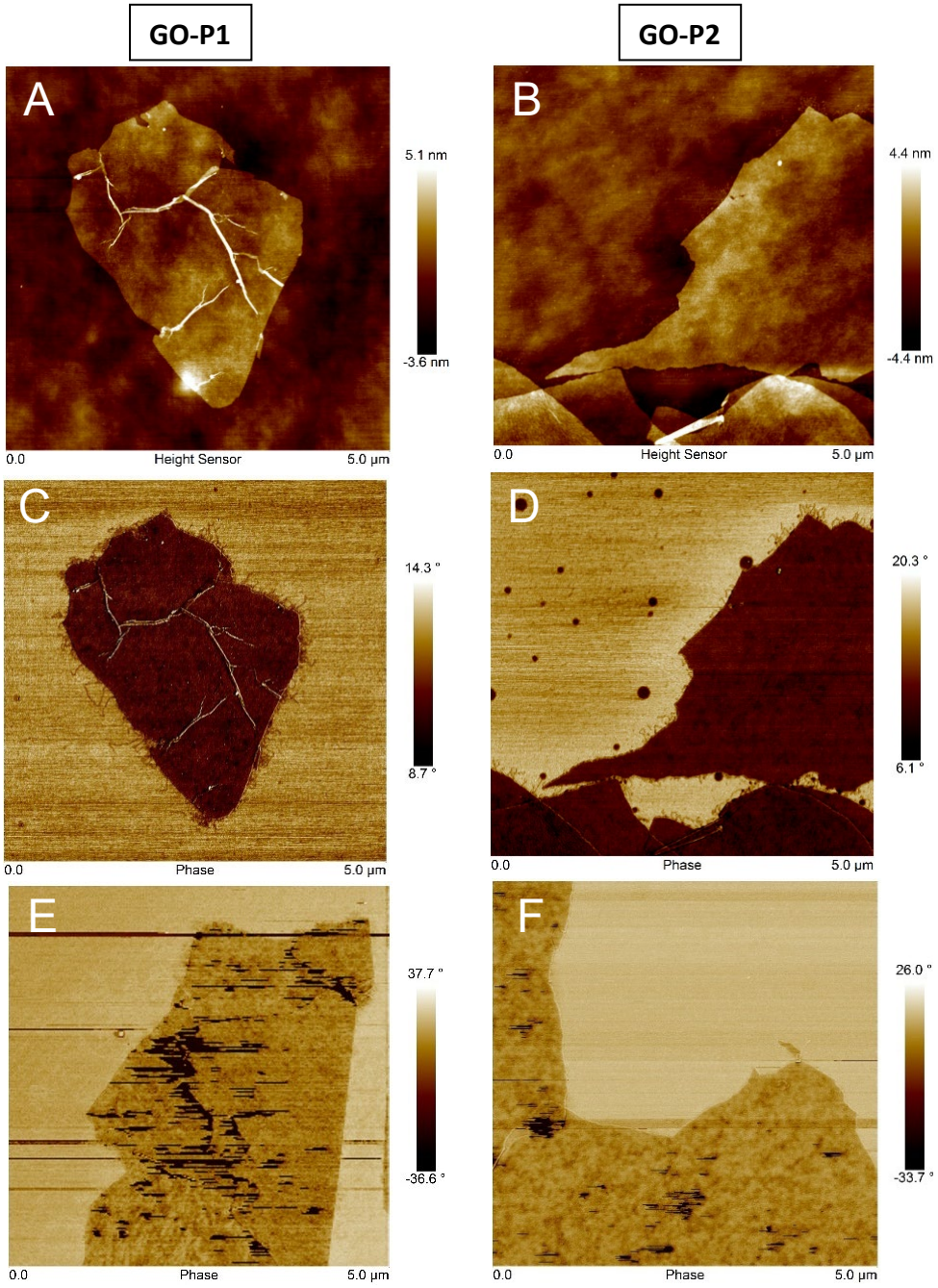

Figure A2. High resolution AFM: height (A, B) and phase images (C, D) of GO-P1 and GO-P2 on hydrophilic SiO_2 surface after deposition from water-methanol solution and water solution (E, F). Layers were deposited by spin-coating.

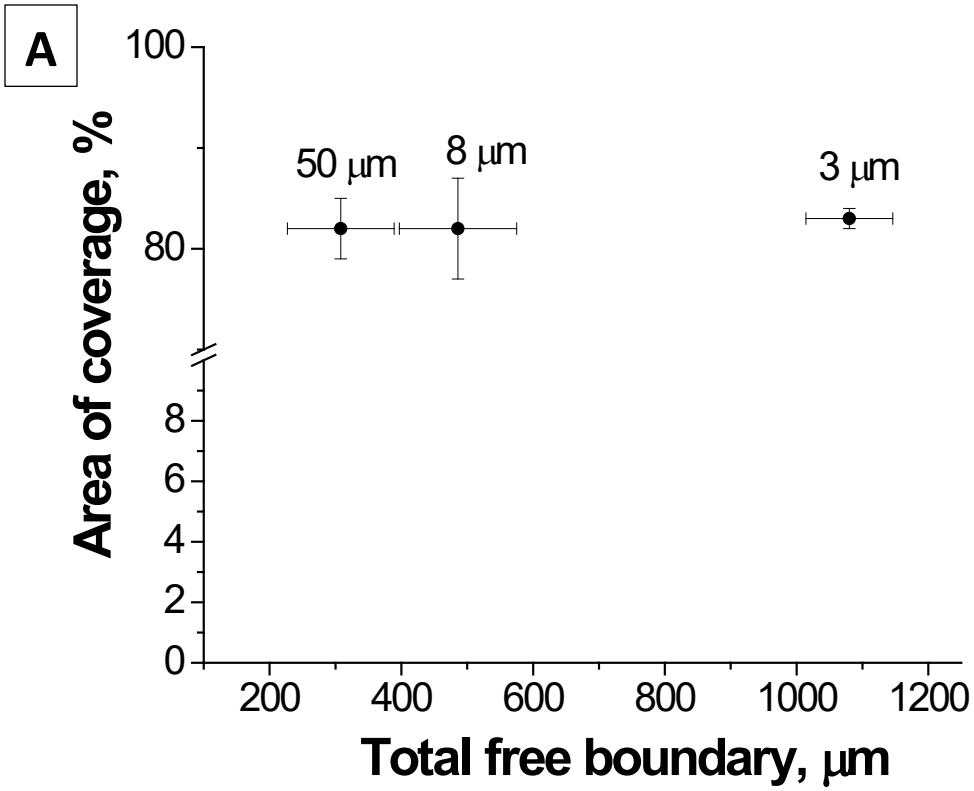

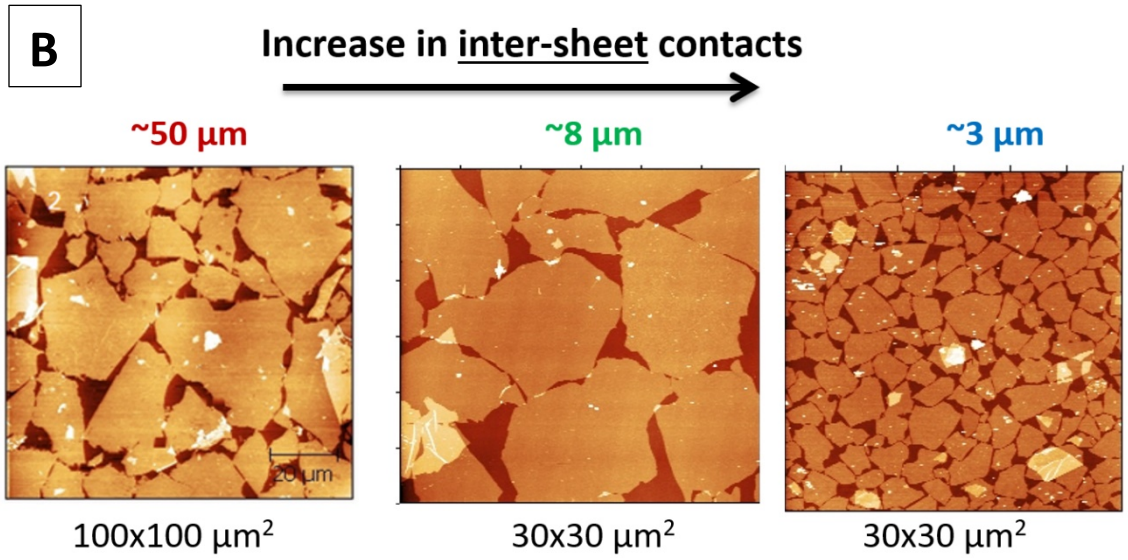

Figure A3. (A): Total free boundary as a function of average sheet size at given percentage of surface coverage for GO-P1 monolayer. (B): Monolayers of different sized GO-P1 sheets on hydrophilic Si substrate.

GO-P1/PAA/GO-P1 on hydrophilic SO_2/Si

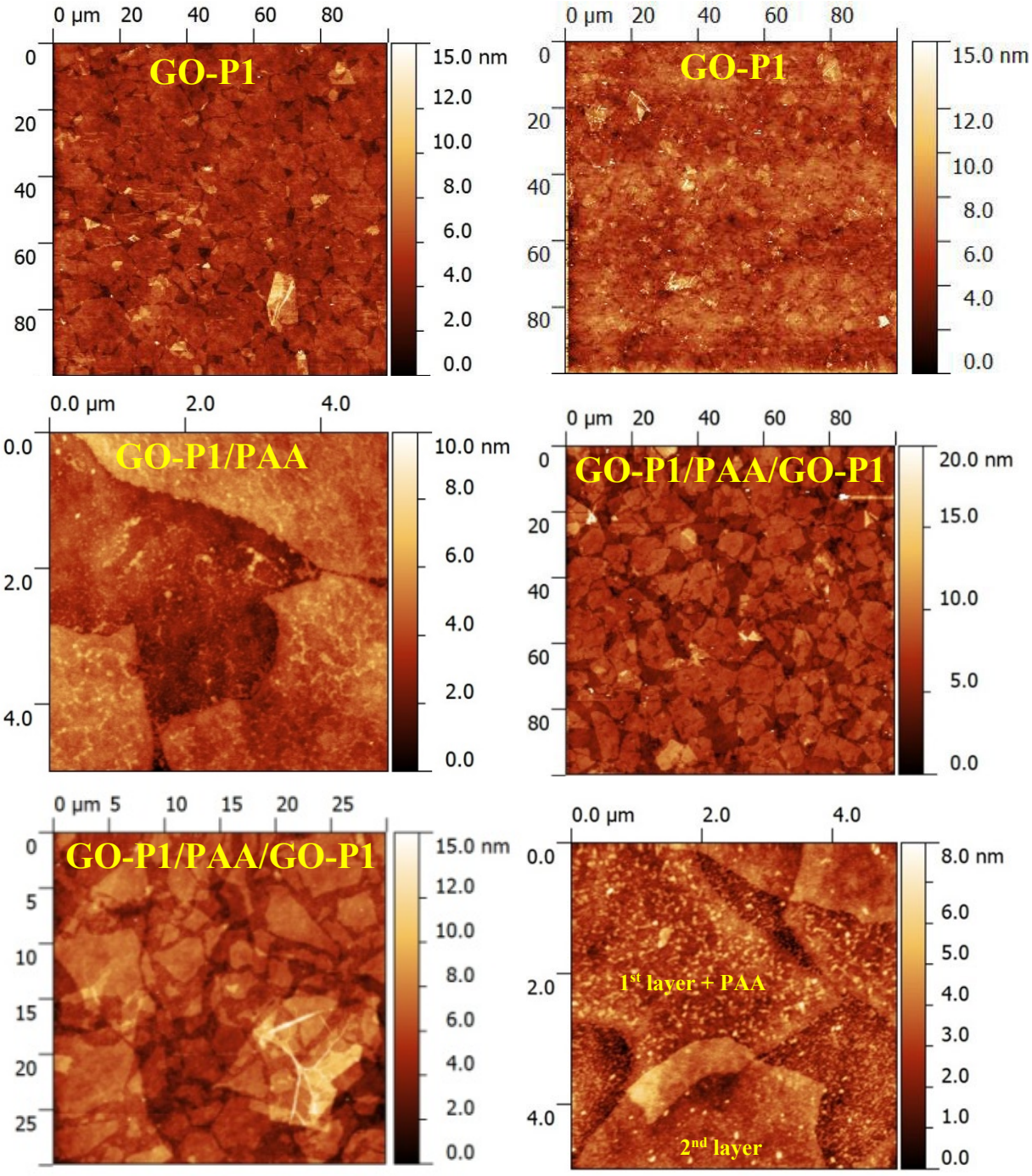

Figure A4. Samples after thermal reduction at 1150 ºC in Argon. The results illustrate the healing/welding process of rGO-P1/PAA/GO-P1 double layers.

rGO-P1 (Argon)

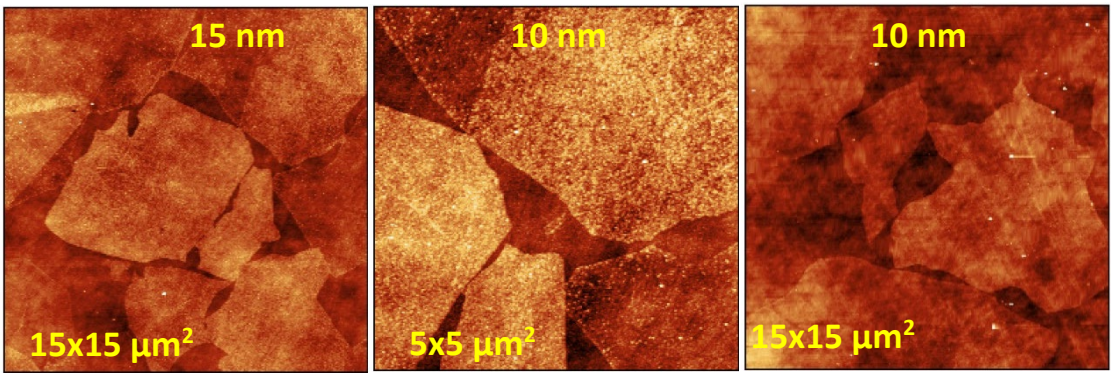

rGO-P1/PAA (Argon)

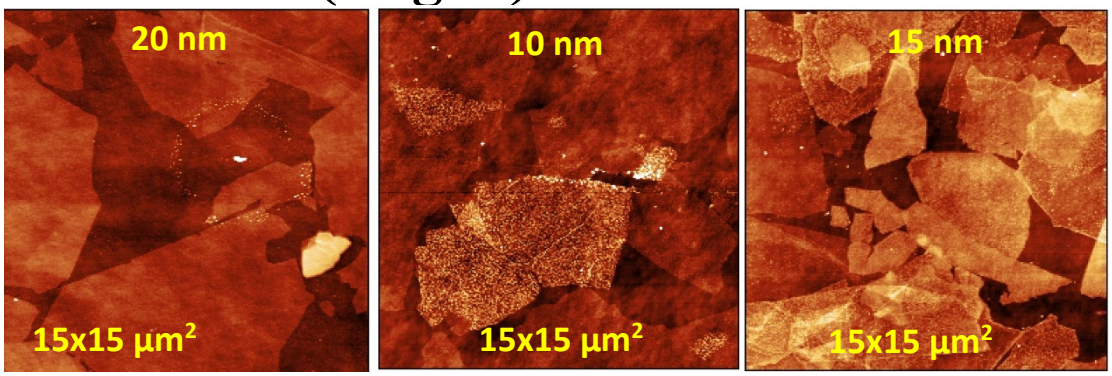

rGO-P1/PAA/GO-P1 (Nitrogen)

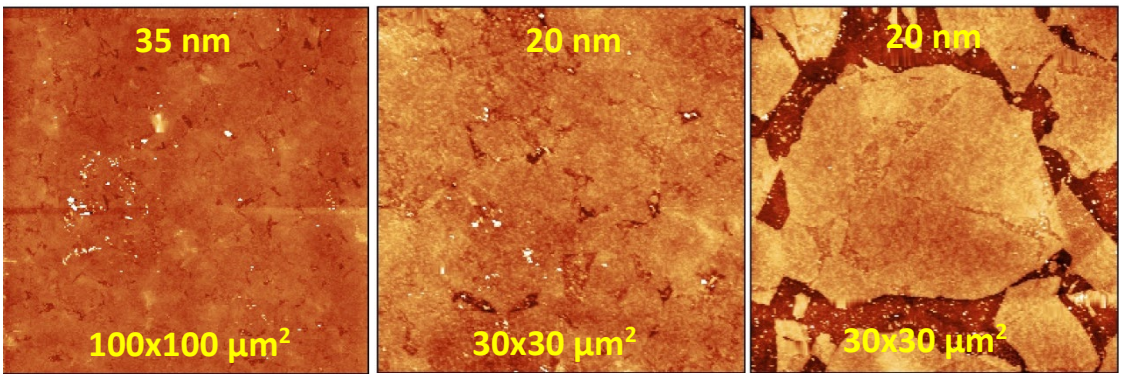

rGO-P1/PAA/GO-P1 (Argon)

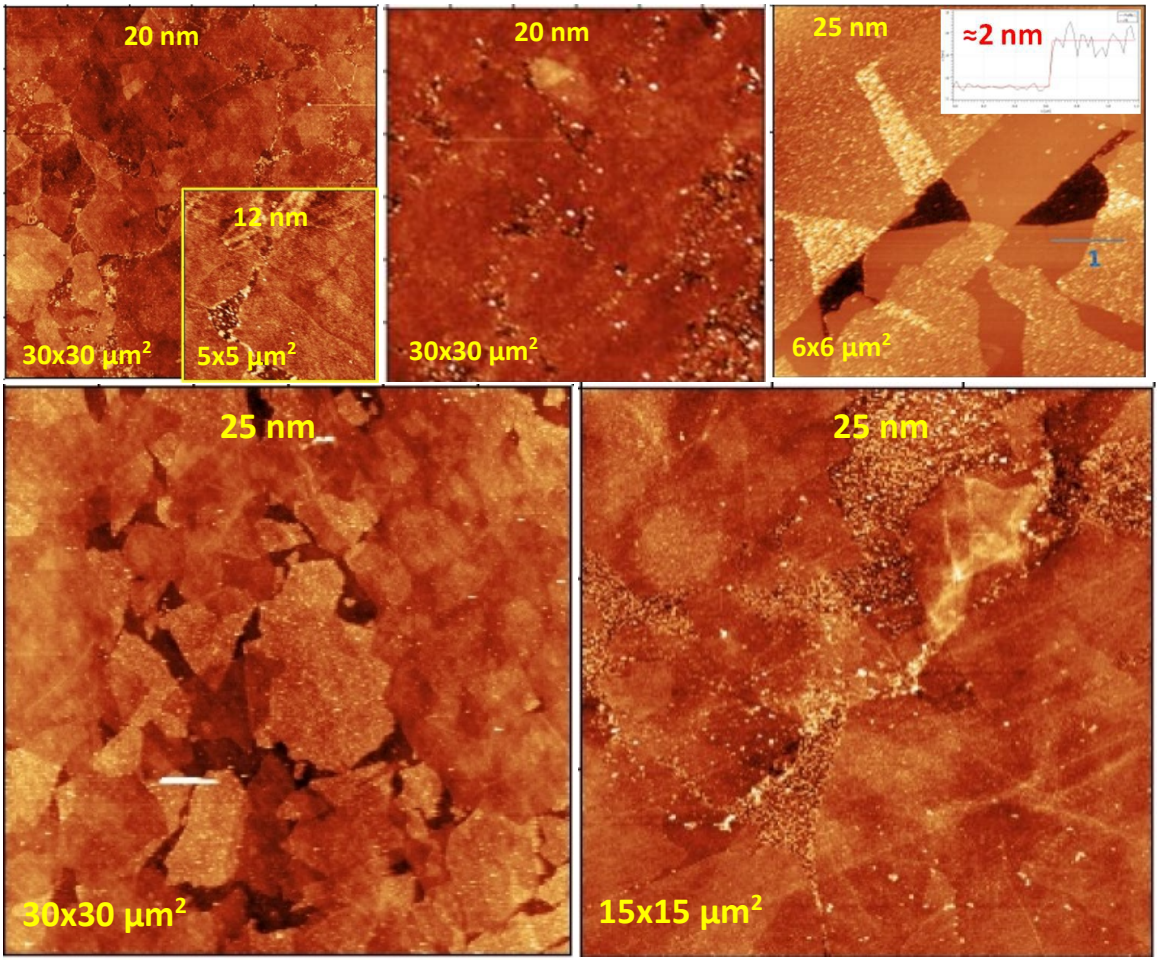

Figure A5. Samples after thermal reduction at 1150 ºC in Argon and Nitrogen. The results illustrate the healing/welding process of rGO-P1/PAA/GO-P1 double layers.

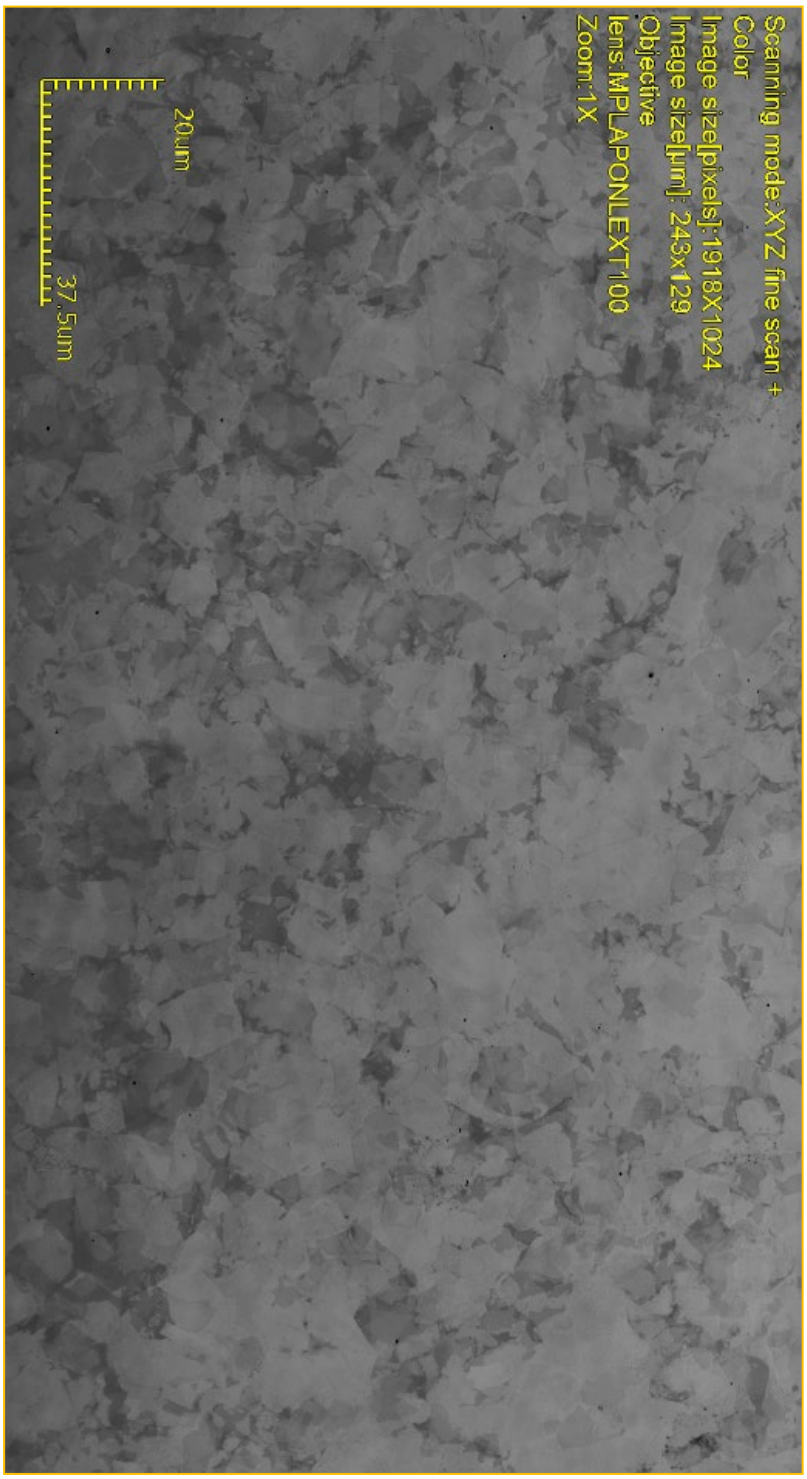

Figure A6. Optical image of rGO-P1/PAA/GO-P1 double layer on hydrophilic Si after thermal reduction at 1150 °C in Argon.

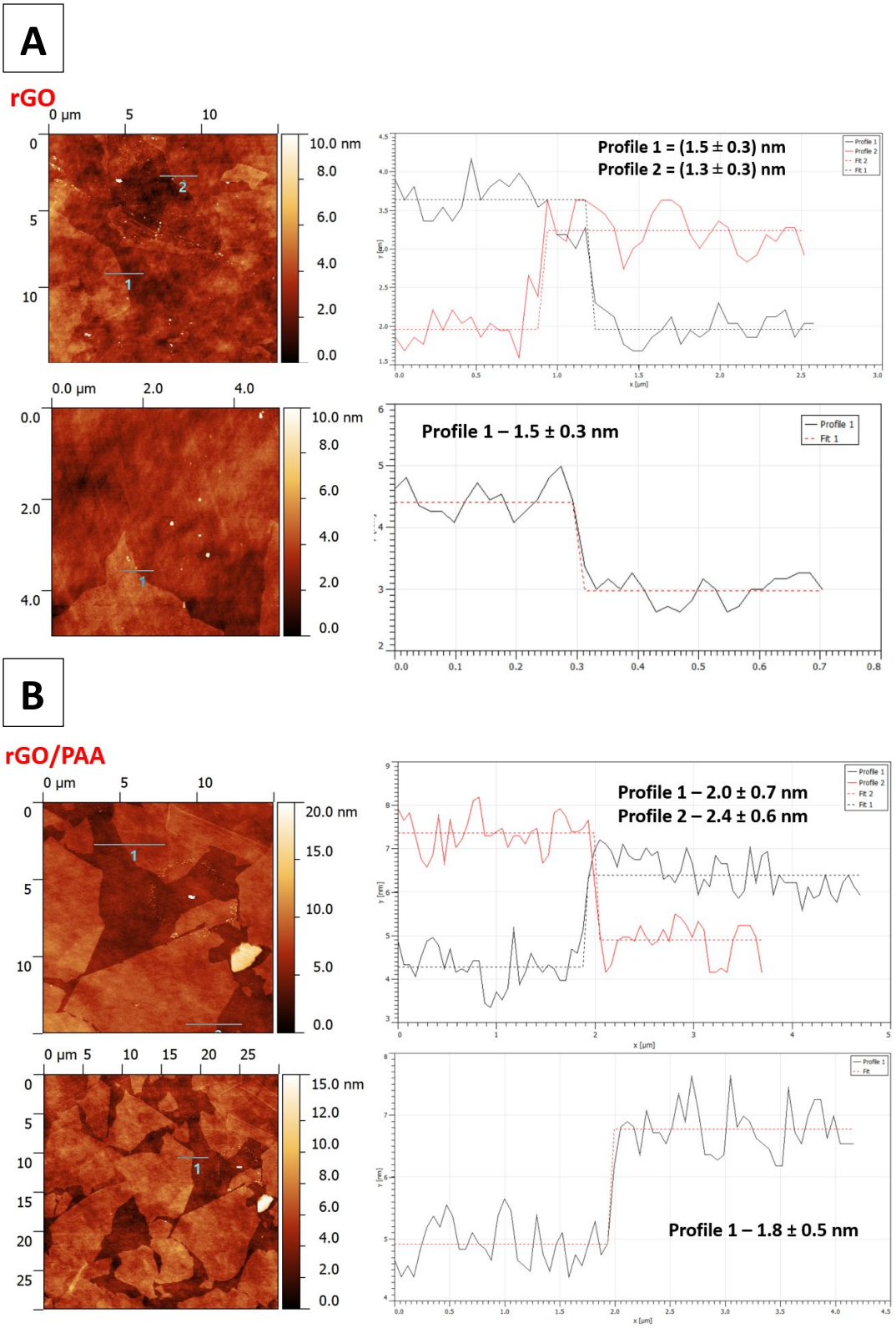

Figure A7: AFM images and corresponding cross-sectional profiles showing (A): rGO-P1 monolayer and (B): GO-P1/PAA. Samples were thermally annealed/reduced at 1150 ºC in Argon atmosphere.

Table A1. XPS data for peak area ratio of each functional group of each sample evaluated by the curve fitting technique with Gaussian-Lorentzian distribution.

GO_PAA_GO	Peak Position (eV)	Area	Peak area ratio (%)	C/O cal.		Reduced GO_PAA_GO	Peak Position (eV)	Area	Peak area ratio (%)	C/O cal.
(0) COOH	288.7	6264.4	9.6	2.5		(0) COOH	288.5	98.1	0.3	17.34
(1) C=O/C-O-C	287.1	11327	17.3			(1) C=O/C-O-C	286.9	906.1	3.0	
(2) C-OH	286.3	24681.8	37.7			(2) C-OH	285.7	1868.2	6.3	
(3) C-C/C=C	284.9	23179	35.4			(3) C-C/C=C	284.3	26984.4	90.4	
GO_PAA	Peak Position (eV)	Area	Peak area ratio (%)	C/O cal.		Reduced GO_PAA	Peak Position (eV)	Area	Peak area ratio (%)	C/O cal.
(0) COOH	288.8	8627.9	16.7	3.01		(0) COOH	288.7	375	1.5	10.68
(1) C=O/C-O-C	286.9	4957.4	9.6			(1) C=O/C-O-C	286.9	1066.2	4.3	
(2) C-OH	286.3	13415.7	25.9			(2) C-OH	285.5	2294.6	9.3	
(3) C-C/C=C	285	24758.3	47.8			(3) C-C/C=C	284.3	20857.1	84.8	
GO	Peak Position (eV)	Area	Peak area ratio (%)	C/O cal.		Reduced GO	Peak Position (eV)	Area	Peak area ratio (%)	C/O cal.
(0) COOH	288.7	2756.3	7.3	2.69		(0) COOH	288.6	284.9	1.5	4.14
(1) C=O/C-O-C	286.9	7393.2	19.7			(1) C=O/C-O-C	286.9	1398.5	7.4	
(2) C-OH	286.2	12717.2	33.8			(2) C-OH	285.5	6156.5	32.6	
(3) C-C/C=C	284.9	14730.3	39.2			(3) C-C/C=C	284.7	11060.6	58.5	
Pristine GO	Peak Position (eV)	Area	Peak area ratio (%)	C/O cal.		Reduced pristine GO	Peak Position (eV)	Area	Peak area ratio (%)	C/O cal.
(0) COOH	289.3	2333.3	7.3	3.02		(0) COOH	288.5	57.3	0.5	6
(1) C=O/C-O-C	287.2	15102.9	47.1			(1) C=O/C-O-C	287	655.2	6.0	
(2) C-OH	286.6	1176.1	3.7			(2) C-OH	286	2712.6	25.0	
(3) C-C/C=C	285	13426.1	41.9			(3) C-C/C=C	284.5	7407.4	68.4	
						Reduced PAA	Peak Position (eV)	Area	Peak area ratio (%)	C/O cal.
						(0) COOH	288.6	2481.8	3.9	11.4
						(1) C=O/C-O-C	287.1	2572.5	4.1	
						(2) C-OH	286.1	4241.6	6.7	
						(3) C-C/C=C	284.6	54156.2	85.3	

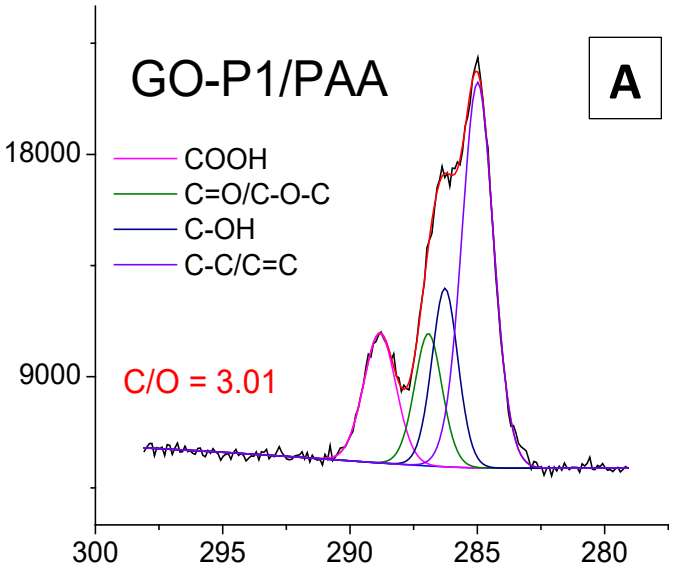
GO-P1/PAA
A
18000
9000
COOH
C=O/C-O-C
C-OH
C-C/C=C
C/O = 3.01
300
295
290
285
280

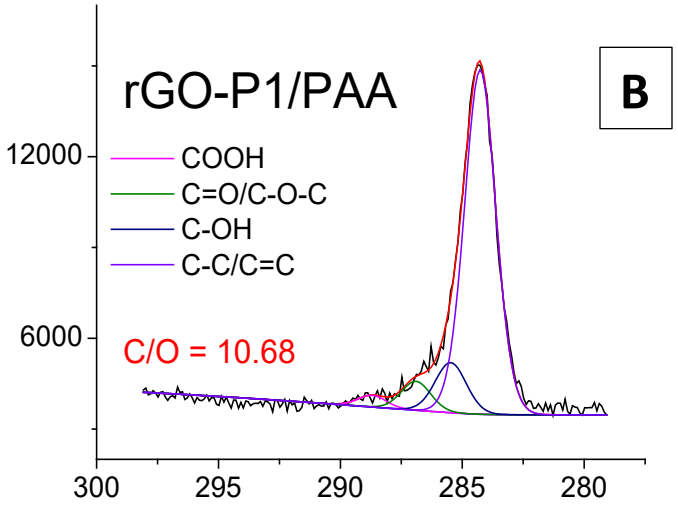
rGO-P1/PAA
B
12000
6000
COOH
C=O/C-O-C
C-OH
C-C/C=C
C/O = 10.68
300
295
290
285
280

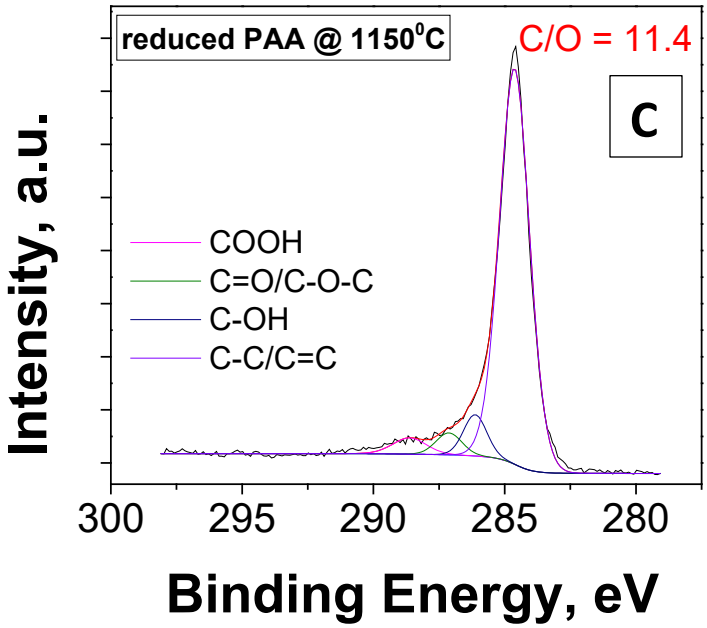

Figure A8. Characteristic XPS data. (A) High resolution C1s spectra of as-prepared GO-P1/PAA before thermal treatment. (B) High-resolution C1s spectra of rGO-P1/PAA and (C) PAA after thermal reduction at 1150 °C in Argon.

Table A2. Hall mobility measurements for reduced GO monolayer, rGO-P1/PAA and rGO-P1 bilayer films. All samples were thermally reduced at 1150 ºC in Argon.

Reduced GO-P1-bilayer

DATE	User_Name	Sample_Name
10-21-2016	gr#146	Ecopia1

I(uA)	B	D	D_T	MN	T(K)
50.000	0.550	0.500	0.100	1000	300

Nb	u	rho	RH	RHA	RHB	NS	SIGMA	DELTA	ALPHA
-1.947E+17	4.965E+02	6.457E-02	-3.206E+01	-3.222E+01	-3.189E+01	-9.736E+12	1.549E+01	3.526E+01	3.593E-01

Vab	Vbc	Vac	Vmac	V-mac	Vcd	Vda	Vbd	Vmbd	V-mbd
+I:									
-22.898	-8.164	-14.405	-16.303	-12.758	-23.022	-8.641	-14.035	-12.440	-15.862
-I:									
22.597	8.235	15.059	16.971	13.427	22.777	7.762	15.006	13.346	16.939

Rs
1.291E+03

Reduced GO-P1/PAA

```
    DATE           User_Name     Sample_Name
10-21-2016          gr#146         Ecopia1
------------------------------------------------------------------
------------------------------------------------------------------
     I(uA)         B          D          D_T           MN         T(K)
    70.000      0.550      0.500      0.100       1000         300
------------------------------------------------------------------
------------------------------------------------------------------
     Nb             u            rho          RH          RHA
RHB          NS          SIGMA          DELTA       ALPHA
  -1.750E+17   7.936E+01   4.495E-01  -3.568E+01  -6.241E+
01  -8.942E+00  -8.748E+12   2.225E+00   6.366E+01   6.657E-01
------------------------------------------------------------------
------------------------------------------------------------------
    Vab         Vbc         Vac       Vmac       V-mac       Vcd
Vda         Vbd      Vmbd       V-mbd
+I:
   206.311  -103.286   367.360   358.840
364.837  -147.825  -677.652   317.360   318.837   321.673
-I:
   393.927   173.974   270.206   275.872   262.646
215.604  -122.544   118.039   115.596   121.186
------------------------------------------------------------------
------------------------------------------------------------------
     Rs
   8.991E+03
==================================================================
==================================================================
```

Reduced GO-P1 monolayer

DATE	User_Name	Sample_Name
10-21-2016	gr#146	Ecopia1

I(uA)	B	D	D_T	MN	T(K)
50.000	0.550	0.500	0.100	1000	300

Nb	u	rho	RH	RHA	RHB	NS	SIGMA	DELTA	ALPHA
-7.944E+17	6.466E+01	1.215E-01	-7.858E+00	-8.464E+00	-7.252E+00	-3.972E+13	8.229E+00	2.274E+01	6.052E-01

Vab	Vbc	Vac	Vmac	V-mac	Vcd	Vda	Vbd	Vmbd	V-mbd
+I:									
-35.666	-27.593	-6.366	-6.088	-4.438	-34.927	-18.690	-20.492	-19.575	-21.461
-I:									
39.955	13.224	16.891	14.897	14.685	25.769	23.103	10.020	9.763	9.472

Rs
2.430E+03

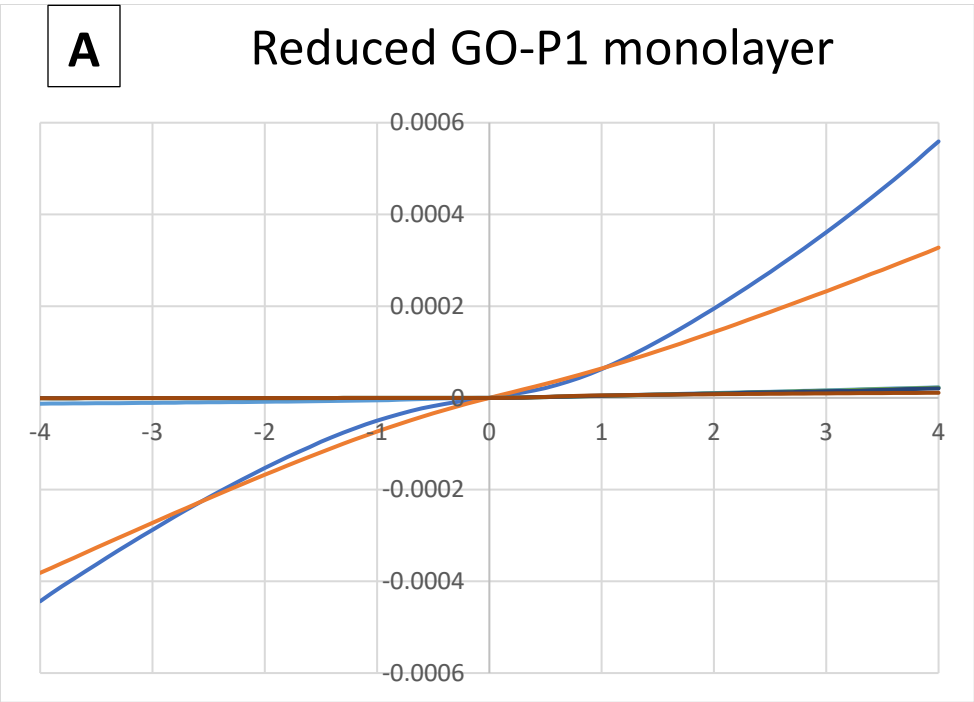
A
Reduced GO-P1 monolayer
0.0006
0.0004
0.0002
0
-0.0002
-0.0004
-0.0006
-4
-3
-2
-1
0
1
2
3
4

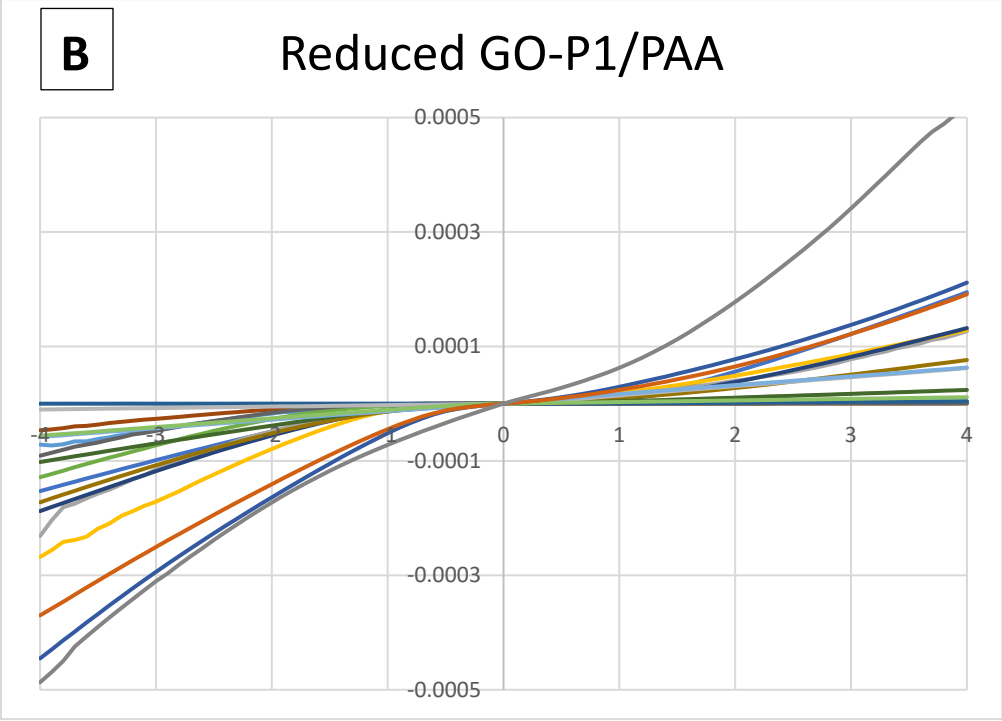
B
Reduced GO-P1/PAA
0.0005
0.0003
0.0001
-0.0001
-0.0003
-0.0005
-4
-3
-2
-1
0
1
2
3
4

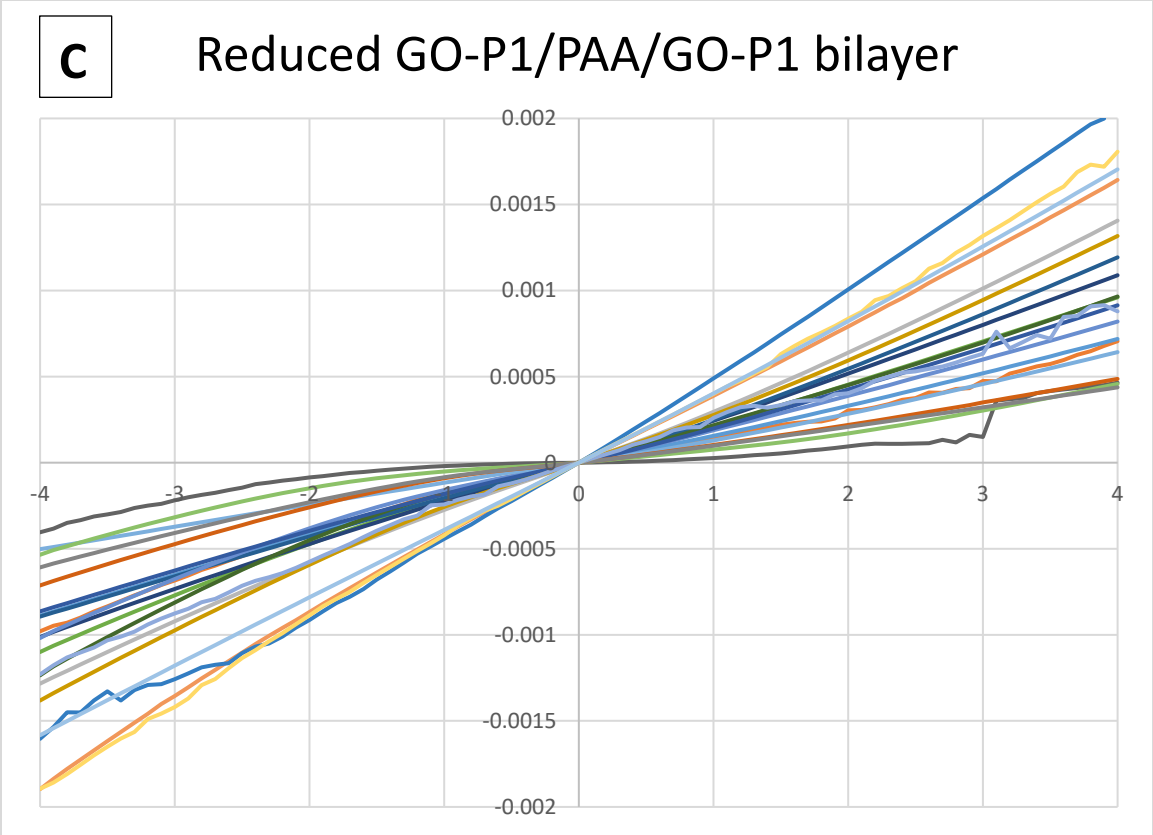

Figure A9. I-V curves for (A) rGO-P1, (B) rGO-P1/PAA, and (C) rGO-P1/PAA/GO-P1 samples. Films were deposited on hydrophilic Si substrates and subjected to thermal reduction at 1150 ºC in Argon.

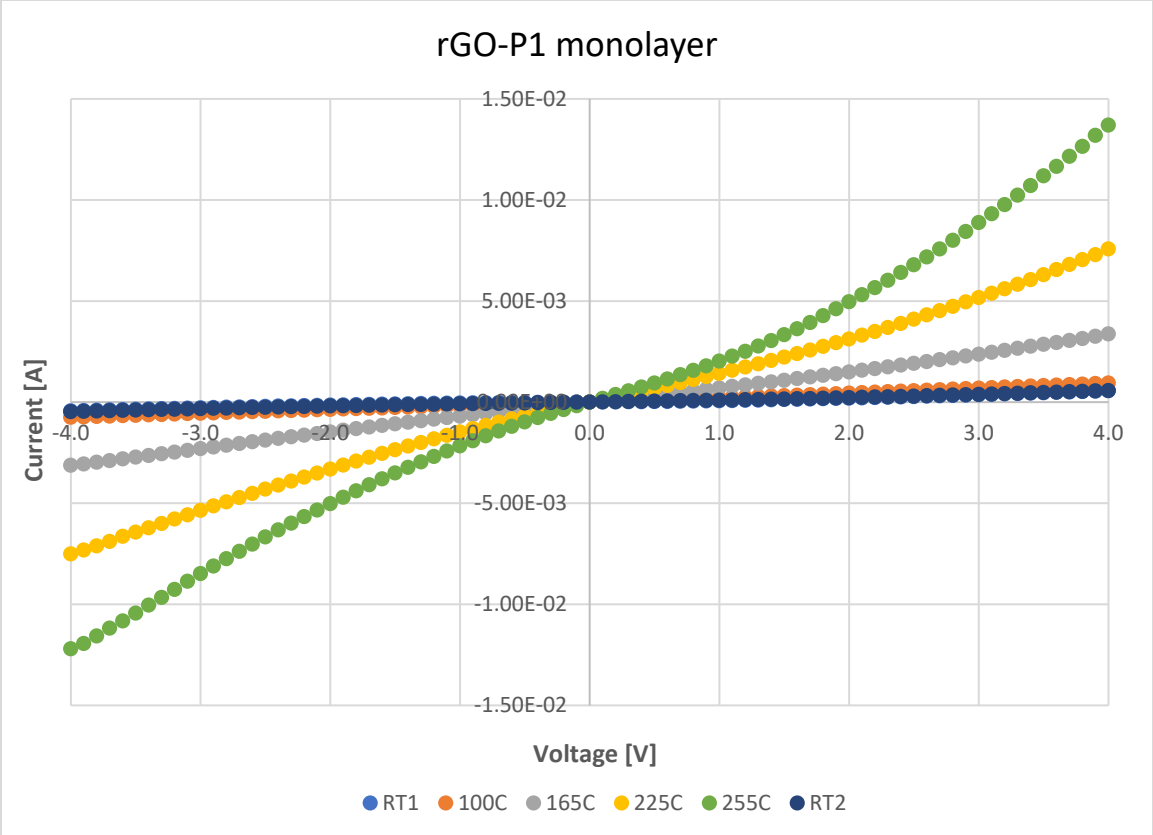
rGO-P1 monolayer
1.50E-02
1.00E-02
5.00E-03
-5.00E-03
-1.00E-02
-1.50E-02
-4.0
-3.0
-2.0
-1.0
0.0
1.0
2.0
3.0
4.0
Current [A]
Voltage [V]
RT1
100C
165C
225C
255C
RT2

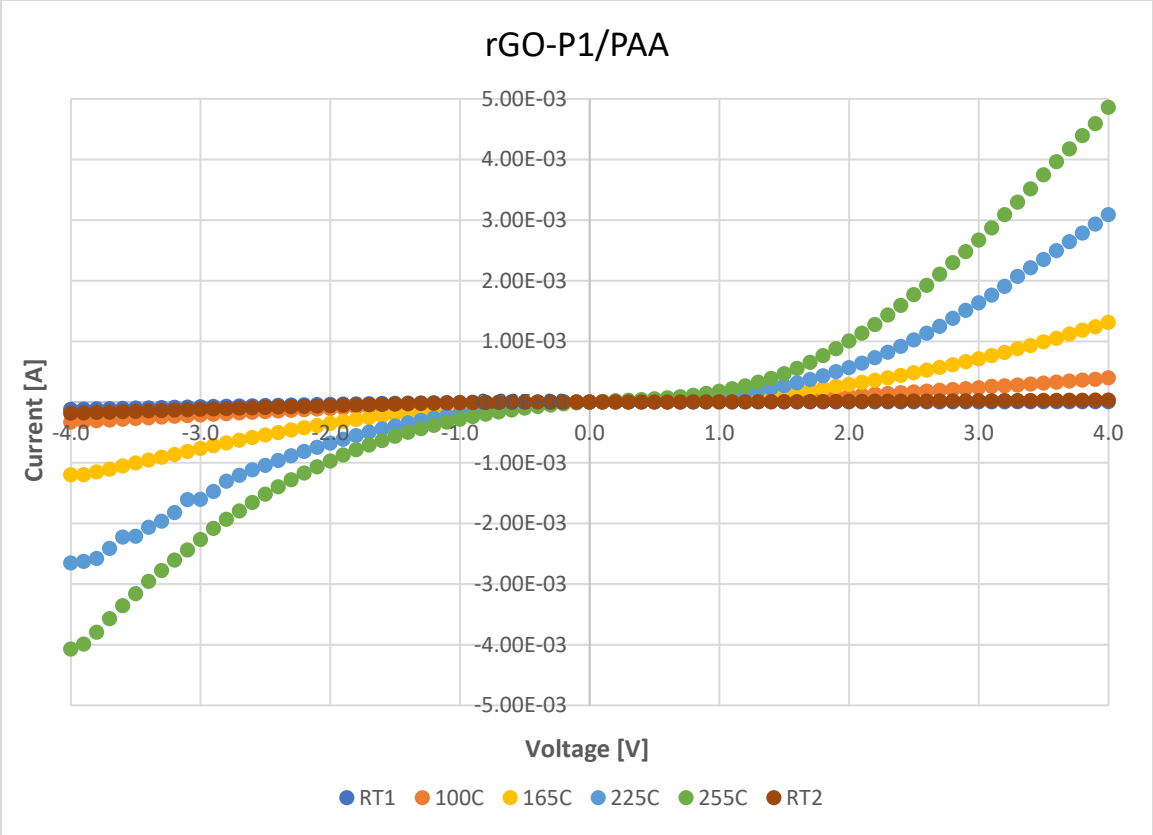
rGO-P1/PAA
5.00E-03
4.00E-03
3.00E-03
2.00E-03
1.00E-03
-1.00E-03
-2.00E-03
-3.00E-03
-4.00E-03
-5.00E-03
-4.0
-3.0
-2.0
-1.0
0.0
1.0
2.0
3.0
4.0
Current [A]
Voltage [V]
RT1
100C
165C
225C
255C
RT2

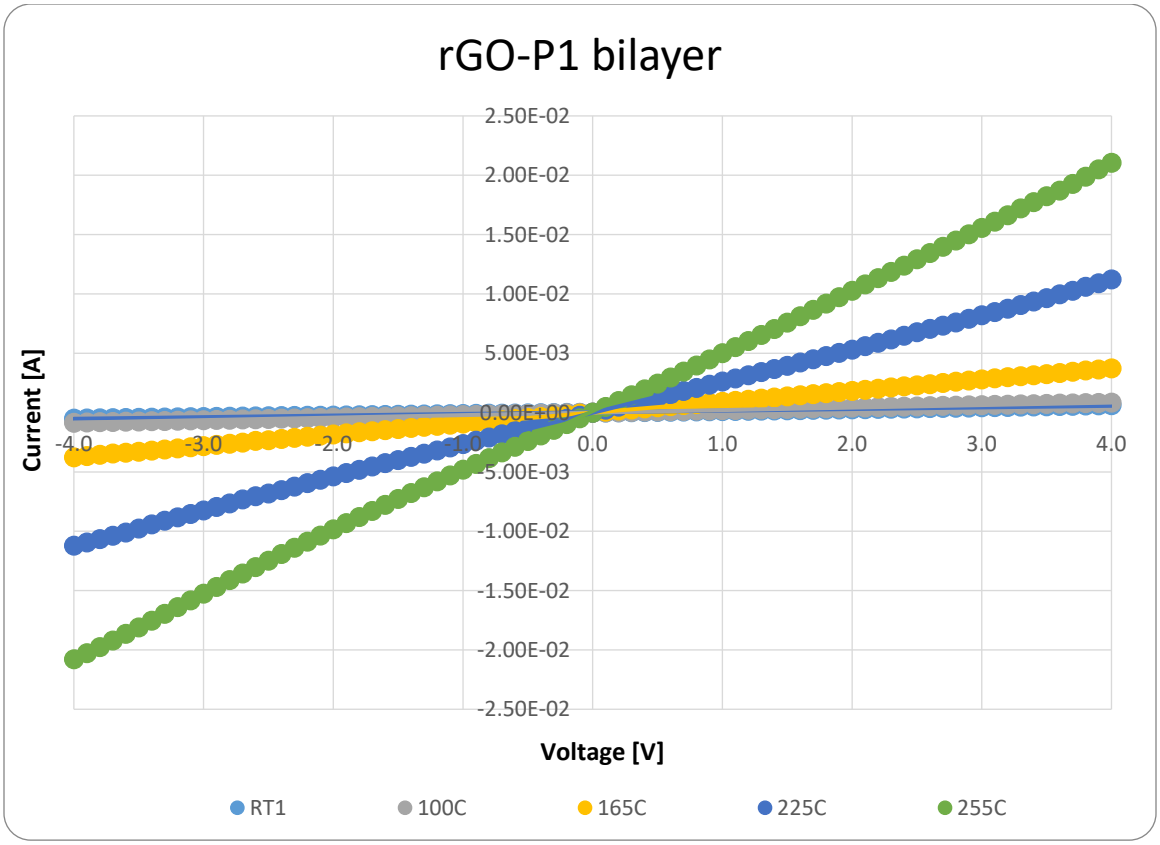

Figure A10. I-V curves for different samples using varying temperatures: Room Temperature (RT), 100, 165, 225, 255 ˚C.

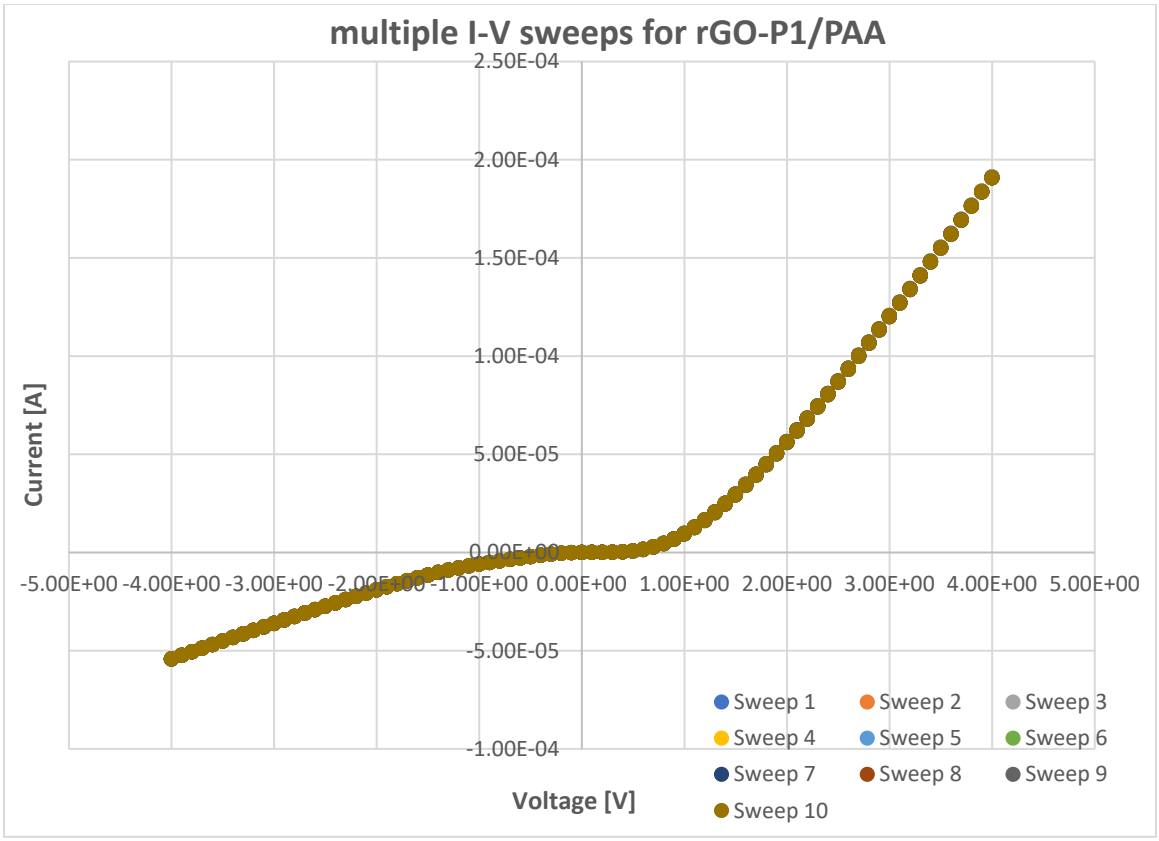

Figure A11. I-V sweeping cycles measured at room temperature for rGO-P1/PAA. Sample was reduced at 1150 ºC in Argon.

I-V sweeping cycles were performed to see whether non-linearity would disappear. From **Figure A11** it is seen that there is still linear behavior after 10 sweep cycles.

Analysis of Raman Spectra

Also, the most used and most debated approach to quantify the Raman spectrum is the one exploiting the Tuinstra-Koenig (TK) equation [1-3], which allows to estimate the average size L_a of the sp^2-hybridized C domains in graphene oxide by measuring the ratio I_D/I_G between the D and G peak intensities:

$$L_a(nm) = (2.4 \times 10^{-10})\lambda_L^4 (\frac{I_D}{I_G})^{-1}$$

where λ_L (nm) is the laser excitation wavelength. The results for all corresponding spectra were tabulated in Table 1. It can be concluded that sheets in rGO/PAA/GO film are comprised of ordered graphitic regions with a size of ~11 nm surrounded by areas of oxidized carbon atoms or point defects [4]

Therefore, the Raman results confirm the conclusion derived from the XPS data that the reduction efficiency is lower for GO-P sheets covered with POEGMA.

Table A3. Raman characteristics for seven selected samples reduced at 1150 ºC in Argon.

	GO	GO-P1 monolayer	GO-P1 bilayer	rGO	rGO-P1 monolayer	rGO/PAA	rGO-P1 bilayer (436 S/cm)	rGO-P1 bilayer (3653 S/cm)
	Non-Reduced Films			Reduced Films (Ar, 1150 °C)				
D (cm^{-1})	1359.6	1352.8	1352.3	1343.9	1343.8	1346.2	1359	1362
G (cm^{-1})	1591.6	1594.8	1597.5	1599.1	1594.9	1599.2	1603.2	1604.1
I_D/I_G	0.95	1.03	1.00	1.26	1.14	1.22	1.88	1.46
L_a (nm)	17.7	16.3	16.7	13.3	14.7	13.8	8.9	11.5
2D/(D+G)	-	-	-	-	-	-	-	3.18

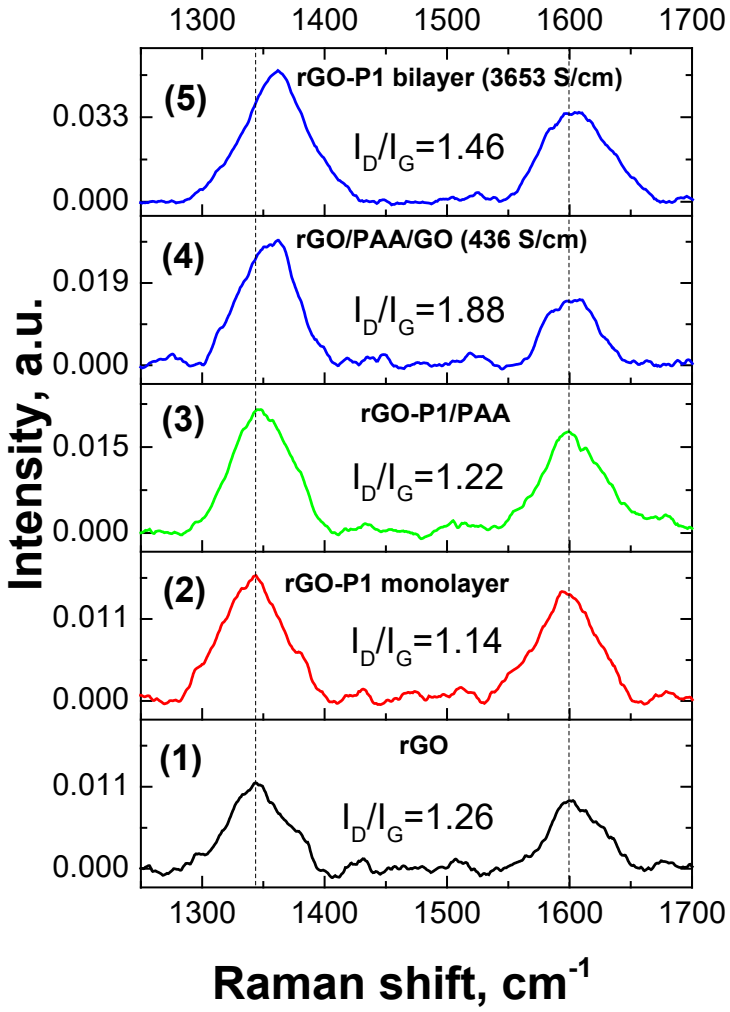

Figure A12. (b) Raman spectra of selected samples after thermal reduction at 1150 °C in Argon: (1) rGO, (2) rGO-P1 monolayer, (3) rGO-P1/PAA, (4) rGO-P1/PAA/GO-P1 bilayer with low conductivity - 436 S/cm and (5) rGO-P1/PAA/GO-P1 double layer with high conductivity - 3653 S/cm.

Beam Profile Calculations

The composite, originally flat plate, is subject to two-dimensional bending under axial load P and bending couples M_0 at its distant ends. The process is two-dimensional, and the Cartesian system of coordinates is introduced with Z-axis parallel to the compression force P. It goes through the centers of mass of every cross-section, and X and Y-axis coincide with the principal axes of inertia of the plate cross-section: they are parallel to the sides of rectangle.

The strained state is described in terms of the Euler-Bernoulli model for beams [5]. In this model the plate is considered as a thin and wide beam of length L with rectangular cross-section of thickness h and width a in the non-deformed state, and the material plane $X = 0$ is called the neutral surface within the two-dimensional bending of Euler-Bernoulli beam. The main model assumption is that every cross-section Z (that is orthogonal to the Z-axis) remains orthogonal to the neutral line after deformation. So, every cross-section only rotates around the Y-axis on the angle θ remaining flat, shear deformations are neglected.

The beam strains could be decomposed into the sum of homogeneous strain $u^{(P)}$, caused by axial loading P, and inhomogeneous part due to bending of the $u^{(M)}$. Due to inextensibility constraint which defines the position of the neutral line, the total strain component in the Z direction is given as:

$$u = u^{(P)} + u^{(M)} = \frac{P}{ahE_{\text{eff}}} + \kappa(s)x, \quad \kappa = \frac{d\theta}{ds}, \tag{1}$$

where κ is the curvature of the neutral line, and s is the arc length along the line. It is attributed to the z coordinate of the undeformed beam. The apparent Young's modulus E_{eff} accounts for the inhomogeneity of the two-layered composite beam, and defined as

$$E_{\text{eff}} = \frac{h_1}{h}E_1 + \frac{h_2}{h}E_2, \quad h = h_1 + h_2,$$

where h_1 and h_2 are thicknesses of plate layers – graphene and lower polymer substrate, and E_1 and E_2 are their Young's moduli respectively.

The axial stress σ is linear in every layer, but due to isostrain condition implicitly assumed in (1) there is a jump at $X = h_1$ surface, i.e.

$$\sigma = E(x)u = \frac{P}{ah}\frac{E(x)}{E_{\text{eff}}} + \kappa x E(x), \quad E(x) = \begin{cases} E_1, & -h/2 < x < h_1 - h/2; \\ E_2, & h_1 - h/2 < x < h/2. \end{cases}$$

(2)

So, the bending moment around the Y-axis in the s cross-section of deformed beam is given as

$$M \equiv a\int_{-h/2}^{h/2} \sigma x dx = \frac{P}{ahE_{\text{eff}}}\int_{-h/2}^{h/2} E(x)x dx + \kappa(s)D, \quad D = \int_{-h/2}^{h/2} E(x)x^2 dx.$$

The first term on the right-hand side of equation is zero for homogeneous material, however in the case of composite beam – it is not. Nevertheless, this term does not depend on cross-section position s. The quantity D is the bending stiffness of the beam:

$$D = \int_{-h/2}^{h/2} E(x)x^2 dx = \frac{E_1}{3}\left(\left(h_1 - h/2\right)^3 + \left(h/2\right)^3\right) + \frac{E_2}{3}\left(\left(h/2\right)^3 - \left(h_1 - h/2\right)^3\right).$$

(*)

For a homogeneous material D is equal to the product of Young's modulus and moment of inertia with respect to Y-axis.

From the free body diagram

$$M(s) = -Pv(s), \tag{3}$$

where $v(s)$ is the vertical displacement of the neutral surface, and $v'(s) = \sin\theta$. Upon differentiation of Eq. (3) with respect to s the following two-point boundary value problem can be written to determine the neutral line curve of the buckled beam under axial load P

$$\frac{d\theta}{ds} = \kappa, \tag{4}$$

$$D\frac{d\kappa}{ds} = -P\sin\theta, \tag{5}$$

$$\theta\big|_{s=0,L} = 0, \quad \kappa\big|_{s=0} = \kappa_0 > 0, \tag{6}$$

$$\frac{dX}{ds} = \cos\theta, \quad \frac{dY}{ds} = \sin\theta, \tag{7}$$

$$X\big|_{s=0} = X_0, \quad Y\big|_{s=0} = Y_0, \tag{8}$$

$$X\big|_{s=L} = X_0 + \Delta X, \quad Y\big|_{s=L} = Y_0. \tag{9}$$

Here the curvature κ_0 proportional to bending couple at the beam end-points has to be found from the condition that both beam ends are clenched, and X_0 and Y_0 are the coordinates of the left beam end-point, where $s = 0$. Boundary conditions (9) determine the location of the right, movable, clenched end of the beam. It is assumed that $\Delta X < L$, so the beam end-points come closer.

The problem (4)–(9) is solved numerically, using shooting method. The unknowns parameters $P(\Delta X, L, D)$ and $\kappa_0(\Delta X, L, D)$ are determined at the iteration process. Starting with the initial guess for P and κ_0 for given values of X_0, Y_0, ΔX, L, and D, the right-hand side boundary conditions (6) and (9) are satisfied minimizing the difference between $\theta(s = L)$, and $X(s = L)$ and their imposed values $\theta|_{s=L} = 0$, and $\theta|_{s=L} = \Delta X + X_0$. When two parameters of the beam, P and κ_0, are determined the parameters X_0, Y_0, ΔX, and L are matched in to order to match the theoretical curve and experimentally observed beam profile. So, every dataset is correlated with respective values of P and κ_0 which allow to calculate curvature $\kappa(s)$ at every point, particularly at the symmetry point, $\kappa_{0.5} = \kappa(s = L/2)$.

Therefore, the distributions of axial components of strain and stress at the central cross-section are given by the following expressions

$$u = \frac{P}{ahE_{\text{eff}}} + \kappa_{0.5} x,$$

$$\sigma = \left(\frac{P}{ahE_{\text{eff}}} + \kappa_{0.5} x \right) E(x), \quad E(x) = \begin{cases} E_1, & -h/2 < x < h_1 - h/2; \\ E_2, & h_1 - h/2 < x < h/2. \end{cases}$$

(10)

$\kappa_{0.5} = \kappa(s = L/2)$ – these values can be found in **Table A4**.

The force P is calculated as follows:

$$P = \pi_2 D / L^2,$$

where total length L and dimensionless complex π_2 are given in **Table A4**.

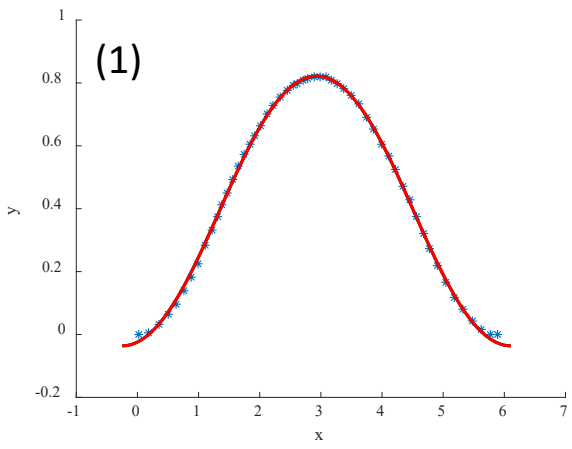
(1)
y
x

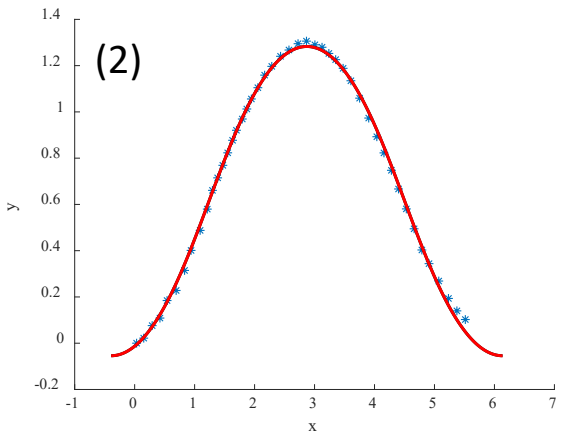
(2)
y
x

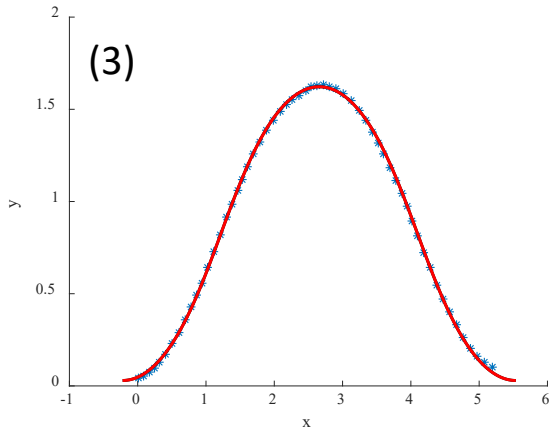
(3)
y
x

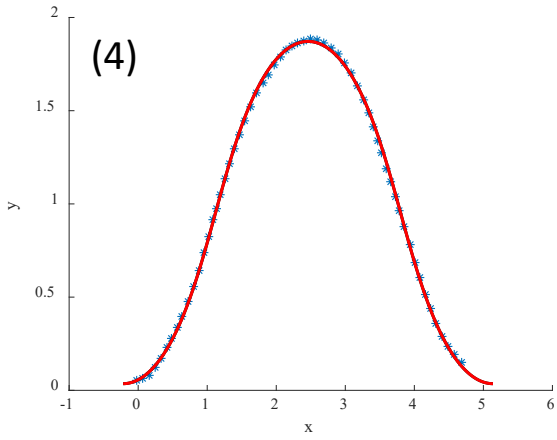
(4)
y
x

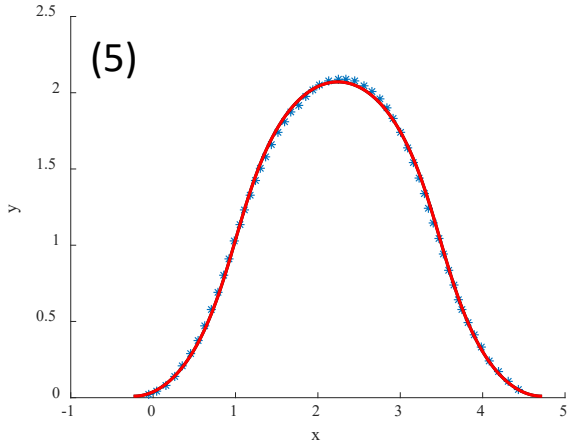
(5)
y
x

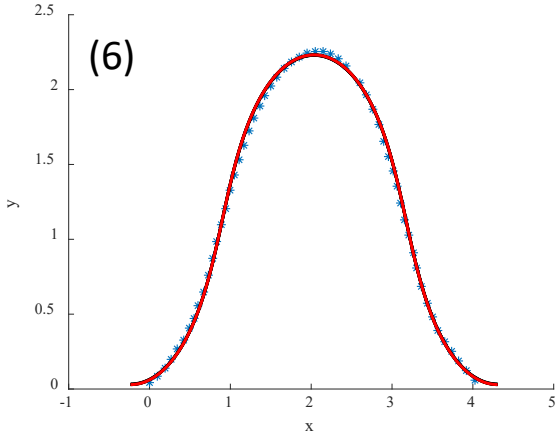
(6)
y
x

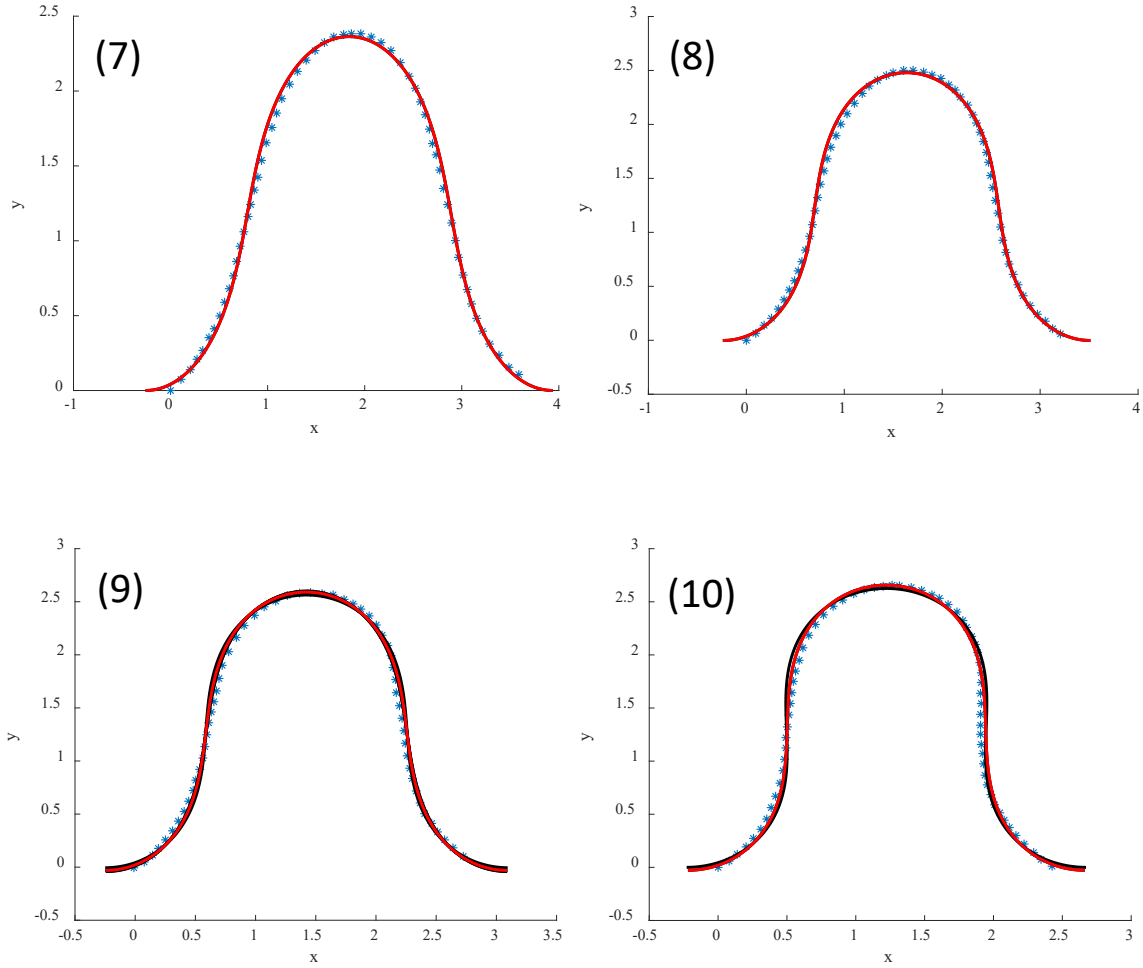

Figure A13. Bending of rGO/Kapton film. Results of fitting using Equation 10 derived based on Euler-Bernoulli beam theory. 10 curve profiles at different radii of bending have been modelled.

Table A4. The results of beam profile calculations.

Curve number	Curvature (1/mm)	PI2 (-)	L (mm)	X (mm)	Y (mm)
1	-0.393	40.336	6.633	2.938	0.822
2	-0.537	41.366	7.179	2.882	1.283
3	-0.741	42.724	6.777	2.669	1.622
4	-0.884	44.149	6.770	2.451	1.872
5	-1.018	45.830	6.813	2.236	2.071
6	-1.141	47.454	6.767	2.027	2.232
7	-1.241	49.286	6.851	1.840	2.364
8	-1.363	51.473	6.847	1.632	2.480
9	-1.472	53.684	6.846	1.411	2.564
10	-1.500	54.128	6.984	1.215	2.637

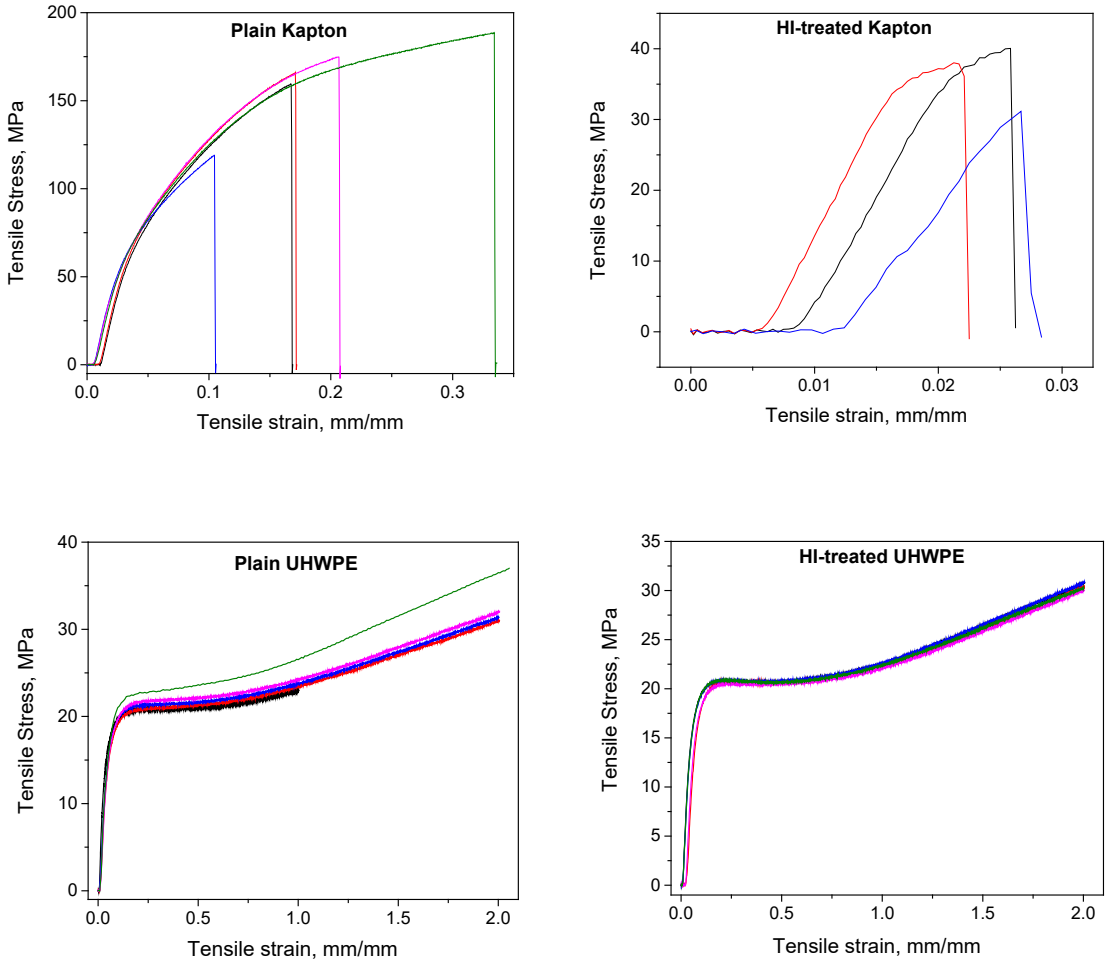

Figure A14. Instron tensile tests performed on various polymeric films before and after HI-treatment.

The above tensile results presented in **Figure A14** suggest that HI-treated Kapton becomes more brittle after chemical reduction with HI acid while mechanical properties of polyethylene do not change.

Table A5. The results of tensile measurements for polymer films before and after chemical reduction.

Sample	Elongation at Maximum Load (mm/mm)	Tensile stress at Maximum Load (MPa)	Area (cm^2)	Modulus (MPa)
Plain Kapton				
#1	0.167	160	0.00250	3055
#2	0.171	166	0.00250	3073
#3	0.104	119	0.00275	3096
#4	0.206	175	0.00250	2914
#5	0.334	189	0.00263	2798
Mean	0.197	162	0.00258	2987
Std. Dev.	0.085	26	0.00011	127
HI-Kapton				
#1	0.026	40	0.00250	2976
#2	0.021	38	0.00244	3375
#3	0.027	31	0.00225	2239
Mean	0.025	36	0.00240	2863
Std. Dev.	0.003	5	0.00013	576
Plain UHWPE				
#1	1.001	23	0.01275	819
#2	1.998	31	0.01213	492
#3	2.002	31	0.01225	502
#4	2.004	32	0.01263	495
#5	2.054	37	0.01250	652
Mean	1.812	31	0.01245	592
Std. Dev.	0.454	5	0.00026	144
HI-UHWPE				
#1	2.005	31	0.01238	472
#2	2.004	30	0.01413	420
#3	2.006	31	0.01250	442
#4	2.003	30	0.01225	428
#5	2.002	30	0.01375	440
Mean	2.004	30	0.01300	440
Std. Dev.	0.002	1	0.00087	20

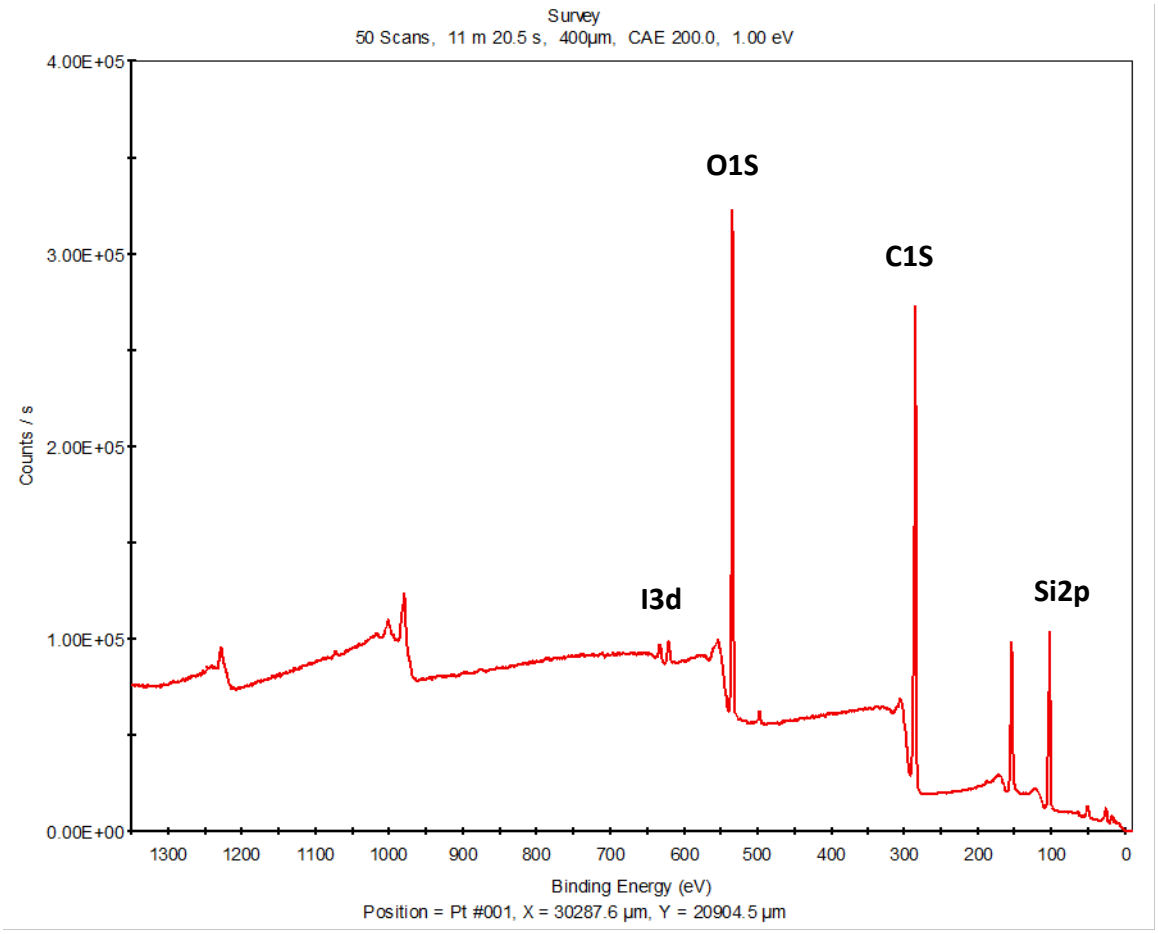

Figure A15. XPS survey scan of chemically reduced rGO on silicon substrate.

```
/NOPR   ! Suppress printing of UNDO process
/PMACRO ! Echo following commands to log
FINISH  ! Make sure we are at BEGIN level
/CLEAR,NOSTART  ! Clear model since no SAVE found
! WE SUGGEST YOU REMOVE THIS LINE AND THE FOLLOWING STARTUP LINES
! WE SUGGEST YOU REMOVE THIS LINE AND THE FOLLOWING STARTUP LINES
! WE SUGGEST YOU REMOVE THIS LINE AND THE FOLLOWING STARTUP LINES
/input,start150,ans,'C:\Program Files\ANSYS Inc\v150\ANSYS\apdl\'
/REPLOT,RESIZE
!*
/NOPR
KEYW,PR_SET,1
KEYW,PR_STRUC,1
KEYW,PR_THERM,0
KEYW,PR_FLUID,0
KEYW,PR_ELMAG,0
KEYW,MAGNOD,0
KEYW,MAGEDG,0
KEYW,MAGHFE,0
KEYW,MAGELC,0
KEYW,PR_MULTI,0
/GO
!*
!*
/PREP7
!*
ET,1,SHELL181
!*
KEYOPT,1,1,0
KEYOPT,1,3,0
```

```
KEYOPT,1,8,2
KEYOPT,1,9,0
!*
!*
MPTEMP,,,,,,,,
MPTEMP,1,0
MPDATA,EX,1,,9.3e8
MPDATA,PRXY,1,,0.46
MPTEMP,,,,,,,,
MPTEMP,1,0
MPDE,EX,1
MPDE,PRXY,1
MPDATA,EX,1,,1.5E+009
MPDATA,PRXY,1,,0.42
MPTEMP,,,,,,,,
MPTEMP,1,0
MPDATA,EX,2,,500e9
MPDATA,PRXY,2,,0.21
sect,1,shell,,
secdata, 6e-6,1,0.0,3
secdata, 6e-9,2,0.0,3
secoffset,MID
seccontrol,,,, , , ,
K,1,0,0,0,
K,2,0.01,0,0,
K,3,0.01,0.005,0,
K,4,0,0.005,0,
K,5,0,0.00065,0,
K,6,0.01,0.00065,0,
K,7,0.01,0.00435,0,
K,8,0,0.00435,0,
FINISH
```

```
/POST1
FINISH
/PREP7
FLST,2,8,3
FITEM,2,1
FITEM,2,2
FITEM,2,6
FITEM,2,7
FITEM,2,3
FITEM,2,4
FITEM,2,8
FITEM,2,5
A,P51X
FINISH
/SOL
FLST,2,3,4,ORDE,2
FITEM,2,4
FITEM,2,-6
!*
/GO
DL,P51X, ,ALL,0
FLST,2,3,4,ORDE,3
FITEM,2,1
FITEM,2,-2
FITEM,2,8
!*
/GO
DL,P51X, ,UX,0
FLST,2,3,4,ORDE,3
FITEM,2,1
FITEM,2,-2
FITEM,2,8
```

```
!*
/GO
DL,P51X, ,UY,0.004
FLST,2,3,4,ORDE,3
FITEM,2,1
FITEM,2,-2
FITEM,2,8
!*
/GO
DL,P51X, ,UZ,0
FLST,2,3,4,ORDE,3
FITEM,2,1
FITEM,2,-2
FITEM,2,8
!*
/GO
DL,P51X, ,ROTX,0
FLST,2,3,4,ORDE,3
FITEM,2,1
FITEM,2,-2
FITEM,2,8
!*
/GO
DL,P51X, ,ROTY,0
FLST,2,3,4,ORDE,3
FITEM,2,1
FITEM,2,-2
FITEM,2,8
!*
/GO
DL,P51X, ,ROTZ,0
FINISH
```

```
/PREP7
AESIZE,ALL,0.0002,
AESIZE,ALL,0.0002,
MSHAPE,0,2D
MSHKEY,0
!*
CM,_Y,AREA
ASEL, , , ,      1
CM,_Y1,AREA
CHKMSH,'AREA'
CMSEL,S,_Y
!*
AMESH,_Y1
!*
CMDELE,_Y
CMDELE,_Y1
CMDELE,_Y2
!*
FLST,5,1350,2,ORDE,2
FITEM,5,1
FITEM,5,-1350
CM,_Y,ELEM
ESEL, , , ,P51X
CM,_Y1,ELEM
CMSEL,S,_Y
CMDELE,_Y
!*
!*
EREF,_Y1, , ,1,0,1,1
CMDELE,_Y1
!*
```

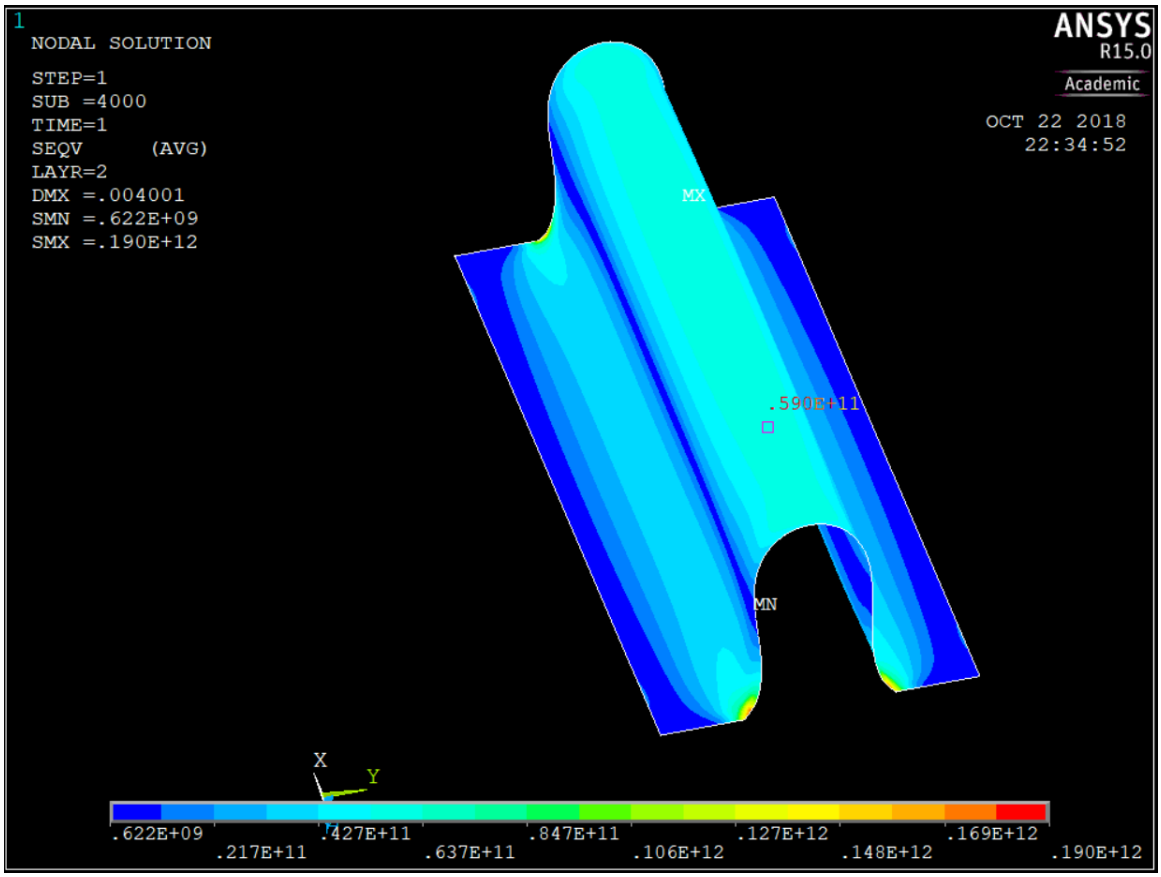
1
NODAL SOLUTION
STEP=1
SUB =4000
TIME=1
SEQV (AVG)
LAYR=2
DMX =.004001
SMN =.622E+09
SMX =.190E+12
ANSYS
R15.0
Academic
OCT 22 2018
22:34:52
MX
.590E+11
MN
X
Y
.622E+09
.217E+11
.427E+11
.637E+11
.847E+11
.106E+12
.127E+12
.148E+12
.169E+12
.190E+12

APPLICATIONS OF REDUCED GO FILMS: rGO/KAPTON BOLOMETER

Introduction

Due to the increased attention towards the usage of reduced graphene oxide (rGO) in light-sensitive applications [6] we utilize rGO/Kapton to show the possibility for the application for an IR detector. One of the key properties of rGO is to have tunable optical absorption and detection window by controlling the level of its oxidation [7]. One can alter the optical band-gap of rGO between ultraviolet and mid infrared spectral range [8, 9]. Furthermore, large specific surface area of GO [10] offers an effective absorption of the incident photons [11]. Thus, much work has been shifted towards using GO as detector of light, especially in near IR/mid IR range [12-15].

There are two main types of detectors: thermal (bolometer) and photonic (photodetector) [16]. Bolometers rely on temperature-dependent resistance change and efficient light absorption [17-19]. Thermal detectors are favored at longer wavelengths and high operating temperatures. Such devices are increasingly important for applications in healthcare [20], astronomy [21], smart energy systems [22], security [23], automotive [24], motion tracking [25]. Moreover, bolometers require no cooling to operate at room temperature (RT). Partially reduced graphene oxide has been known to reveal strong bolometric effect, since its residual functional groups actively absorb in near and mid IR [13, 17]. In this chapter we demonstrate the use of rGO/Kapton as bolometer-sensitive material in near-IR range.

Experimental

The schematic diagram of bolometric measurements setup and rGO/Kapton sensor configuration is shown in **Figure 7.1**. Silver paste was used to attach two nickel-plated copper wires to the sample. As source of irradiation we used green, red and near-IR lasers with power of 0.3 mW, 3.7 mW and 280 mW respectively, placed at a distance of 50 mm above the sample. We used power and energy meter (Scientech 365, provided by Dr. Chumanov) to determine output power of the lasers. The laser beam was aligned perpendicular to the center of rGO/Kapton sensor with the laser spot covering the rGO film and electrode area. Distance between electrodes was ≈1.6 mm and channel width ≈5.1 mm. Initial resistance R_0 = 70.9 kΩ and room temperature T_{room} = 21.3 ºC. The sample was irradiated with ON/OFF alternative pulses with duration of 2 minutes.

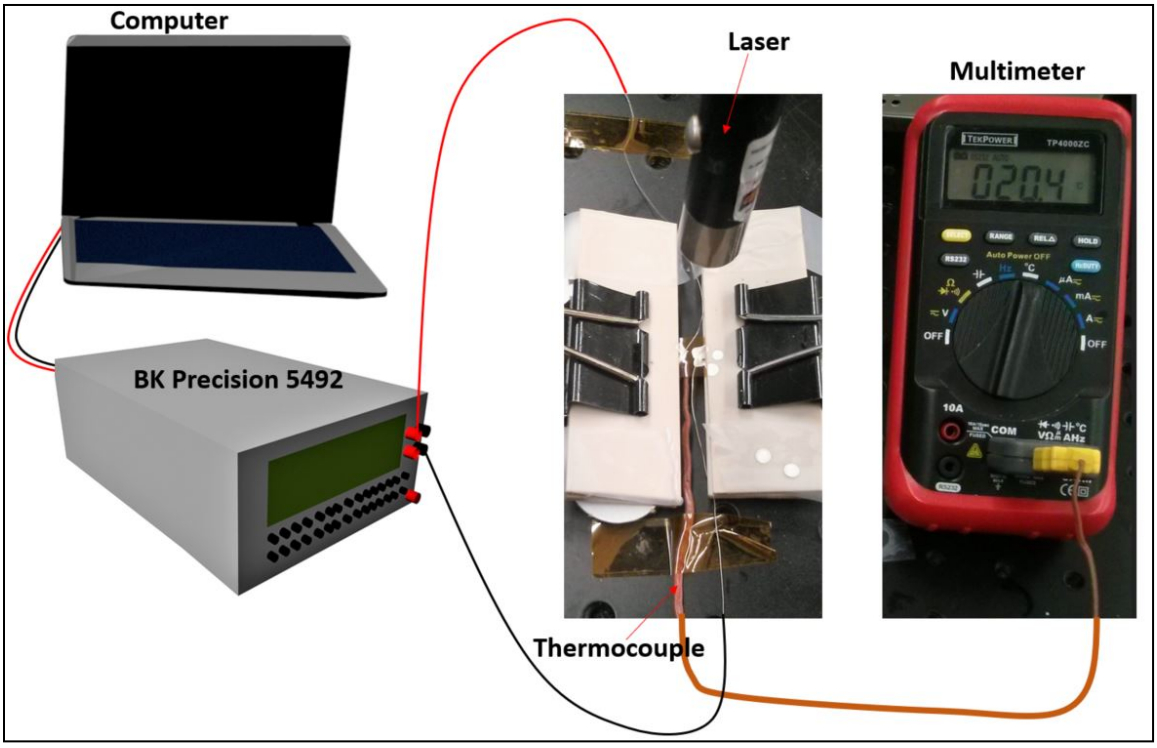

Figure A16: Schematic of the photoresponse measurement setup.

The experiment to determine the temperature dependence of resistance of rGO/Kapton sensor was conducted by keeping the rGO/Kapton sample on a regulated hot plate. The surface of the plate was in full contact with the back side of the Kapton substrate to ensure proper thermal equilibrium between the plate and the sample. Temperature was monitored with thermocouple attached to the plate.

Results and Discussion

Flexible bolometric sensor

The performance of a bolometer is dependent on various parameters such as IR absorption, temperature coefficient of resistance (TCR), thermal isolation, and noise properties [12, 26]. One of the most important performance indicators for a bolometer is TCR (in units $\%K^{-1}$) and it is defined as [15]:

$$TCR(R_0) = \frac{1}{R_0}\frac{dR}{dT} * 100\%, \quad (7.1)$$

The TCR corresponds to the normalized resistance change per Kelvin around the operating point R_0 (Equation 7.1). For instance, typical values of TCR in metallic and semiconducting bolometers are ~ 0.4 $\%K^{-1}$, and ~ -2 – -4 $\%K^{-1}$ respectively [15], whereas the largest reported value for carbon nanomaterials corresponds to vertically aligned graphene nanosheets [19] with TCR of ~ 11 $\%K^{-1}$. The largest TCR, to date, for reduced GO films has values of approximately -2 to -4 $\%K^{-1}$ [17].

In order to evaluate the TCR the temperature dependence of the resistance of this typical device was measured (**Figure A17**). It was found that the resistance decreased almost linearly with increase in temperature over the temperature range 295 - 483 K, which indicates semiconducting behavior of rGO-P2 films. A similar trend has been reported for PECVD-grown nanographene on quartz [27], reduced graphene oxide on silicon [17] and Kapton [13] substrates. Thus, TCR is found to be -0.42% K^{-1} at 295 K. According to Ref. [28], the negative TCR coefficient originates from the thermal generation of charge carriers, while the slope and shape of the R-T curve are determined by electron and hole scattering and acoustic phonons.

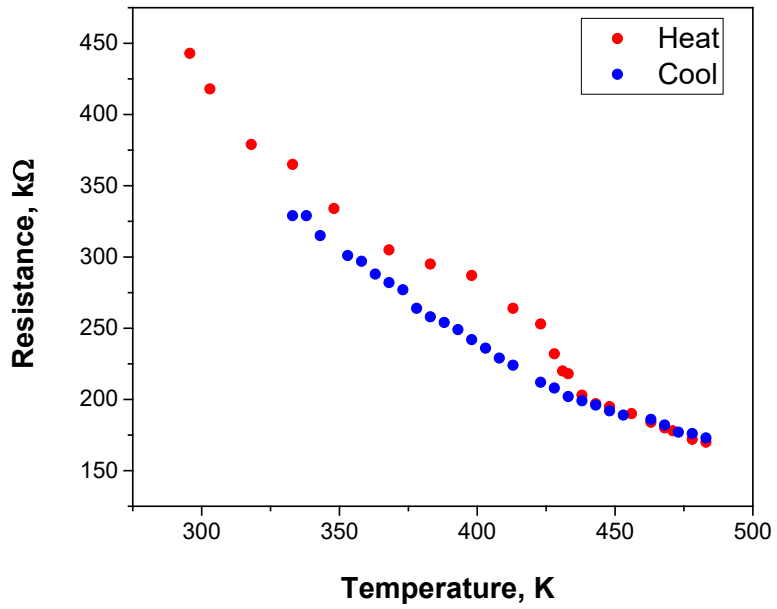

Figure A17: Resistance as a function of temperature for rGO-P2 on Kapton.

We have analyzed the photoresponse of as prepared rGO-Kapton film to a different white light power densities, since bolometers are often required to measure power of incident light. For this we used halogen fiber optic illuminator (Fiber-Lite Model 190) that emits a broad spectrum, ranging from ~400 to ~2000 nm as reported by the manufacturer [29].

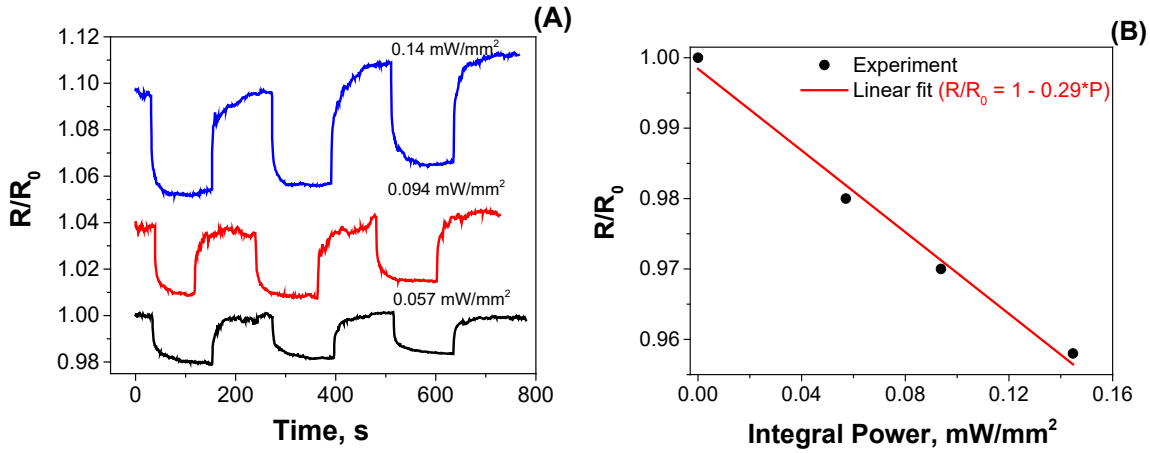

Figure A18: A: Temporal response of rGO/Kapton at different white light illumination powers. **B:** Relation between the incident integral power of LED lamp and relative change of resistance.

Similar configuration was used as with lasers, except the sensing surface of the sample was placed at a distance of 10 mm from the light source (the radius of light spot was ≈ 12 mm). The rGO/Kapton bolometer showed a change in resistance up to -2%, -3% and -4.5 % for power density of 0.057 mW/mm^2, 0.094 mW/mm^2 and 0.14 mW/mm^2, respectively (**Figure A18A**). Based on power-dependent studies we established linear relation between integral power and sensitivity (relative resistance change), which is shown in **Figure A18B**. To the best of our knowledge such rGO/Kapton bolometric sensor has not been reported yet. Despite not having the greatest TCR and sensitivity, the advantage of our bolometric device lies in the fact that it is transparent, lightweight and it can be easily

produced on flexible substrate by dip-coating in large quantities which is viable for practical applications in the mass market. In addition, it can be simultaneously used as a robust strain sensor which we demonstrated before. Rather moderate bolometric response reported here shows the potential of rGO-Kapton films to function as a sensitive element of infrared radiation where excellent mechanical stability is required. If needed, the TCR can be further increased by varying the degree of rGO reduction and rGO film thickness [30].

Conclusions

The following conclusions can be made as a result of the study presented in Chapter 7:

- Transparent and lightweight bolometric device has been made using rGO/Kapton material.
- Negative TCR coefficient has been found to be -0.42% K^{-1} at 295 K.
- Linear relation between integral power of irradiation and sensitivity has been established.

Thermally Reduced GO-P2 layers on polymeric substrate

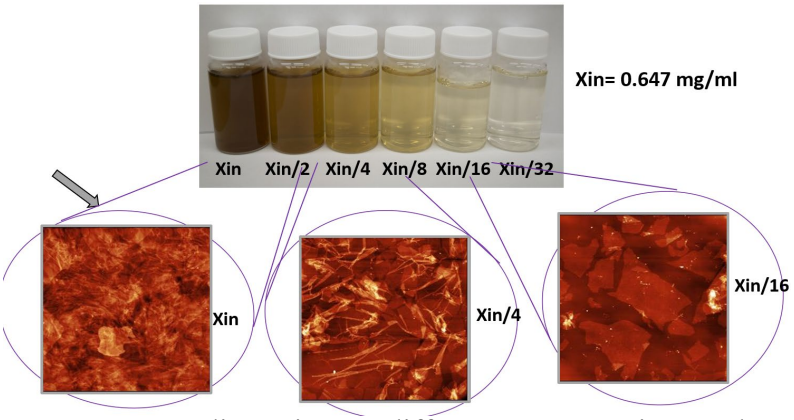

Figure A19: GO-P2 water dispersions at different concentrations and corresponding AFM images

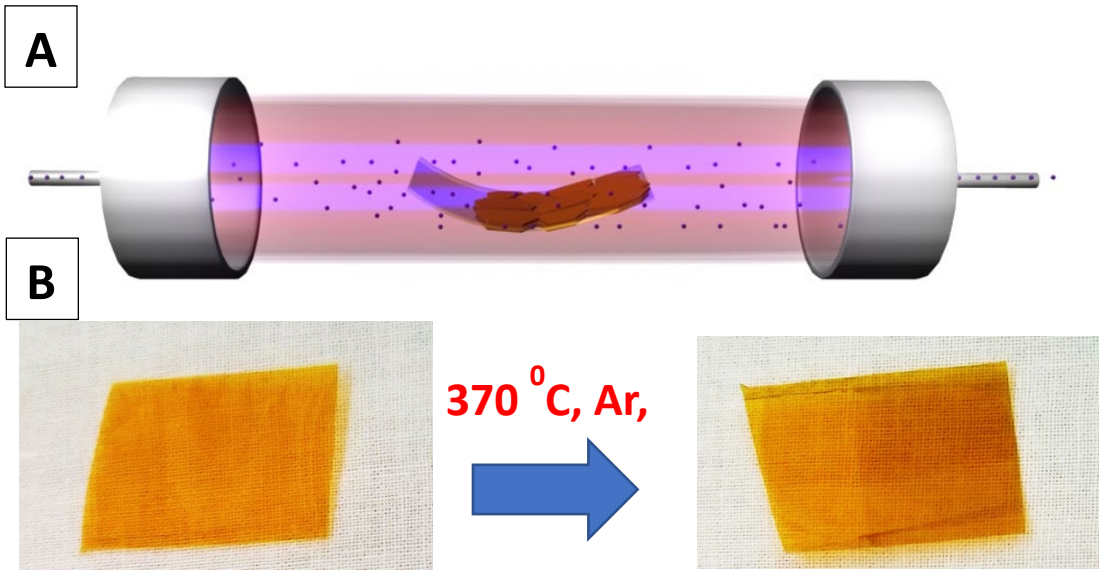

Figure A20: (A) Schematic of reduction (thermal conversion) procedure of GO-P2 on Kapton (termed as GO/Kapton) and (B) GO/Kapton (left) and thermally reduced (@ 370 ºC) rGO/Kapton (right).

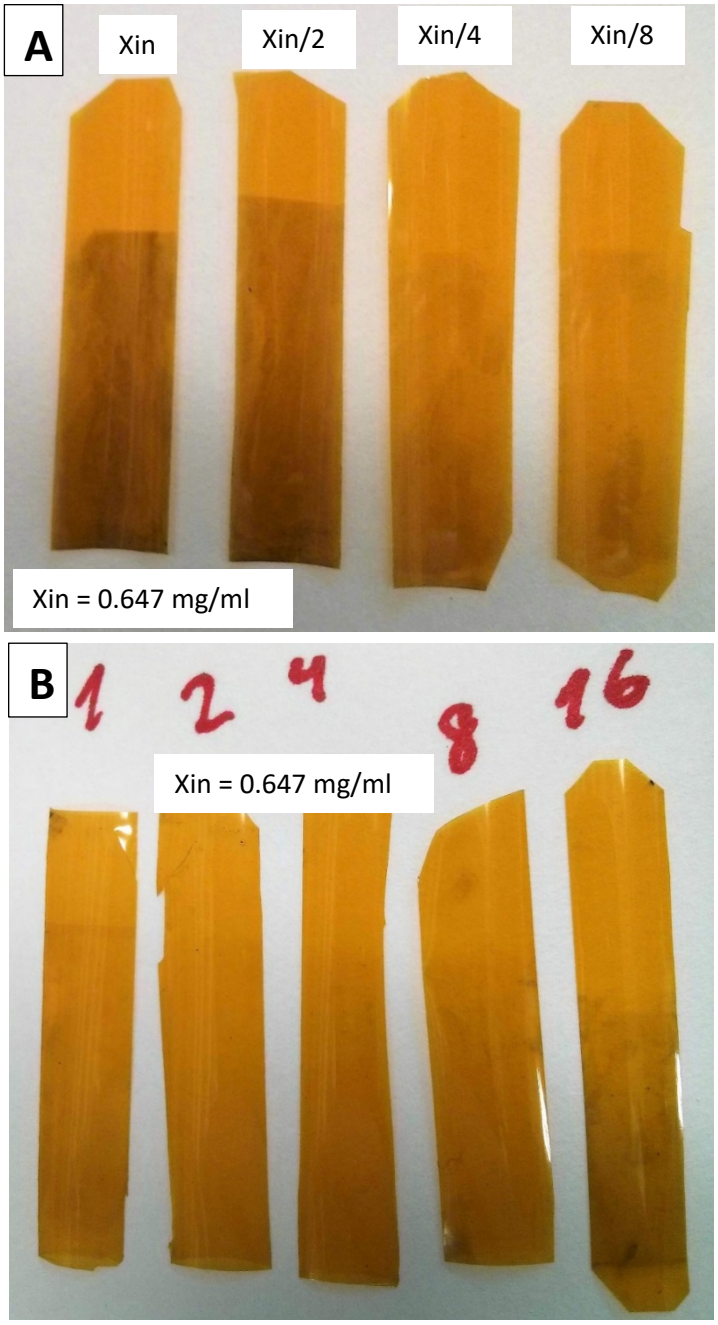

Figure A21: (A) Thermally reduced (@ 370 ºC) rGO/Kapton prepared from different concentrations of GO-P2 solution using dip-coating method. (B) Thermally reduced rGO/Kapton films prepared from Xin = 0.647 mg/ml using multiple dipcoating cycles (number of dipcoating cycles specified by marker).

Morphology of thermally reduced rGO (6nm) on Kapton

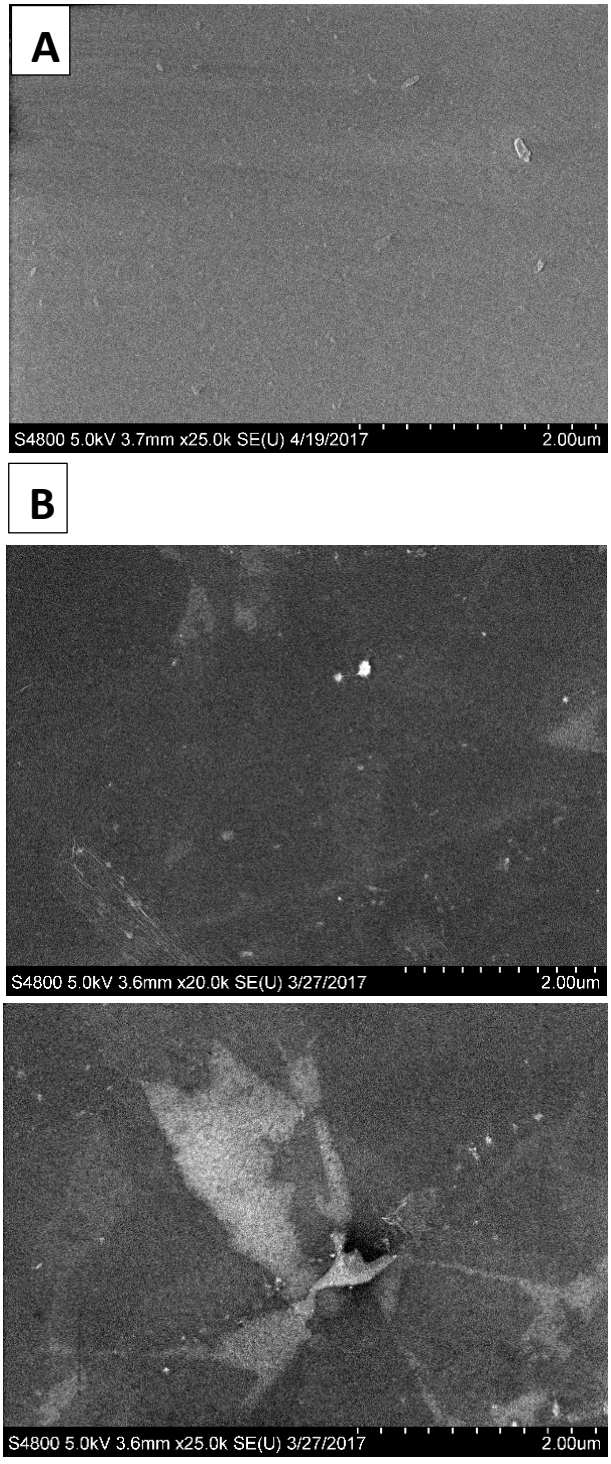

Figure A22: SEM images of (A) pristine Kapton film and (B) thermally reduced (@ 370 ºC) rGO/Kapton film.

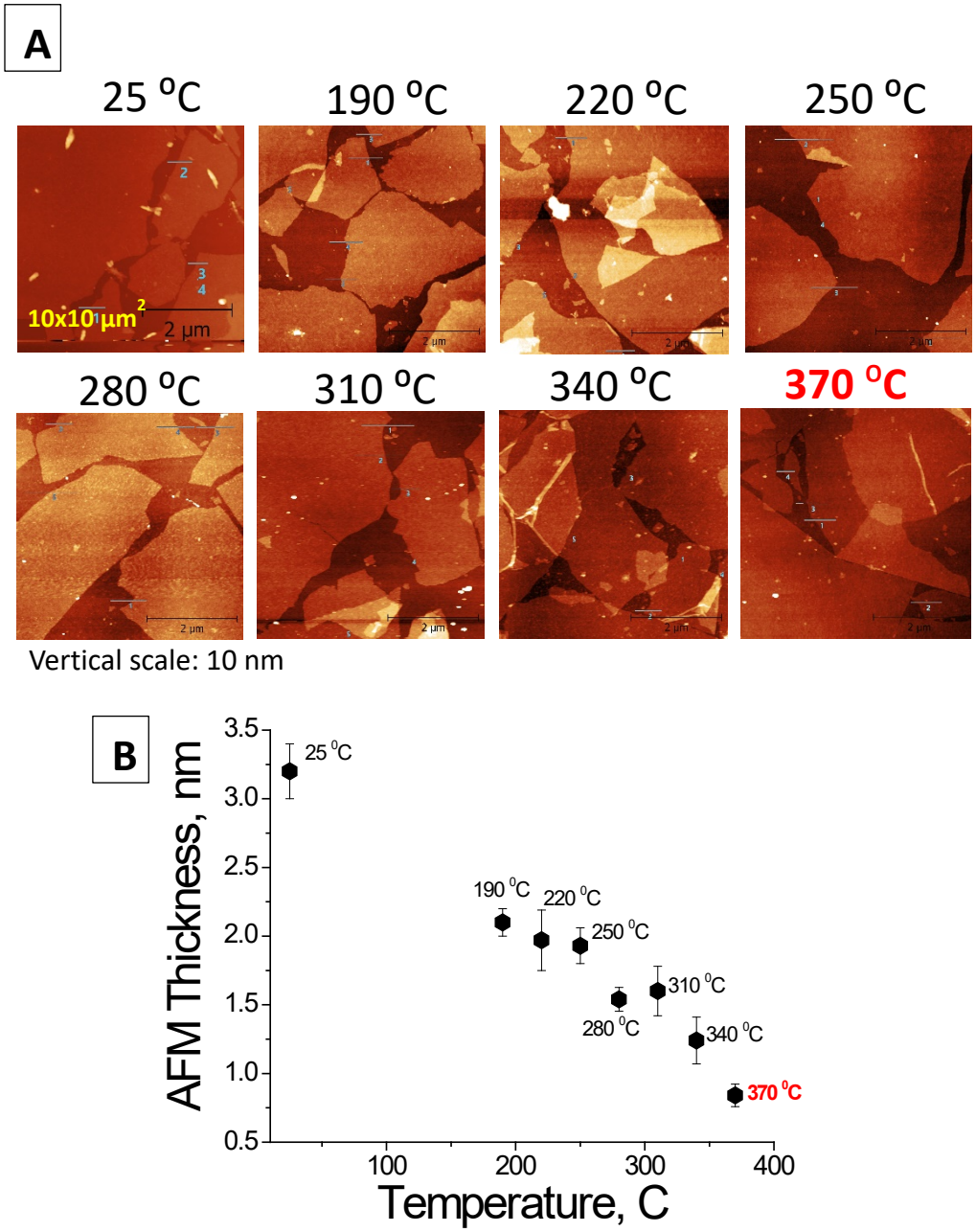

Figure A23: (A) AFM images of thermally reduced (@ 370 ºC, Argon) rGO-P2 on hydrophobic Si substrate and (B) thickness of GO-P2 layer as a function of reduction temperature.

The results from **Figure A24** showed that minimum reduction temperature of 370 ºC is needed to remove/decompose P2 polymer from GO-P2 structure. Such temperature is low enough not to cause the decomposition of Kapton substrate.

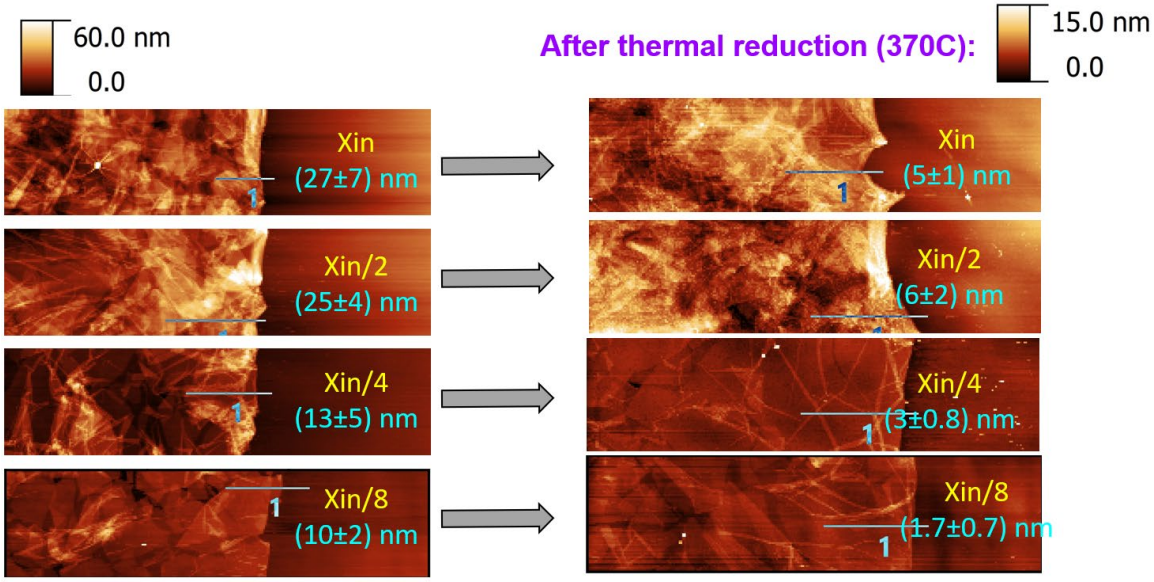

Figure A24: GO-P2 films on model hydrophobic Si substrate before (left) and after (right) thermal reduction at 370 ºC.

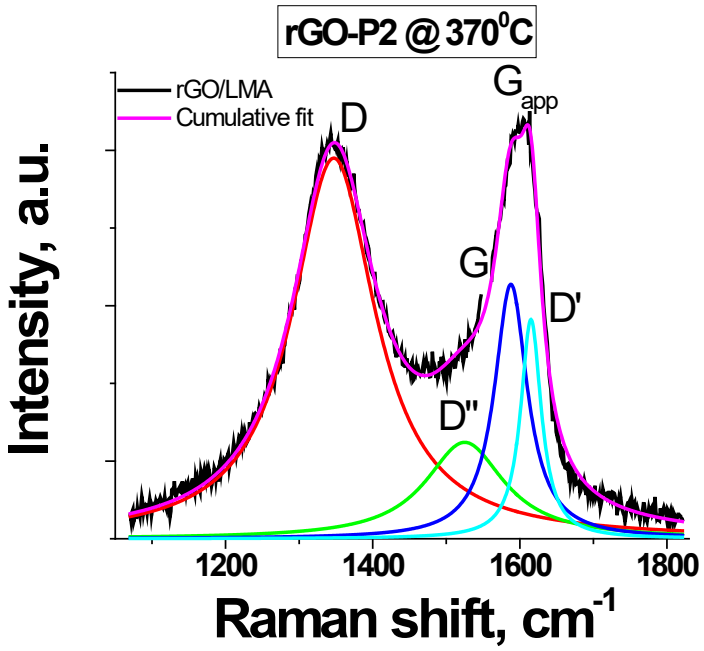

Model	Lorentz			
Equation	y = y0 + (2*A/PI)*(w/(4*(x-xc)^2 + w^2))			
Plot	**Peak D**	**Peak D"**	**Peak G**	**Peak D'**
y0	0.3 ± 0	0.3 ± 0	0.3 ± 0	0.3 ± 0
xc	1347.10755 ± 0.29418	1525.06498 ± 4.28875	1587.85188 ± 1.2373	1615.11281 ± 0.62152
w	137.99124 ± 0.9816	130.27384 ± 8.0626	54.25454 ± 4.63679	33.97201 ± 2.17632
A	106.19088 ± 0.83688	25.38987 ± 3.20882	27.90952 ± 4.47887	15.05486 ± 2.27974
Reduced Chi-Sqr	1.15234E-4			
R-Square(COD)	0.99558			
Adj. R-Square	0.9955			

Figure A25: Raman spectrum of GO-P2 film after thermal reduction at 370 ºC.

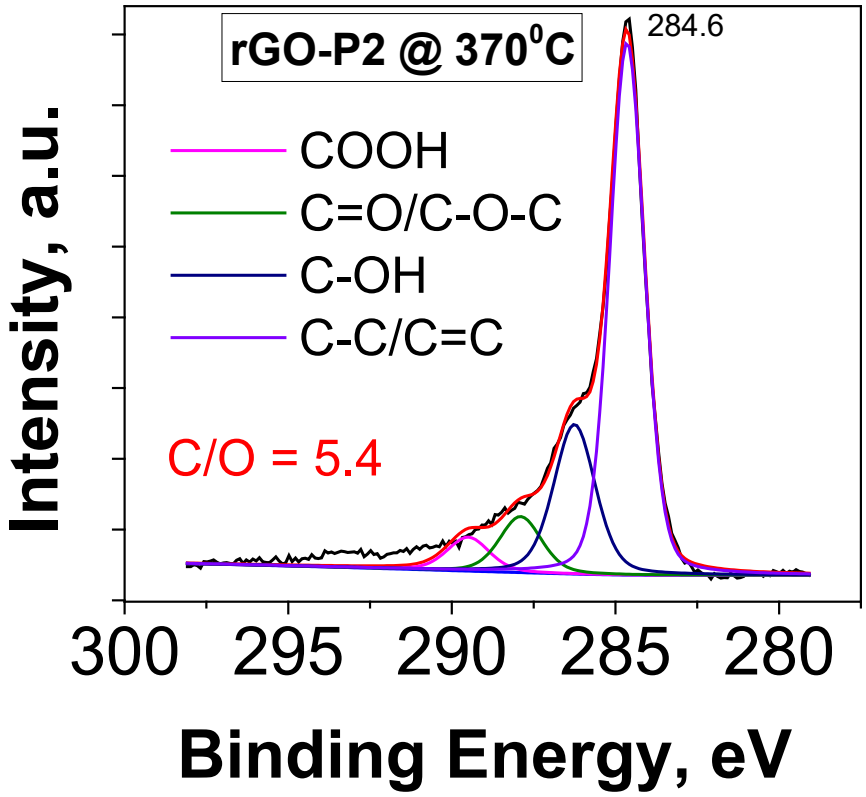

Figure A26: XPS spectrum of GO-P2 film after thermal reduction at 370 ºC.

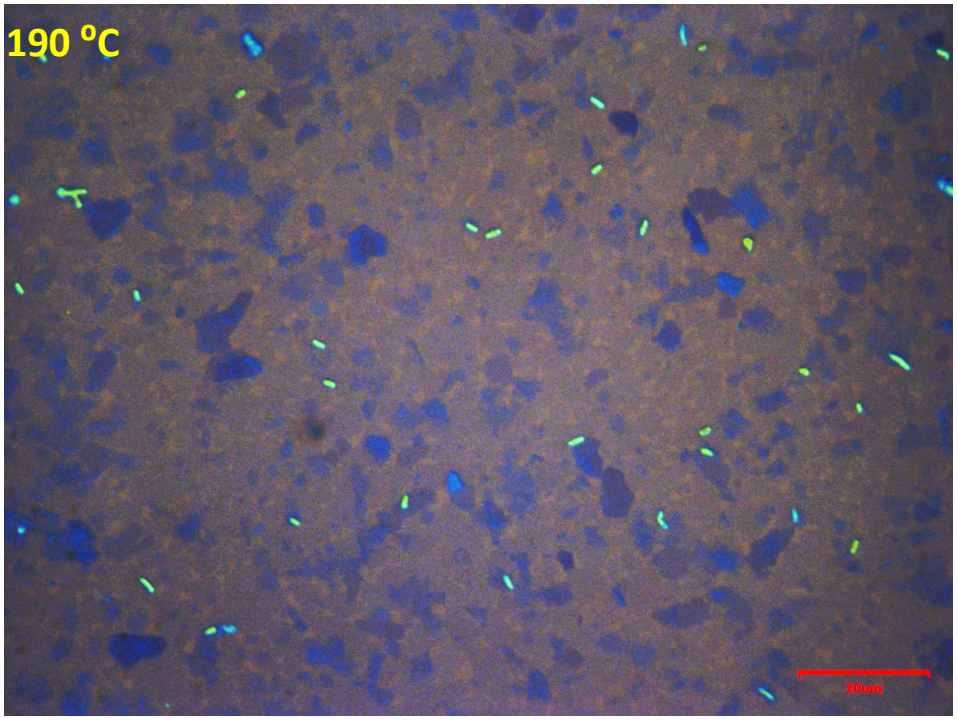
190 °C
20um

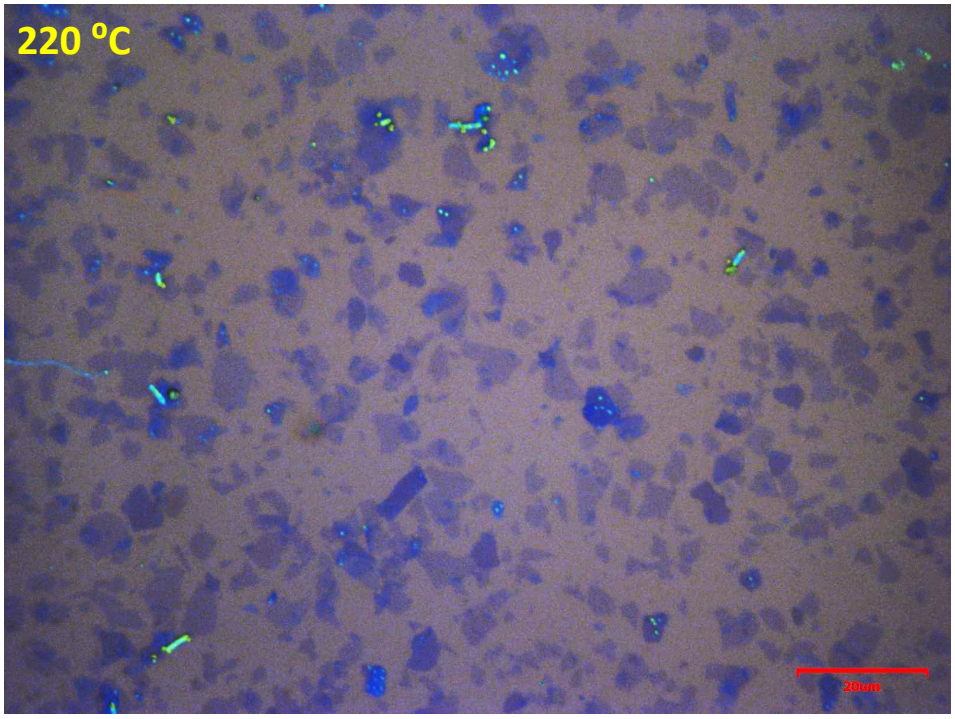
220 °C
20um

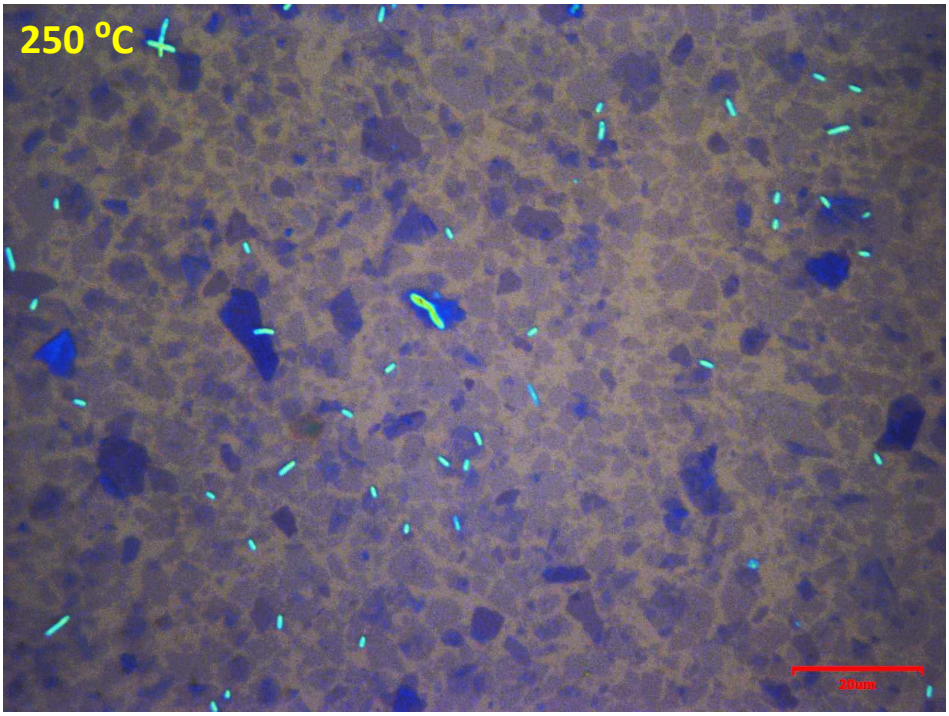
250 °C
20um

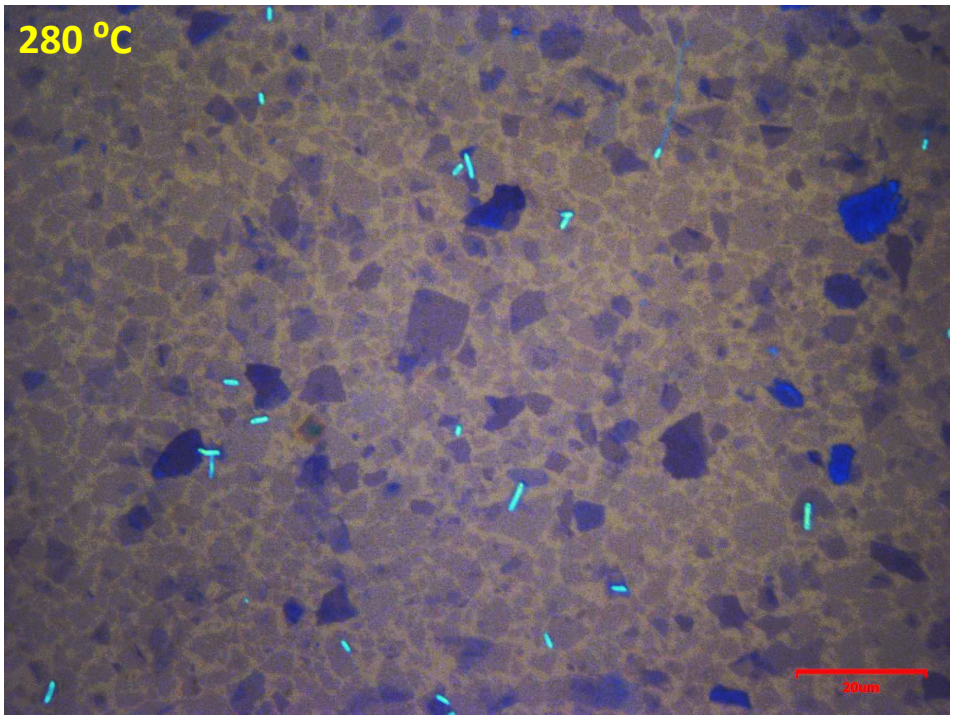
280 °C
20um

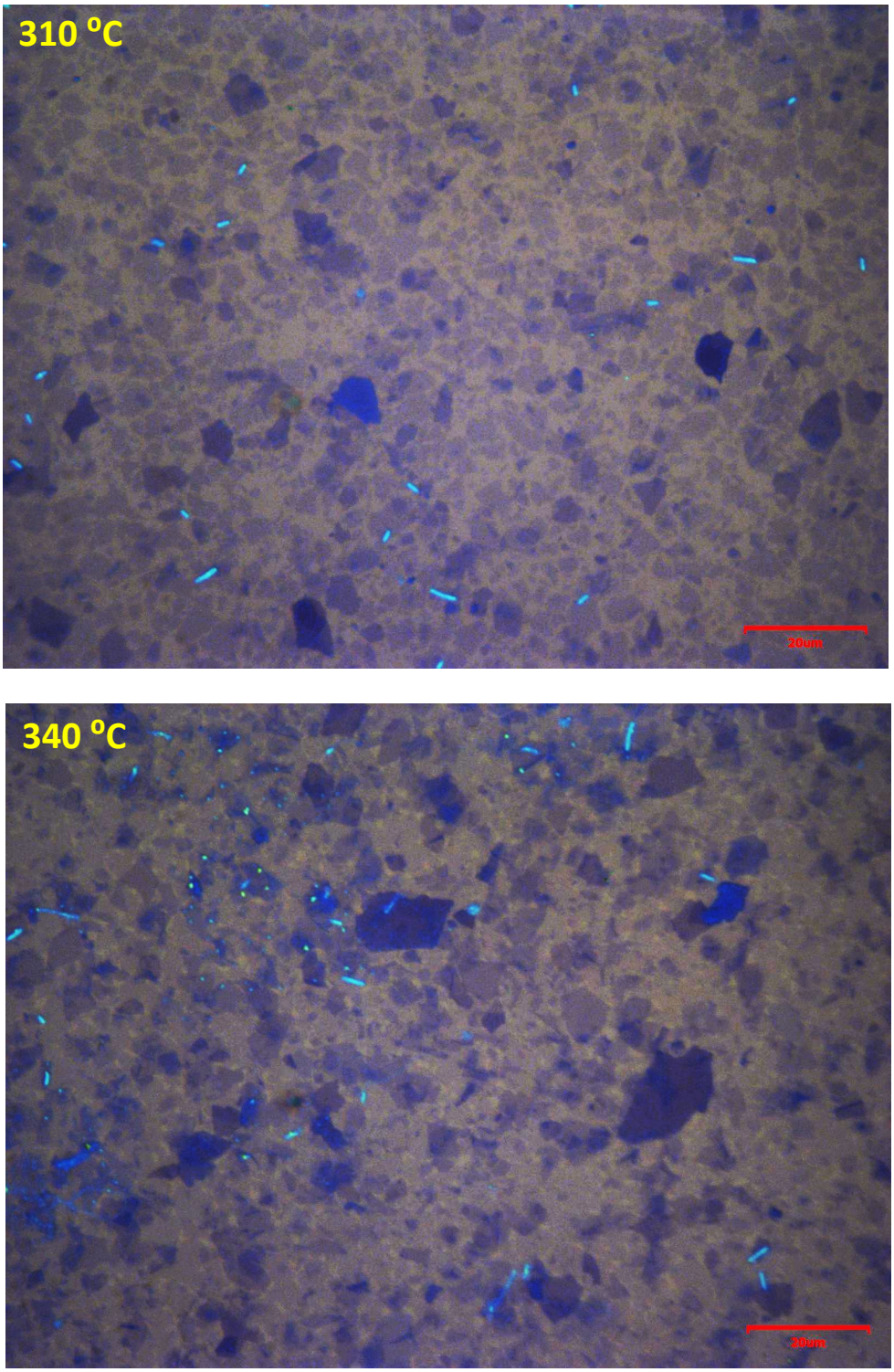

Figure A27: Optical images of GO-P2 film after thermal reduction at different temperatures. GO-P2 film was deposited on hydrophobic (silane-modified) Si substrate with thick SiO_2 layer (approx. 300nm) using 0.64 mg/ml GO-P2 solution.

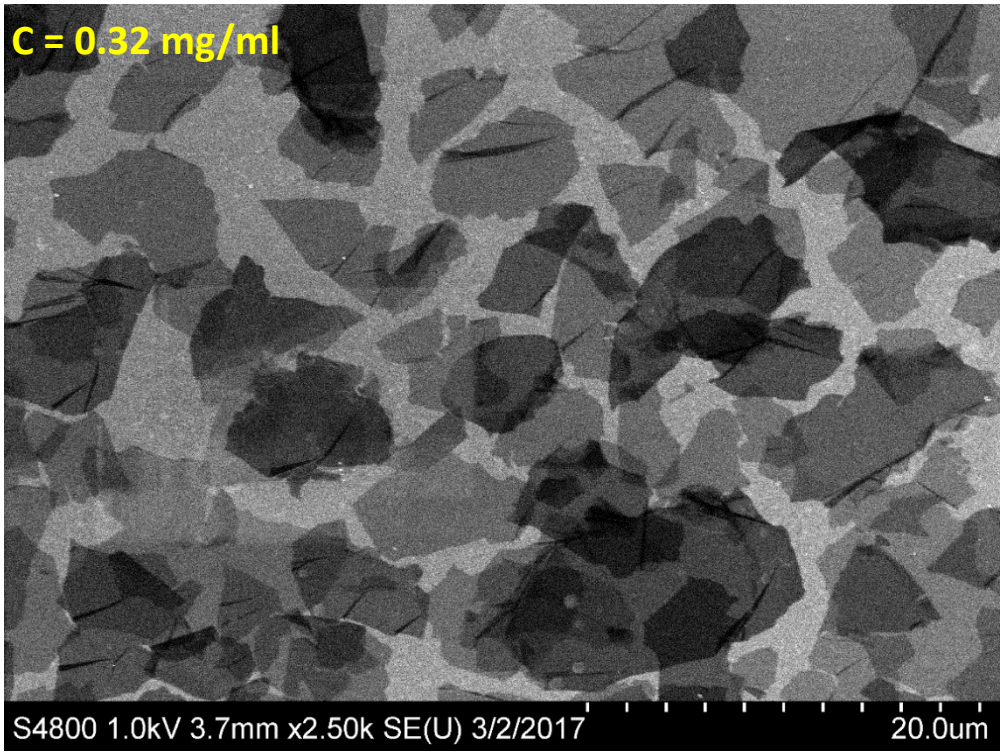
C = 0.32 mg/ml
S4800 1.0kV 3.7mm x2.50k SE(U) 3/2/2017
20.0um

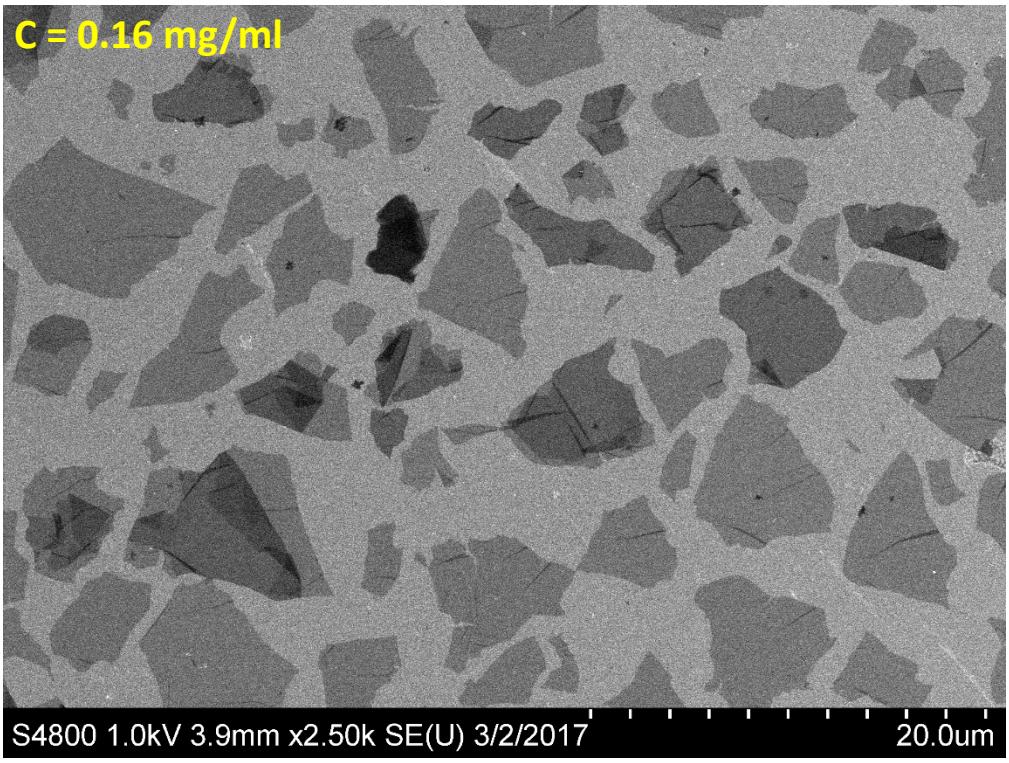
C = 0.16 mg/ml
S4800 1.0kV 3.9mm x2.50k SE(U) 3/2/2017
20.0um

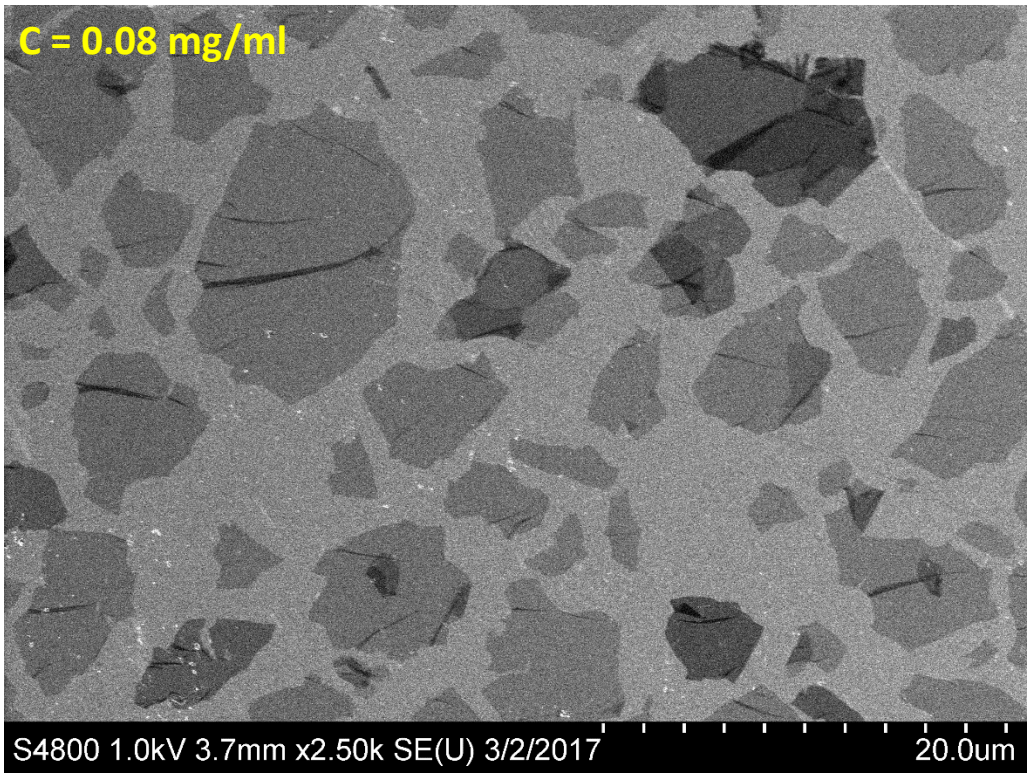

Figure A28: SEM images of thermally reduced rGO-P2 films with different concentration of GO sheets.

Electrical conductivity

To assess the electrical properties of the rGO-P2 films on hydrophobic silane-modified substrates, we conducted two-point I-V measurements. We used 2-point probe method, since the channel resistance is sufficiently large therefore the contact resistance to be neglected. Figure X shows the representative I-V characteristics at room temperature for thermally reduced Kapton samples with different rGO film thicknesses. The distance between electrodes was between 1 and 3 cm. An average of 3 independent measurements on 3 different samples has been carried out. Using thickness found by means of AFM we can estimate electrical conductivity.

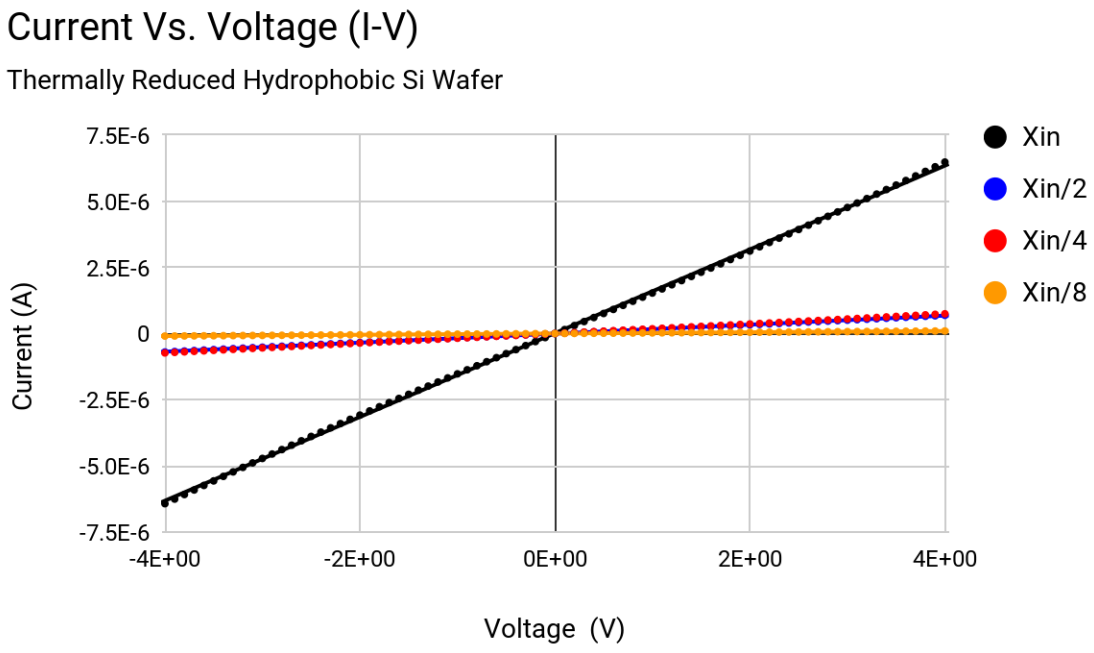

Figure A29: I-V curves acquired under ambient conditions for rGO-P2 on model hydrophobic Si substrate. All samples were thermally reduced at 370 ºC in Argon atmosphere.

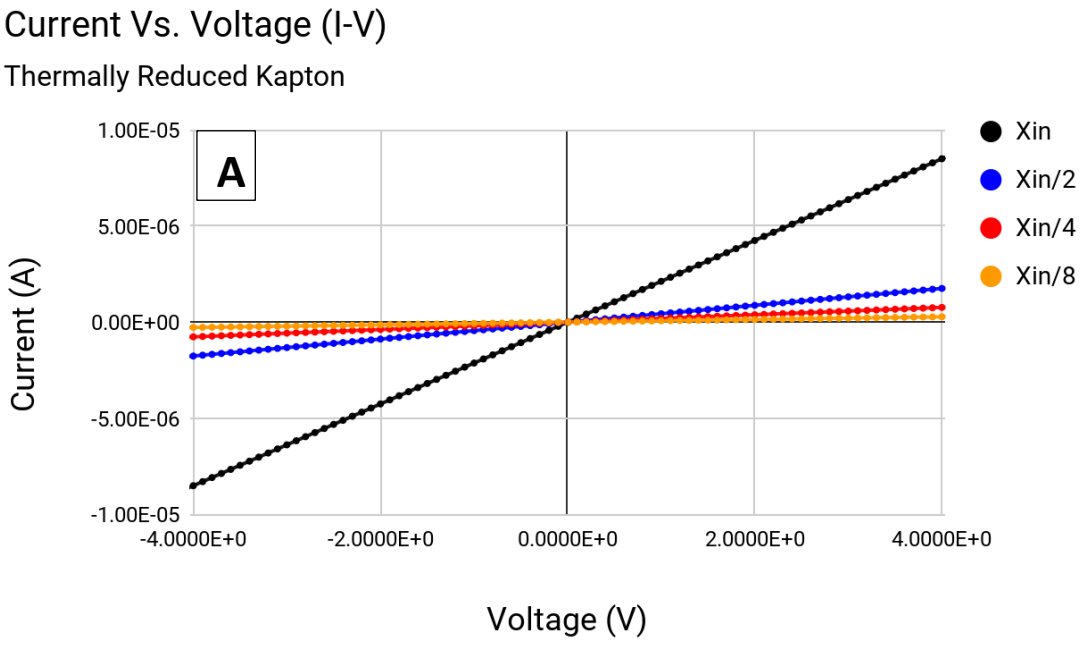

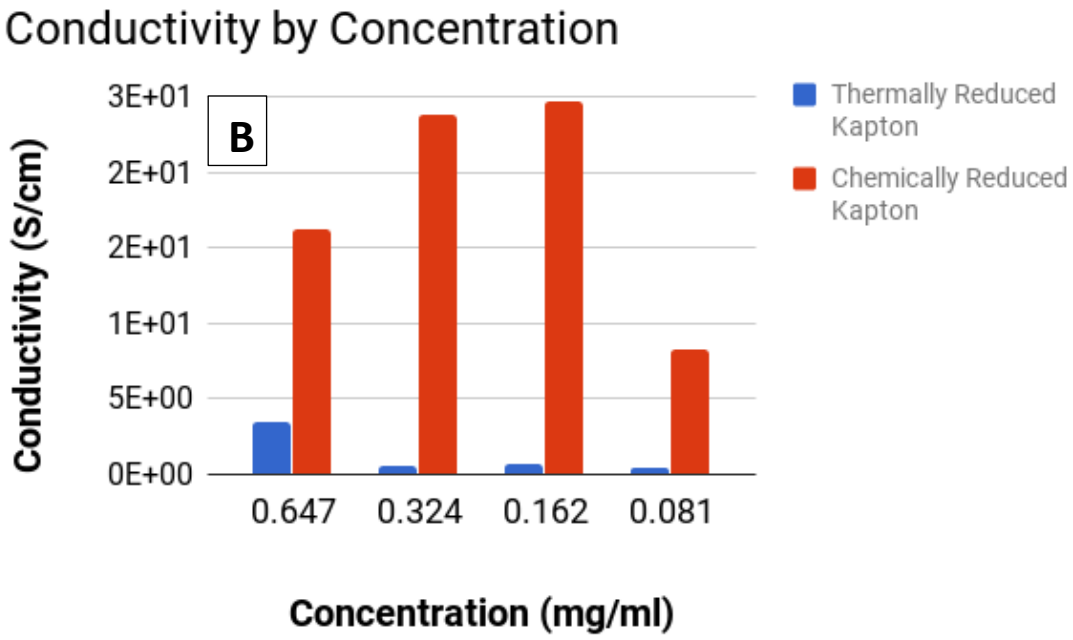

Figure A30: (A) I-V curves acquired under ambient conditions for rGO-P2 on Kapton substrates. All samples were thermally reduced at 370 ºC in Argon atmosphere. (B) Comparison between electrical conductivities of thermally reduced and chemically reduced GO-P2 films deposited Kapton substrate.

GO-based composites

Electrically conductive composites may become very effective in lightweight transparent electromagnetic interference (EMI) shields for the radio frequency range in defense and aerospace applications [31]. For EMI shielding the conductivity should be at least 10^{-3} - 10^{-1} S/cm [31-32]. The EMI shielding is particularly important and very difficult to attain in the areas of visual observation - observation windows [33], electronic displays [34], etc. Various transparent materials [35-36] have been investigated for this role, but the promising and low cost are carbon-based materials [35, 37-39], especially in applications where mass should be as low as possible. The fabrication method of EMI shields is based on two approaches the introduction of the conductive material into the polymer matrix or the deposition of conductive coatings to the surface of polymeric substrate [40], [41]. For example, Kim et. al [40] demonstrated that 20 nm thick and 73% transparent (in visible range) rGO film with conductivity of only 12 S/cm exhibited ~ 50 % shielding of incident waves. Thus, we believe that our rGO films can be practically used in the above mentioned applications.

The procedure of the introduction of the conductive material (reduced GO) into the polymer (polypropylene (PP)) matrix is shown in **Figure A32 (A, B)**. The approach involves the following steps: (1) GO-P2 layer is deposited on PP film via conventional dipcoating to obtain GO-PP film; (2) GO-PP film is sandwiched inbetween two plain PP films (**Figure A32A**) to obtain PP/GO-PP/PP triple layer. Finally, PP/GO-PP/PP is placed into home-built steal mold and pressed with weight of at least 10 kg. Then, the mold with samples was placed into preheated oven at 220 ºC for at least 2 hours. Slight vacuum was

maintained inside the oven. After annealing, the mold was taken out of the oven and was slowly cooled down to room temperature under ambient conditions.

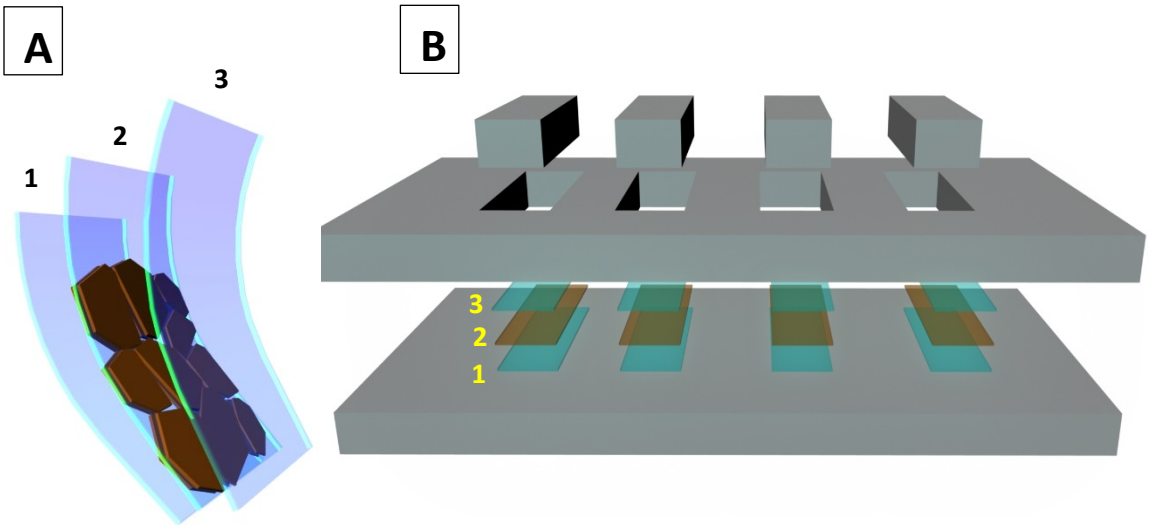

Figure A31: Preparation of rGO-PP composite material. (A) rGO-covered polypropylene sandwiched between two plain PP films PP/GO-PP/PP. (B) Schematic of the procedure for rGO-PP fabrication. 12 µm-thick PP films were used for composite preparation.

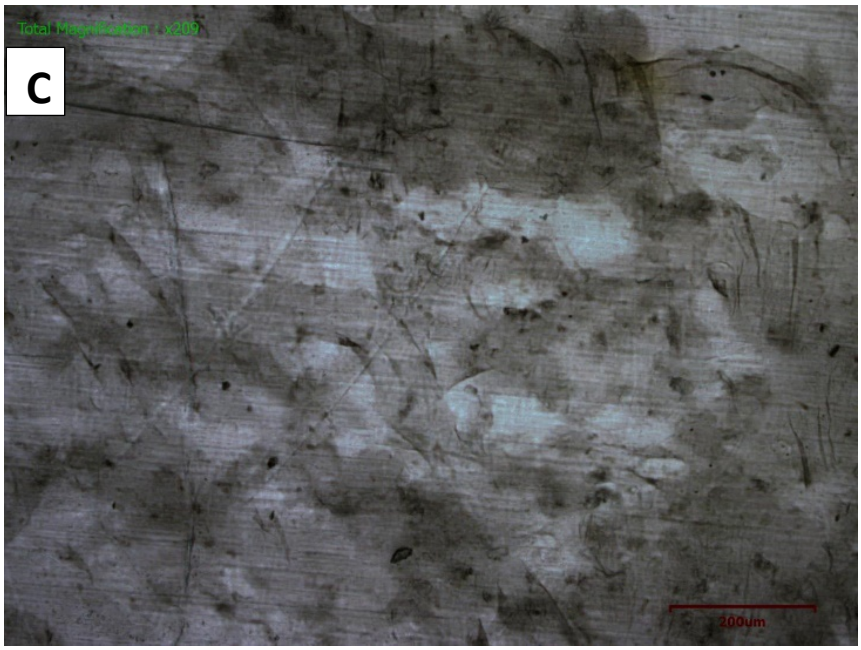

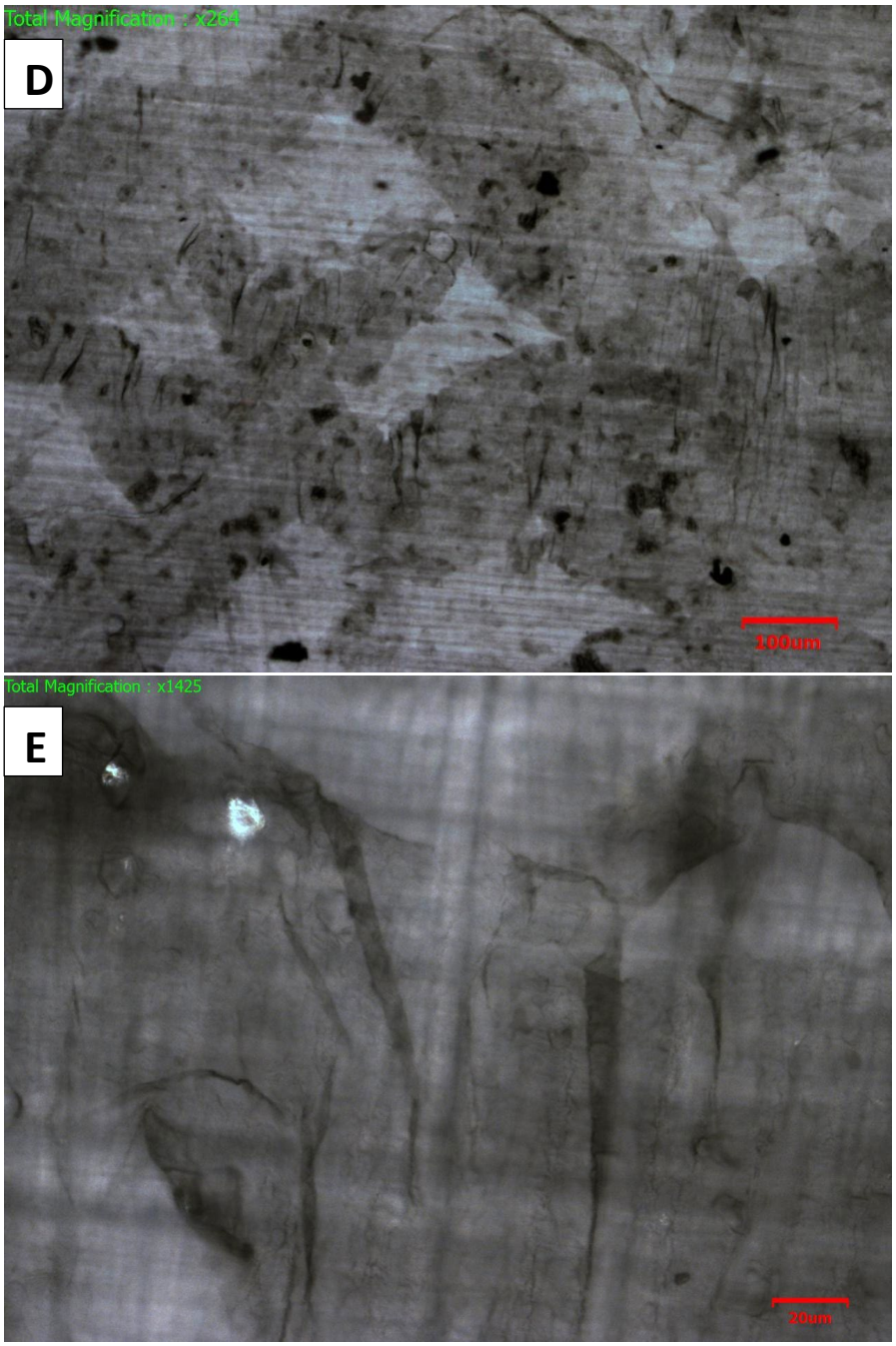
Total Magnification : x264
D
100um
Total Magnification : x1425
E
20um

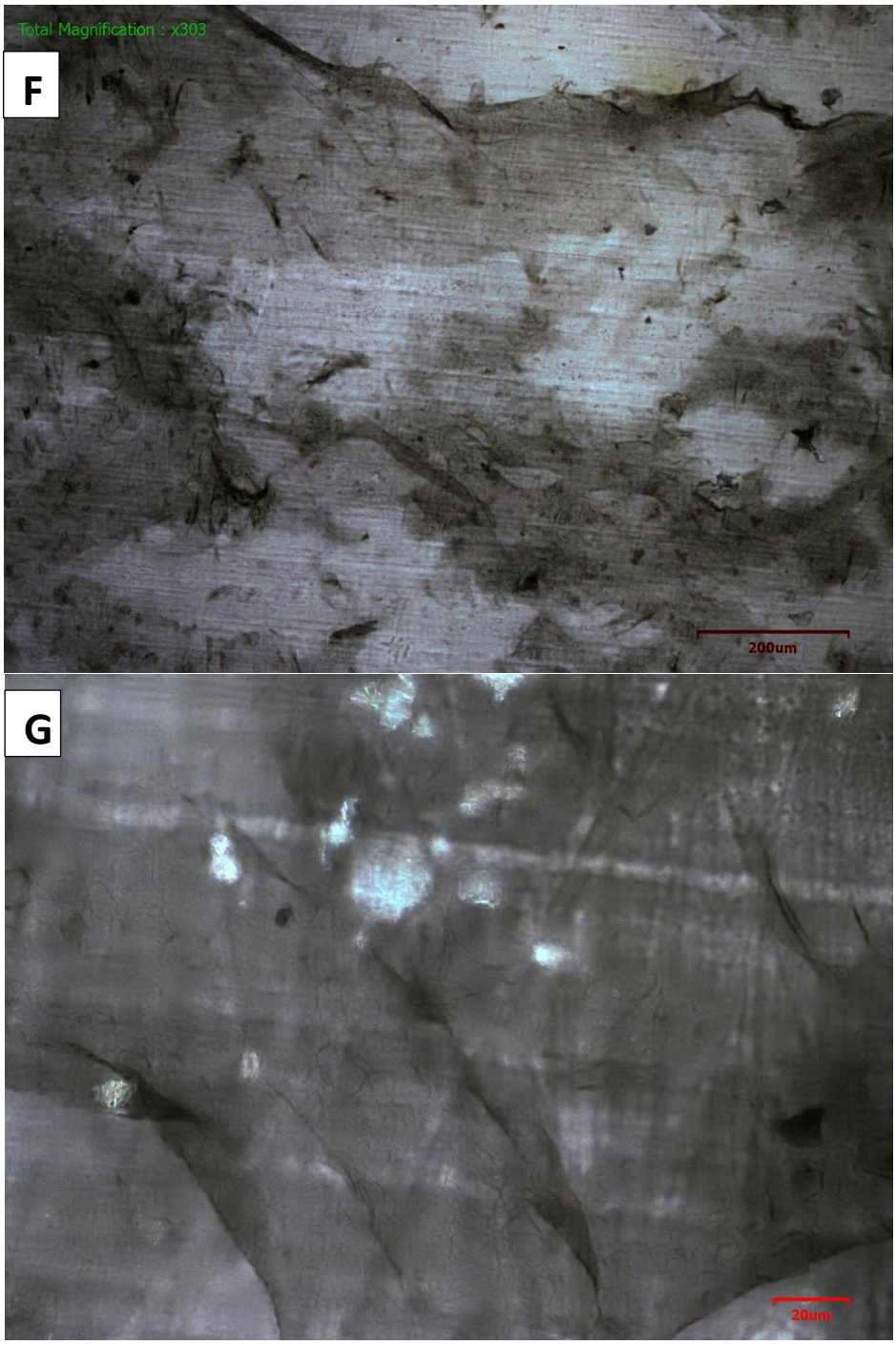
Total Magnification : x303
F
200um
G
20um

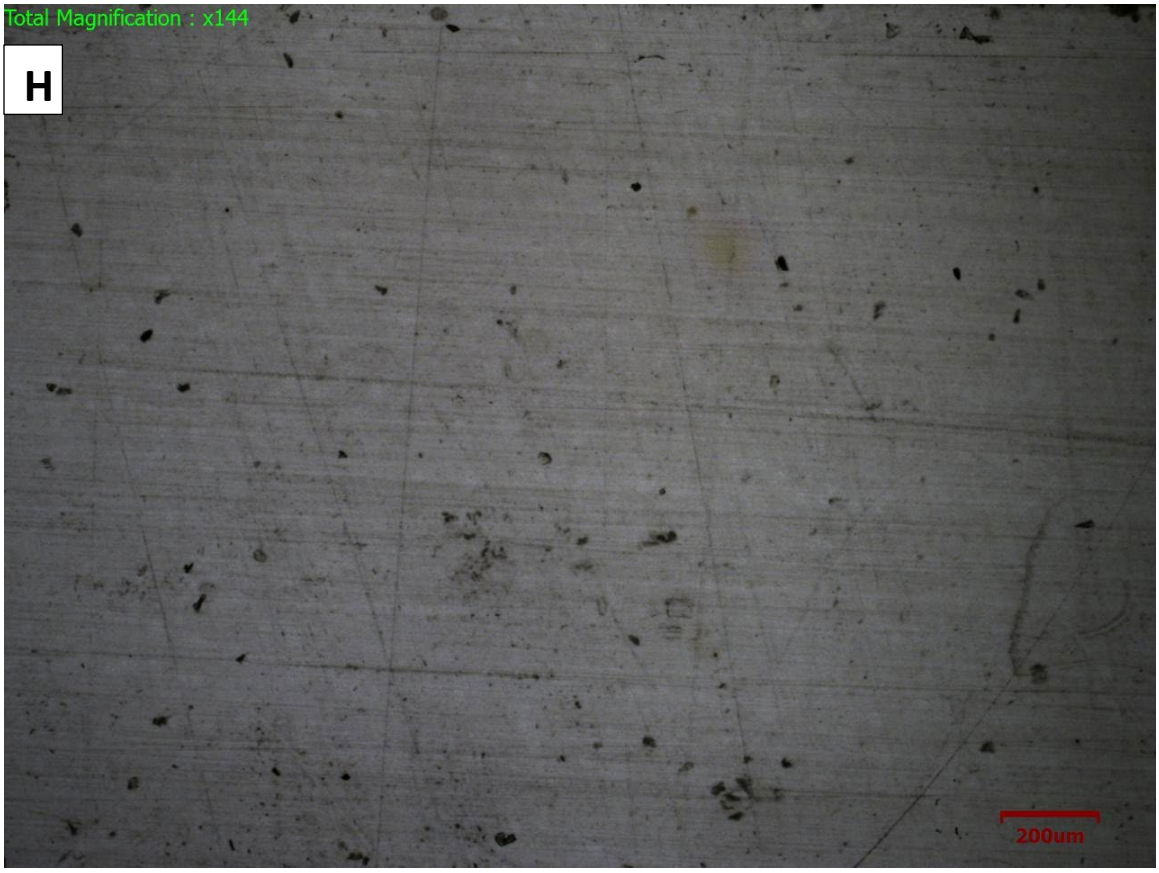

Figure A32: Optical images of (C-G) PP/GO-PP/PP composite films and (H) plain PP film.

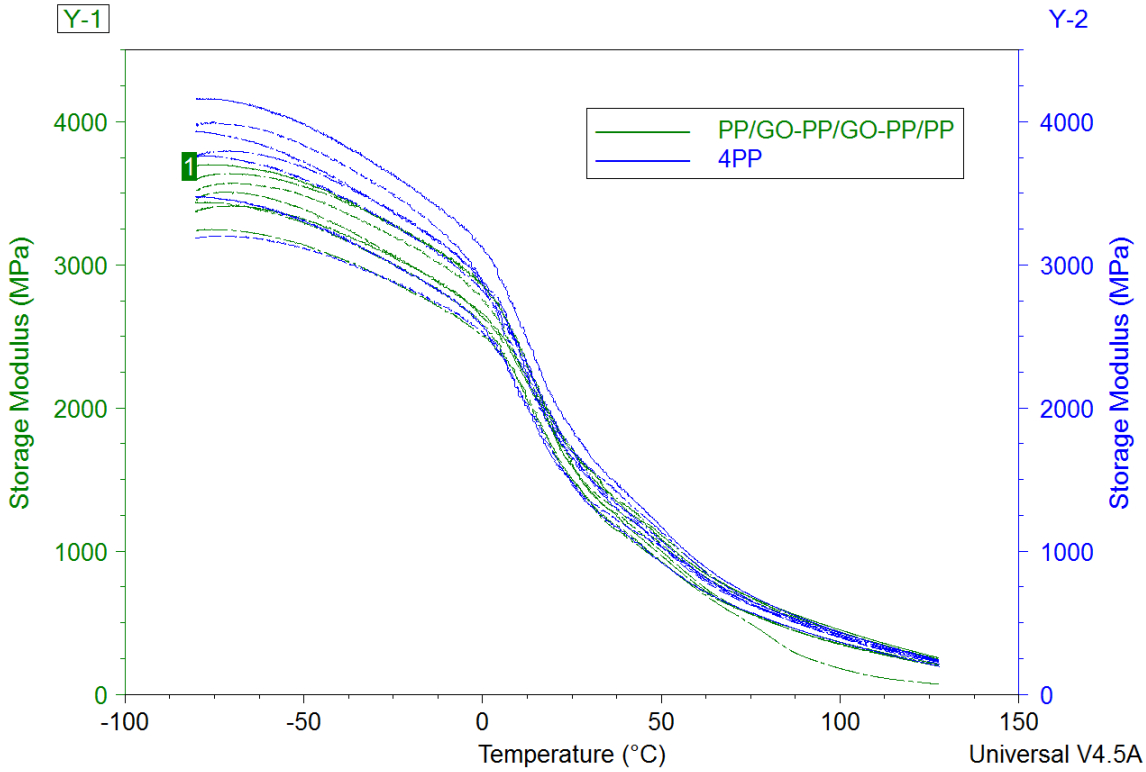

Figure A33: DMA testing of 4 layer rGO-PP composites.

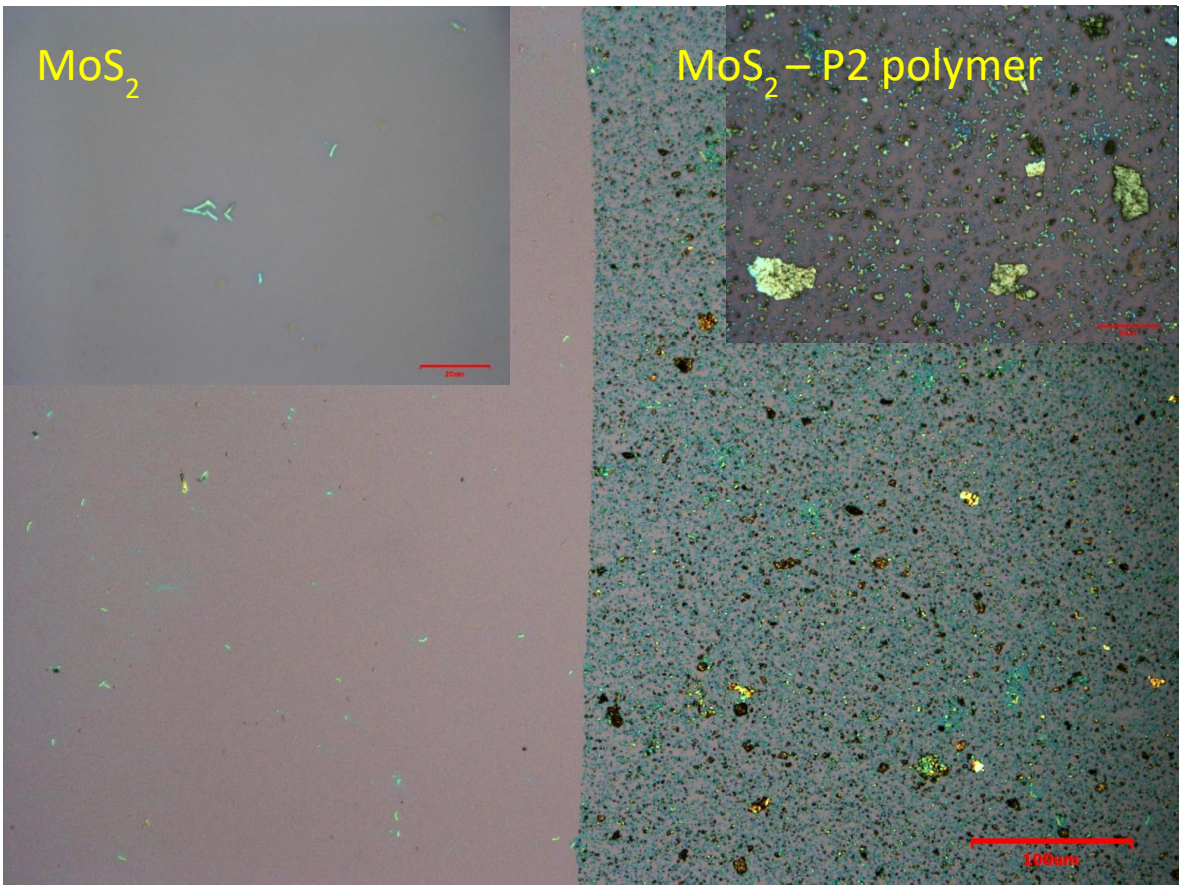

Figure A34: MoS_2 (left) and MoS_2-P2 (right) on model hydrophobic substrate.

Synthesis and Properties of Composite Material for Photocatalysis Based on Zinc Oxide Nanostructures and Reduced Graphene Oxide Bilayers (Data obtained in collaboration with Dr. Kapustianyk and Dr. Turko)

A promising method of water purification from the organic dyes is photocatalysis based on employment of semiconductor materials. In this respect the most studied and used are the photoactive materials based on TiO_2, WO_3, Zn_2SnO_4 and ZnO. Among them zinc oxide-based catalysts are low cost, stable, non-toxic materials that do not require reactivation. ZnO is a wide-band semiconductor (Eg 3.37 eV) in which electron-hole pairs are generated by ultraviolet illumination. To this end we prepared composite materials from zinc oxide nanorods and reduced graphene oxide (rGO) sheets. Nano- and microstructures of zinc oxide were obtained by hydrothermal methods on the surface of rGO layers [42].

The photocatalytic properties of ZnO/rGO-based nanocomposites (**Figure A36**) were tested using photocatalytic degradation of the aqueous solution of methyl orange (MO) dye as a model. ZnO nanostructures were grown on the silicon (001) substrates by two different methods. rGO monolayers were formed by the thermal reduction techniques. The samples and aqueous dye solutions were irradiated using UV light. The source of UV radiation was a DRT-125 Hg-quartz lamp with a radiation power not higher than 26 W in the wavelength range of 315-400 nm. The lamp was warmed up for 10 min before the experiments in order to stabilize its light intensity. Test samples were placed into a standard 3.5 mL quartz cuvette at a distance of 10 cm from the radiation source. The dye photodegradation kinetics was studied by its concentration change, determined with

Specord M-40 spectrophotometer measuring the optical density at the dye absorption maximum (465 nm). The degradation efficiency of MO was calculated using the formula:

$$C_r = (C_0 - C_t)/C_0 \cdot 100\% = (A_0^{465} - A_t^{465})/A_0^{465} \cdot 100\%, \quad (1)$$

where C_0 – is the starting dye concentration; C_t - the dye concentration after UV irradiation during time t; A_t^{465} and A_0^{465} – the dye solution optical densities at 465 nm before and after irradiation during time t.

After one hour of UV irradiation *the* samples grown by the hydrothermal method on a rGO-P1 monolayer had C_r = 85% (**Figure A37**).

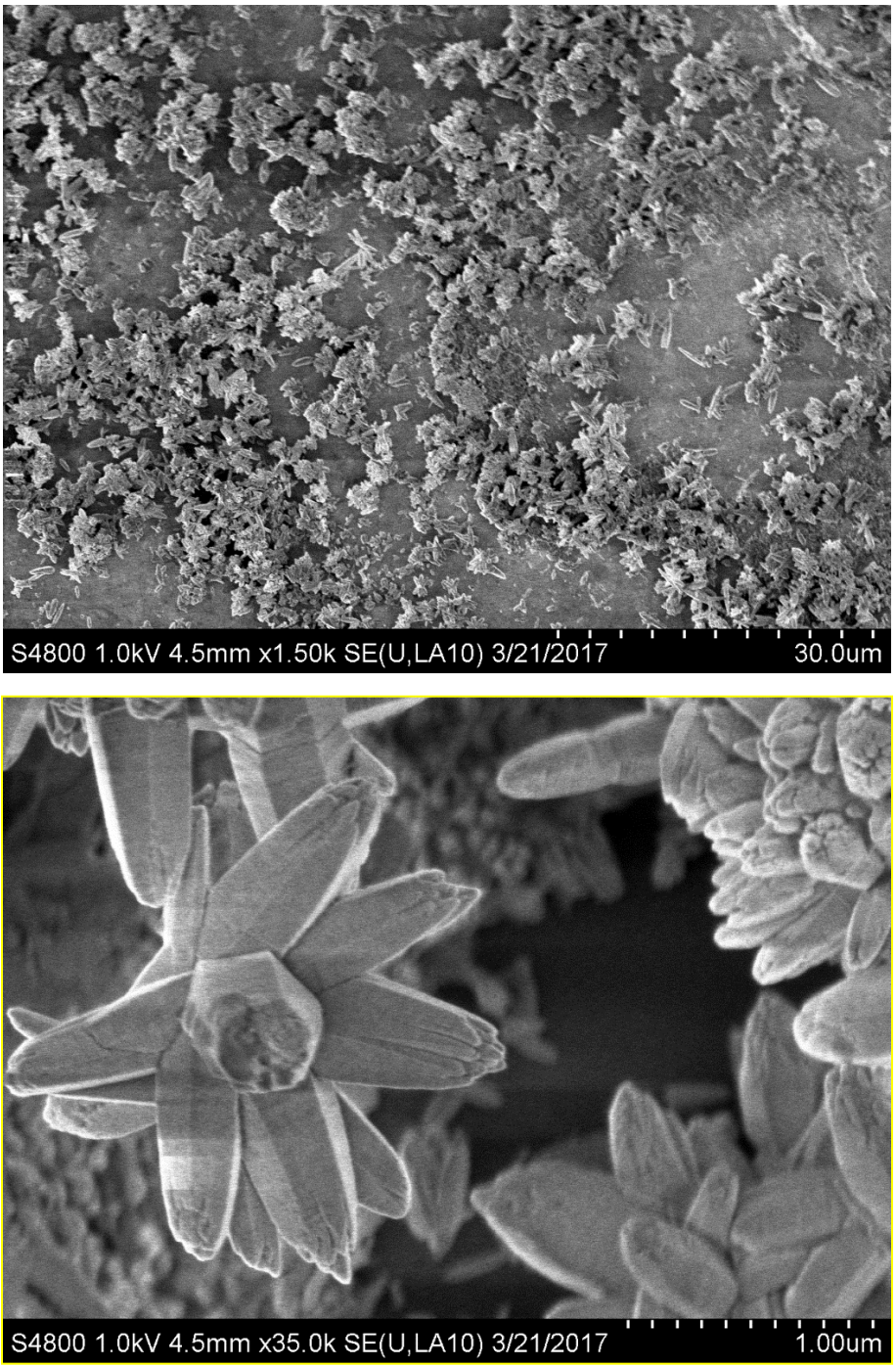

Figure A35: ZnO nanorods grown by hydrothermal method on rGO-P1 mono- and bilayer films.

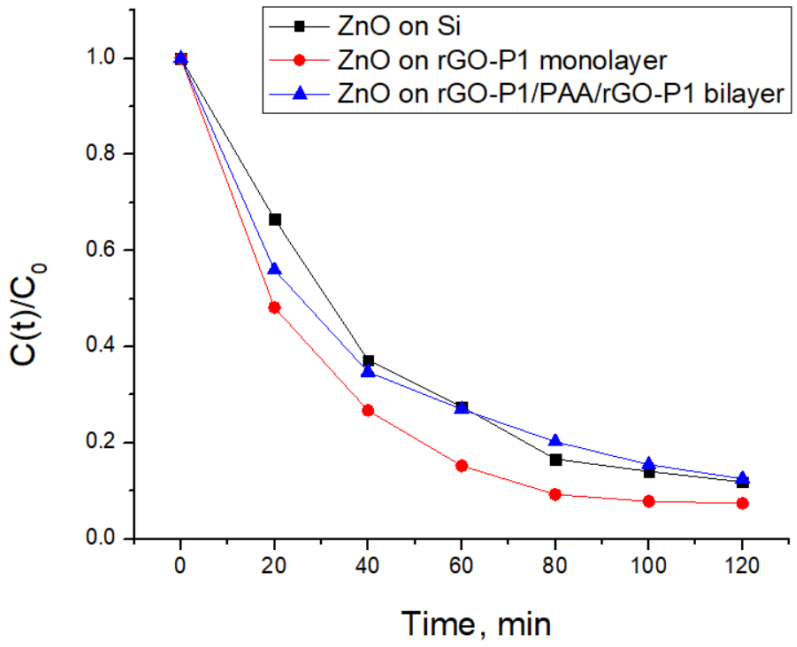

Figure A36: The dye photodegradation kinetics

Thermoresponsive mixed polymer brushes

Introduction

The reported study focuses on the synthesis and characterization of mixed polymer brush platform that can respond to temperature variations. The brush is based on the tethered chains of polyethylene glycol [PEG] and poly(N-isopropylacrylamide) [PNIPAAM]. Specifically, the responsive surface was obtained by sequential grafting of carboxy-terminated PEG and PNIPAAM to a silicon wafer using poly(glycidyl methacrylate) anchoring layer. Quartz microbalance (QCM-D) was used as a primary tool to test the switchability of the brush and its affinity towards protein (fibrinogen) adsorption. Also kinetics of the protein adsorption process and viscoelastic properties of the polymer brush layer was studied by that technique. It is expected that the switchable polymer brush

platform will have a broad applications in bioengineering, medicine as a tool for the guided differentiation of stem cells or as a targeted drug delivery system.

Experimental and materials

Grafting

Firstly, using "grafting to" method we investigated grafting of polymer brushes to the reference surface. Silicon wafers used as model surfaces in our experiments. Highly polished single crystal silicone wafers (Semiconductor Processing Co.) were cleaned in an ultrasonic bath for 30 minutes, placed in a hot "piranha solution" (3:1concentrated sulfuric acid/30% hydrogen peroxide) for 1 hour and then rinsed several times with high purity water. Next, the surface of the wafers was covered with ultrathin polyglycidyl methacrylate (PGMA) film (M_n=176000, M_w=640409 ρ=1.08g/cm3) from 0.05% chloroform solution and subsequently annealed in a vacuum at 120˚C for 10 minutes. Unbounded polymer was removed from the surface by multiple washing with chloroform. Then, monocarboxy terminated poly(*N*-isopropylacrylamide) (PNIPAM_1x) (Mn=23000, M_w=26500, PDI=1.15, ρ=1.05g/cm^3) from 1% methylethyl ketone (MEK) solution was grafted to the surface covered with the primary PGMA anchoring layer and also annealed in a vacuum at 150˚C for 1 hour. The same procedure was held for the dicarboxy terminated poly(*N*-isopropylacrylamide) (PNIPAM_2x) (Mn=35500, PDI=1.55, ρ=1.05g/cm^3) from 1% methylethyl ketone (MEK) solution. Unbounded polymers were extracted by multiple washing with MEK. Polyethylene glycol (PEG) (M_n=5000) grafting to PGMA anchoring layer was performed from the melt in a vacuum at 110˚C. Unbounded PEG was removed from the surface by multiple washing with methanol. The polymer brushes attached to the

surface of PGMA-modified Si-wafers were examined by scanning probe microscopy (Dimension 3100, Digital Instruments, Inc.) and ellipsometry. The static contact angle measurements were carried out by goniometer (Kruss, model DSA 10). Secondly, the same grafting procedure was applied to the SiO_2-coated AT-cut quartz crystals (QSX 303 - 14 mm in diameter with ≈60 nm thick SiO_2 layer on the top of the gold electrode) from Q-Sense AB. Before grafting, all sensors were treated by UV/ozone for 10 minutes. Next, sensors were immersed in the 2% Sodium Dodecyl Sulfate (SDS) solution in milliQ water for 30 min. Then careful rinsing with milliQ water, followed by drying with nitrogen gas took place. Finally, UV/ozone treatment for 10 minutes was repeated.

Interfacial processes (protein adsorption/desorption) were monitored in situ with subsecond time resolution. QCM-D measurements were performed with a Q-Sense E1 system (Biolin Scientific AB). The system was operated in flow mode with a flow rate of 100 μL/min (PBS buffer) using a peristaltic pump (ISMATEC, IPC-N). Time-resolved Δf and ΔD were measured at the fundamental (n = 1) and six overtones (n = 3, 5, ...,13), corresponding to resonance frequencies of fn ≈ 5, 15, 25, ..., 65 MHz.

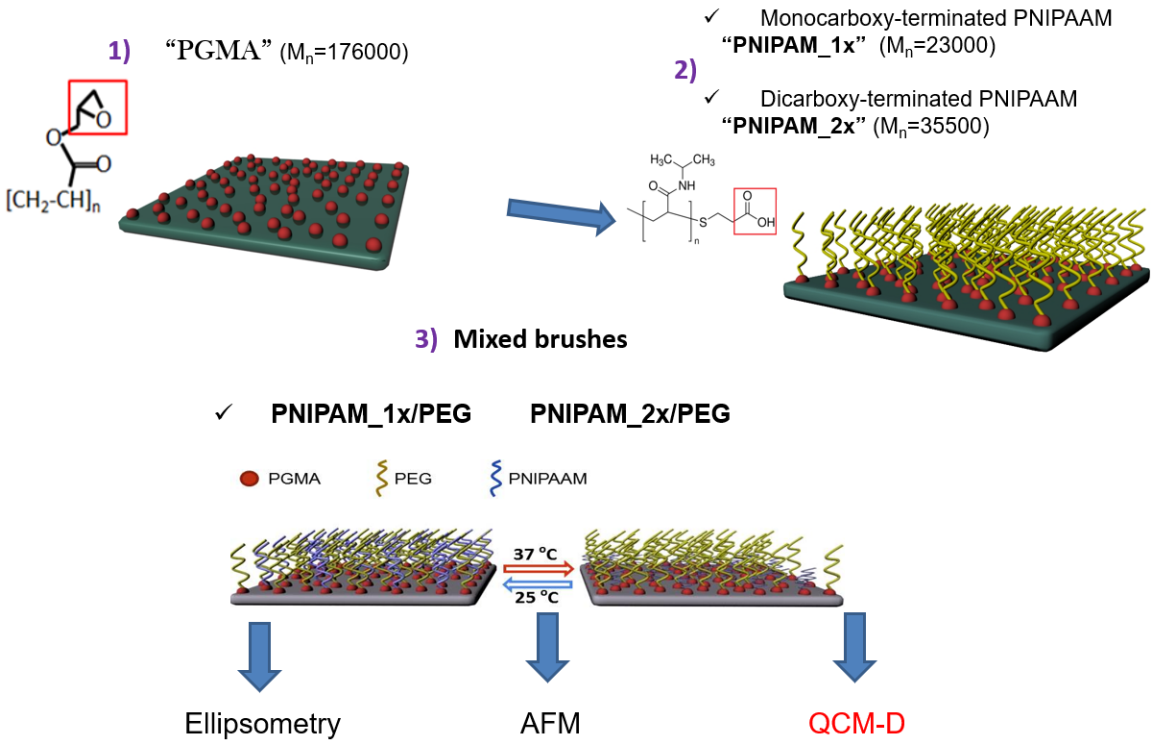

Figure A37: Synthesis of mixed polymer brushes.

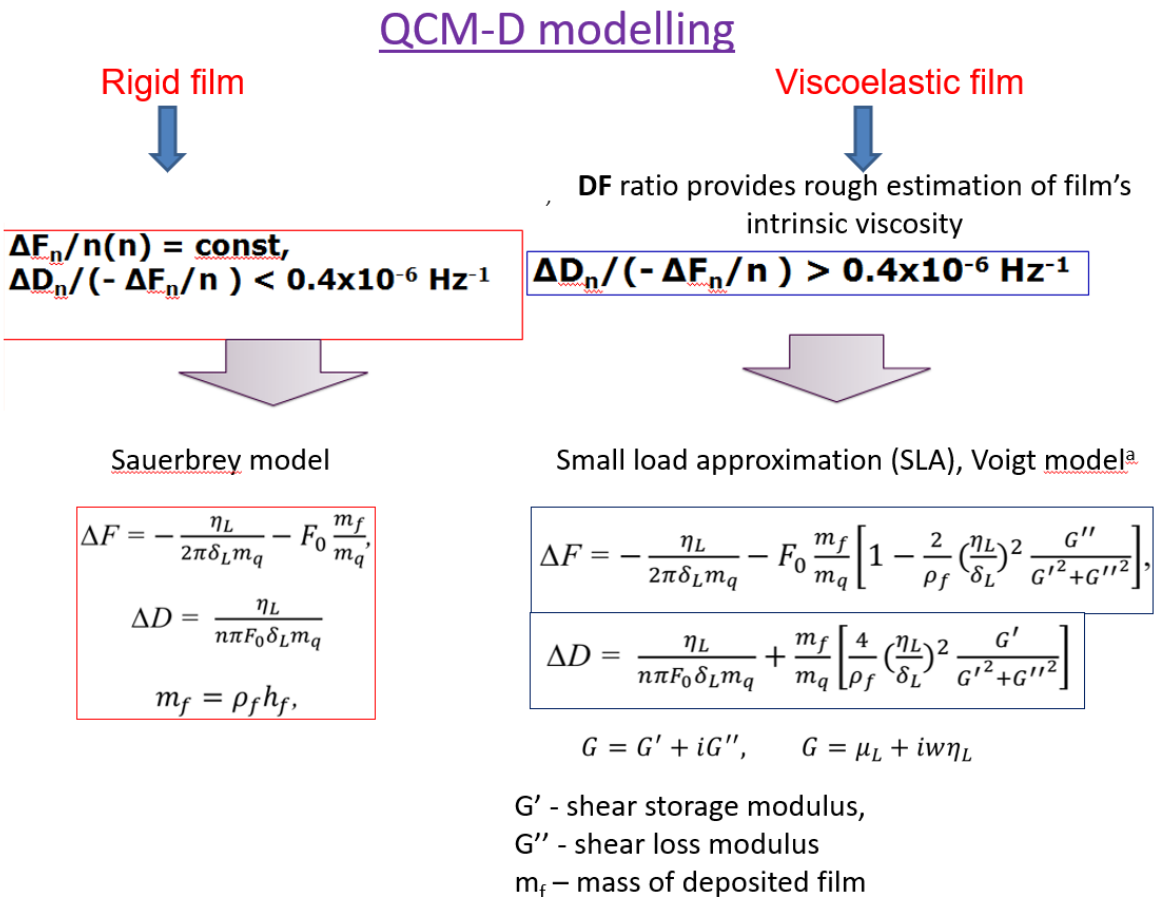

Figure A38: QCM-D modelling principles.

Below viscoelastic modeling of **QCM-**D data by QTM (SLA model) are presented for the following brushes: PEG+monocarboxy terminated PNIPAM (PEG_PNIPAM_1x, Figure 2), monocarboxy (PNIPAM_1x, Figure 3) and dicarboxy (PNIPAM_2x, Figure 4.) terminated PNIPAM and PEG (Figure 5).

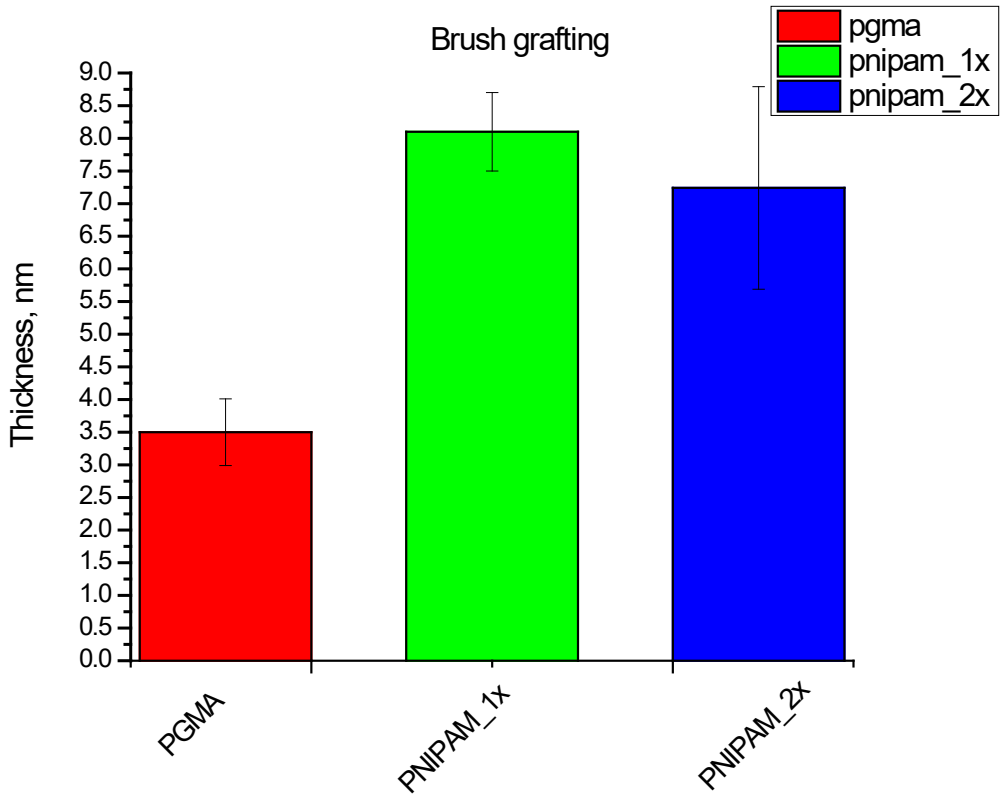

Figure A39: Thickness of thin films grafted to SiO_2/Si substrate as measured by single wavelength ellipsometer.

Table A6: The results of modelling based on small load approximation (SLA) approach.

Polymer brush		G_0' (MPa)	G_0'' (MPa)	$\|G^*\|$ (MPa)
PNIPAAM_1x	*25°C*	0.51 ± 0.21	0.48 ± 0.11	0.71 ± 0.23
	37°C	0.75 ± 0.18	0.73 ± 0.13	1.07 ± 0.03
PNIPAAM_2x	*25°C*	0.35 ± 0.14	0.38 ± 0.07	0.53 ±0.08
	37°C	0.76 ± 0.12	1.06 ± 0.05	1.3 ± 0.07
PEG	*25°C*	0.22	0.49	0.53
	37°C	0.18	0.36	0.40
PNIPAAM_1x/PEG	*25°C*	0.33 ± 0.01	0.98 ± 0.45	1.04 ± 0.43
	37°C	0.29 ± 0.21	0.88 ± 0.35	0.97 ± 0.23
PNIPAAM_2x/PEG	*25°C*	0.52 ± 0.25	0.54 ± 0.14	0.75 ± 0.26
	37°C	0.48 ± 0.23	0.45 ± 0.09	0.66 ± 0.23

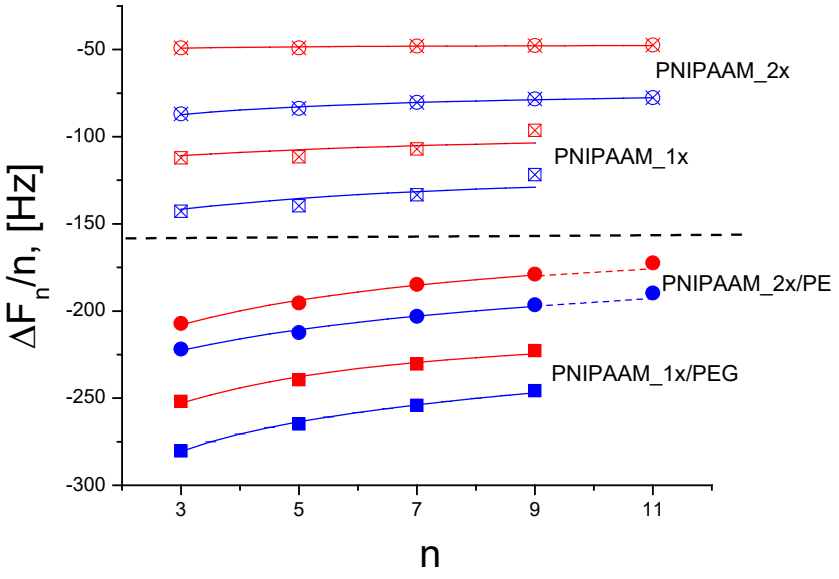

Figure A40: The dependency of normalized frequency upon overtone number (n) indicating a viscoelastic nature of grafted polymer brushes.

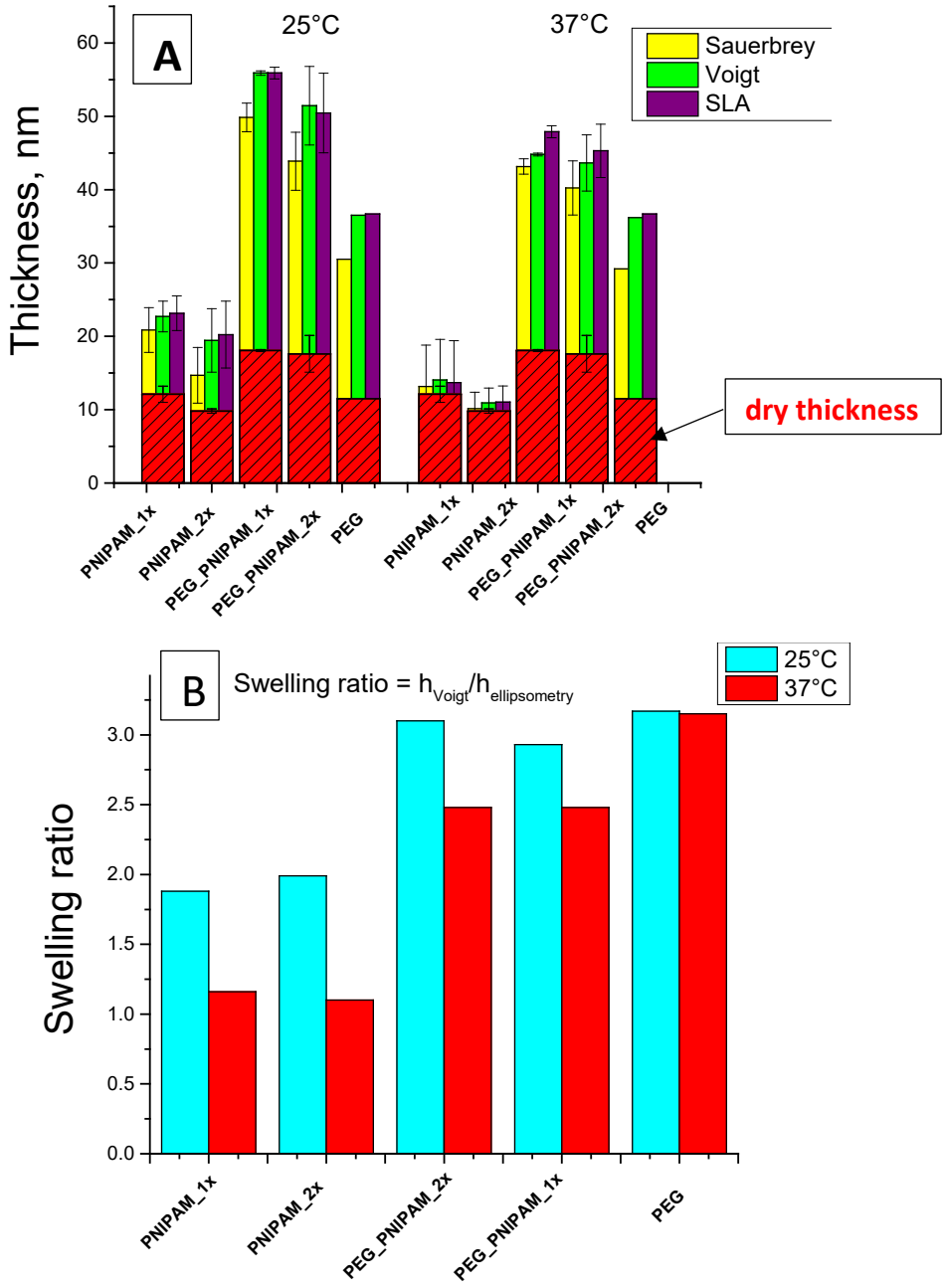

Figure A41: (A) Thickness change upon brush swelling in water and (B) swelling ratio of homo and mixed polymer brushes during temperature change. "Dry thickness" was found from ellipsometry. The results (A) show good correlation between viscoelastic Voigt and SLA models while Sauerbrey model underestimated thickness of polymer brushes.

Adsorption of fibrinogen protein to PNIPAM homobrush

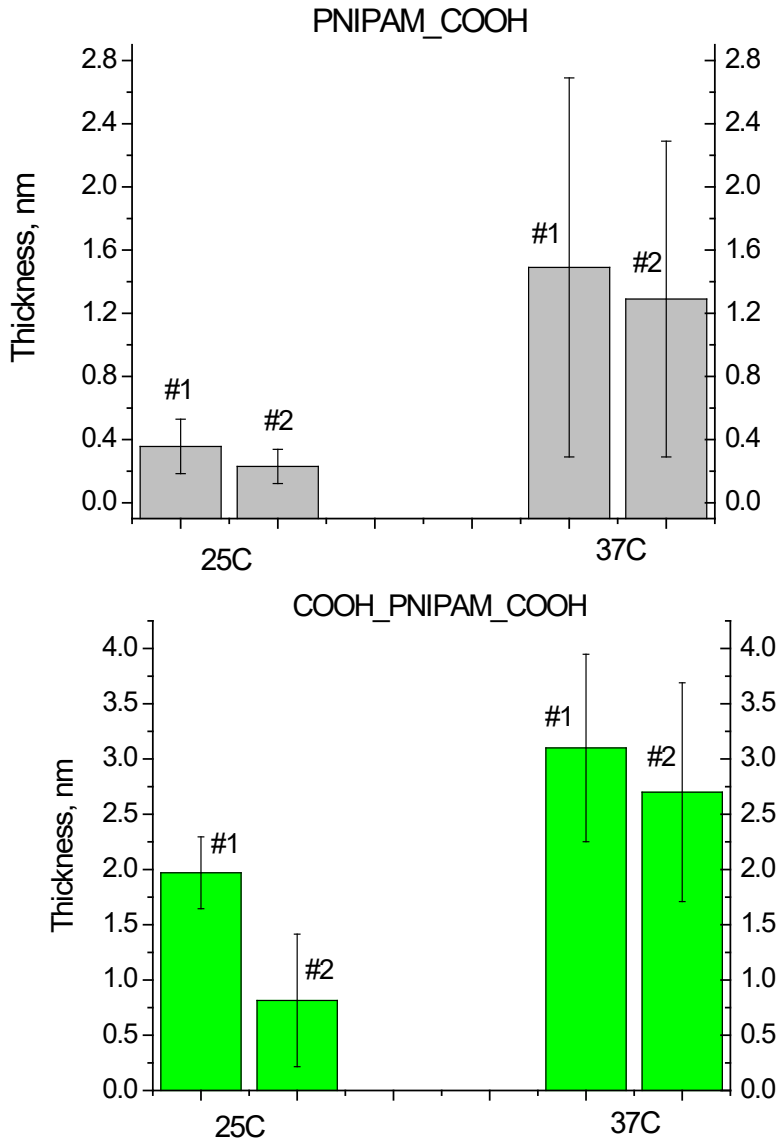

Figure A42: PNIPAM homobrush. Adsorption studies of Fibrinogen protein to mixed

Viscoelastic properties of Fbg adsorbed on PNIPAM_1x homobrush

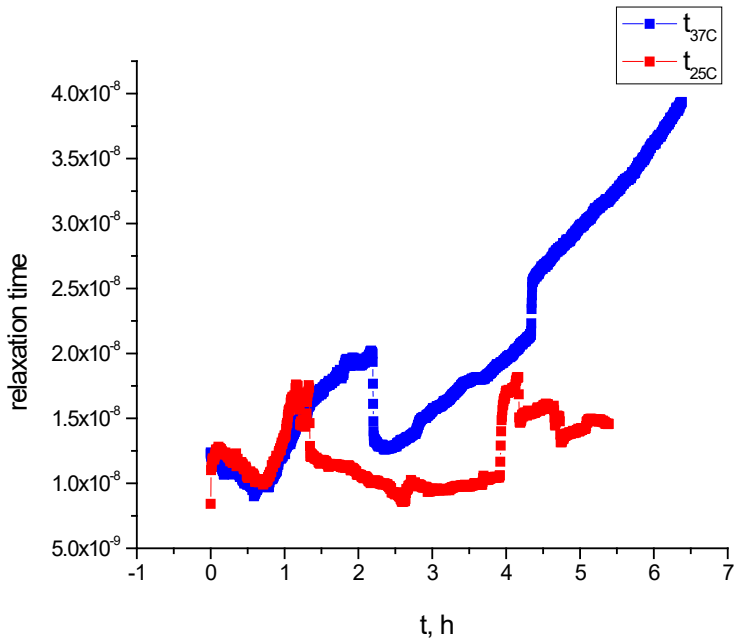

Figure A43: Relaxation time of Fibrinogen adsorbed onto carboxy-terminated PNIPAM homobrush above LCST (37 ºC) and below LCST (25 ºC). Higher relaxation time indicates more compact structure/morphology (less dissipative) of the protein or tighter binding with the surface.

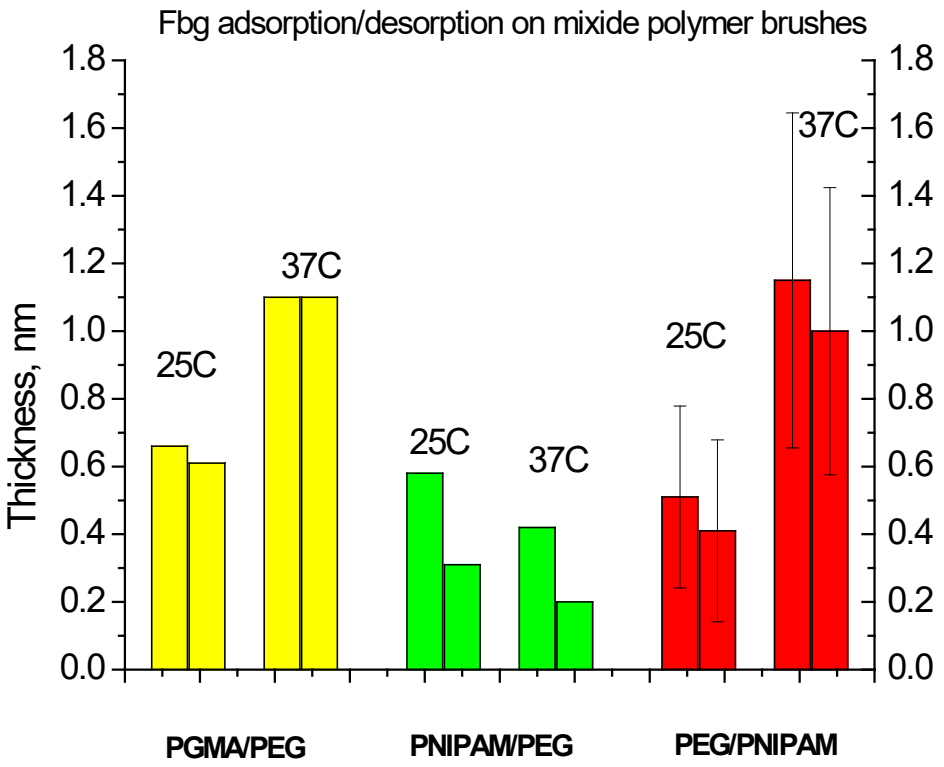

Figure A44: PNIPAM/PEG mixed polymer brushes. Adsorption studies of Fibrinogen protein to mixed polymer brushes.

Fabric Modification with Nanocellulosic Fibers as Functional Carriers

Grinded from inexpensive pulp sheets, cellulose powders are processed *via* high-pressure homogenization, which produces a stable nanocrystalline (NC) hydrogel containing NC fibers. The prepared nanocellulose fibers exhibit a gel-like appearance, which remains stable and shows no signs of phase separation or precipitation after several months.

- **<u>Homogenization Process:</u>**

Grinded from inexpensive pulp sheets, cellulose powders are processed *via* high-pressure homogenization, which produces a stable NC hydrogel containing NC fibers. The prepared nanocellulose fibers exhibit a gel-like appearance, which remains stable and shows no signs of phase separation or precipitation after several months

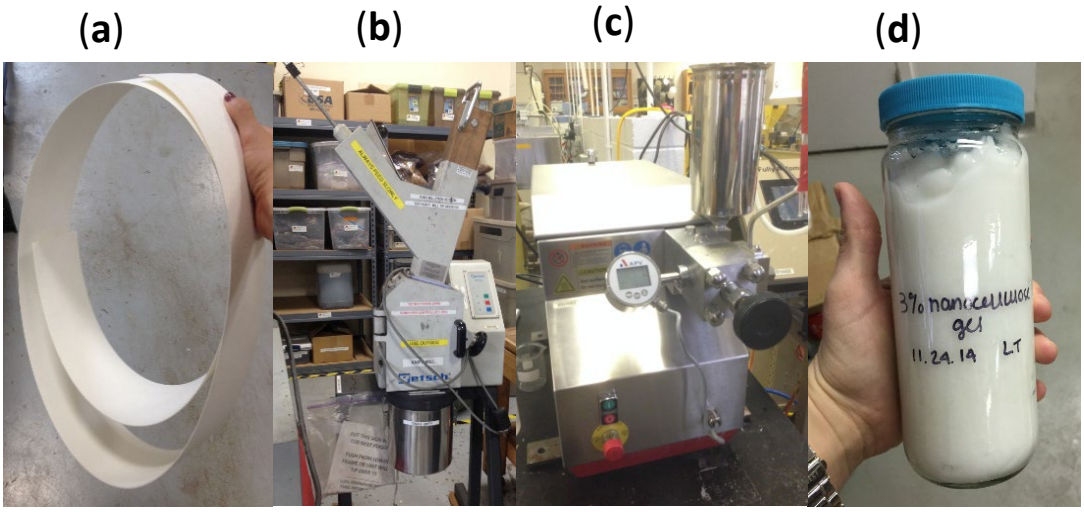

Figure A45: **Manufacturing of NC fiber gel**. (**a**) cellulose pulp sheet, (**b**) knife mill, (**c**) homogenizer, and (**d**) stable hydrogel containing nanocellulose fibers.

- **<u>Nanofibril cellulose (NFC) vs crystalline nanocellulose (CNC):</u>**

Main focus of a project: innovative approach to fabric dyeing using nano-cellulose

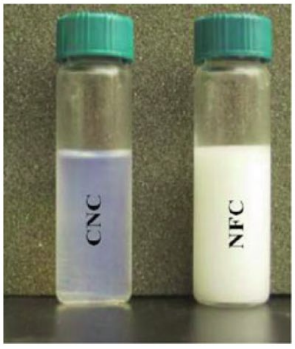

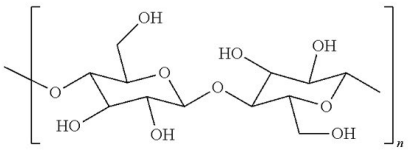

Size distribution of NFC and CNC by volume (by DLS)

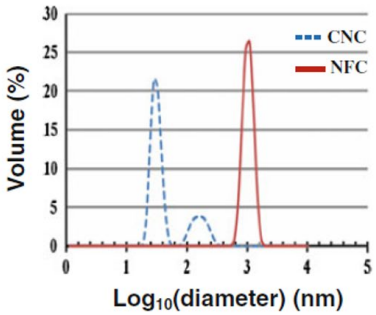

NFC: 712 – 1484 nm

CNC: 76%: 21–51 nm
24%: 79–342 nm

Data provided by Dr. Yucheng Peng

- Hydroxyl functionalities that can covalently bond with the conventional reactive dye moieties
- CNC does not have adhesive properties due to the absence of hemicellulosic amorphous part

- **NFC and CNC structure and morphology (AFM studies):**

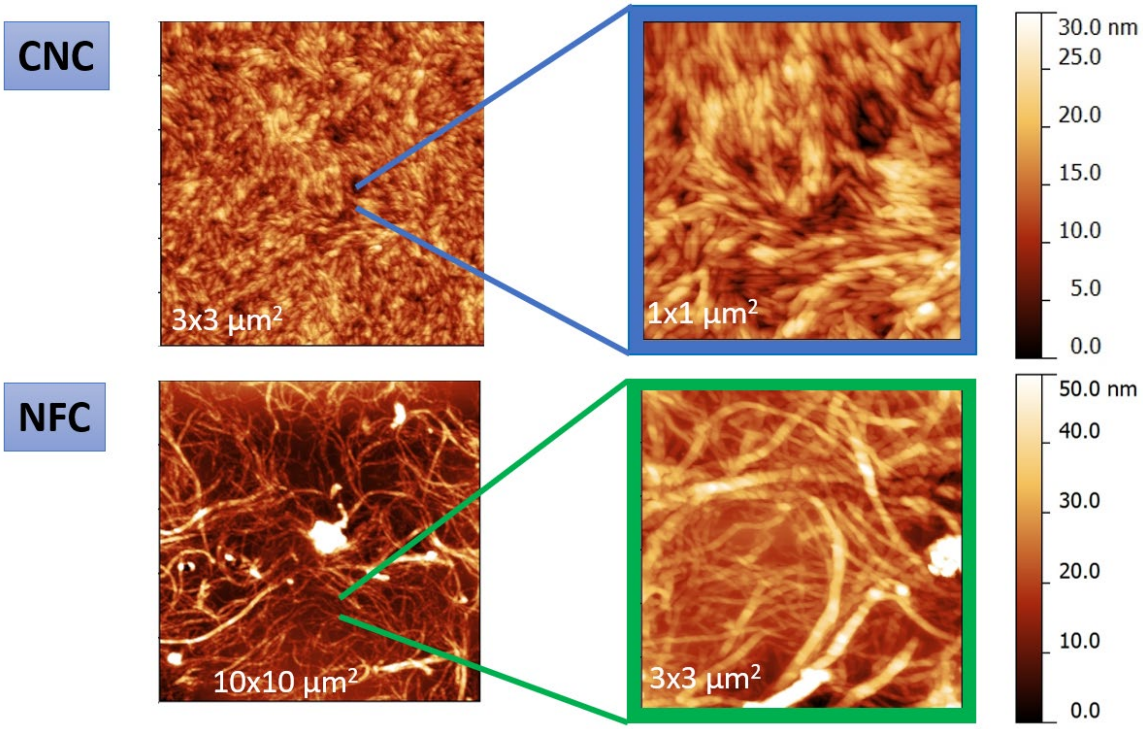

Figure A45: AFM images of dropcasted and dried CNC and NFC cellulose on silicon wafer.

The surfaces of dried CNC were much smoother than those of NFC, indicating a denser packing for CNC. This is attributed to the much smaller size of cellulose nanocrystals in the suspensions compared with that of NFC

- **Pad dying process**

NC gel is mixed with reactive dyes and dye auxiliaries, and subsequently applied to cotton fabric by pad dyeing or printing method. Thermal curing at 120°C completes the coloration of cotton fabrics.

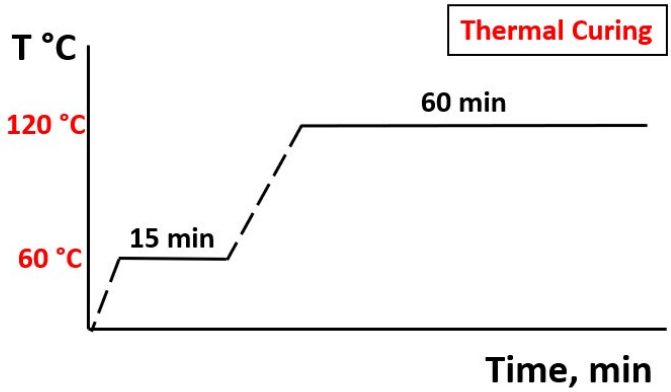

Before

After Washing

- **NFC test results:**

The performance of dyeing is assessed by dye exhaustion and dye fixation:

1) Commercially available reactive red 120 (chemical structure shown in Figure 2a) is selected because of high reactivity with cellulosic fibers
2) Dye exhaustion is a measure of how many dye molecules are consumed and absorbed to textile fibers during dyeing process, which is determined by the ratio between the absorbance of dyeing solution associated with dye molecule employed before and after dyeing process.
3) Dye fixation is a measure of how many dye molecules are permanently fixed on fabric surfaces during dyeing process, which is determined by the ratio between the color strength of colored fabrics associated with dye molecule employed before and after soaping process.

The performance of dyeing is assessed by dye exhaustion and dye fixation:

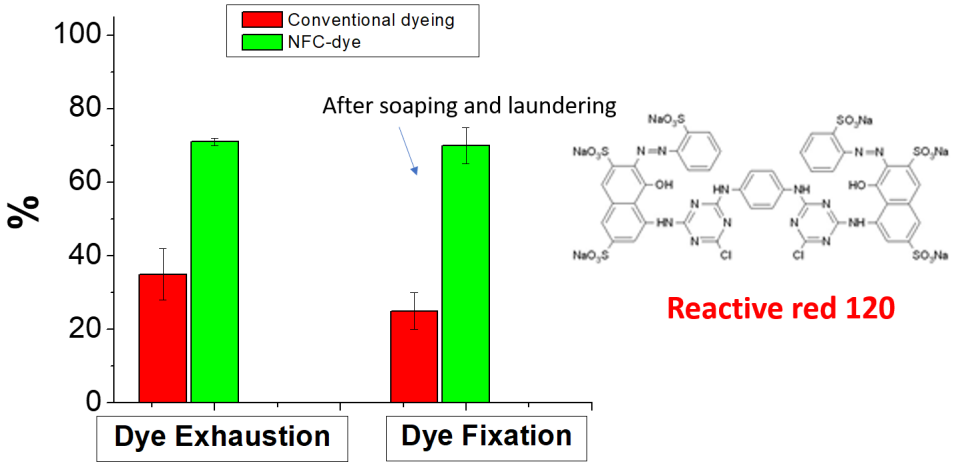

- Concentration of dye in **effluent** during dyeing and rinsing processes is greatly decreased
- The dye exhaustion and dye fixation for NC-dye-based dyeing surpasses traditional technology due to the high specific area and high chemical reactivity of NC to dyes.

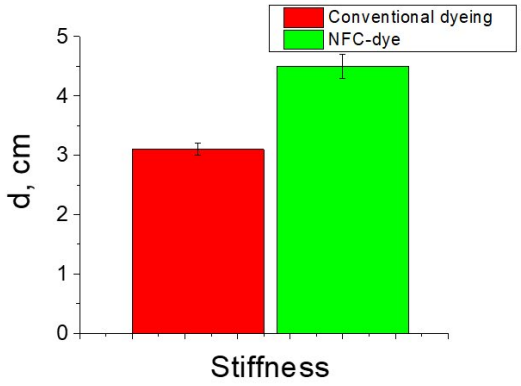

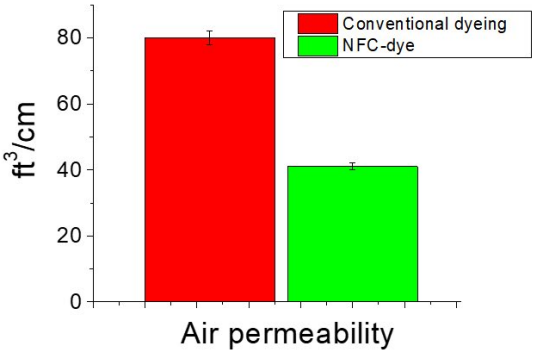

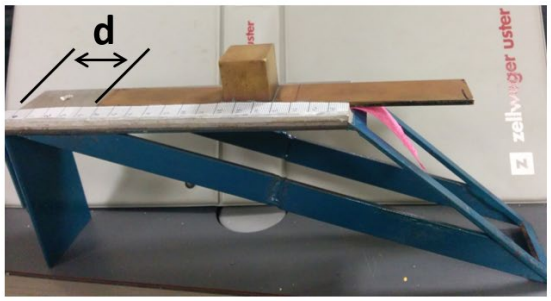

➢ **<u>Surface modification of NFC by POEGMA copolymer (type I):</u>**

Can we further improve dye fixation and decrease stiffness of the fabric?

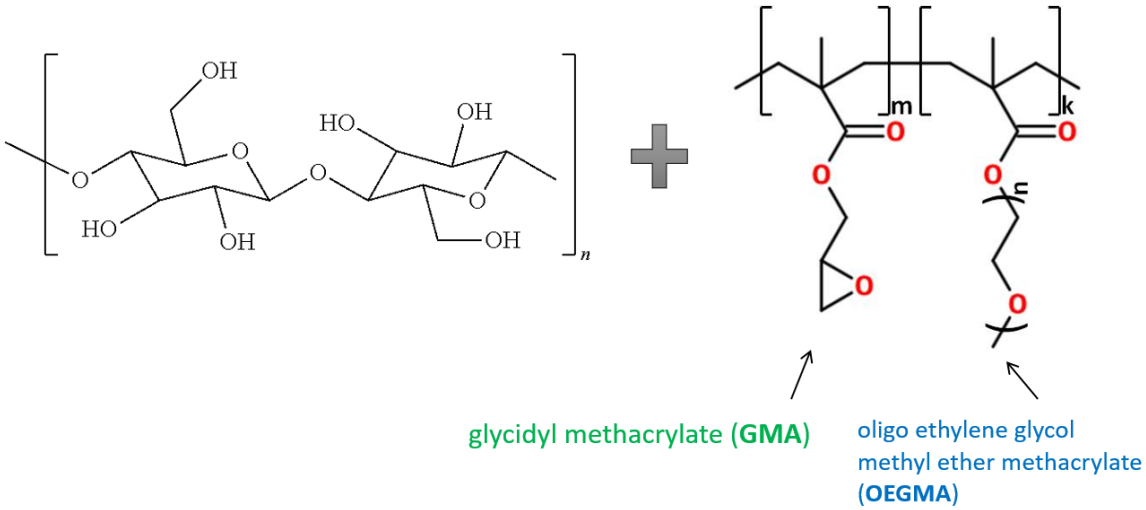

- Types of bonding between NFC and POEGMA:
  1) non-condensation reaction btw epoxy and –OH
  2) H-bonding

➢ **NFC-POEGMA structure and morphology (FTIR, AFM and SEM studies)**

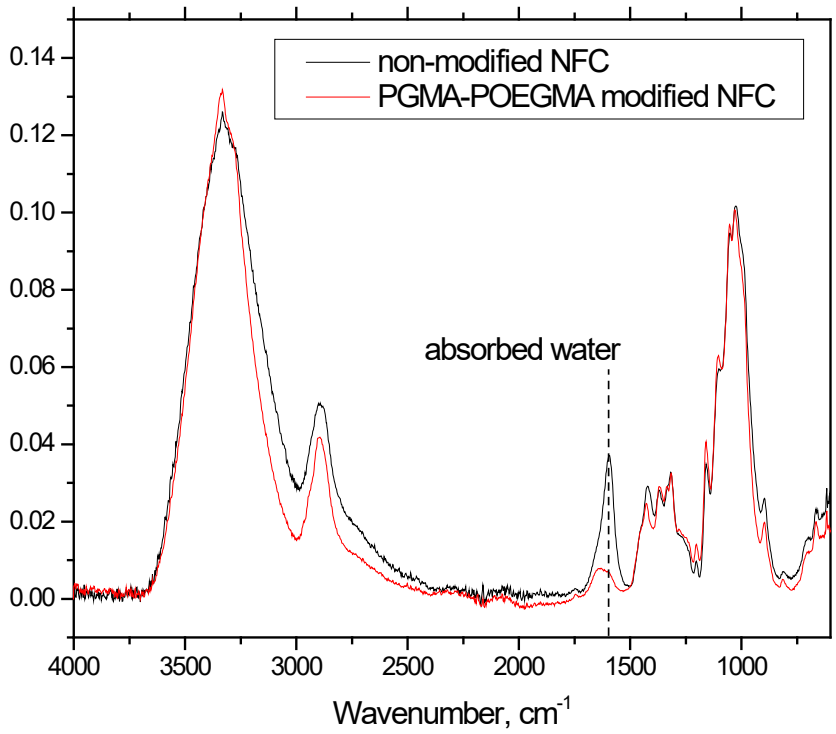

	water	CH
Non-modified	24.4	22.9
modified	6.0	26.2

The disappearing band (11595 cm^{-1}) is related to the absorbed water. After modification with POEGMA those sites become unavailable, thus less water can be bound to NFC

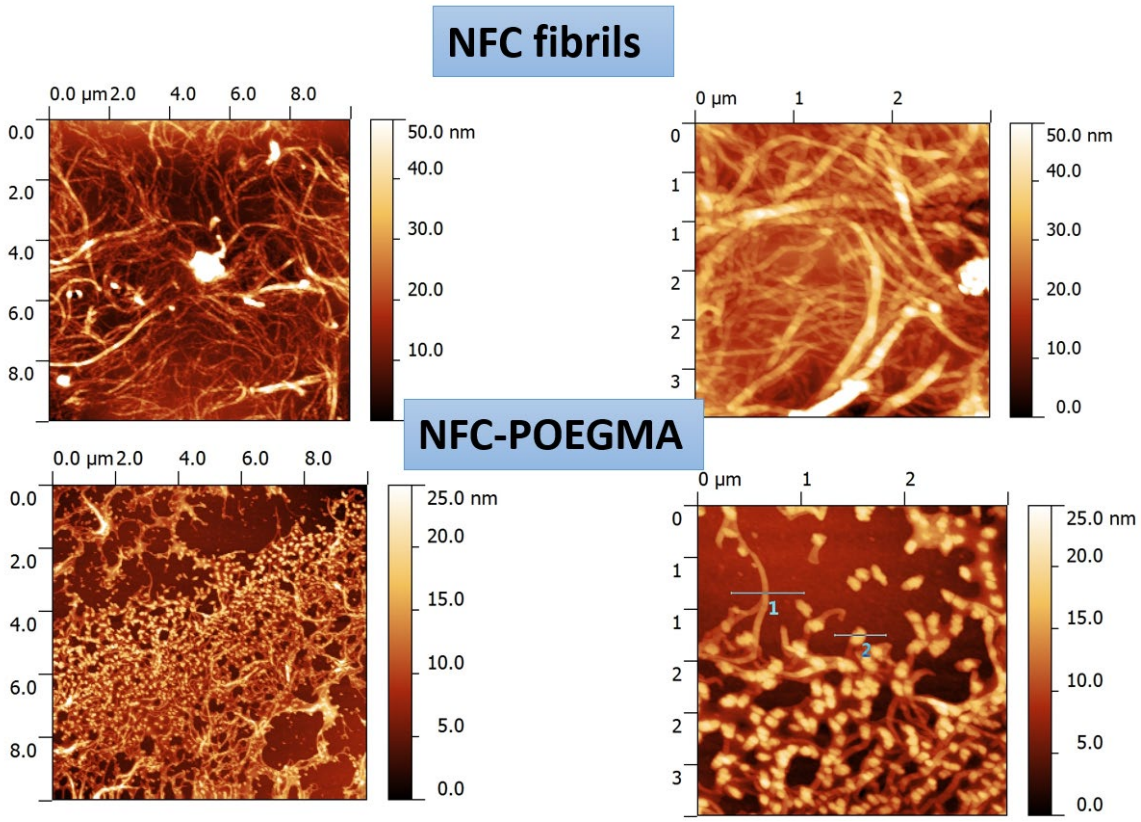
NFC fibrils
0.0 µm 2.0 4.0 6.0 8.0
0.0
2.0
4.0
6.0
8.0
50.0 nm
40.0
30.0
20.0
10.0
0 µm 1 2
0
1
1
2
2
3
50.0 nm
40.0
30.0
20.0
10.0
0.0
NFC-POEGMA
0.0 µm 2.0 4.0 6.0 8.0
0.0
2.0
4.0
6.0
8.0
25.0 nm
20.0
15.0
10.0
5.0
0.0
0 µm 1 2
0
1
1
2
2
3
1
2
25.0 nm
20.0
15.0
10.0
5.0
0.0

NFC on cotton fabric

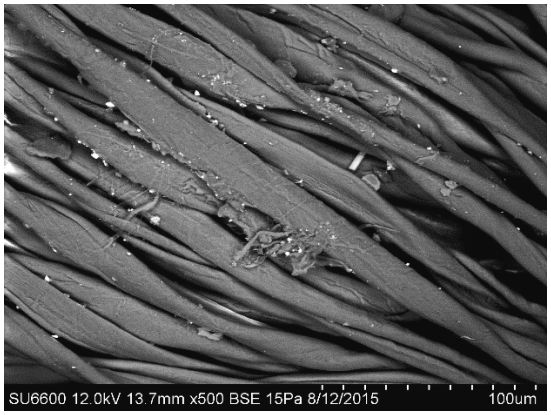

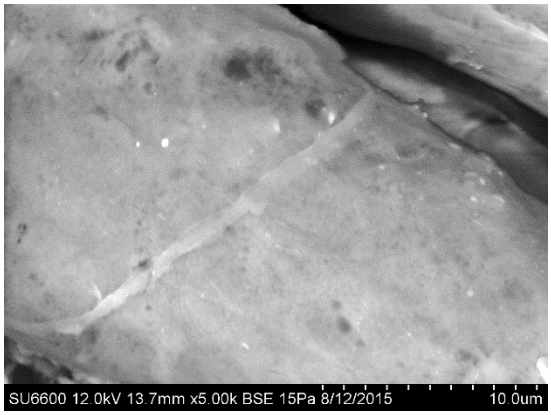

NFC-POEGMA on cotton fabric

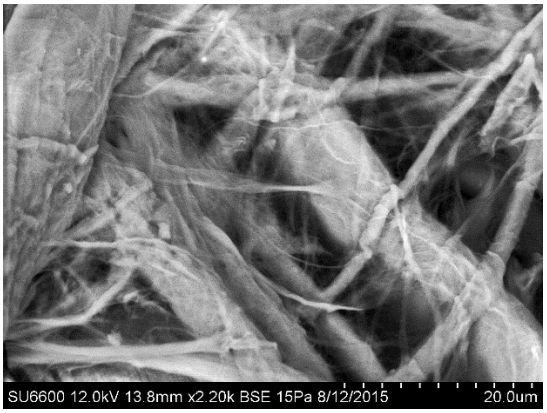

➢ **NFC-POEGMA test results:**

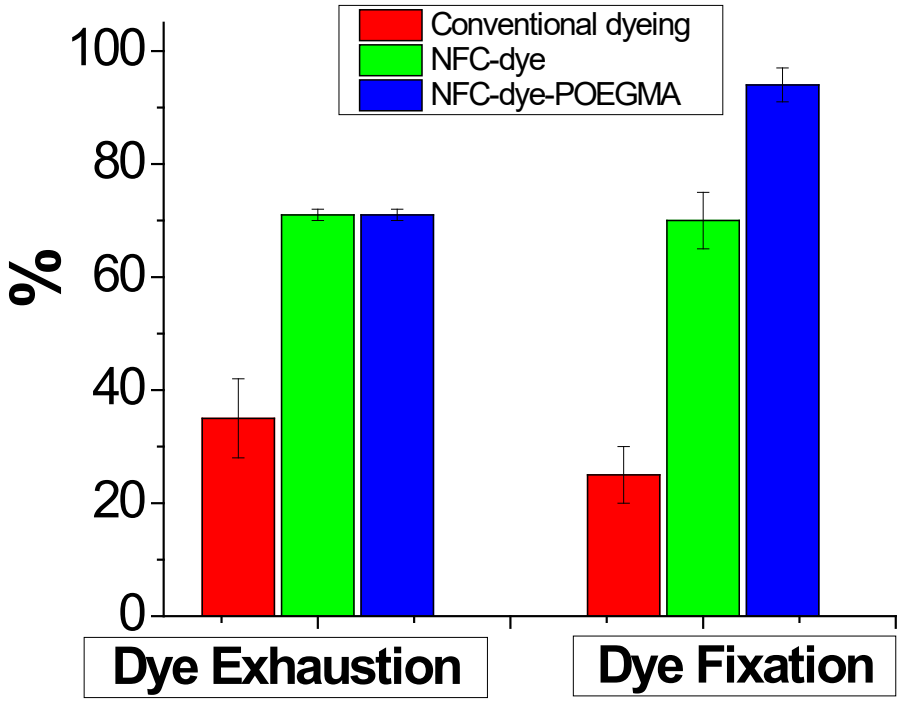

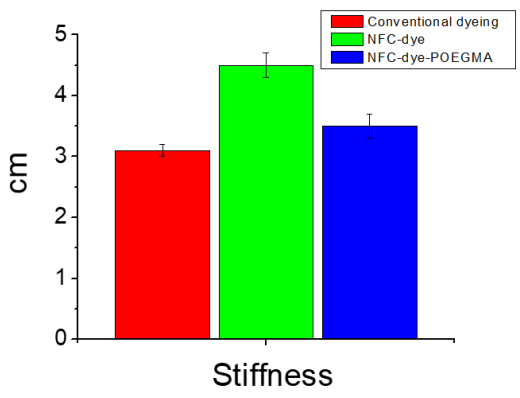

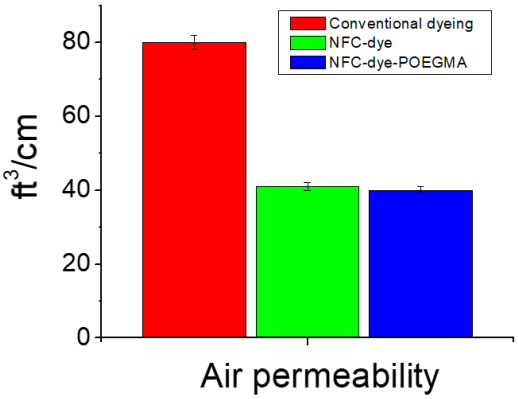

Colofastness to laundering

		Initial NFC	Initial NFC_P	Washed NFC	Washed NFC_P	%changed NFC	%changed NFC_P
Cotton	Lightness	61.87	66.91	71.47	67.82	-15.52	-1.36
Cotton	Redness	39.96	33.27	24.82	32.26	37.89	3.04
PET	Lightness	71.09	69.91	76.62	71.57	-7.78	-2.37
PET	Redness	18.46	20.19	8.56	15.57	53.63	22.88
Nylon	Lightness	71.61	73.02	77.06	73.19	-7.61	-0.23
Nylon	Redness	21.05	20.92	12.96	19.47	38.43	6.93

CROCKING test

NFC

Before washing

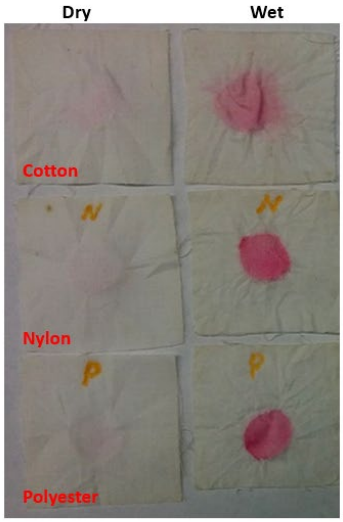

After washing

NFC_POEGMA

Before washing

After washing

50 cycles

CROCKING test results

		reference NFC	reference NFC_P	dry NFC	dry NFC_P	wet NFC	wet NFC_P
Cotton	Lightness	61.87	66.91	81.61	82.62	74.38	74.45
Cotton	Redness	39.96	33.27	2.77	2.3	15.48	17.57
washing							
Cotton	Lightness	71.47	67.82	83.19	82.07	78.42	76.16
Cotton	Redness	24.82	32.26	0.76	3.06	9.48	15.11

Abrasion test

Cotton

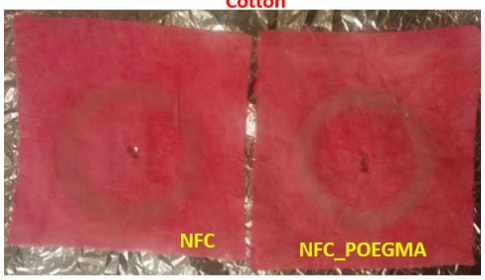

Nylon

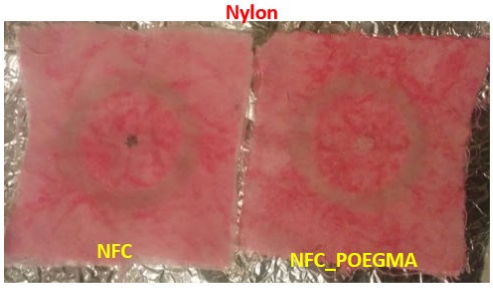

Type of weel used: Calibrase CS-10

Determination of the abrasion resistance of textile fabrics
Using the rotary platform, double-head tester (RPDH)

Polyester

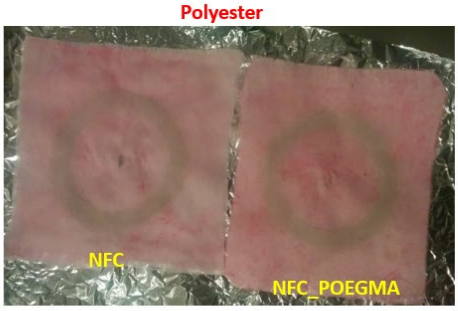

The number of revolutions was kept at 100 for each specimen →

Conclusions

- Using NC-dye the performance of dyeing is substantially improved: about 70% of the dye was bound while only 30% was lost.
- All fabrics modified with NFC_POEGMA retain more color even after washing as compare to NFC.
- The experiments demonstrate 100 fold lower rate of waste water as compared with a traditional dyeing technology (1:2 ratio)
- Relatively high stiffness of fabric with NFC-dye-POEGMA is another issue which needs more thorough investigation

Methodology and Experiments

- **Modification of NFC with POEGMA (poly oligo ethylene glycol methyl ether methacrylate):**
  - Gel of dyed fibril nanocellulose (NFC_red) was diluted 10 times in water and then mixed with 0.5 % PGMA-POEGMA **(**for polyester - PGMA-POEGMA with slightly less M_w) in DI water in ratio 1:1. After that it was kept at room temperature on orbital shaker at least for 4 hrs to let polymer adsorb to the surface of NFC.
  - All NFC solutions have been centrifuged 3 times before modification and thoroughly rinsed with water to remove all free dye.
  - Each piece of fabric has been soaked in NFC/NFC_P solution for two hours, then roller squeegee at 30 psi of hydraulic pressure were used for pushing excess

solution off the fabric. Afterwards, samples were dried in the oven at 60 ℃ for 15 min and at 120 ℃ for 1 hour subsequently.

- **Colorfastness to laundering:** AATCC test method 61, test No. 1A
- **Stiffness test:** Cantilever method (Shirley stiffness tester)
- **Air permeability:** ASTM D737-96
- **Colorfastness to crocking:** AATCC test method 8 (dry and wet crock testing)
- **Abrasion test:** rotary platform, double-head method; ASTM test method D 3884

References

1. Tuinstra, F.; Koenig, J. L., RAMAN SPECTRUM OF GRAPHITE. *Journal of Chemical Physics* **1970,** *53* (3), 1126-&.

2. Perrozzi, F.; Prezioso, S.; Ottaviano, L., Graphene oxide: from fundamentals to applications. *Journal of Physics-Condensed Matter* **2015,** *27* (1), 21.

3. Pimenta, M. A.; Dresselhaus, G.; Dresselhaus, M. S.; Cancado, L. G.; Jorio, A.; Saito, R., Studying disorder in graphite-based systems by Raman spectroscopy. *Physical Chemistry Chemical Physics* **2007,** *9* (11), 1276-1291.

4. Gomez-Navarro, C.; Weitz, R. T.; Bittner, A. M.; Scolari, M.; Mews, A.; Burghard, M.; Kern, K., Electronic transport properties of individual chemically reduced graphene oxide sheets. *Nano Letters* **2007,** *7* (11), 3499-3503.

5. Landau, L. D.; Lifshitz, E. M.; Kosevich, A. M.; Sykes, J. B.; Pitaevskii, L. P.; Reid, W. H., *Theory of Elasticity*. Elsevier Science: 1986.

6. Abid; Sehrawat, P.; Islam, S. S.; Mishra, P.; Ahmad, S., Reduced graphene oxide (rGO) based wideband optical sensor and the role of Temperature, Defect States and Quantum Efficiency. *Scientific Reports* **2018,** *8* (1), 3537.

7. Acik, M.; Lee, G.; Mattevi, C.; Pirkle, A.; Wallace, R. M.; Chhowalla, M.; Cho, K.; Chabal, Y., The Role of Oxygen during Thermal Reduction of Graphene Oxide Studied by Infrared Absorption Spectroscopy. *The Journal of Physical Chemistry C* **2011,** *115* (40), 19761-19781.

8. Fernandes, G. E.; Kim, J. H.; Oller, D.; Xu, J., Reduced graphene oxide mid-infrared photodetector at 300 K. *Applied Physics Letters* **2015,** *107* (11), 111111.

9. Velasco-Soto, M. A.; Pérez-García, S. A.; Alvarez-Quintana, J.; Cao, Y.; Nyborg, L.; Licea-Jiménez, L., Selective band gap manipulation of graphene oxide by its reduction with mild reagents. *Carbon* **2015,** *93* (Supplement C), 967-973.

10. Youn, H.-C.; Bak, S.-M.; Kim, M.-S.; Jaye, C.; Fischer, D. A.; Lee, C.-W.; Yang, X.-Q.; Roh, K. C.; Kim, K.-B., High-Surface-Area Nitrogen-Doped Reduced Graphene Oxide for Electric Double-Layer Capacitors. *ChemSusChem* **2015,** *8* (11), 1875-1884.

11. Bonaccorso, F.; Sun, Z.; Hasan, T.; Ferrari, A. C., Graphene photonics and optoelectronics. *Nature Photonics* **2010,** *4*, 611.

12. Liang, H., Mid-infrared response of reduced graphene oxide and its high-temperature coefficient of resistance. *AIP Advances* **2014,** *4* (10), 107131.

13. Al-Hamry, A.; Sharma, R.; Mueller, C.; Kanoun, O. In *Near Infrared sensor based on Graphene Nanomaterials on Flexible Substrates*, Sensors and Measuring Systems 2014; 17. ITG/GMA Symposium, 3-4 June 2014; 2014; pp 1-6.

14. Tang, L.; Ji, R.; Li, X.; Bai, G.; Liu, C. P.; Hao, J.; Lin, J.; Jiang, H.; Teng, K. S.; Yang, Z.; Lau, S. P., Deep Ultraviolet to Near-Infrared Emission and Photoresponse in Layered N-Doped Graphene Quantum Dots. *ACS Nano* **2014,** *8* (6), 6312-6320.

15. Sassi, U.; Parret, R.; Nanot, S.; Bruna, M.; Borini, S.; De Fazio, D.; Zhao, Z.; Lidorikis, E.; Koppens, F. H. L.; Ferrari, A. C.; Colli, A., Graphene-based mid-infrared room-temperature pyroelectric bolometers with ultrahigh temperature coefficient of resistance. *Nature Communications* **2017,** *8*, 14311.

16. Kruse, P. W., A comparison of the limits to the performance of thermal and photon detector imaging arrays. *Infrared Physics & Technology* **1995,** *36* (5), 869-882.

17. Bae, J. J.; Yoon, J. H.; Jeong, S.; Moon, B. H.; Han, J. T.; Jeong, H. J.; Lee, G.-W.; Hwang, H. R.; Lee, Y. H.; Jeong, S. Y.; Lim, S. C., Sensitive photo-thermal response of graphene oxide for mid-infrared detection. *Nanoscale* **2015,** *7* (38), 15695-15700.

18. Du, X.; Prober Daniel, E.; Vora, H.; McKitterick Christopher, B., Graphene-based Bolometers. In *Graphene and 2D Materials*, 2014; Vol. 1.

19. Hazra, K.; Sion, N.; Yadav, A.; McLauhglin, J.; Misra, D., *Vertically aligned graphene based non-cryogenic bolometer*. 2013.

20. Koh, A.; Gutbrod, S. R.; Meyers, J. D.; Lu, C.; Webb, R. C.; Shin, G.; Li, Y.; Kang, S.-K.; Huang, Y.; Efimov, I. R.; Rogers, J. A., Ultrathin Injectable Sensors of Temperature, Thermal Conductivity, and Heat Capacity for Cardiac Ablation Monitoring. *Advanced healthcare materials* **2016,** *5* (3), 373-381.

21. Richards, P. L.; McCreight, C. R., Infrared Detectors for Astrophysics. *Physics Today* **2005,** *58* (2), 41-47.

22. Meijer, G. C. M., Smart sensor systems. **2008**.

23. Rudol, P.; Doherty, P., *Human Body Detection and Geolocalization for UAV Search and Rescue Missions Using Color and Thermal Imagery*. 2008; p 1-8.

24. Simon, I.; Arndt, M., Thermal and gas-sensing properties of a micromachined thermal conductivity sensor for the detection of hydrogen in automotive applications. *Sensors and Actuators A: Physical* **2002,** *97-98*, 104-108.

25. Yun, J.; Lee, S.-S. Human Movement Detection and Identification Using Pyroelectric Infrared Sensors. Sensors 2014, 14, 8057-8081

26. Vadnala, S.; Paul, N.; Agrawal, A.; Singh, S. G., Enhanced infrared sensing properties of vanadium pentoxide nanofibers for bolometer application. *Materials Science in Semiconductor Processing* **2018,** *81*, 82-88.

27. Zhang, L.; Shi, Z.; Wang, Y.; Yang, R.; Shi, D.; Zhang, G., Catalyst-free growth of nanographene films on various substrates. *Nano Research* **2011,** *4* (3), 315-321.

28. Shao, Q.; Liu, G.; Teweldebrhan, D.; Balandin, A. A., High-temperature quenching of electrical resistance in graphene interconnects. *Applied Physics Letters* **2008,** *92* (20), 202108.

29. http://www.dolan-jenner.com/hubfs/products/illuminators/model-190-data-sheet.pdf

30. Tian, H.; Cao, Y.; Sun, J.; He, J., Enhanced broadband photoresponse of substrate-free reduced graphene oxide photodetectors. *RSC Advances* **2017,** *7* (74), 46536-46544.

31. Chauhan, S. S.; Abraham, M.; Choudhary, V., Electromagnetic shielding and mechanical properties of thermally stable poly(ether ketone)/multi-walled carbon nanotube composites prepared using a twin-screw extruder equipped with novel fractional mixing elements. *RSC Adv.* **2016,** *6* (114), 113781-113790.

32. Anh Son, H., Electrical conductivity and electromagnetic interference shielding characteristics of multiwalled carbon nanotube filled polyurethane composite films. *Advances in Natural Sciences: Nanoscience and Nanotechnology* **2011,** *2* (2), 025007.

33. Hu, M. J.; Gao, J. F.; Dong, Y. C.; Li, K.; Shan, G. C.; Yang, S. L.; Li, R. K. Y., Flexible Transparent PES/Silver Nanowires/PET Sandwich-Structured Film for High-Efficiency Electromagnetic Interference Shielding. *Langmuir* **2012,** *28* (18), 7101-7106.

34. Bright, C. I.; Le, J. D.; Fitzer, R. C.; Maki, S. P., Ultrathin transparent EMI shielding film comprising a polymer basecoat and crosslinked polymer transparent dielectric layer. Google Patents: 2013.

35. Chaudhary, A.; Kumar, R.; Teotia, S.; Dhawan, S. K.; Dhakate, S. R.; Kumari, S., Integration of MCMBs/MWCNTs with Fe3O4 in a flexible and light weight composite paper for promising EMI shielding applications. *Journal of Materials Chemistry C* **2017,** *5* (2), 322-332.

36. Gulrez, S. K. H.; Ali Mohsin, M. E.; Shaikh, H.; Anis, A.; Pulose, A. M.; Yadav, M. K.; Qua, E. H. P.; Al-Zahrani, S. M., A review on electrically conductive polypropylene and polyethylene. *Polymer Composites* **2014,** *35* (5), 900-914.

37. Hong, S. K.; Kim, K. Y.; Kim, T. Y.; Kim, J. H.; Park, S. W.; Kim, J. H.; Cho, B. J., Electromagnetic interference shielding effectiveness of monolayer graphene. *Nanotechnology* **2012,** *23* (45), 5.

38. Wu, Z. P.; Cheng, D. M.; Ma, W. J.; Hu, J. W.; Yin, Y. H.; Hu, Y. Y.; Li, Y. S.; Yang, J. G.; Xu, Q. F., Electromagnetic interference shielding effectiveness of composite carbon nanotube macro-film at a high frequency range of 40 GHz to 60 GHz. *AIP Advances* **2015,** *5* (6), 067130.

39. Wei, C.; Jun, W.; Bin, Z.; Qilei, W.; Xiaogang, S., Enhanced electromagnetic interference shielding properties of carbon fiber veil/Fe 3 O 4 nanoparticles/epoxy multiscale composites. *Materials Research Express* **2017,** *4* (12), 126303.

40. Kim, S.; Oh, J.-S.; Kim, M.-G.; Jang, W.; Wang, M.; Kim, Y.; Seo, H. W.; Kim, Y. C.; Lee, J.-H.; Lee, Y.; Nam, J.-D., Electromagnetic Interference (EMI) Transparent Shielding of Reduced Graphene Oxide (RGO) Interleaved Structure Fabricated by Electrophoretic Deposition. *ACS Applied Materials & Interfaces* **2014,** *6* (20), 17647-17653.

41. Sarto, F.; Sarto, M. S.; Larciprete, M. C.; Sibilia, C., TRANSPARENT FILMS FOR ELECTROMAGNETIC SHIELDING OF PLASTICS. *Rev. Adv. Mater. Sci.* **2003,** *5* (4), 329-336.

42. Turko, B.; Kapustianyk, V.; R. Toporovska, L.; P. Rudyk, V.; S. Tsybulskyi, V.; Serkiz, R., *Photoluminescence Study of ZnO Nanostructures Grown by Hydrothermal Method*. 2018; Vol. 10, p 02002-1.